KfK 4438
September 1988

Experimental Investigation on the Structure of Turbulence in Symmetrical Wall Subchannels and Comparison with the Results in an Asymmetrical Channel

S. R. Wu, K. Rehme
Institut für Neutronenphysik und Reaktortechnik

Kernforschungszentrum Karlsruhe

KERNFORSCHUNGSZENTRUM KARLSRUHE

Institut für Neutronenphysik und Reaktortechnik

KfK 4438

Experimental Investigation on the Structure of Turbulence in Symmetrical Wall Subchannels and Comparison with the Results in an Asymmetrical Channel

S.R.Wu* and K.Rehme

Kernforschungszentrum Karlsruhe GmbH, Karlsruhe

* visiting scientist from Institute of Nuclear Energy Technology, Tsing Hua University, Beijing, China.

Als Manuskript vervielfältigt

Kernforschungszentrum Karlsruhe GmbH
Postfach 3640, 7500 Karlsruhe 1

ISSN 0303-4003

Experimental Investigation on the Structure of Turbulence in Symmetrical Wall Subchannels and Comparison with the Results in an Asymmetrical Channel

Abstract

Measurements of the mean velocity, the wall shear stresses, and the turbulent Reynolds stresses were performed in two symmetrical wall subchannels of a rod bundle. The rod bundle of four parallel rods was arranged symmetrically in a rectangular channel with a pitch-to-diameter ratio of P/D = 1.148 and a wall-to-diameter ratio of W/D = 1.045. The Reynolds number of this investigation was $Re = 6.11 \times 10^4$.

The experimental results show that the structure of turbulence in this rod bundles differs greatly from the structure in circular tubes. Especially in the narrow gaps between the rods and the channel walls there are increased levels of turbulent intensities in the axial and azimuthal directions and, hence, of the kinetic energy of turbulence. In contrast to a previous investigation of this geometry, however arranged asymmetrically in the rectangular channel, the momentum transport between the subchannels across the gap between the rods is negligible.

The comparison between experimental wall shear stress distributions and those computed by the VELASCO code shows strong deviations, especially in the gaps between the rods and channel walls.

Experimentelle Untersuchung der Turbulenzstruktur in symmetrischen Wandkanälen und Vergleich mit den Ergebnissen in einem asymmetrischen Kanal

Zusammenfassung

In zwei symmetrischen Wandkanälen eines Stabbündels wurden Geschwindigkeits-, Wandschubspannungsverteilungen und Verteilungen der Reynoldschen Spannungen gemessen. Das Stabbündel aus vier parallelen Stäben war symmetrisch in einem Rechteckkanal mit einem Stababstandsverhältnis von P/D = 1.148 und einem Wandabstandsverhältnis von W/D = 1.045 angeordnet. Die Reynoldszahl der Untersuchung betrug $Re = 6.11 \times 10^4$.

Die Meßergebnisse zeigen, daß die Struktur der Turbulenz in Stabbündeln stark von der Struktur in Kreisrohren abweicht. Besonders im engen Spalt zwischen Stab- und Kanalwänden gibt es erhöhte Turbulenzintensitäten in axialer und azimutaler Richtung und damit auch eine erhöhte kinetische Energie der Turbulenz. Im Gegensatz zur früheren Untersuchung an dieser Geometrie, jedoch in asymmetrischer Anordnung, ist der Impulstransport durch den Spalt zwischen den Stäben vernachlässigbar.

Der Vergleich der gemessenen mit den vom Rechenprogramm VELASCO berechneten Wandschubspannungsverteilungen zeigt starke Abweichungen, insbesondere in den Spalten zwischen Stab- und Kanalwänden.

Experimental Investigation on the Structure of Turbulence in Symmetrical Wall Subchannels and Comparison with the Results in an Asymmetrical Channel

S.R.Wu* and K. Rehme

* visiting scientist from Institute of Nuclear Energy Technology, Tsing Hua University, Beijing, China.

1. Introduction

The prediction of the detailed temperature distribution on the fuel elements in rod bundles is of particular significance in the design, safe and reliable operation and safety analysis of nuclear reactors. The methods of the thermal-hydraulic analysis can be classified into three categories /1/: Subchannel analysis, porous body model analysis, and distributed parameter analysis. Among them, only the distributed parameter analysis method with turbulence models under development /2,3,4/ could be used to calculate detailed velocity and temperature distributions. But the calculated results and their accuracy depend on the accuracy of the turbulence modelling. Empirical information on turbulent momentum and energy transport properties between subchannels is needed for the development of distributed parameter codes. Detailed experimental data of velocity, turbulence and temperature distributions are necessary for validation and improvement of turbulence modelling. For this reason, a series of experimental investigations on flow through subchannels of rod bundles were performed at KfK during the past ten years. An overview is presented in /5/ on the investigations performed, the important observations, and the main impact on turbulence modelling for distributed parameter analysis. A vast amount of valuable data and a profound knowledge on turbulent flow through rod bundles has been achieved.

In the previous work /6/, the experimental results were presented on flow through a wall subchannel with the same pitch-to-diameter ratio of P/D = 1.148 and a wall-to-diameter ratio W/D = 1.045 as in this investigation recently performed. But in that case, the investigated subchannel was located in a

geometrically asymmetrical arangement of subchannels of rod bundle. That means, the investigated wall subchannel was adjacent to a wide subchannel. It has been found that a strong momentum transport from the adjacent wide subchannel obviously affects the flow characteristics in the narrow subchannel. Moreover, in that investigation the Kjellström method /7/ was used to evaluate the measured data. The difficulty in solving the set of six simultaneous equations from the measurements at six different positions of the hot-wire against the flow was overcome by disregarding the shear stress $\overline{v'w'}$. The measurements were performed by traversing the probes by hand in the experiment. Mainly due to above three effects (asymmetry, Kjellström evaluation method and hand travesing of the probes), the accuracy of the experimental results displayed apparent differences from those of the investigation recently performed. In this report, the results of an experimental investigation are presented on the flow through two symmetric wall subchannels of a rod bundle divided into four symmetric quadrants (Q1 to Q4) with a pitch-to-diameter ratio P/D = 1·148 and wall-to-diameter ratio of W/D = 1.045 . In this case, all measurements were performed by a fully automated system controlled by a computer /8/. The full Reynolds stress tensor was measured. Hooper's method /9/ was applied for evaluation of the hot wire data /10/. The results are compared with previous work /6/. The accuracy of the measurement results is remarkably improved and some new observations are achieved.

2. Experimental Setup

The experiment was performed on the computer controlled experimental rig /8/ of KfK-INR with air as the working fluid. Figure 1 shows the schematic of the test rig. Air was taken in through a silencer and entered the test section through a honeycomb grid located in the lower plenum.

The test section consists of a rectangular channel of 151.4x700 mm^2 cross section and a rod bundle of four parallel rods (139.0 mm O.D.) enclosed in the channel. The rods were fixed inside the channel with small pins of 2 mm O.D. as spacers at four levels along the longitudinal axis of the test section. The full length of the test section of L = 7000 mm was made up by four parts each of which had a length equal to 1750 mm. The rods were made of aluminium tubes, the outer surfaces of which were machined. The mean roughness depths of the surface amounted to only 0.6µm. The rod bundle is symmetrically arranged with a

P/D = 1.148 and W/D = 1.045 as shown in Fig. 2. The hydraulic diameter of the investigated wall subchannel was $D_h = 4.65 \times 10^{-2}$m.

The measurements were performed at a level 30 mm upstream of the open outlet, so the ratio of length to hydraulic diameter at the measuring plane was 146.3. Table 1 shows the measured geometry parameters of the four quadrants in detail. It is clear from Tab. 1 that there are only very small deviations from symmetry between the four quadrants due to assembling tolerances.

Each quadrant was divided into two parts by the imaginal line of maximum normal distance from the walls. The measurements were carried out in 8 parts of the four quadrants. The data was recorded in kartesian coordinates in the part close to channel walls and in cylindrical coordinates in the part close to the rod wall with some overlapping.

In order to achieve the necessary accuracy of the gradients of the measured data, the flow cross section was covered by a fine network of mesh points. Measurements were taken on traverses every 5° along the rod walls and every 5 mm along the channel walls at 7 to 20 points on each traverse normal to the walls depending on the width of the flow cross section. The total number of measuring point was about 400 in each quadrant.

The following physical parameters were measured:

1. the time-mean values of the axial velocity measured with a Pitot tube of 0.6 mm diameter,

2. the wall shear stresses measured with a Preston tube using the correlations of Patel /11/, and

3. the turbulence intensities and the full Reynolds stress tensor measured with a single normal hot-wire DISA Model 55P12 and a single slanting wire DISA Model 55P11 and a constant-temperature anemometer bridge DISA Model 55M01.

The nonlinear output signal of the anemometer was used for calculation of the Reynolds stresses. The hot-wire probes were statically calibrated before every time of use.

During the experiment, the Reynolds number remained constant at a fixed point in the channel by setting a reference pressure drop under reference conditions

(p_{ref} = 0.1 MPa, T = 25°C) and automatically adjusting the speed of the blower. The average Reynolds number of this investigation was calculated to:

$$Re = 6.11 \times 10^4$$

The reference condition was defined by T_{ref} = 25°C and p_{ref} = 0.1 MPa, resulting in a reference velocity at the fixed point in the channel of U_{ref} = 27.75 ms^{-1}.

3. Experimental Results and Discussion

All experimental data are corrected to reference conditions. The corrections were discussed in detail in /9,10/. Hooper's method /9/ was used for evaluation of the hot-wire data.

All tabulated results are available from the authors. The axial velocities and turbulence results are shown in complete contour plots of the four quadrants and in linear plots in order to describe the flow characteristics in the field more distinctly.

In this report, the experimental results are discussed in the same sequences of the sections as in /6/ for convenience of comparison.

3.1 Time mean axial velocity

The time-mean axial velocity distribution is shown as a contour-plot (Fig. 5) and in linear-plots. The time-mean axial velocity measured by a Pitot tube is related to the reference velocity at the fixed point under reference conditions in the contour-plots. In the linear-plots, the velocities shown are related to the average velocity in the quadrant. The velocity distributions on each traverse are shown as a function of the relative distance from the wall Y/L (L is distance from the wall to the line of maximum normal distance from the walls). Figures 3-1 to 3-4 show the time-mean velocity distributions along each traverse from the wall in the area near the rod walls in x/y coordinates. (Notice, in this report a number with two digits is used to describe the sequence of the figures. The first digit shows the sequence of the figures and the second digit shows the quadrant number).

Figures 4-1 to 4-4 show the time mean velocity distributions in the area near the channel walls in r/ϕ coordinates. The following characteristics of the time-mean velocity distributions are noticeable:

1. The velocity distributions in the four quadrants show a good symmetry.

2. The lowest velocities are found in the gaps between the rods and channel walls (x = 0 mm, ϕ = 90°).

3. There exists a maximum velocity area near the center of the widest position of the channel, that is at x = 80 mm, ϕ = 35°. The maximum velocities are not found at the intersection point of the lines of maximum normal distance from the walls but with a little deviation towards the channel walls.

4. The smooth velocity contour lines are almost parallel to the walls with quite perfect symmetry.

5. The contour lines are perpendicular to the boundary lines of the subchannel in the gap regions, that means there is no momentum transport by viscous shear stress and a mean velocity gradient between two adjacient subchannels.

6. It can be judged from the trend of the contour lines that there is no significant secondary flow influence.

The average velocities in each part (r/ϕ or x/y) of the four quadrants and in each quadrant were obtained by integration of the velocity distribution. Table 2 shows the average velocities in each part and their deviations from the average. The maximum discrepancy between the four symmetric parts (r/ϕ) is $\Delta_{max,r/\phi} = 0.56\%$ between the four symmetric parts (x/y) it is $\Delta_{max,Q} = 0.47\%$. The discrepancies show further quantitatively the perfect symmetry of the flow field in the four quadrants.

A comparison of the local velocities at every four symmetric points on all four symmetric traverses in the four quadrants shows that the maximum discrepancy is 4.04% for the r/ϕ-parts and 3.65% for the x/y-parts. (see Table 3). The total average velocity in the two wall subchannels investigated is 20.19 m/s. The nondimensional velocity U^+ scaled by the local friction velocity U^*($U^* = \sqrt{\tau_w/\rho}$, $U^+ = U/U^*$) distribution is shown in Figs. 6-1 to 6-4 for the r/Φ-parts and in Figs. 7-1 to 7-4 for the x/y-parts of the four quadrants as a function of the nondimensional distance from the wall y^+ ($y^+ = y.U^*/\nu$ with y as the distance

from the wall along the traverses). The Nikuradse law of the wall in circular tubes /12/

$$U^+ = 2.5 \ln y^+ + 5.5 \qquad (1)$$

is also shown in the figures.

It should be noted that the nondimensional velocity distributions closely agree with the law in circular tubes, except for the small deviation in the area far from the walls.

3.2 Wall shear stress

The wall shear stress distributions on the tube and channel walls were measured with a Preston tube. The measurement results of the wall shear stress scaled by the average in the relevant quadrant are listed in Tab. 4 to Tab. 7 for quadrant 1 to quadrant 4, respectively. Figure 8 shows the wall shear stress distribution along the channel walls of the whole wall subchannel and Fig. 9 shows the wall shear stress distribution along the rod walls.

Following characteristics are observed:

1. The wall shear stress gradient in circumferential direction both at the rod gap and at the gaps between the rod and channel walls is close to zero. This once more demonstrates that there is no momentum transport due to the average velocity distribution through the boundaries between symmetric subchannels or quadrants. This result agrees with the result of the velocity distribution.

2. The wall shear stresses reach maxima at the positions on the wall with widest traverse ($\Phi = 35°$, $X = 0$ mm on Fig. 8 and Fig. 9 respectively), where the average velocity displays also maximum values (see Fig. 5).

3. The distributions of the wall shear stress show good symmetry. The maximum discrepancy of the average wall shear stresses in the four quadrants is only 1%.

The average wall shear stress in the two wall subchannels is:

$$\tau_{w,av} = 1.137 \quad Nm^{-2}$$

3.3 Friction factors

The average friction factors were calculated from measured wall shear stresses in the four quadrants:

$$\lambda_t = 8\tau_{w,av}/(\rho U_{av}^2) \qquad (2)$$

The friction factors also were calculated from the measured pressure drop along the channel axis:

$$\lambda_{\Delta p} = \frac{\Delta p/\Delta L}{\rho U_{av}^2/2D_h} \qquad (3)$$

Here, the measured pressure drop across $\Delta L = 1.262$, m under the measurement conditions is $\Delta p_m = 116$ Pa. This measured pressure drop was correlated to the reference conditions by:

$$\Delta p_{ref} = \Delta pm \left(\frac{\rho_m}{\rho_{ref}}\right)\left(\frac{\mu_{ref}}{\mu_m}\right)^2 \qquad (4)$$

$\Delta p_{ref} = 122.5$ Pa

Based on the corrected pressure drop, the friction factors $\lambda_{\Delta p}$ were calculated and the results are listed in Tab. 8.

The friction factors based both on the pressure drop measurement and on the wall shear stress measurement agree very well. This is due to the good symmetry of the flow field. The results of the friction factors indicate once more that there is no influence of viscous momentum transport through the boundaries between the quadrants.

In order to compare the experimental results with a theoretical value, the friction factor was also calculated by Rehme's method /13/ and /14/. Under laminar flow conditions:

$$\lambda \cdot Re = K \qquad (5)$$

For P/D = 1.148 and W/D = 1.045,

$K = 5.17$,

while under turbulent conditions

$A = 1.046$

$G^* = 5.58.$

The friction factor λ in the wall subchannel of this rod bundle is described by the equation:

$$\sqrt{\frac{8}{\lambda}} = A\,[2.5 \ln(Re\sqrt{\frac{\lambda}{8}}) + 5.5] - G^* \qquad (6)$$

For $Re = 6.106 \times 10^4$, the friction factor was computed to

$\lambda_{th} = 0.01811.$

Compared with the experimental result of λ_t, the deviation between the theoretical value and the measured data is within 5% and, thus, both values are in satisfactory agreement. However, according to Maubach's equation for circular tubes /15/:

$$\frac{1}{\sqrt{\lambda}} = 2.035 \lg Re\sqrt{\lambda} - 0.989 \qquad (7)$$

the friction factor of a circular tube is calculated to $\lambda = 0.2025$ at the same Reynolds number. The friction factor of the rod bundle is 9.6% lower than the value for the circular tube.

The relative average velocities in all parts of the region investigated raised to the power of 1.8 agree with the relative average wall shear stresses to within 3.5% (see Table 9.)

3.4 Turbulent intensities and turbulent kinetic energy

The distributions of the turbulent intensities and of the kinetic energy are displayed with both linear plots along the traverses from the walls (scaled with the local friction velocity) and by contour plots. In the contour plots, the turbulent intensity was scaled by the friction velocity based on the wall shear stress on the rod wall at $\Phi = 0°$ in quadrant 1.

3.4.1 Axial turbulence intensity

Figures 10-1 to 10-4 and Figs. 11-1 to 11-4 show the distributions of the axial turbulent intensity along the traverses from the rod walls (r/ Φ-part) and channel walls (x/y-part) in the four quadrants, respectively. The axial turbulent intensity is also shown in Fig. 12 as contours. The following characteristics are found:

1. The axial turbulent intensity decreases with increasing distance from the walls in the rod gap area, $\Phi = 0°\text{-}35°$ and x = 70-80 mm. In the area near the walls, the axial intensity reaches relative high values $\sqrt{u'^2}/u^* = 2.0\text{-}2.6$, while at the line of maximum distance from the wall, the axial turbulence intensity is relatively low, only about 1.2.

2. In the area $\Phi = 40°\text{-}90°$, x = 0-65 mm, the axial turbulence intensity changes slowly along the traverses.

3. In the area $\Phi = 50°\text{-}65°$ and x = 35-50mm, there exist regions with very strong axial turbulence intensity, which indicate a strong turbulence momentum transport through the narrow gaps between the rods and channel walls due to a large-scale eddy motion.

4. The minimum axial turbulence intensity is located at the center of the subchannel, which is coincident with the location of the maximum time-mean velocity. Another relative maximum of the axial intensity appeares near the gap between the rods at $\Phi = 25°$, which forms a saddle-point region of the turbulence intensity in this area.

5. The contour plots show a smooth, symmetric distribution of the axial turbulence intensity.

6. Fig. 12A shows the distribution of the axial turbulence intensity along the line of maximum normal distance from the walls. A first small maximum can be noticed at $\Phi = 25°$, a very strong maximum appears at $\Phi = 55°$.

3.4.2 Azimuthal turbulence intensity

Figures 13-1 to 13-4 and Figs. 14-1 to 14-4 show the distribution of the measured azimuthal turbulence intensity along the traverses in the area near rod walls (r/Φ-part) and channel walls (x/y-part) in the four quadrants, respectively.

In the area $\Phi = 0\text{-}40°$, $x = 50\text{-}80$ mm, the azimuthal turbulence intensity $\sqrt{\overline{w'^2}}/u^*$ is relatively low and decreases with increasing distance from the walls, while near the walls it is close to the value on the wall of circular tubes. In the center part of the wall subchannel ($x = 0$ mm, $\Phi = 0\text{-}35°$, on the line of maximum distance from the walls) it reaches a minimum of 0.9. In the area $\Phi = 45\text{-}90°$ and $x = 0\text{-}45$ mm, the azimuthal turbulence intensity is relatively high and almost independent on the distance from the walls. The azimuthal intensity reaches maximum values in the gaps between the rods and channel walls at $\Phi = 85°\text{-}90°$, $x = 0\text{-}10$ mm, $(\sqrt{\overline{w'^2}}/u^*)_{max} = 3.0$. The strong turbulent momentum transport through narrow gaps between the rods and channel walls is demonstrated once more. The azimuthal turbulence intensity is also shown in Fig. 15 as a contour plot. The contour lines are perpendicular to the boundary line of the wall subchannel at the gap between rods. This indicates no significant turbulence momentum transport through the boundary between two symmetric wall subchannels. A comparison with the contour plots of the azimuthal turbulence intensity in /6/ (Abb.16) shows that the present measurement results were improved greatly due to the fully automated measuring system controlled by a computer.

Figure 15a shows a monotonous distribution of the azimuthal turbulence intensity along the line of maximum normal distance from the walls. The maximum of the azimuthal turbulence intensity appears at $\Phi = 90°$.

3.4.3 Radial turbulence intensity

The measurement results of the radial turbulence intensity displays nonuniform distributions in some regions due to the uncertainty of the measurement. Especially in the gap region between the rod and channel walls the very small signal for the radial turbulence intensity is obtained by subtracting two large signals, due to the high levels of both the axial intensity and azimuthal intensity, respectively (see contour plot Fig. 18). But in the gap between rods, the contour plot of the radial turbulence intensity is reasonable. Here, the axial and azimuthal components of the fluctuating velocity are relatively small (see Figs. 16-1 to 16-4 for the x/y-parts near the channel walls and Figs. 17-1 to 17-4 for r/Φ-parts near the rod walls, respectively). Generally, the radial turbulence intensity decreases with increasing distance from the walls. It reaches a maximum in the area near the walls.

3.4.4 Turbulent kinetic energy

The results of the turbulent kinetic energy

$$\overline{k'} = 1/2(\overline{u'^2} + \overline{v'^2} + \overline{w'^2}) \qquad (8)$$

scaled by the square of the local friction velocity for the linear plots for each traverse in the four quadrants and by the square of the friction velocity based on the wall shear stress at $\Phi = 0°$ for the contour plots are shown in Figs. 19-1 to 19-4 (for the r/Φ-parts), in Figs. 20-1 to 20-4 (for the x/y-parts) and in Fig. 21 as a contour plot.

In the area near both the rod and channel walls, the relative kinetic energy on all traverses does not differ very much (within 4.5 to 5.5) However, it is higher than the value in circular tubes (4.0). The variation of the kinetic energy along the traverses depends on the circumferential position of the traverse. In the wide area of the wall subchannel ($\Phi = 0°$-$40°$, x = 65-80mm), the turbulent kinetic energy decreases with increasing distance from the walls and at the position on the line of maximum distance from the walls, it reaches a minimum of about 1.5. It is still higher than the value in circular tube (1.0). Closer to the gap between the rod and channel wall, at $\Phi = 45°$-$50°$, x = 55-60 mm, the turbulent kinetic energy appears without significant variation along the traverses. In the narrow area of the subchannel ($\Phi = 55°$-$90°$, x = 0-50mm), the kinetic energy increases significantly with increasing distance from the wall. On the line of maximum distance from the walls, it reaches maximum values of about 6.5 in the linear plots. The turbulent kinetic energy displays a smooth and symmetric distribution on the contour plot (Fig. 21). It is clear, that in the four symmetric areas of $\Phi = 55°$-$65°$ and x = 35-55 mm, there are four regions of strong kinetic energy formed by the turbulence momentum transport through narrow gaps between the rods and channel walls.

3.5 Turbulent shear stress and correlation coefficient

3.5.1 Azimuthal turbulence shear stress $-\overline{u'w'}$

The measurement results of the azimuthal shear stress along the traverses scaled by the square of the local friction velocity are shown in Figs. 22-1 to 22-4 in linear plots for the r/Φ-part and in Figs. 23-1 to 23-4 in linear plots for the x/y-part in the four quadrants, respectively. In the area near both the rod and channel walls, the

azimuthal turbulent shear stresses decrease to zero. On several traverses, the shear stresses are close to zero. This is found on the traverses located between $\Phi = 0°$ (the boundary between the symmetrical wall subchannels), and $\Phi = 35°$ (the widest traverse), in the gap between the rods and the channel wall at $\Phi = 90°$ and at x = 0 mm, and for x = 75-80 mm, i.e. on the symmetry line. For all the traverses mentioned above, the gradient of the mean velocity in the azimuthal direction is close to zero. In the contour plot of the mean velocity, Fig.5, it is clearly shown that the contours in these areas are parallel to the rod walls (in the r/Φ-part) or the channel walls (in the x/y-part), respectively.

On the other traverses, the azimuthal turbulence shear stresses increase to a varying degree with increasing distance from the walls. In the area of x = 20-40 mm and $\Phi = 60°$-75°, respectively, the azimuthal shear stresses reach maximum values of about: $-\overline{u'w'}/u^{*2} = 4.0$. The four symmetrical regions of the maximum values of the azimuthal shear stress near the gaps between rods and channel walls are clearly displayed in the contour plot of the azimuthal shear stress (see Fig. 24). And in the area near the gap between the rods there exists a relatively wide region of zero azimuthal shear stress (also on Fig. 24).

3.5.2 Shear stress perpendicular to the walls $-\overline{u'v'}$

The measured distribution of the normal shear stress (the shear stress perpendicular to the walls) along the traverses scaled by the square of local friction velocity are shown in Figs. 25-1 to 25-4 for the r/Φ-parts and in Figs. 26-1 to 26-4 for the x/y-parts of the four quadrants. Generally, the normal shear stresses decrease almost linearly with increasing distance from the walls. In the area near the walls, the normal shear stresses are very close to each other and also close to the value at the wall of circular tubes (1.0) on all traverses.

In the area of $\Phi = 0°$-40°, $\Phi = 80°$-90°, x = 0-15 mm, and x = 70-80mm, the distributions of the normal shear stress along the traverses in the subchannel of the rod bundle agree with that in circular tubes perfectly. But in the rest area, the normal shear stresses in the subchannel of the rod bundle are always much higher than that in circular tubes.

3.5.3 Transverse shear stress $-\overline{v'w'}$

In this experiment, the distributions of the transverse turbulent shear stresses were also measured. The results (shown in Figs. 27-1 to 27-4 for the r/Φ-parts and Figs. 28-1 to 28-4 for the x/y-parts) scaled by the square of the local friction velocity scatter about zero. Whereas in the areas near the walls, the measurement results are close to zero, in the area far away from the walls, the results scatter even more. Generally, a definite regularity of the distribution of the transverse shear stress cannot be found from the measurements because of the uncertainty in measuring small signals.

3.5.4 Correlation coefficient R_{uv}

The measured distributions of the correlation coefficient in the direction perpendicular to the walls are described by

$$R_{uv} = \frac{-\overline{u'v'}}{\sqrt{\overline{u'^2}}\ \sqrt{\overline{v'^2}}} \qquad (9)$$

and shown in Figs. 29-1 to 29-4 for the r/Φ-parts and in Figs. 30-1 to 30-4 for the x/y-parts of the four quadrants. In a relative wide region, the correlation coefficient R_{uv} is about 0.4. In the area near the walls, the values of the correlation coefficient are close to each other. The correlation coefficients decrease with increasing distance from the walls and tend to zero at the position near the line of maximum distance from the walls. This variation is similar to that in circular tubes. In the area of x = 15-45 mm, and Φ = 60°-80° (the gap region between the rods and the channel walls) the results of the correlation coefficient are unreasonably much higher and scattered. This is caused by the very small radial turbulence intensity and its uncertainty of measurement in these aeas.

3.5.5 Correlation coefficient R_{uw}

The experimental results of the correlation coefficients of the shear stress parallel to the walls are described by:

$$R_{uw} = \frac{-\overline{u'w'}}{\sqrt{\overline{u'^2}}\ \sqrt{\overline{w'^2}}} \qquad (10)$$

and shown in Figs. 31-1 to 31-4 for the r/Φ-parts and in Figs. 32-1 to 32-4 for the x/y-parts of the four quadrants. In Fig. 33 the results are also presented as a contour plot.

The following characteristics can be observed:

1. The distribution of the correlation coefficient parallel to the walls R_{uw} agrees very well with the distribution of the azimuthal shear stress. Four regions of maximum value are displayed at the symmetrical positions in the gap areas between the rod and channel walls ($x = 20\text{-}40$ mm, $\Phi = 60°\text{-}75°$). The maximum of the correlation coefficient R_{uw} is about 0.7.

2. On several traverses ($\Phi = 0°\text{-}35°$, $\Phi = 90°$, $x = 0$ mm, and $x = 80$ mm) the correlation coefficient R_{uw} is close to zero.

3. Close to both the rod and channel walls, the correlation coefficients R_{uw} trend towards zero. But they increase with increasing distance from the walls along the traverses (except for the traverses mentioned above (2)).

4. Compared with the results of /6/, the present results are more precise due to the use of the automatic measurement system and Hooper's method for evaluating the data. In the evaluation of the experimental results of /6/, there was an error in the calculation of the correlation coefficient R_{uw} in the data reduction program. In that case, the correlation coefficient was calculated incorrectly, which lead to some unreasonable results, e.g. some correlation coefficients were higher than 1.0. This error has been eliminated in present work.

3.5.6 Correlation coefficient R_{vw}

The distribution of the correlation coefficient R_{vw} scatters about zero and is distributed within a narrow range of $\pm$ 0.3 in most of the area of the four quadrants. (see Figs. 34-1 to 34-4 for the r/Φ-parts and Figs. 35-1 to Figs. 35-4 for the x/y parts of the four quadrants). But there are also some data scattered away within a wider range due to the measurement uncertainty of small signals.

3.6 Difference of turbulence intensities parallel and perpendicular to the walls

A finite gradient of the difference in the turbulent stresses in the plane of the channel cross section in the peripheral direction is considered as a driving force for the secondary flow in the plane of the channel cross section. The normal stresses only are significant in secondary flow production /17/.

In this investigation the distribution of the difference of turbulent intensities (w'^2-v'^2) was measured. The results scaled by the square of local friction velocity are shown in Figs. 36-1 to 36-4 for the r/ϕ-parts and in Figs. 37-1 to 37-4 for the x/y-parts of the four quadrants.

1. In the gap region between the rods and the channel walls (x = 0-40 mm, ϕ = 55°-90°), the difference of the turbulent intensities (w'^2-v'^2) is relatively high due to the very high azimuthal intensity and the low radial intensity. Directly in the gap between the rods and channel walls, it reaches maximum values (w'^2-v'^2) = 8.0. And in this area, the difference of the turbulent intensities increases with increasing distance from the walls, while it varies greatly in peripheral direction.

2. In the gap region between rods (α = 0-50°, x = 45-80 mm), the difference of the turbulent intensities is relatively low and it varies slowly in peripheral direction.

3. In the area near the walls, the peripheral gradient of the difference of the turbulent intensities is small, it increases with increasing distance from the walls. The maximum gradient of the difference of the turbulent intensities appears on the line of maximum normal distance from the walls. Figure 38 shows a contour plot of the difference between the intensities parallel and normal to the walls.

4. Comparison between the experimental wall shear stresses and the predictions by the VELASCO code

The distributions of the mean velocities and of the wall shear stresses have been computed by the VELASCO code /18/ for the wall subchannels of this experiment (P/D = 1.148, W/D = 1.045). The calculated wall shear stresses are shown in Fig. 39 together with the experimental data. All results are related to the average wall shear stress of the four quadrants. The plot on the top of the figure displays the

data for the channel walls whereas the plot at the bottom shows the data along the rod walls.

As observed in the previous experiment /6/, the variations of the wall shear stresses predicted by VELASCO are much more pronounced as the experimental results. Especially in the gaps between the rods and the channel walls, the calculated wall shear stresses are 31% lower than the experimental results. The main reason for this deviation is the cyclic momentum transport between neighboring subchannels not modelled in the code. In the gap between the rods, the computed results are much higher than the experimental data.

The comparison shows that the VELASCO code based on experimental results in tubes and annuli is not suited for the analysis of rod bundles with narrow gaps between the rods and the rods and channel walls, respectively. Turbulent flow through rod bundles is different from turbulent flow through tubes and annuli.

5. Conclusion

1. The comparison between the measurements in a rectangular channel with a symmetrically arranged rod bundle and in an asymmetrical wall subchannel indicates that:

   a. for the symmetrical arrangement, the momentum transport through the rod gap dissappears, and therefore

   b. the friction factors based on the measurement of the wall shear stress and on the measurement of the pressure drop agree very well in all quadrants.

   c. The distributions of the time mean velocity, the wall shear stress, and the turbulent structure in the gap area between rods are quite different from that in an asymmetrical arrangement.

   d. The experimental results of the turbulent intensities, of the turbulent shear stress, and of the turbulent kinetic energy indicate once more a strong turbulent momentum transport through the narrows gaps between rods and channel walls.

2. Compared with the previous work /6/, the results of the present investigation are significantly improved due to the fully automatic measurement system and the use of Hooper's evaluation method.

3. The comparison with calculated results by VELASCO shows that turbulent flow through rod bundles is different from turbulent flow through tubes and annuli, the basis of the models of VELASCO. The VELASCO code is not well suited for the analysis of turbulent flow through rod bundles with narrow gaps.

ACKNOWLEDGMENT

The authors thank Mr. G. Wörner for this cooperation in performing the experiments and in evaluation of the results.

Nomenclature:

a	m	Distance
A	-	Geometry Parameter
C_{sec}	-	Secondary flow amplitude in VELASCO
D	m	Rod diameter
D_h	m	Hydraulic diameter
G*	-	Geometry parameter
K	-	Geometry parameter
$\overline{k'}$	$m^2 \cdot s^{-2}$	Turbulent kinetic energy
L	m	Distance between walls and the line of maximum normal distance from the wall
P	m	Distance between rods
p	Pa	Pressure
R_{uv}	-	Correlation coefficient of uv
R_{uw}	-	Correlation coefficient of uw
Re	-	Reynolds number
r	m	Radius
T	°C	Temperature
U	ms^{-1}	Velocity in axial direction
u'	ms^{-1}	Turbulent velocity in axial diraction
U_{ref}	ms^{-1}	Reference velocity
U_m	ms^{-1}	Average velocity
U*	ms-1	Friction velocity

U^+	-	Dimensionless velocity
v'	ms^{-1}	Turbulent velocity normal to the wall
W	m	Distance between rod and channel wall
w'	ms^{-1}	Turbulent velocity parallel to the wall
x	m	Position along the channel wall
y	m	Distance from the wall
y^+	m	Dimensionless distance
λ		Friction Coefficient
ϕ	-	Angle Coordinate
p	Kgm^{-3}	Density
v	m^2s^{-1}	Kinematic viscosity
τ_w	Nm^{-2}	Wall shear stress
τ_{wm}	Nm^{-2}	Average wall shear stress
Δ	-	Discrepancy

Indices

r	Radial
ϕ	Angle in the direction along the rod wall
th	Theory
av	Average

References

1. ***K. Rehme***, "Turbulent flow through two asymmetric rod bundles", Heat & Technology, Vol. 5, No 1-2, 19-37 (1987)

2. ***W. Slagter and K. Konig***, "Finite element, stream function-vorticity solution of secondary flow in the cross-plane of non-circular channels", Report ECN-175, Netherlands Energy Research Foundation, Petten (1985)

3. ***H.-G. Kaiser***, "Näherungslösungen für den Impulstransport bei turbulenter Strömung in engen Stabgitterbündeln nach der Methode der finiten Elemente", Dr.-Ing. Dissertation, Technische Universität Braunschweig (1985)

4. ***W. Zeggel, N. Neelen***, "Validation of a wall parallel eddy viscosity formulation", IAHR 5th International Meeting on Liquid Metal Thermal Hydraulics, Grenoble (1986)

5. ***K. Rehme***, "The structure of turbulent flow through rod bundles", Nuclear Engineering and Design 99, 141-154, (1987)

6. ***K. Rehme***, "Strömungsuntersuchungen an einem asymmetrischen Stabbündel (P/D = 1.148, W/D = 1.045), Report KfK-3597, Nuclear Research Center Karlsruhe (1983)

7. ***B. Kjellström***, "Studies of turbulent flow parallel to a rod bundle of triangular array", Report AE-487, Aktiebolaget Atomenergi, Studsvik, (1974)

8. ***K. Rehme***, "Computer-controlled rig for measurements of velocity and turbulence distributions by hot-wires", Report KfK-3744, Nuclear Research Center Karlsruhe (1984) (in German)

9. ***J.D.Hooper***, "Fully developed turbulent flow through a rod cluster", Ph.D.Thesis, University of New South Wales, Sydney, Australia (1980)

10. ***L. Vosáhlo***, "Computer programs for evaluation of turbulence characteristics from hot-wire measurements", Report KfK-3743, Nuclear Research Center Karlsruhe (1984)

11. ***V.C.Patel***, "Calibration of the Preston tube and limitation of its use in pressure gradients", J.Fluid Mech. 23 185-208, (1965)

12. ***J. Nikuradse***, "Gesetzmäßigkeiten der turbulenten Strömung in glatten Rohren", VDI Forsch. Heft No. 356 (1932)

13. ***K. Rehme***, "Laminarströmung in Stabbündeln", Chemie-Ing.-Technik 43, (17), 962-966 (1971)

15. ***K. Maubach***, "Reibungsgesetze turbulenter Strömungen", Chemie-Ing.-Technik 42 (15), 995-1004 (1970)

16. ***K. Rehme***, "The structure of turbulence in wall subchannel of a rod bundle", Atomkernenergie, Kerntechnik, Vol. 49, No.3 145-150 (1987).

17. ***M.A.Haque, A.K.A.Hassan, J.T.Turner and H. Barrow***, "An observation on the origin of secondary flow in strait noncircular ducts, Wärme- und Stoffübertragung 17, 93-95 (1983)

18. ***W. Eifler and R. Nijsing***, "VELASCO-Velocity field in asymmetric rod configurations", Report EUR-4950e (1973)

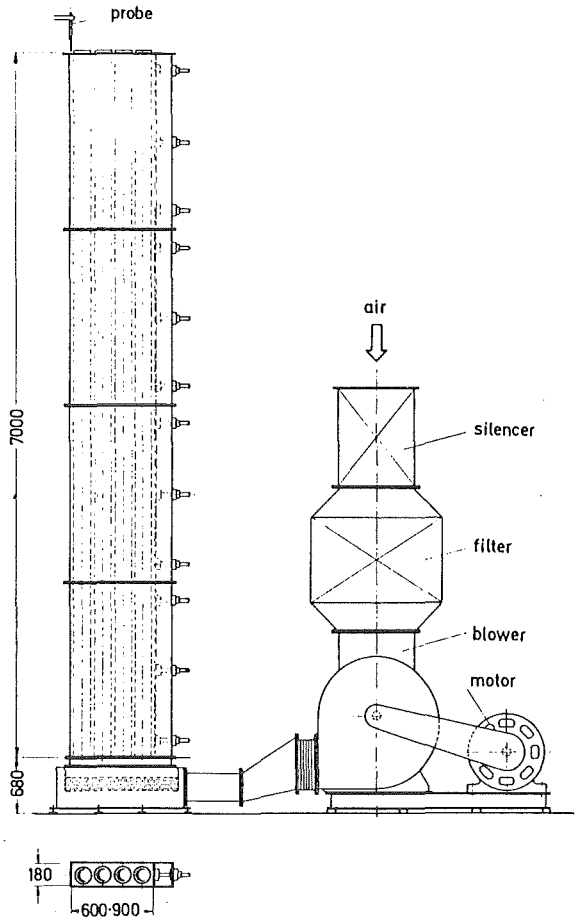

Fig. 1 Schematic of the test rig

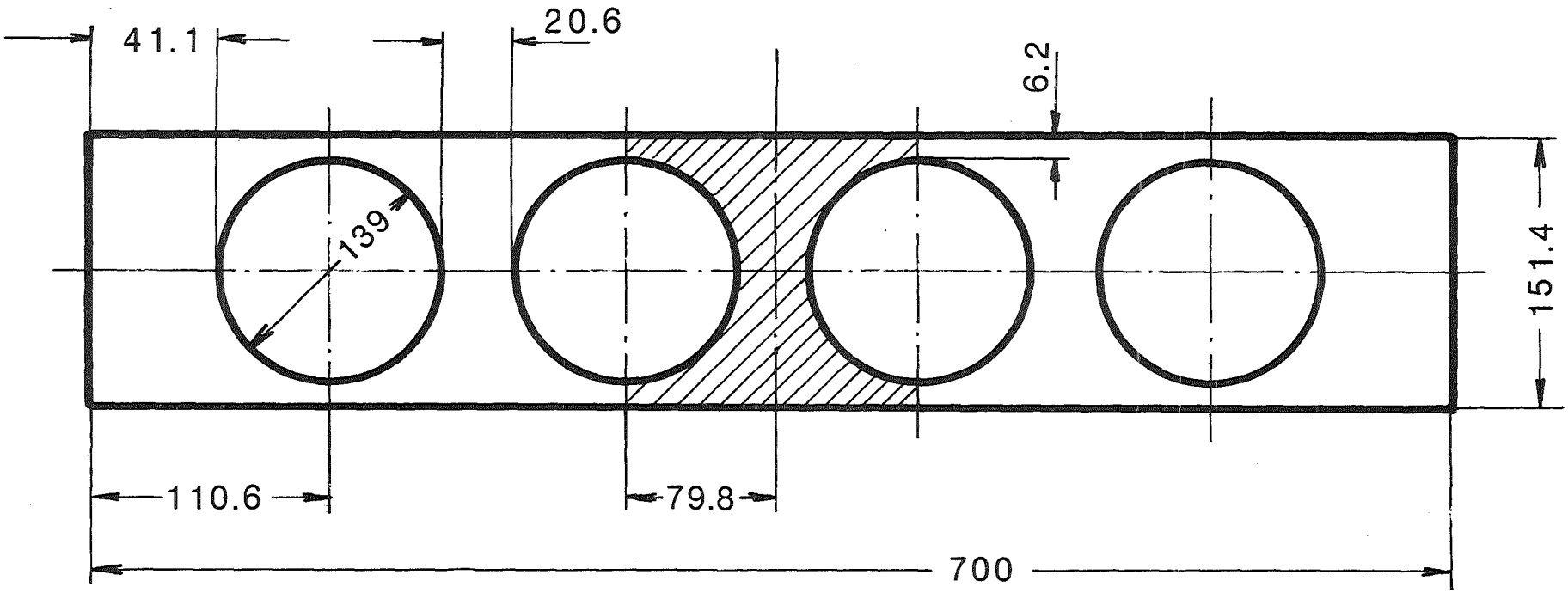

P/D = 1.148

W/D = 1.045

Fig. 2 Cross section of the test section

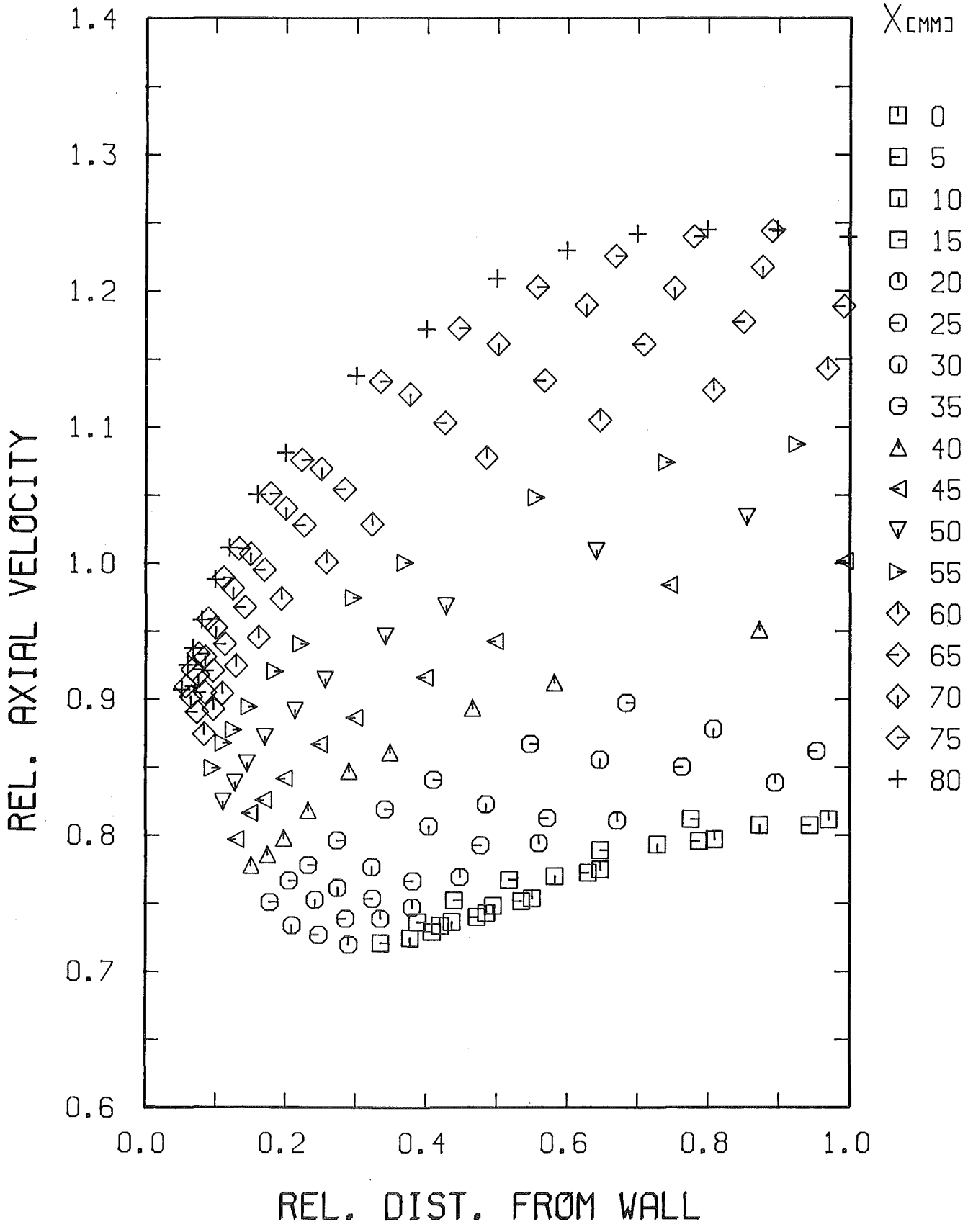

Fig. 3-1 Distribution of axial velocity in the x/y-part of quadrant 1

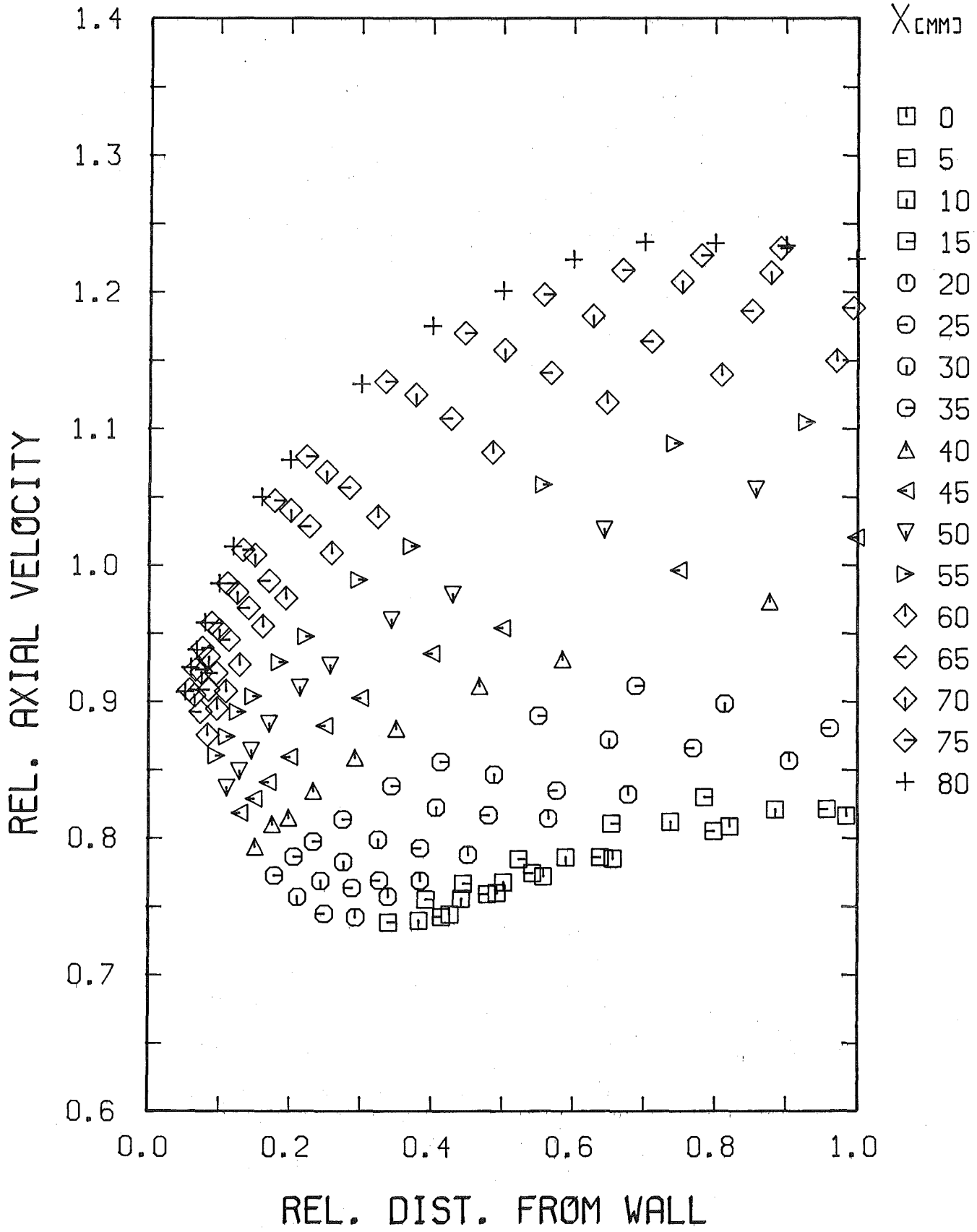

Fig. 3-2 Distribution of axial velocity in the x/y-part of quadrant 2

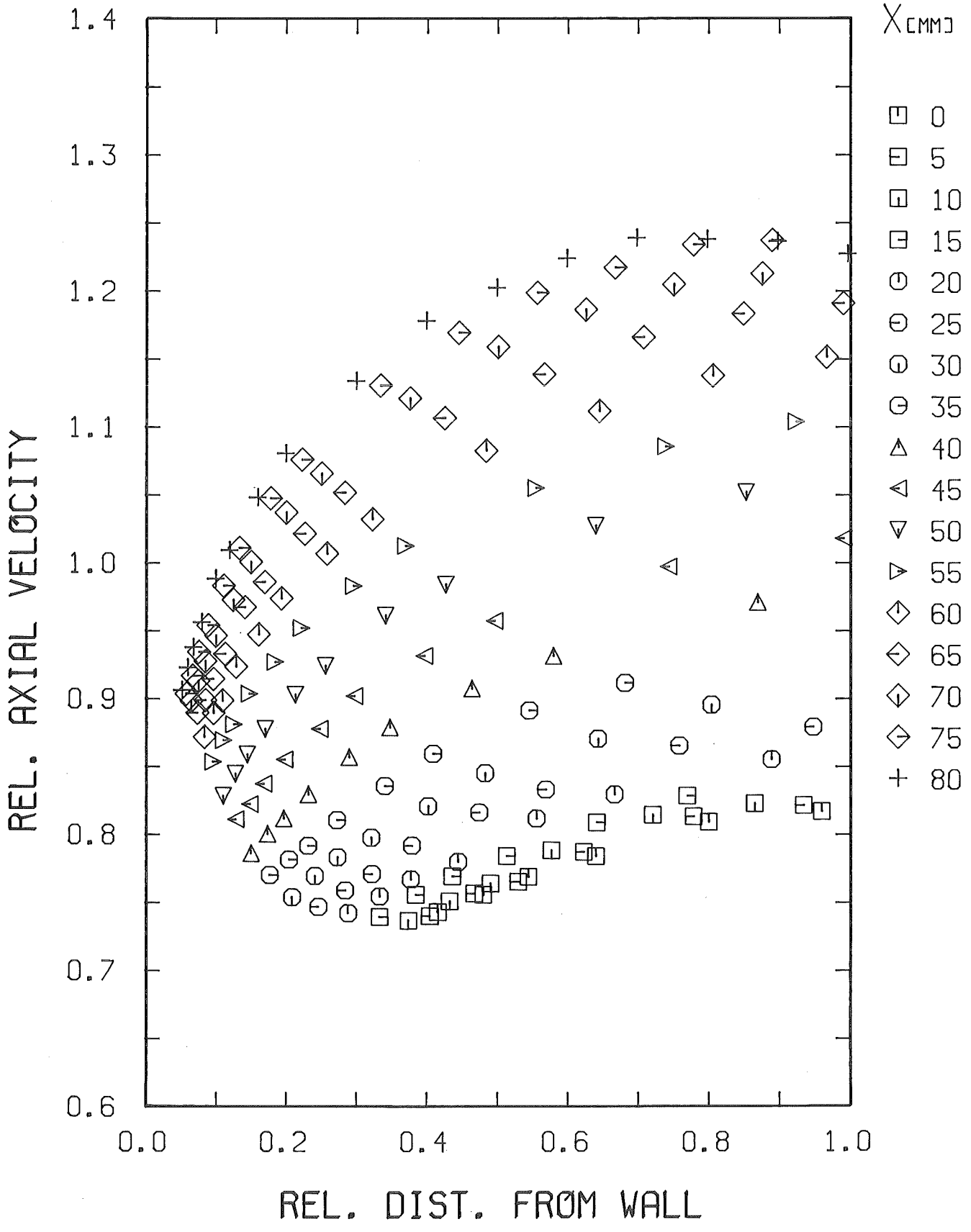

Fig. 3-3 Distribution of axial velocity in the x/y-part of quadrant 3

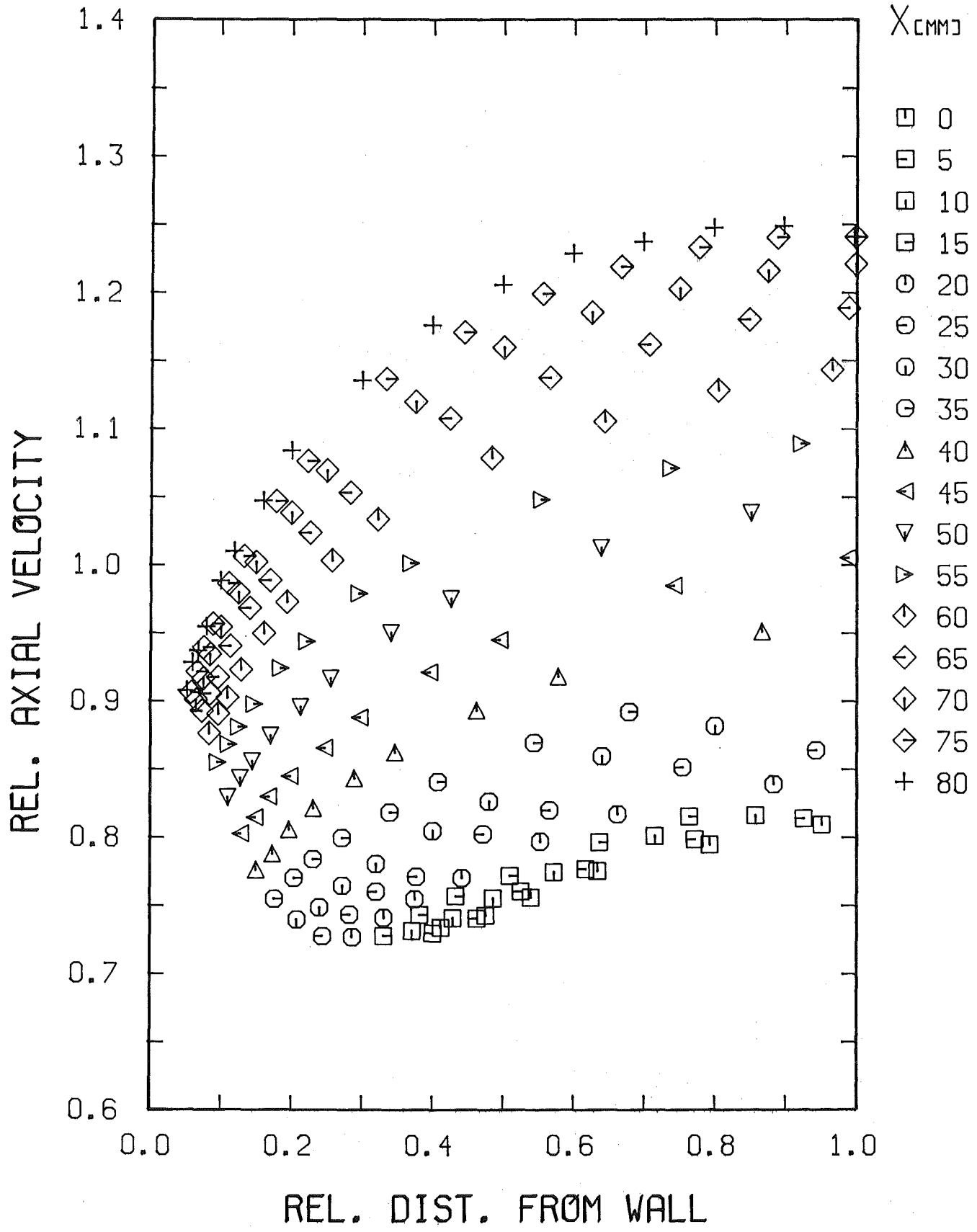

Fig. 3-4 Distribution of axial velocity in the x/y-part of quadrant 4

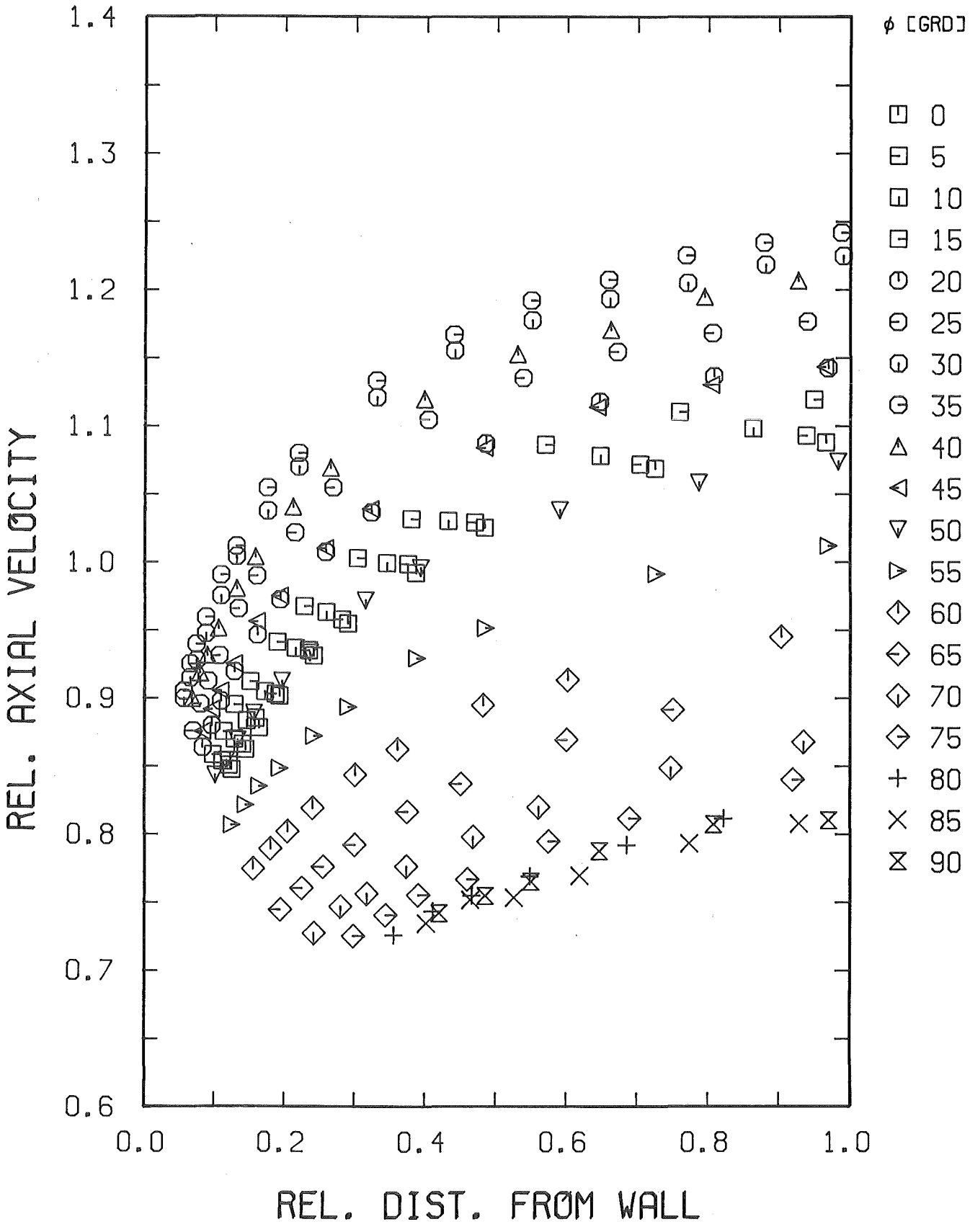

Fig. 4-1 Distribution of axial velocity in the r/φ-part of quadrant 1

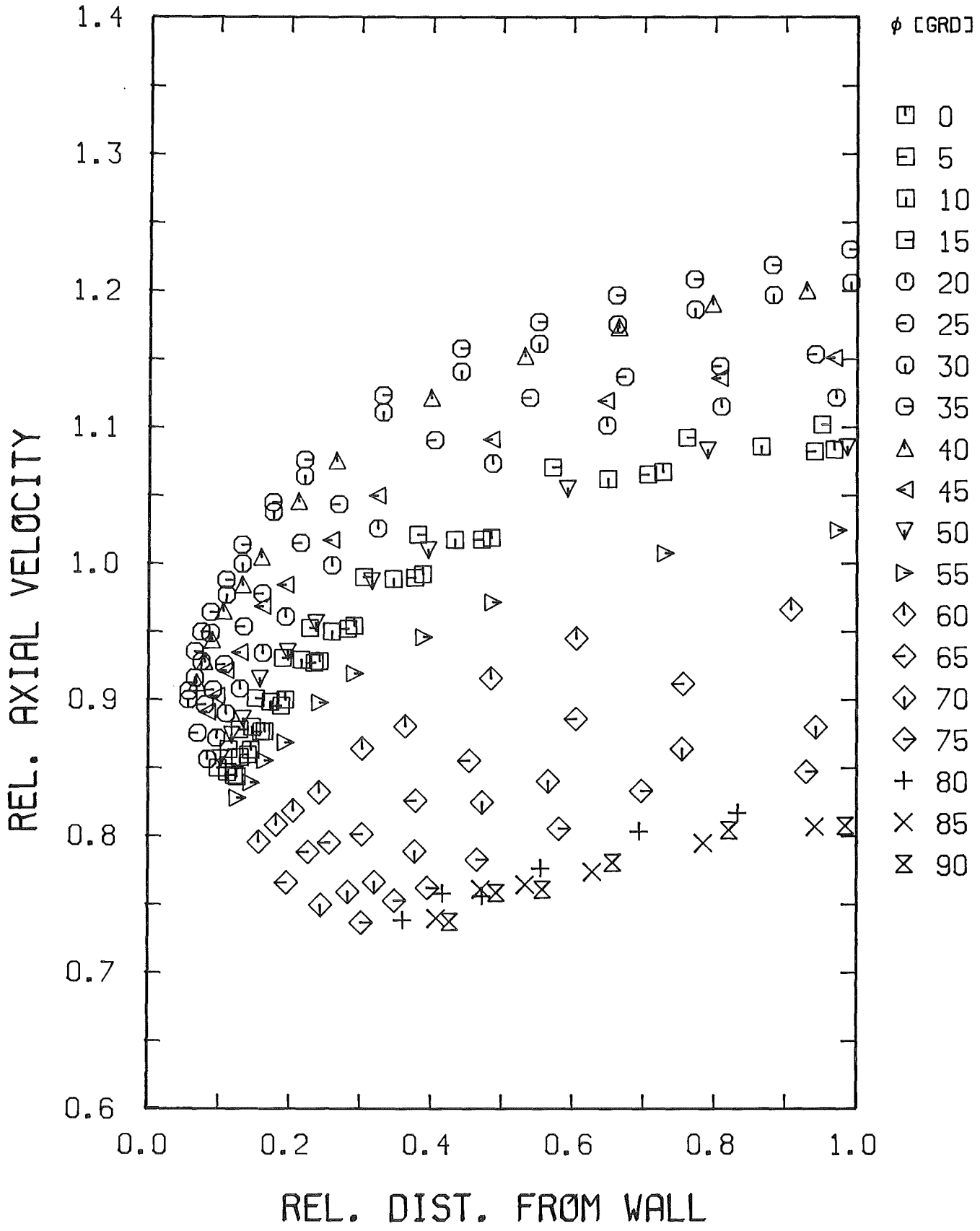

Fig. 4-2 Distribution of axial velocity in the r/φ-part of quadrant 2

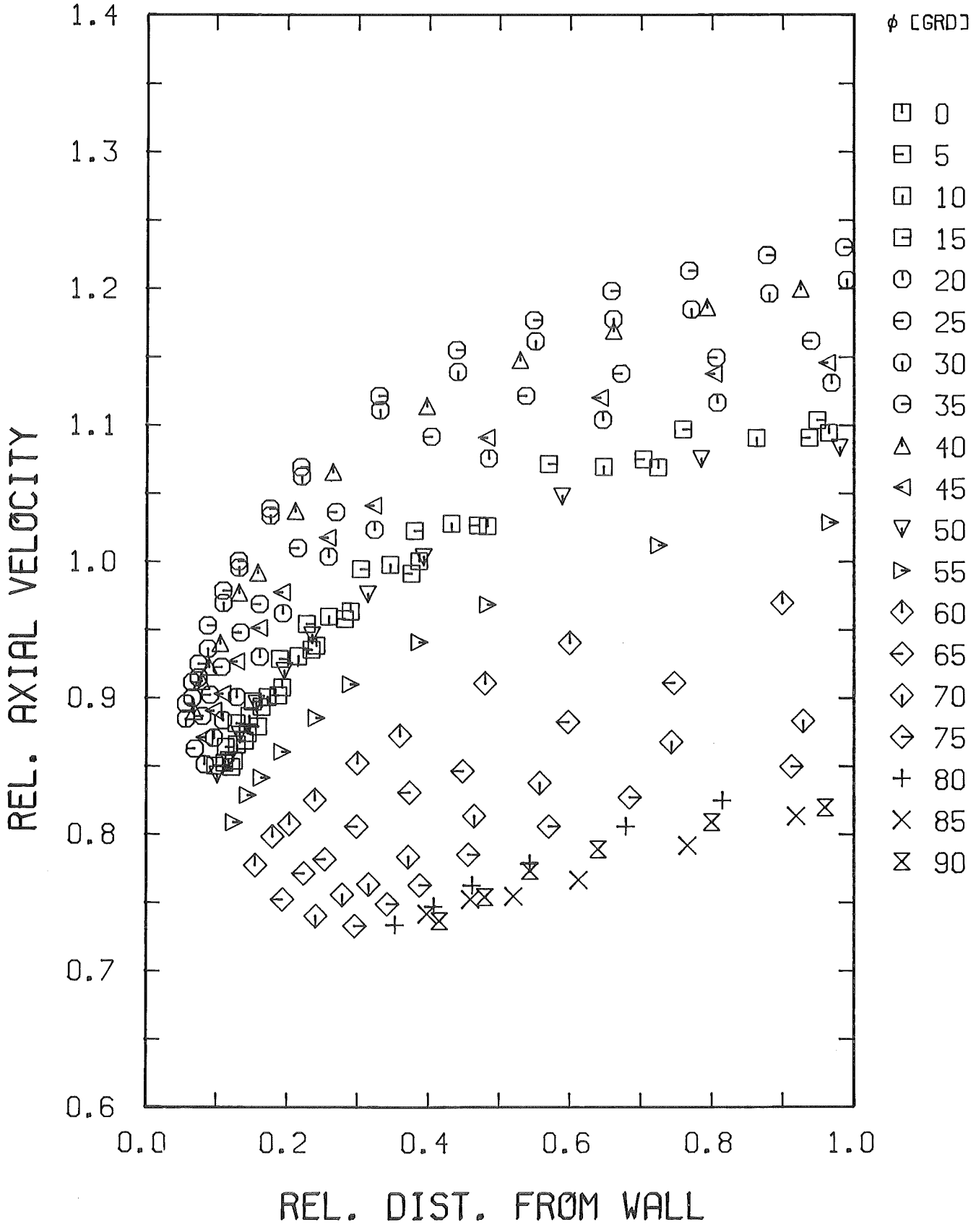

Fig. 4-3 Distribution of axial velocity in the r/φ-part of quadrant 3

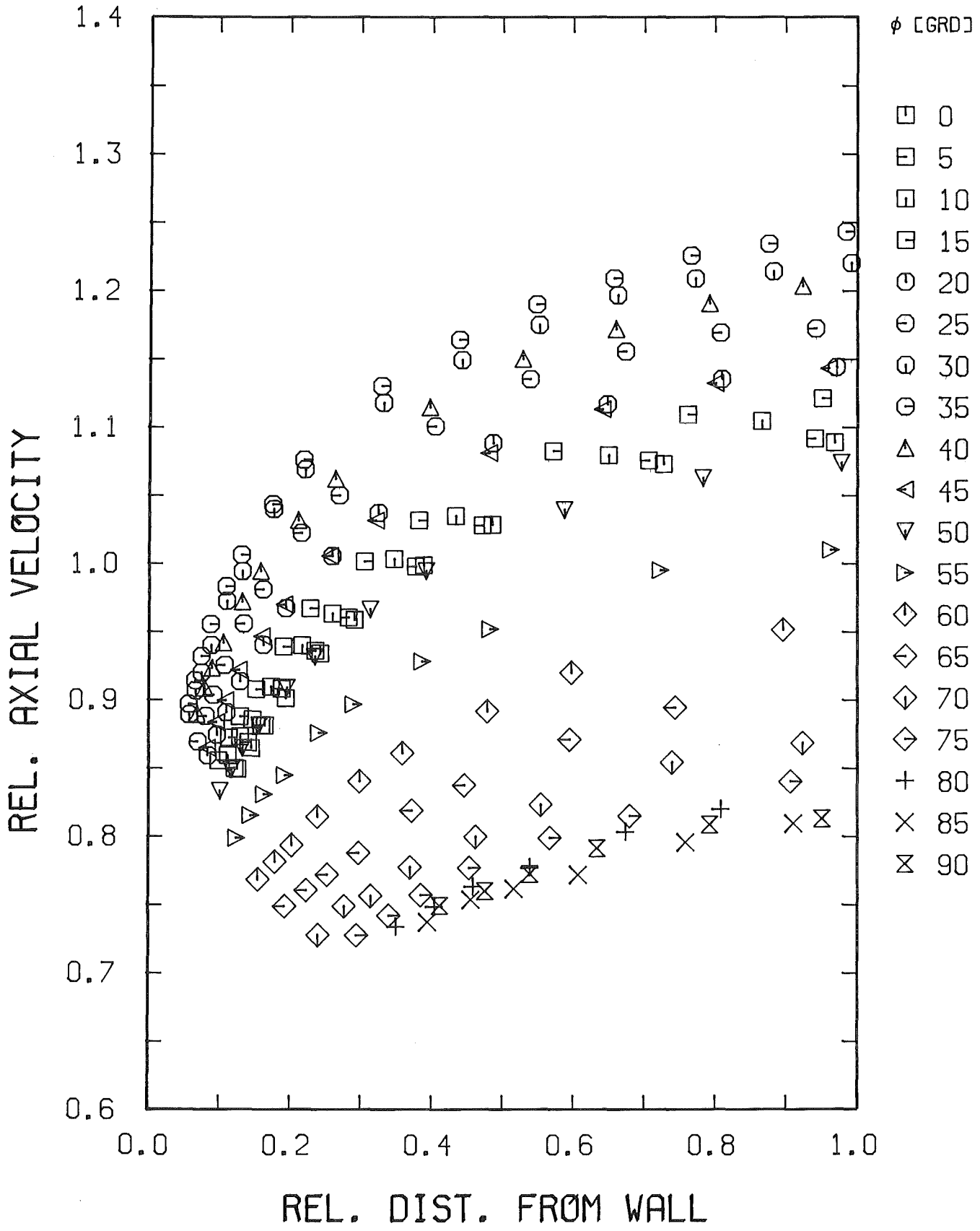

Fig. 4-4 Distribution of axial velocity in the r/ϕ-part of quadrant 4

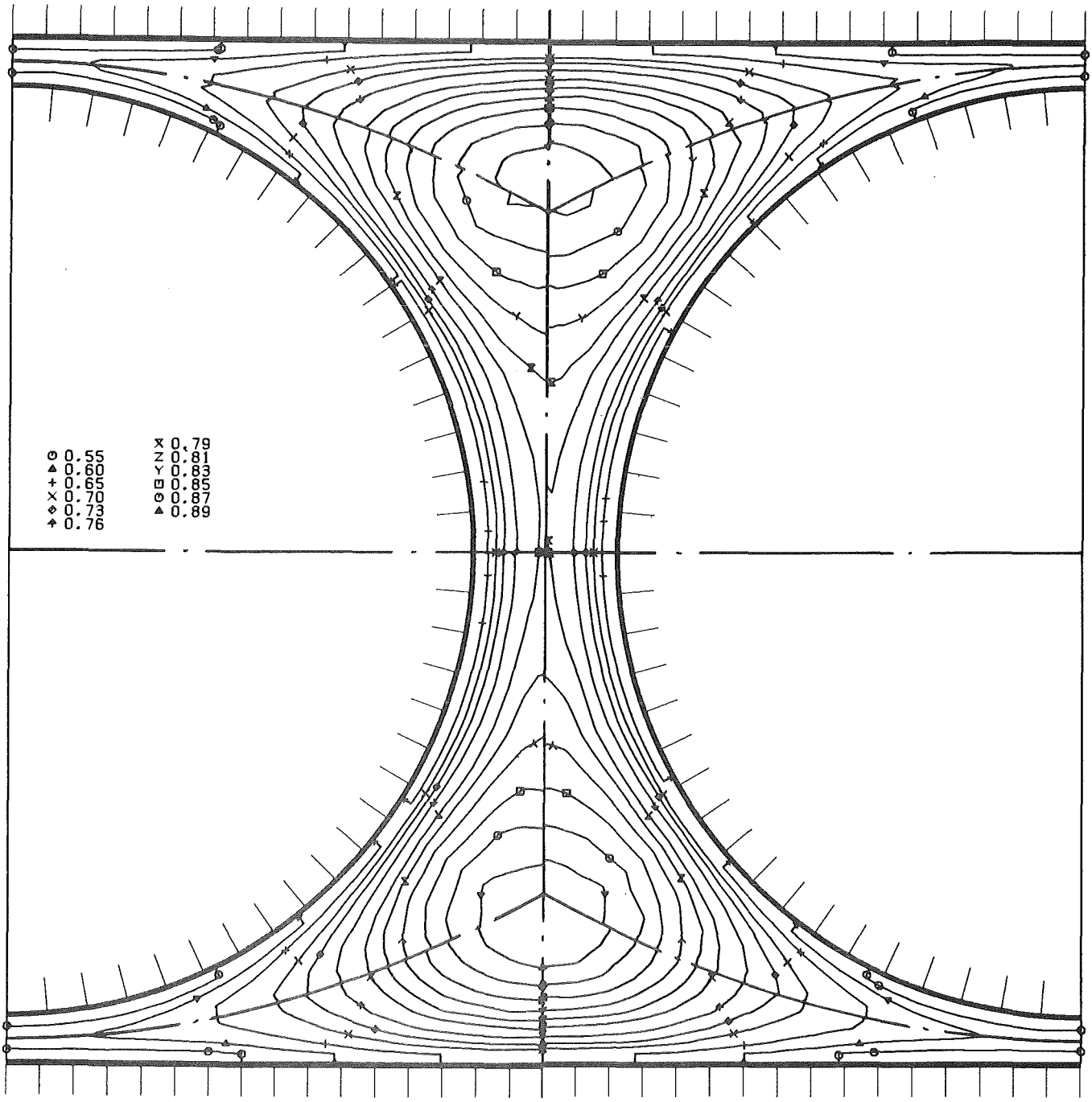

Fig. 5 Contours of axial velocity in the four quadrants

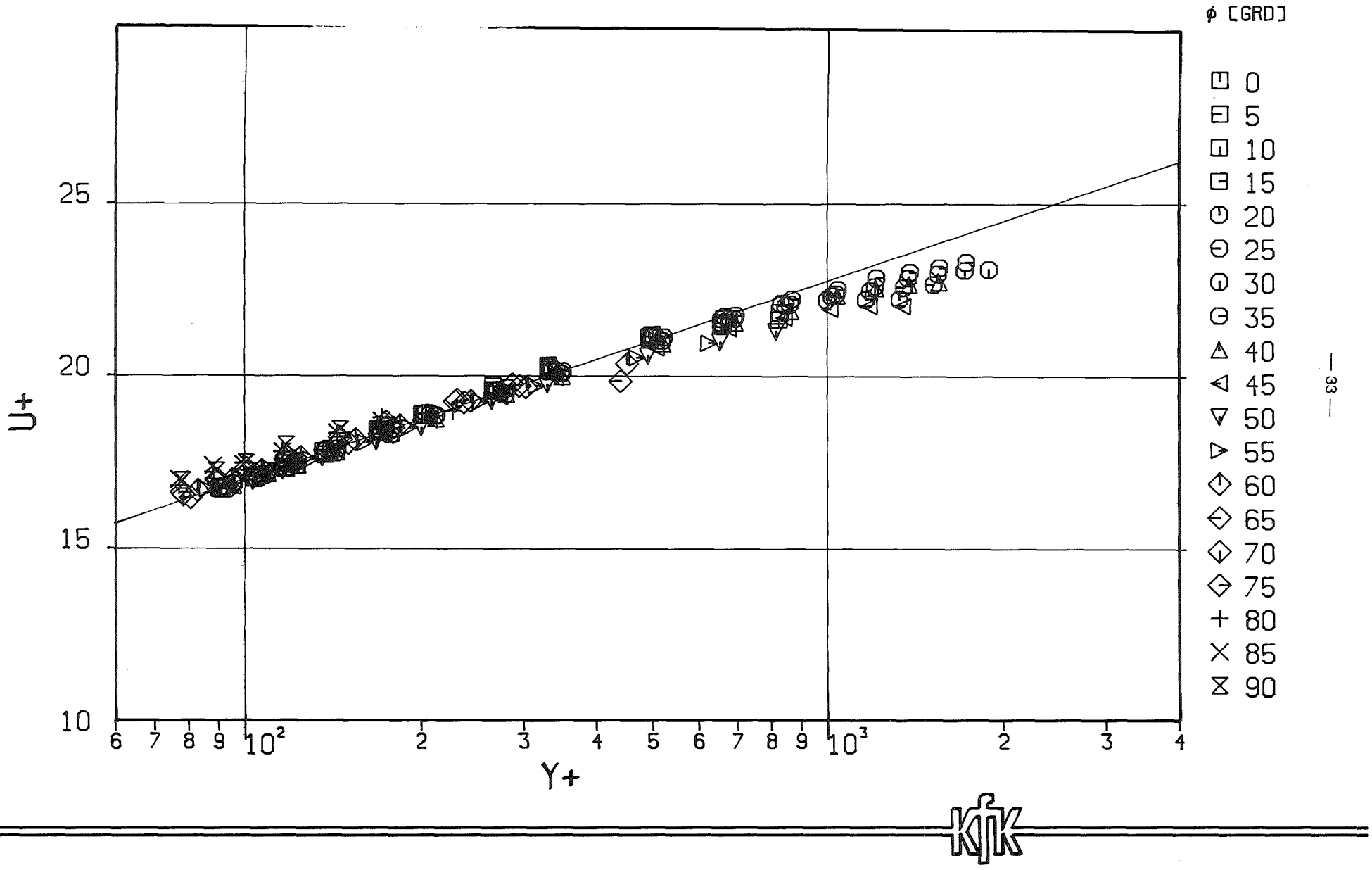

Fig. 6-1 Distribution of dimensionless velocity in the r/φ-part of quadrant 1

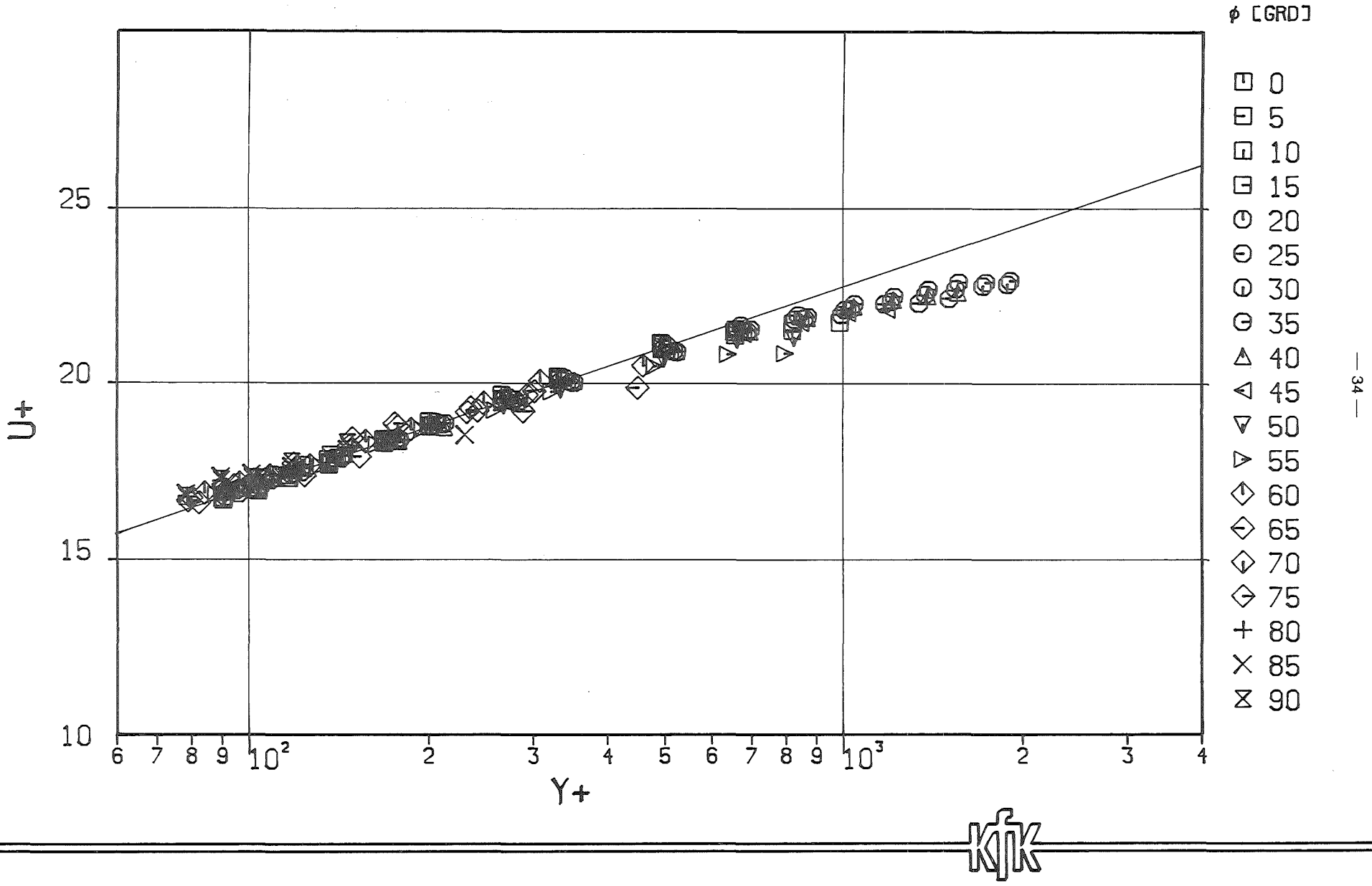

Fig. 6-2 Distribution of dimensionless velocity in the r/ϕ-part of quadrant 2

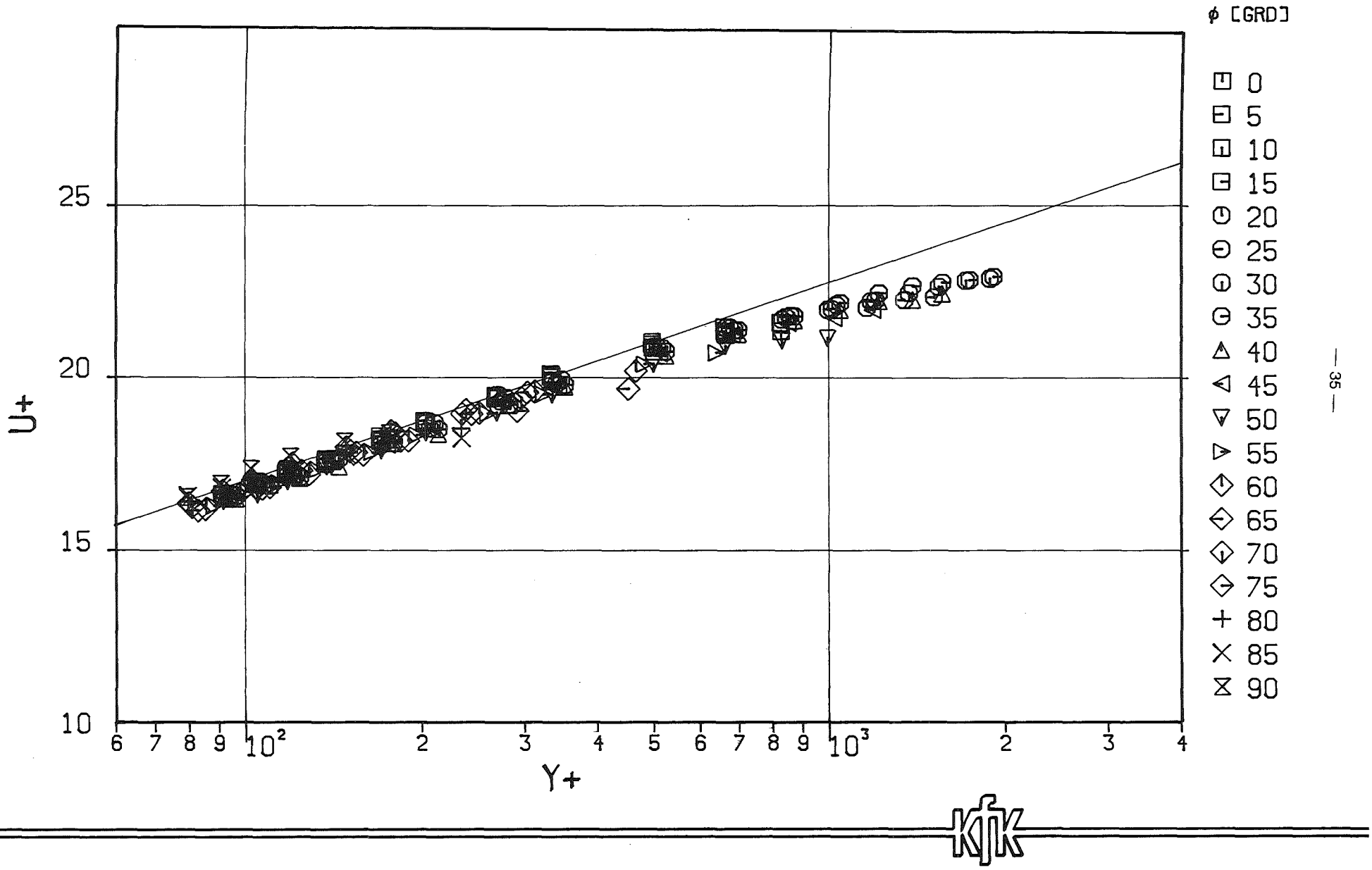

Fig. 6-3 Distribution of dimensionless velocity in the r/ϕ-part of quadrant 3

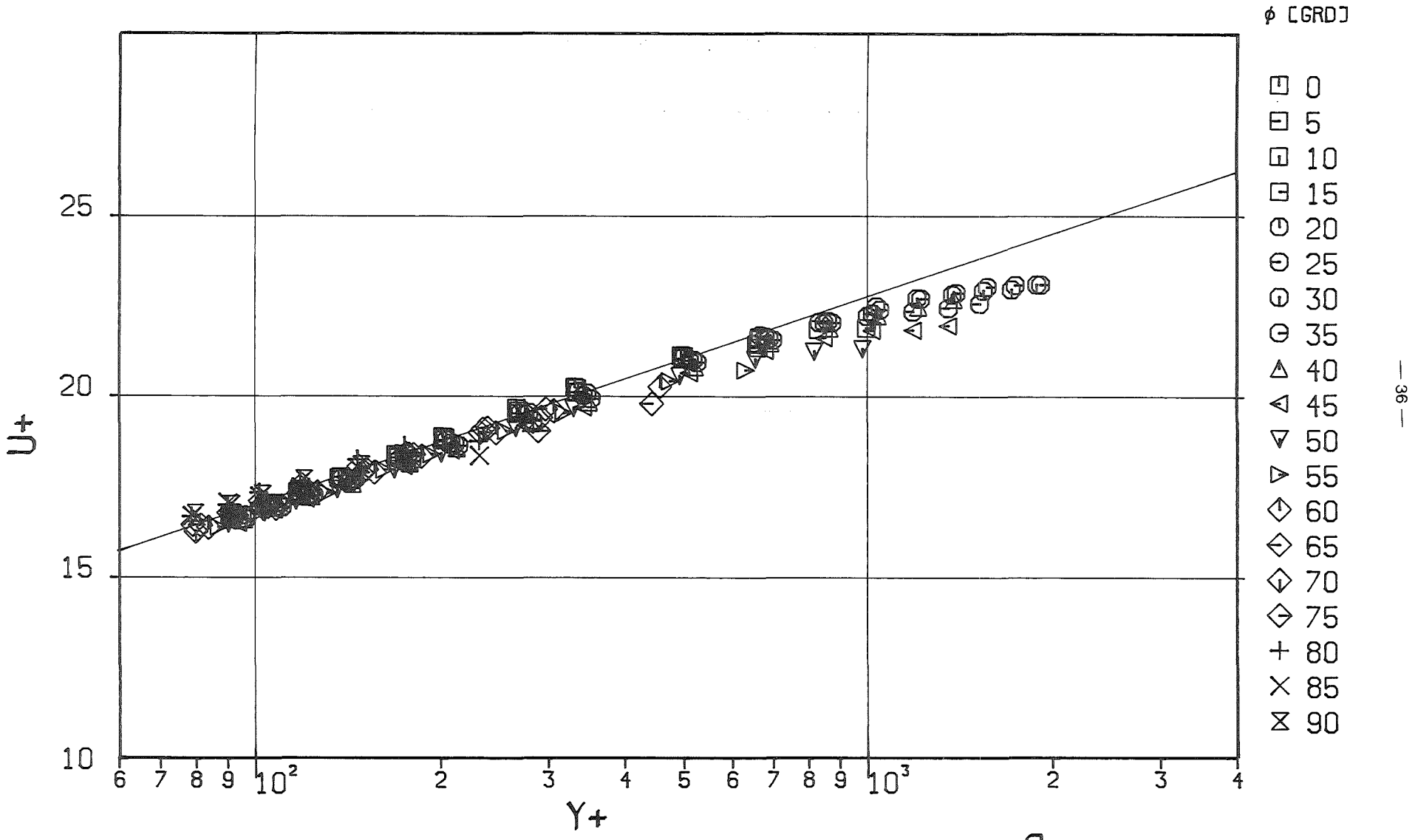

Fig. 6-4 Distribution of dimensionless velocity in the r/ϕ-part of quadrant 4

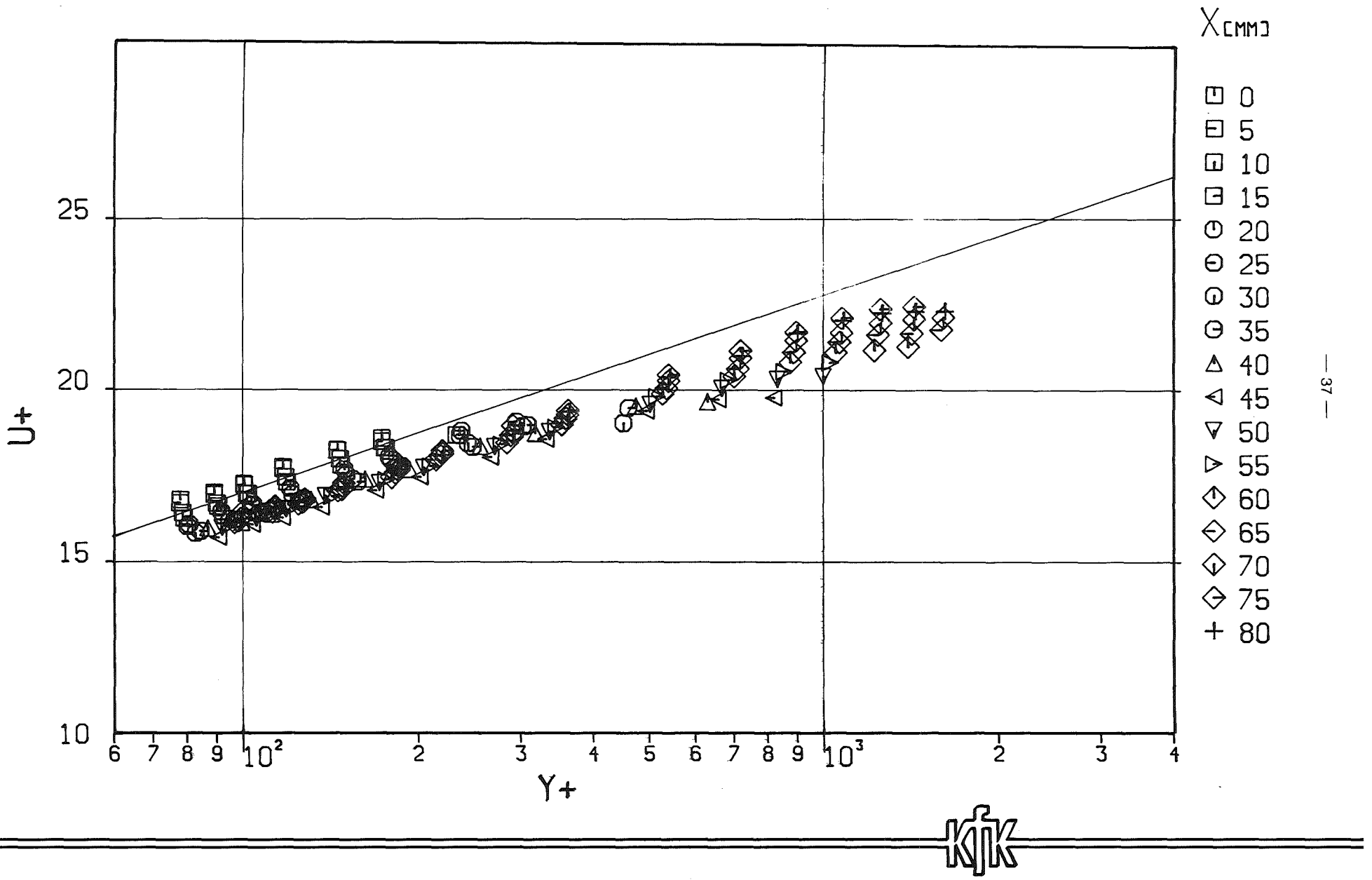

Fig. 7-1 Distribution of dimensionless velocity in the x/y-part of quadrant 1

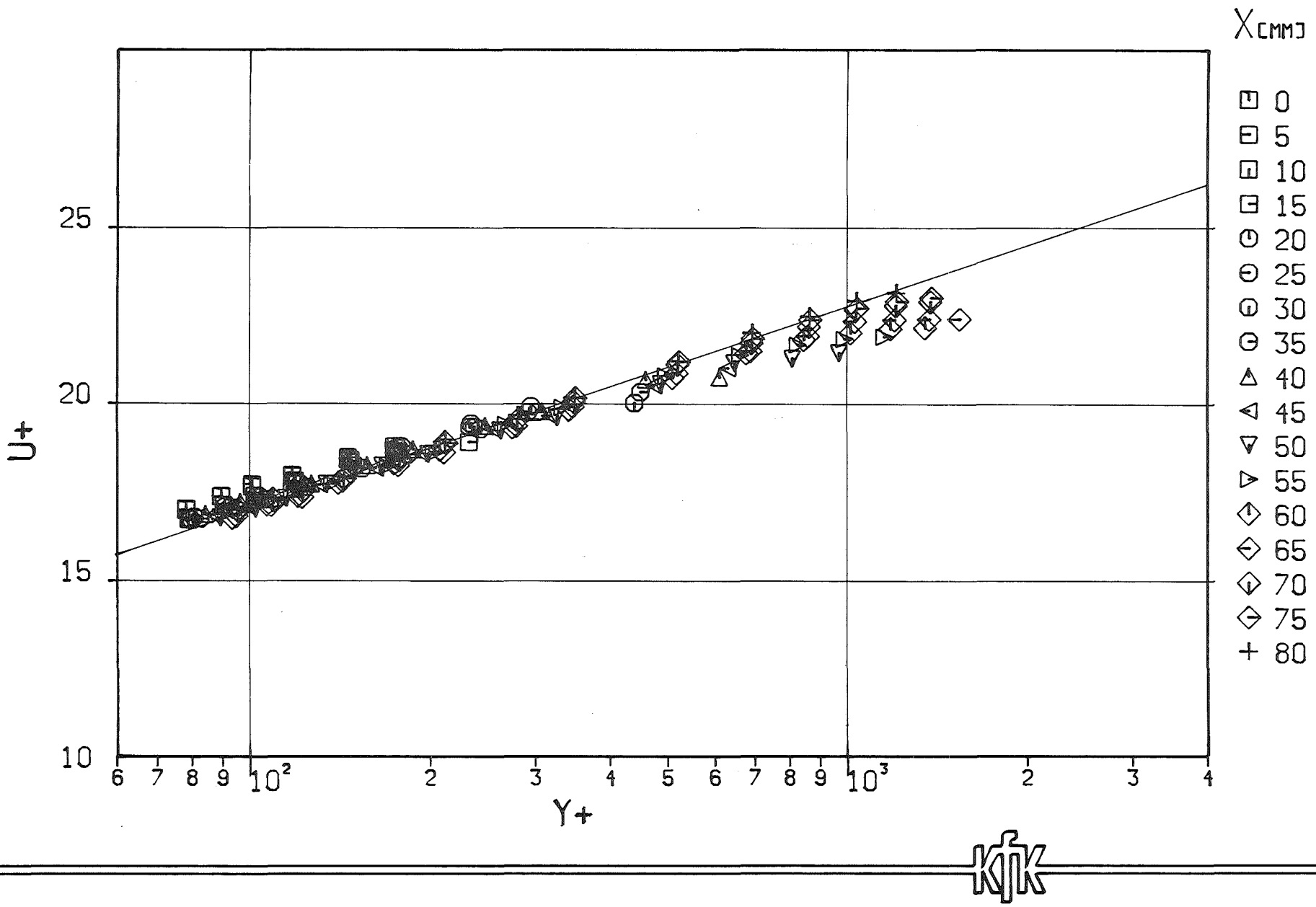

Fig. 7-2 Distribution of dimensionless velocity in the x/y-part of quadrant 2

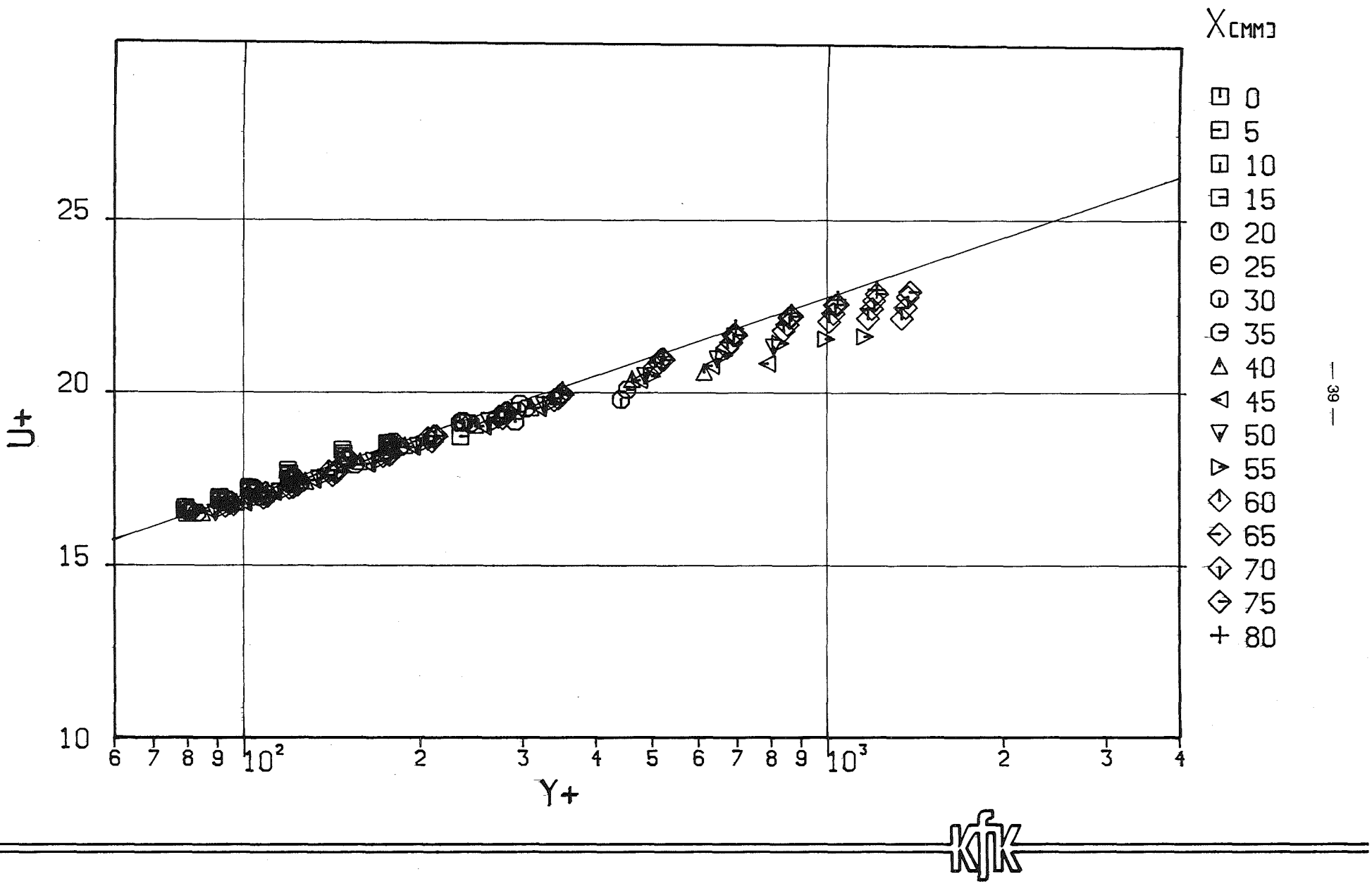

Fig. 7-3 Distribution of dimensionless velocity in the x/y-part of quadrant 3

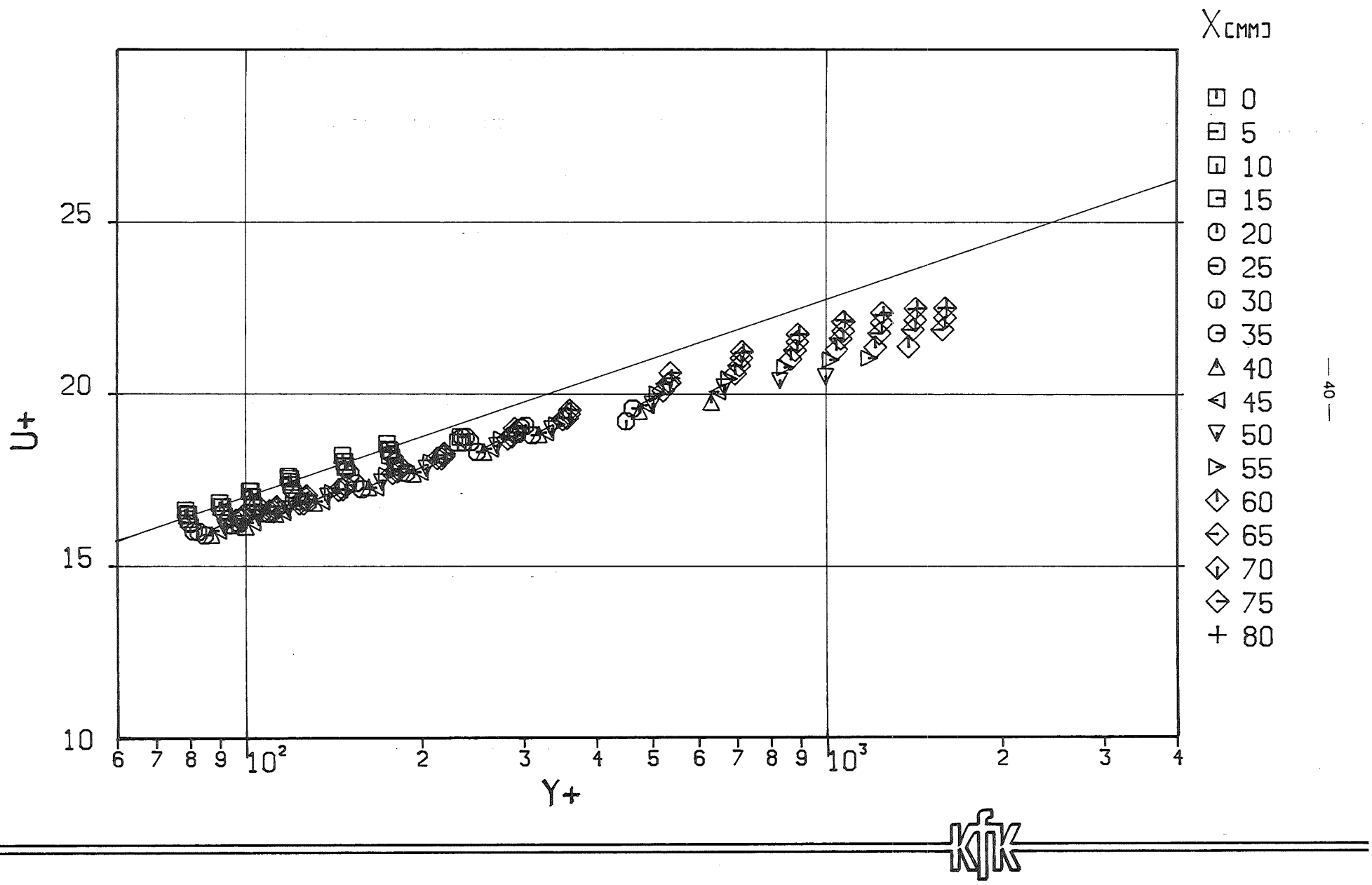

Fig. 7-4 Distribution of dimensionless velocity in the x/y-part of quadrant 4

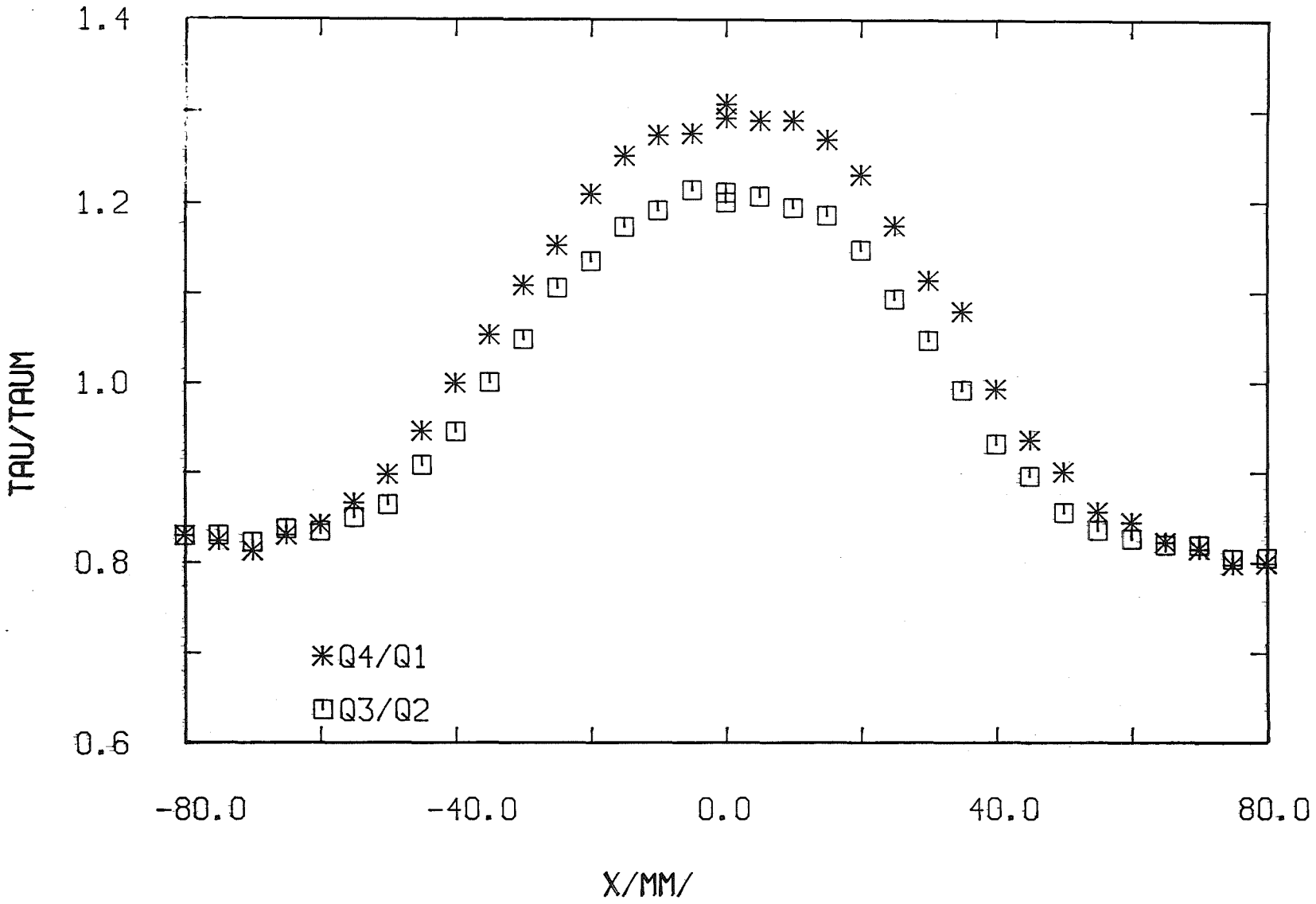

Fig. 8 Distribution of wall shear stress on the channel walls

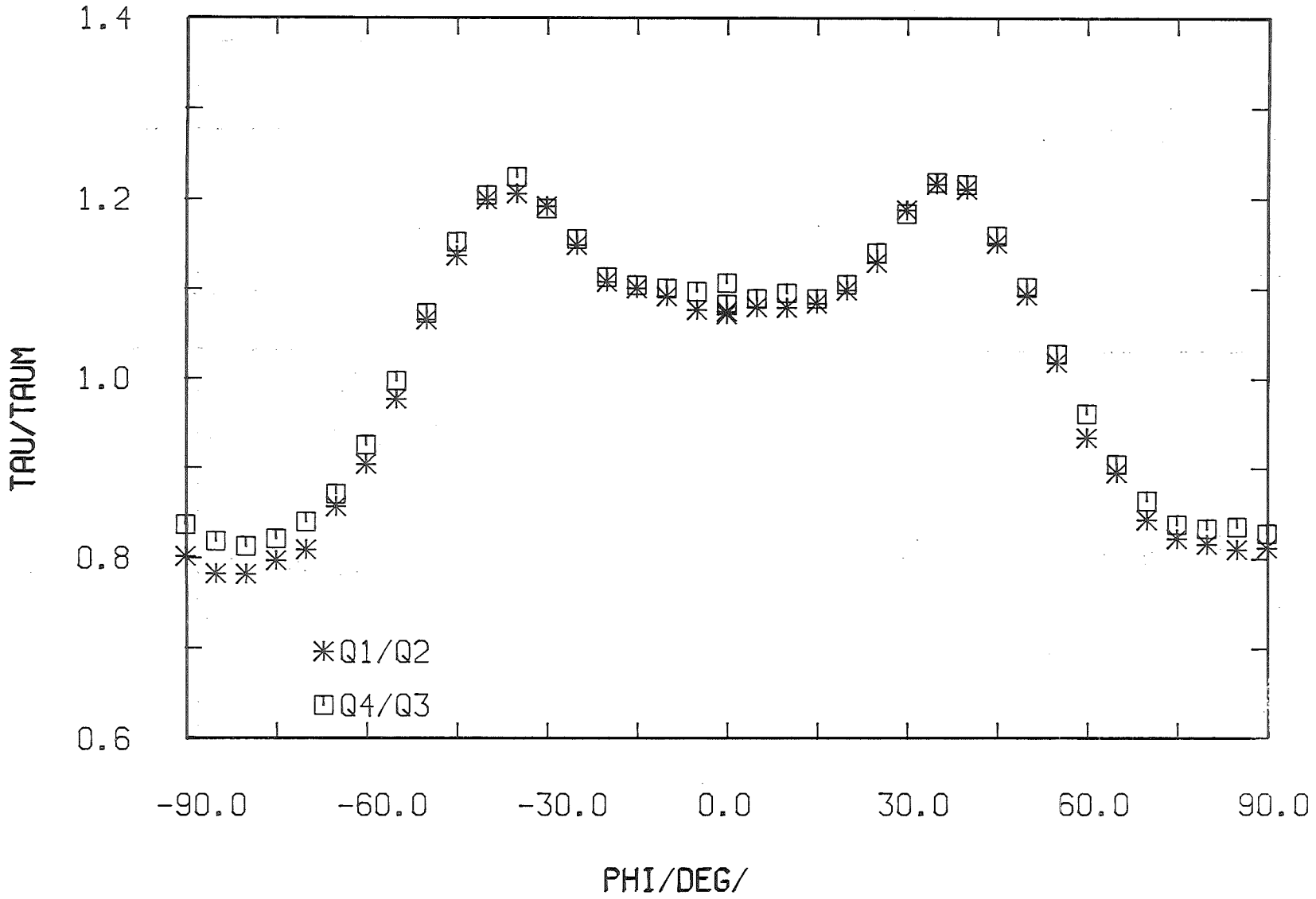

Fig. 9 Distribution of wall shear stress on the rod walls

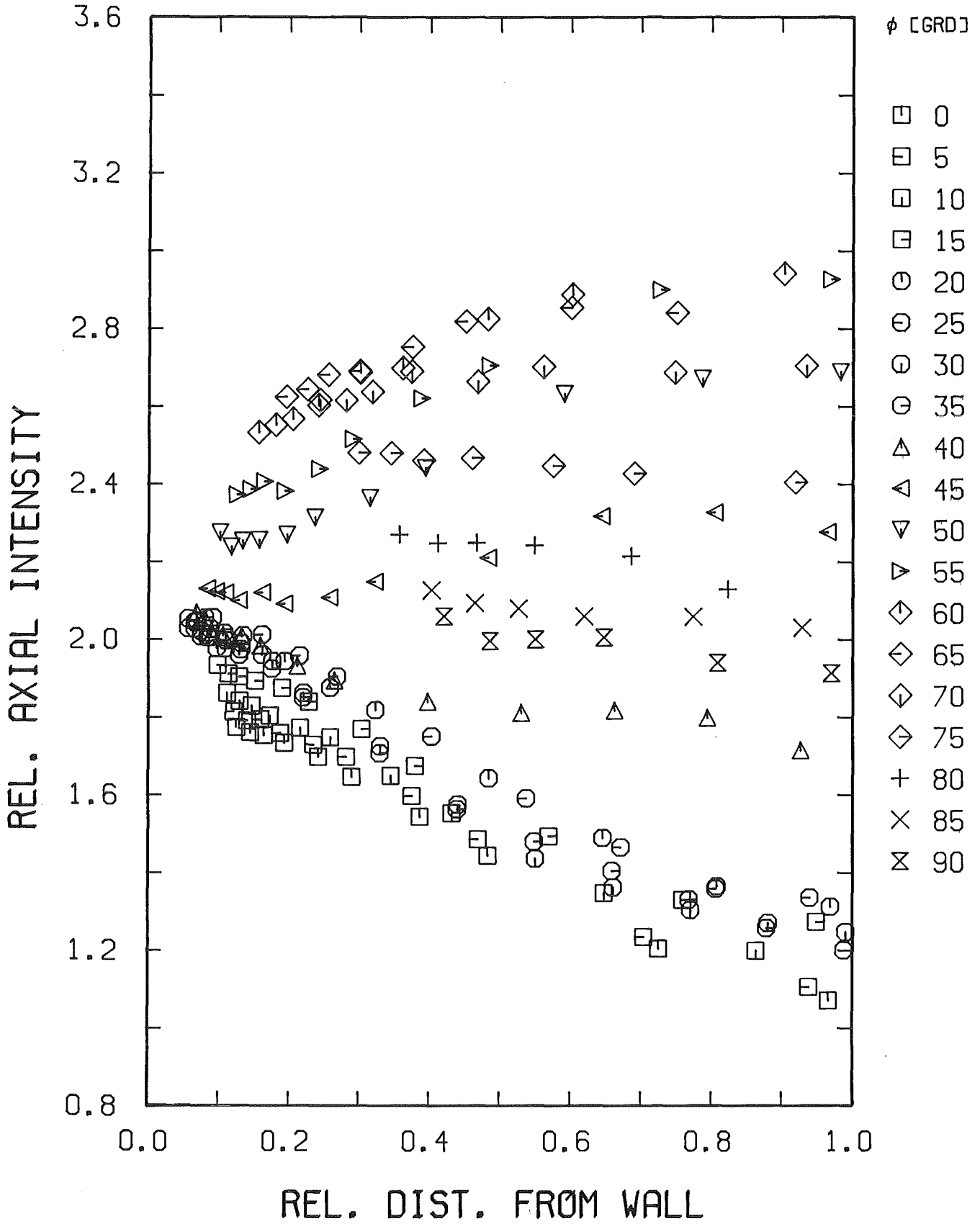

Fig. 10-1 Distribution of axial intensity in the r/ϕ-part of quadrant 1

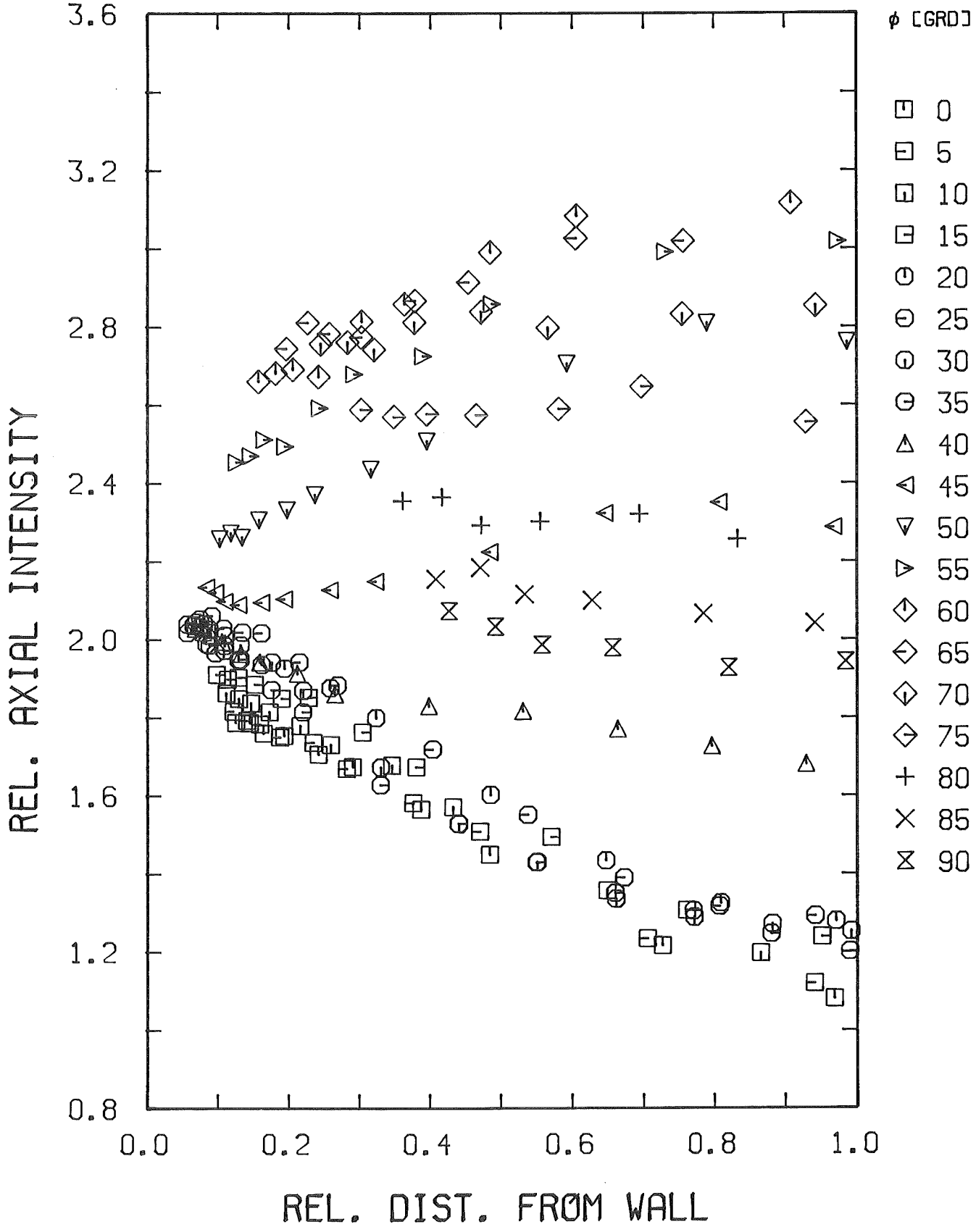

Fig. 10-2 Distribution of axial intensity in the r/φ-part of quadrant 2

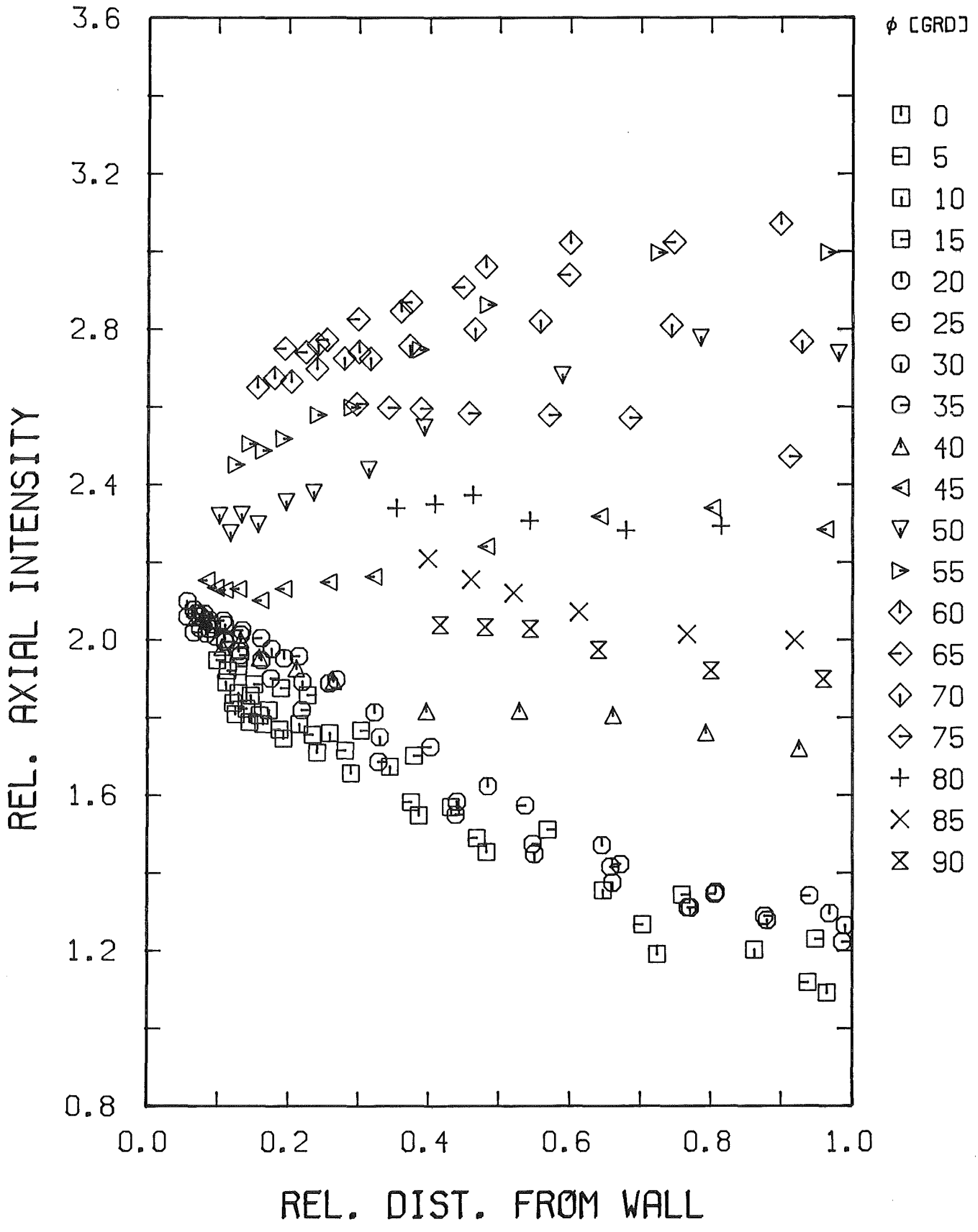

Fig. 10-3 Distribution of axial intensity in the r/ϕ-part of quadrant 3

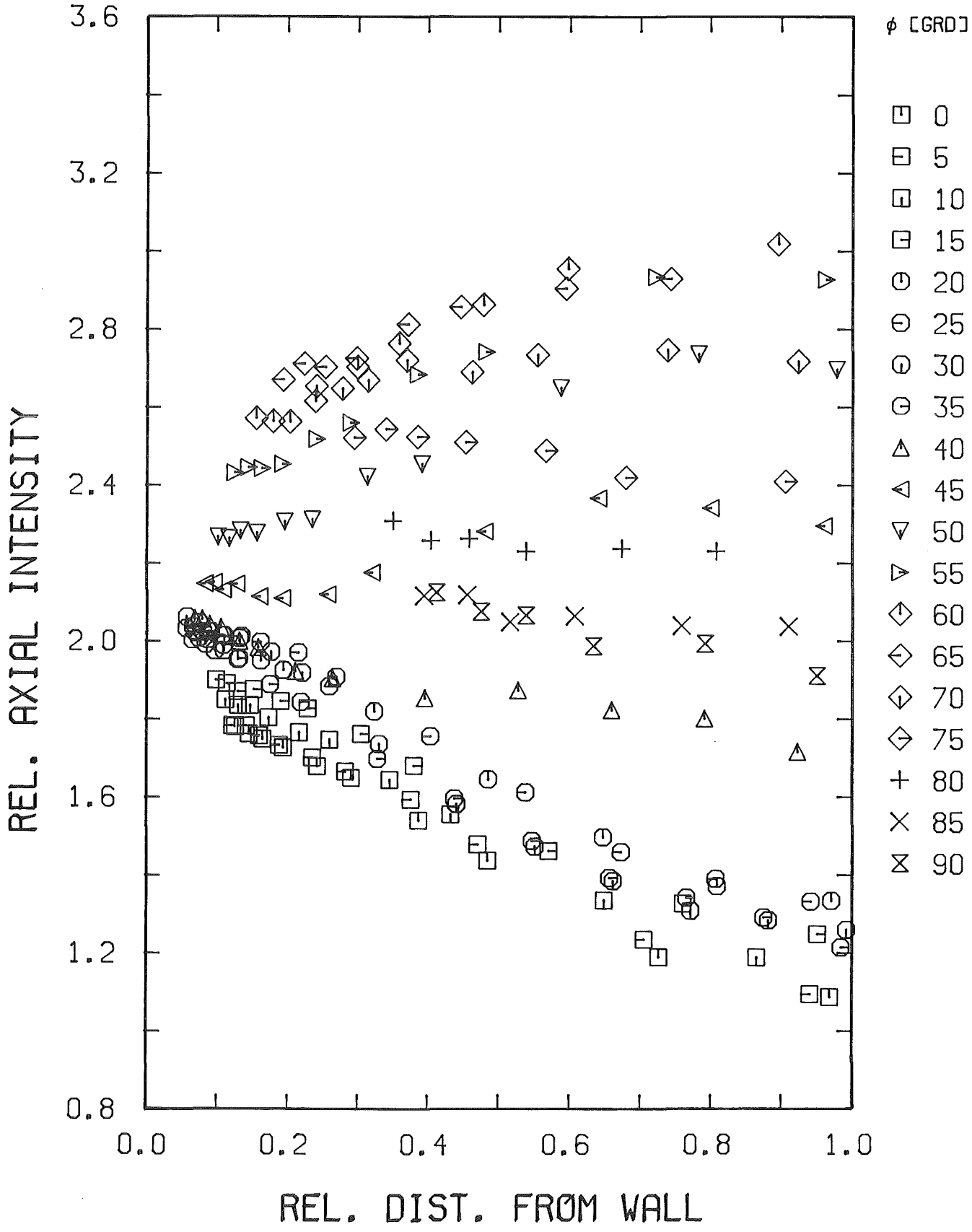

Fig. 10-4 Distribution of axial intensity in the r/ϕ-part of quadrant 4

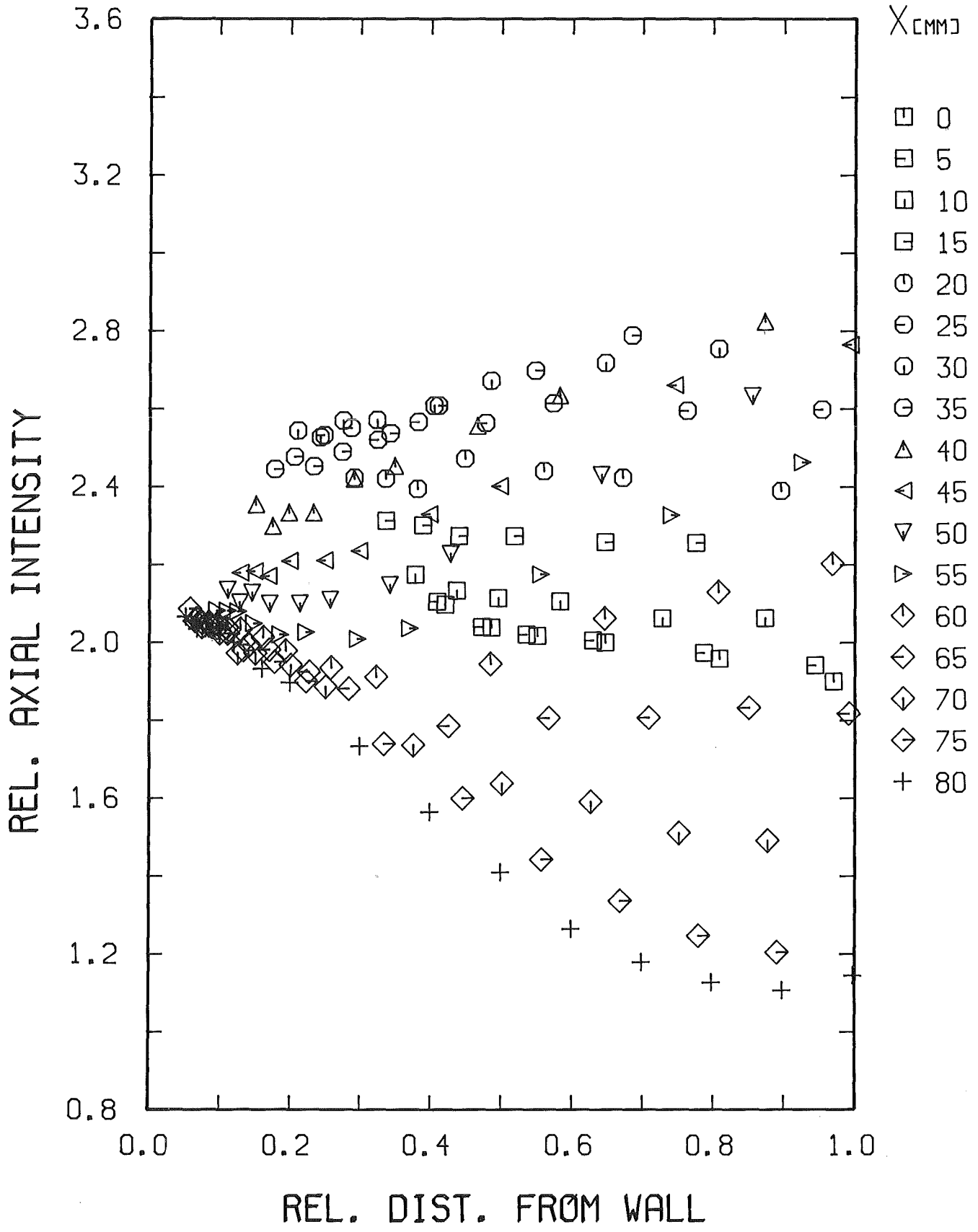

Fig. 11-1 Distribution of axial intensity in the x/y-part of quadrant 1

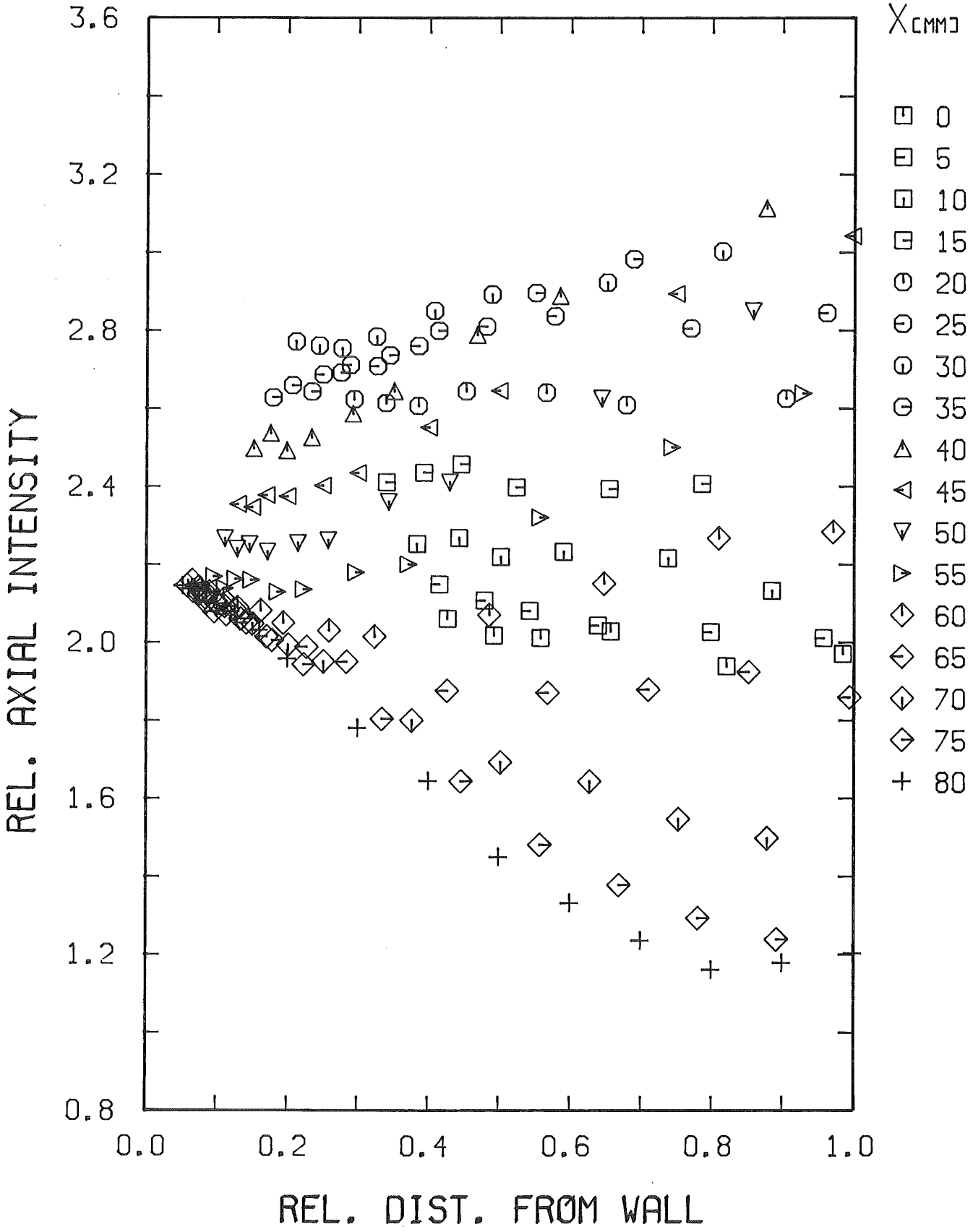

Fig. 11-2 Distribution of axial intensity in the x/y-part of quadrant 2

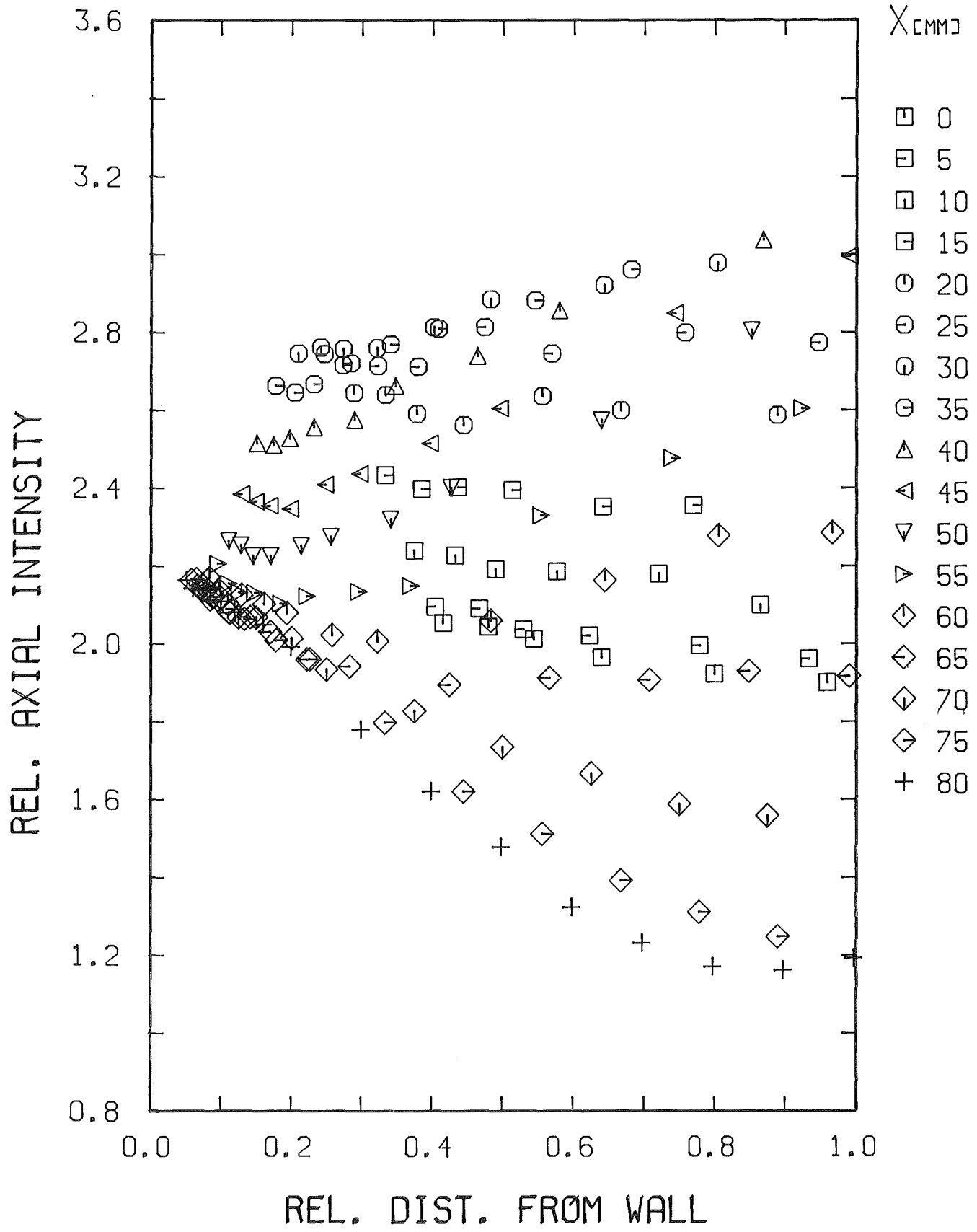

Fig. 11-3 Distribution of axial intensity in the x/y-part of quadrant 3

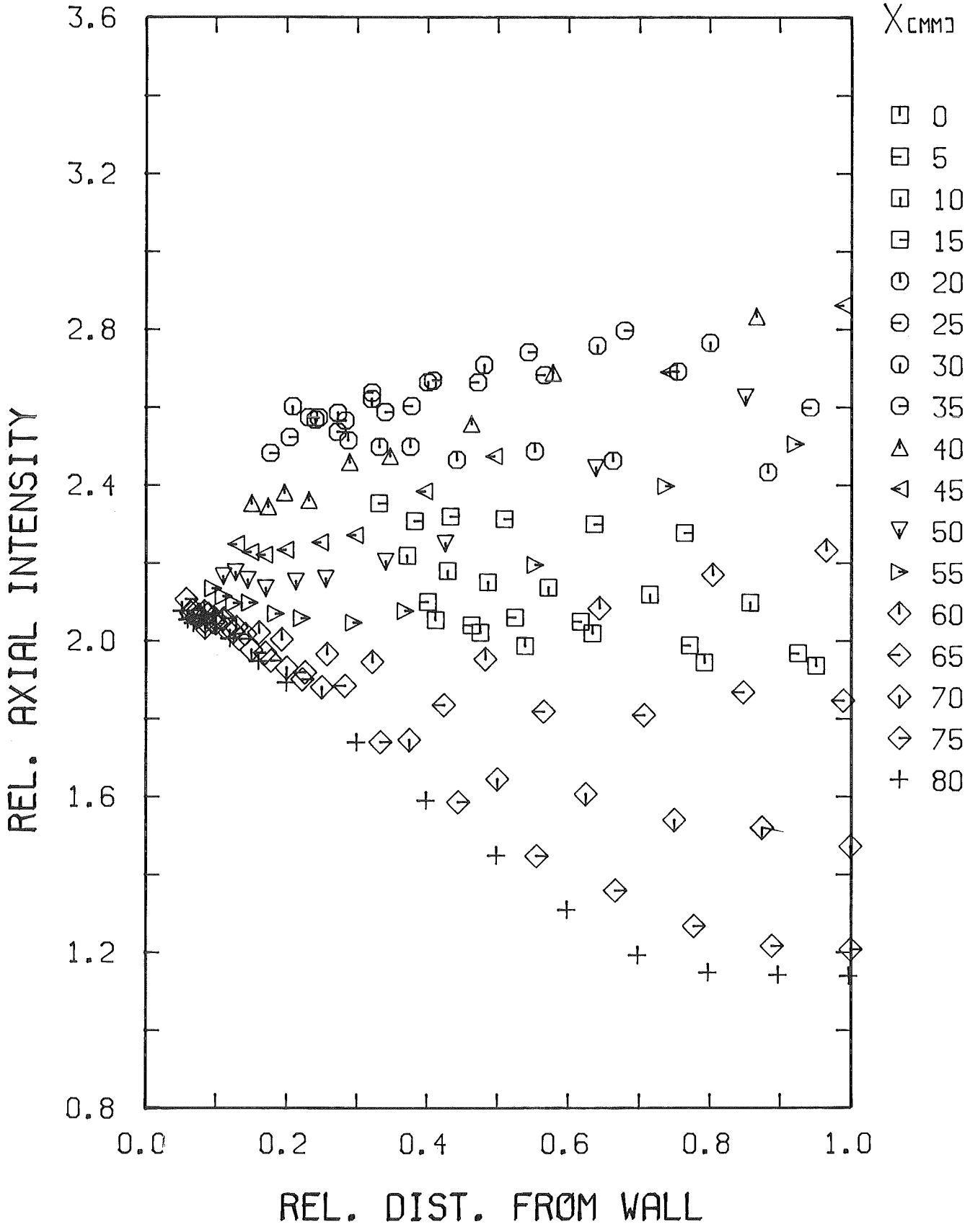

Fig. 11-4 Distribution of axial intensity in the x/y-part of quadrant 4

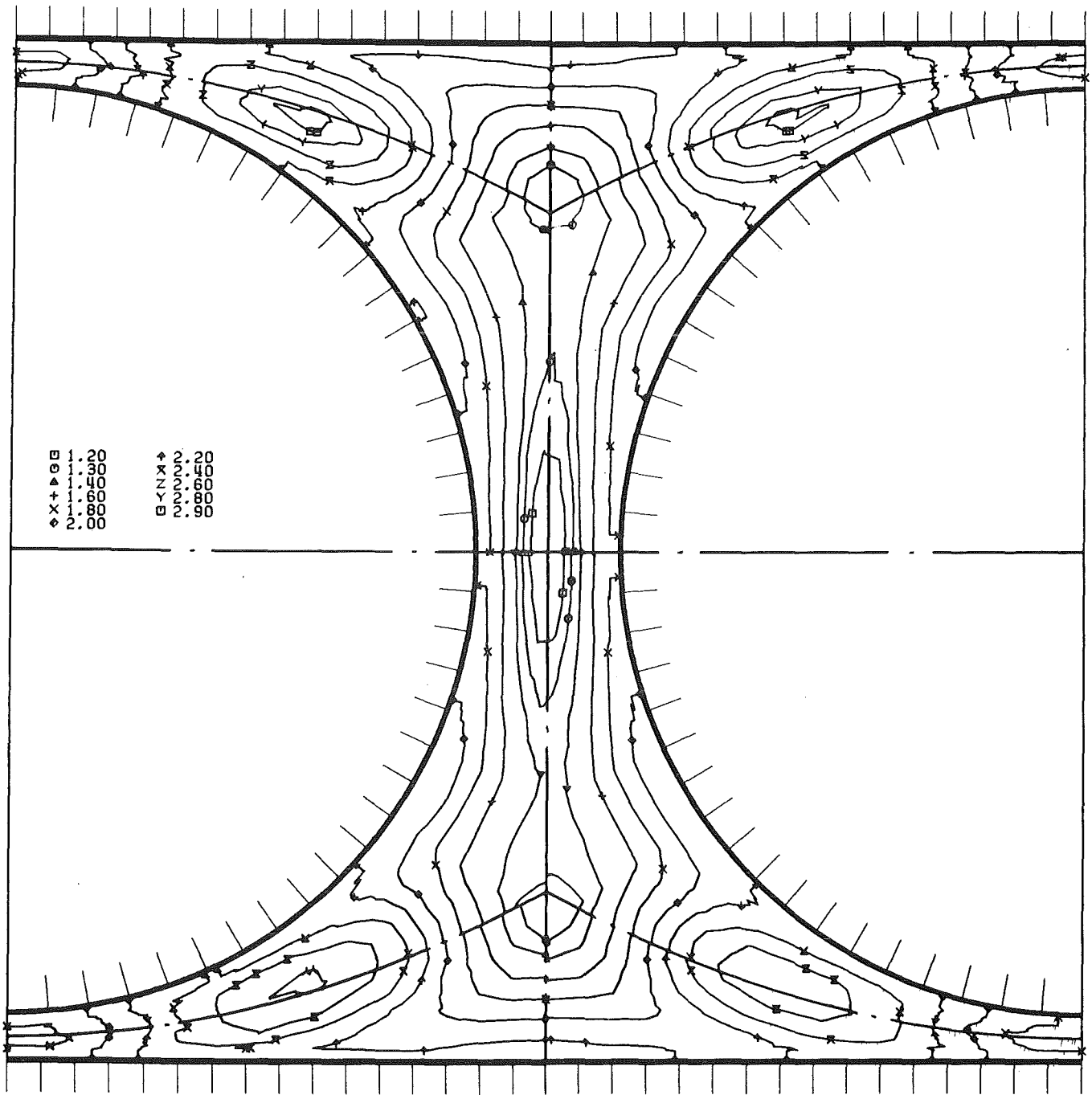

Fig. 12 Contours of axial intensity in the four quadrants

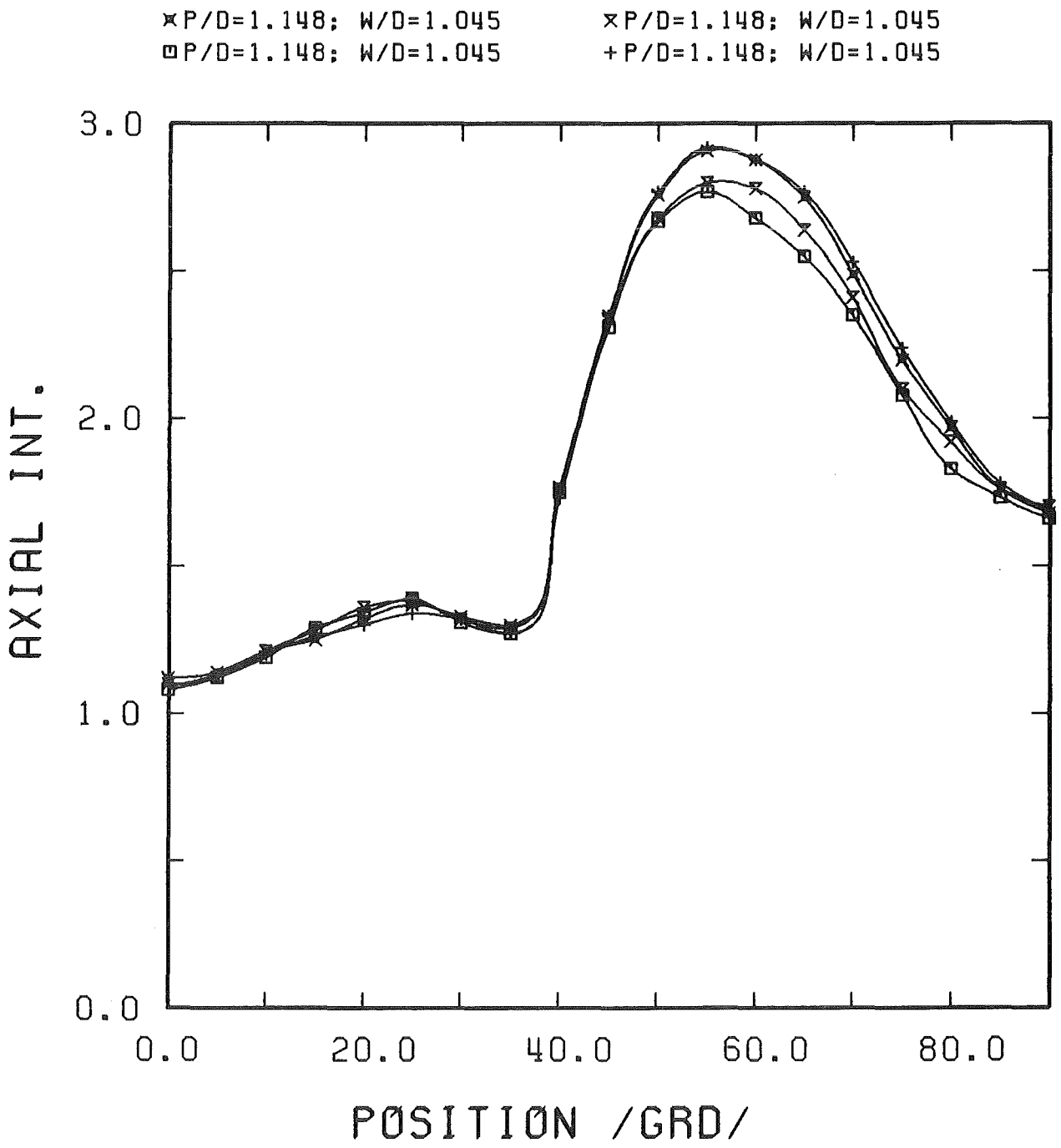

Fig. 12 a) Distribution of axial intensity along the lines of maximum distance from the wall

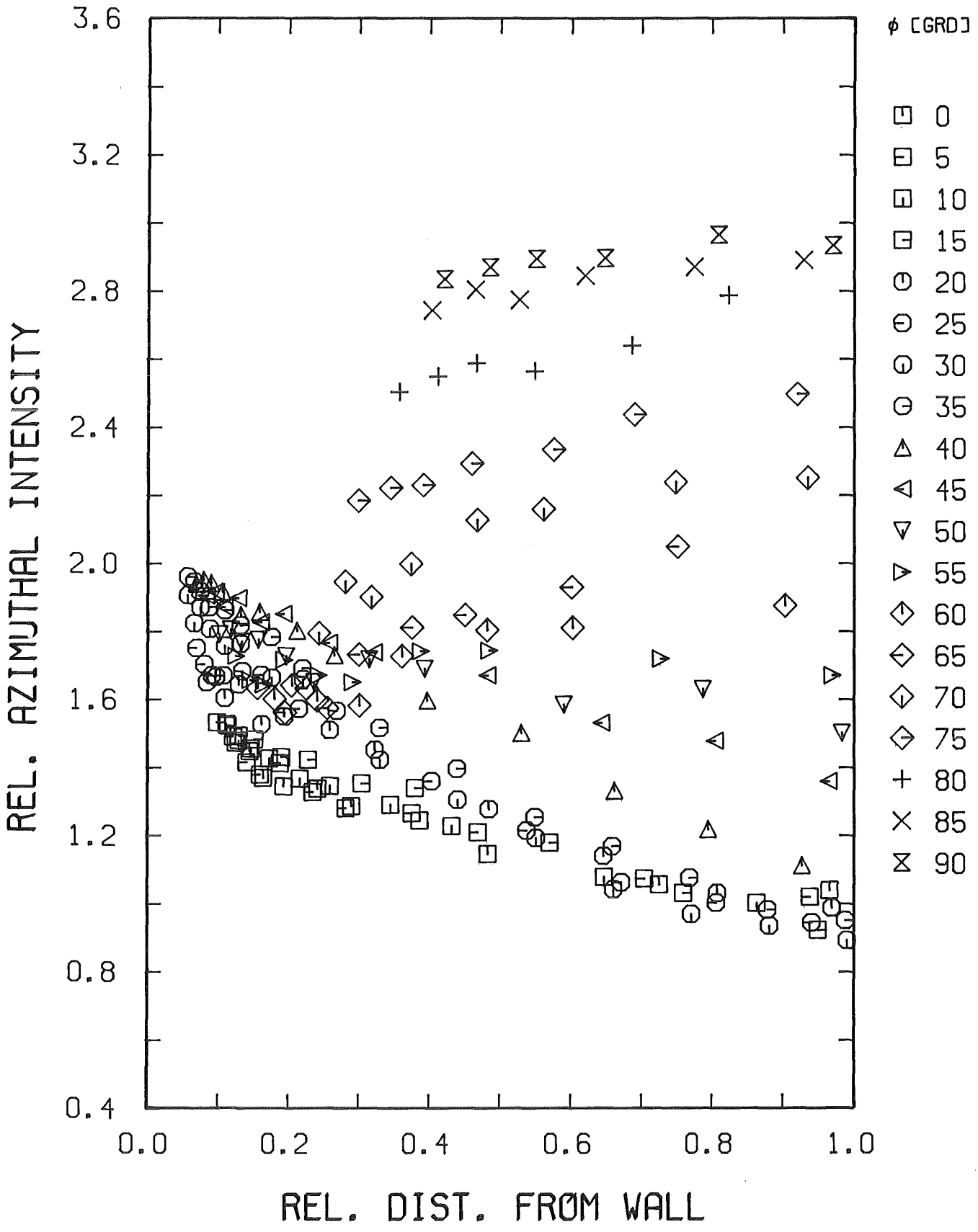

Fig. 13-1 Distribution of azimuthal intensity in the r/ϕ-part of quadrant 1

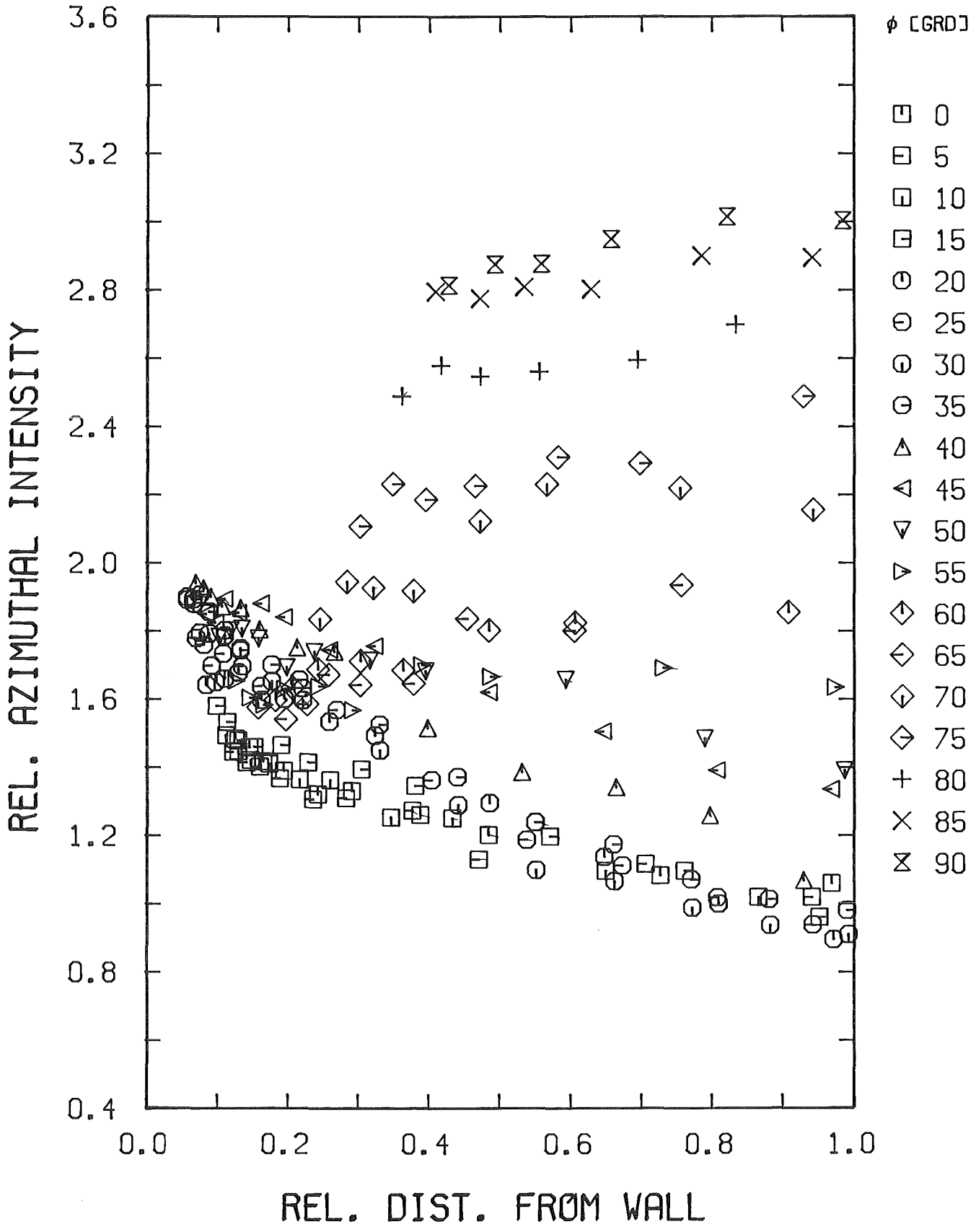

Fig. 13-2 Distribution of azimuthal intensity in the r/φ-part of quadrant 2

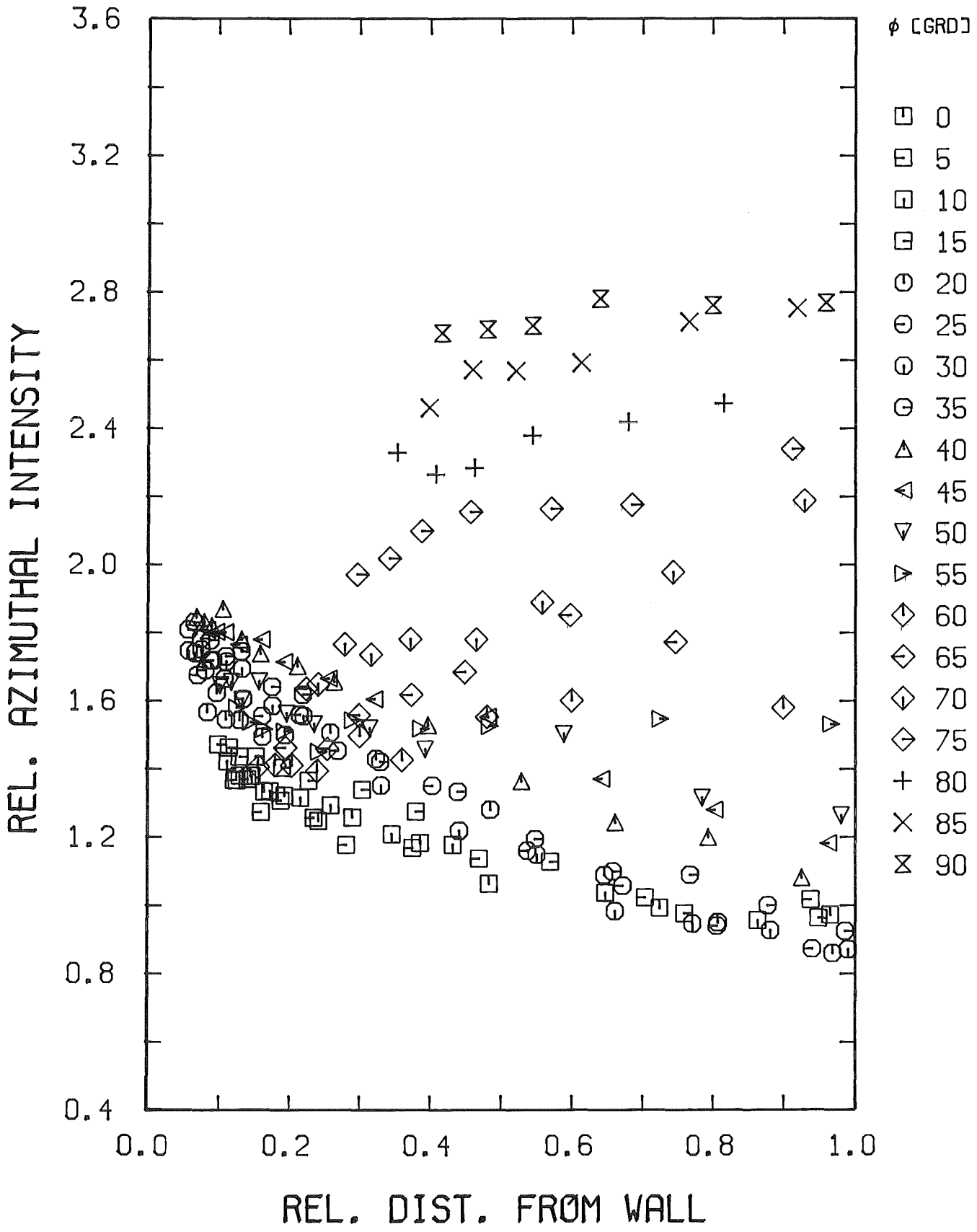

Fig. 13-3 Distribution of azimuthal intensity in the r/ϕ-part of quadrant 3

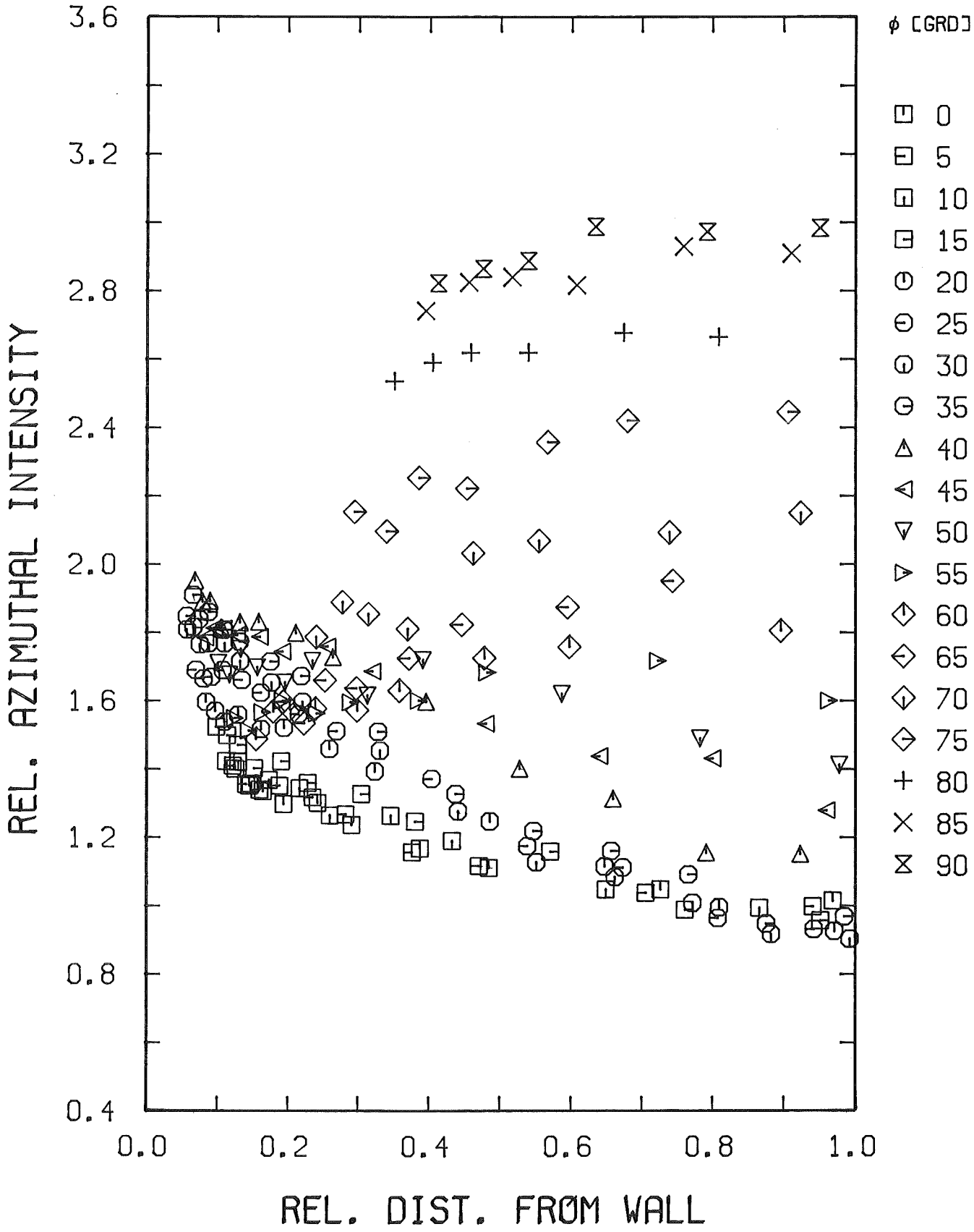

Fig. 13-4 Distribution of azimuthal intensity in the r/φ-part of quadrant 4

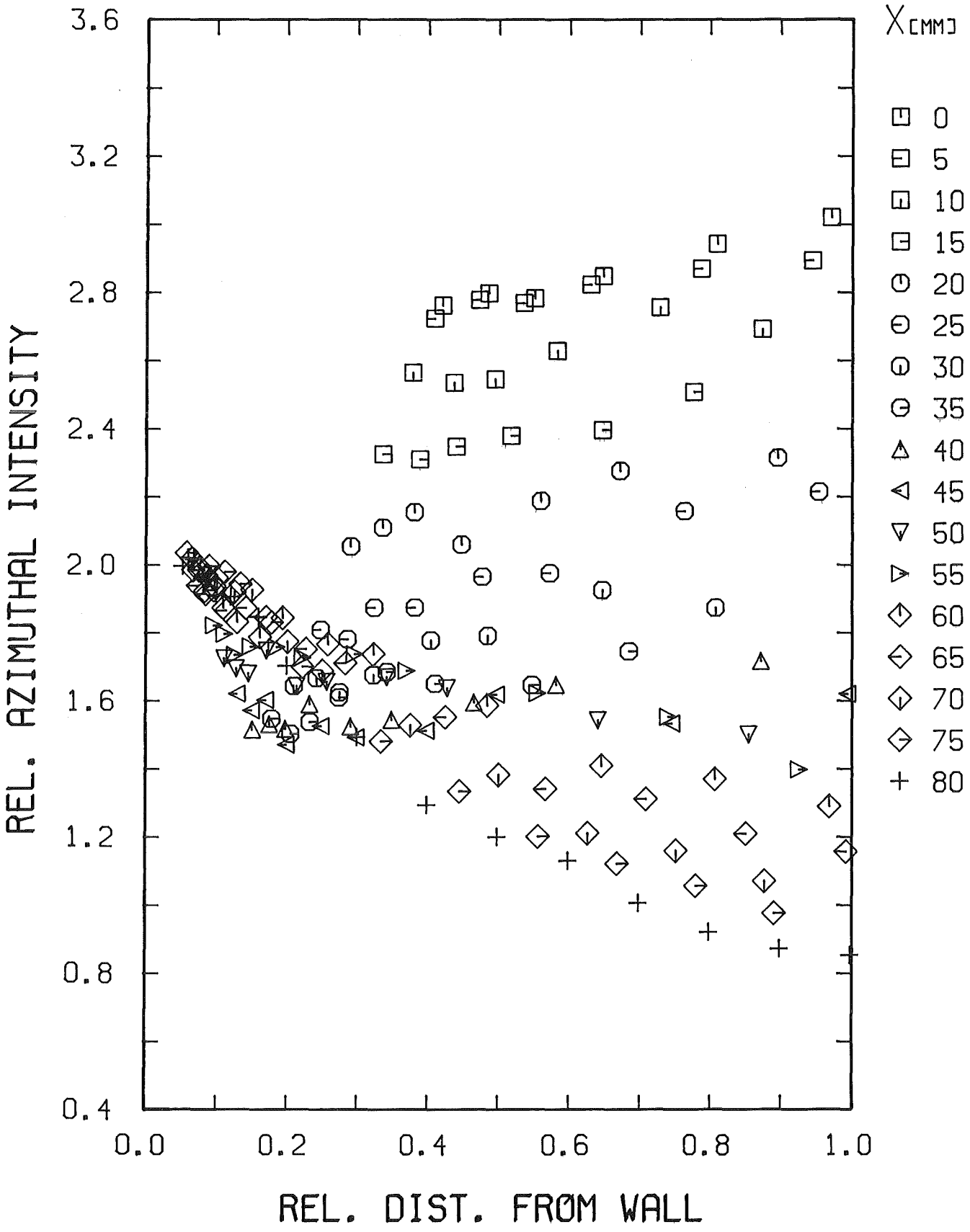

Fig. 14-1 Distribution of azimuthal intensity in the x/y-part of quadrant 1

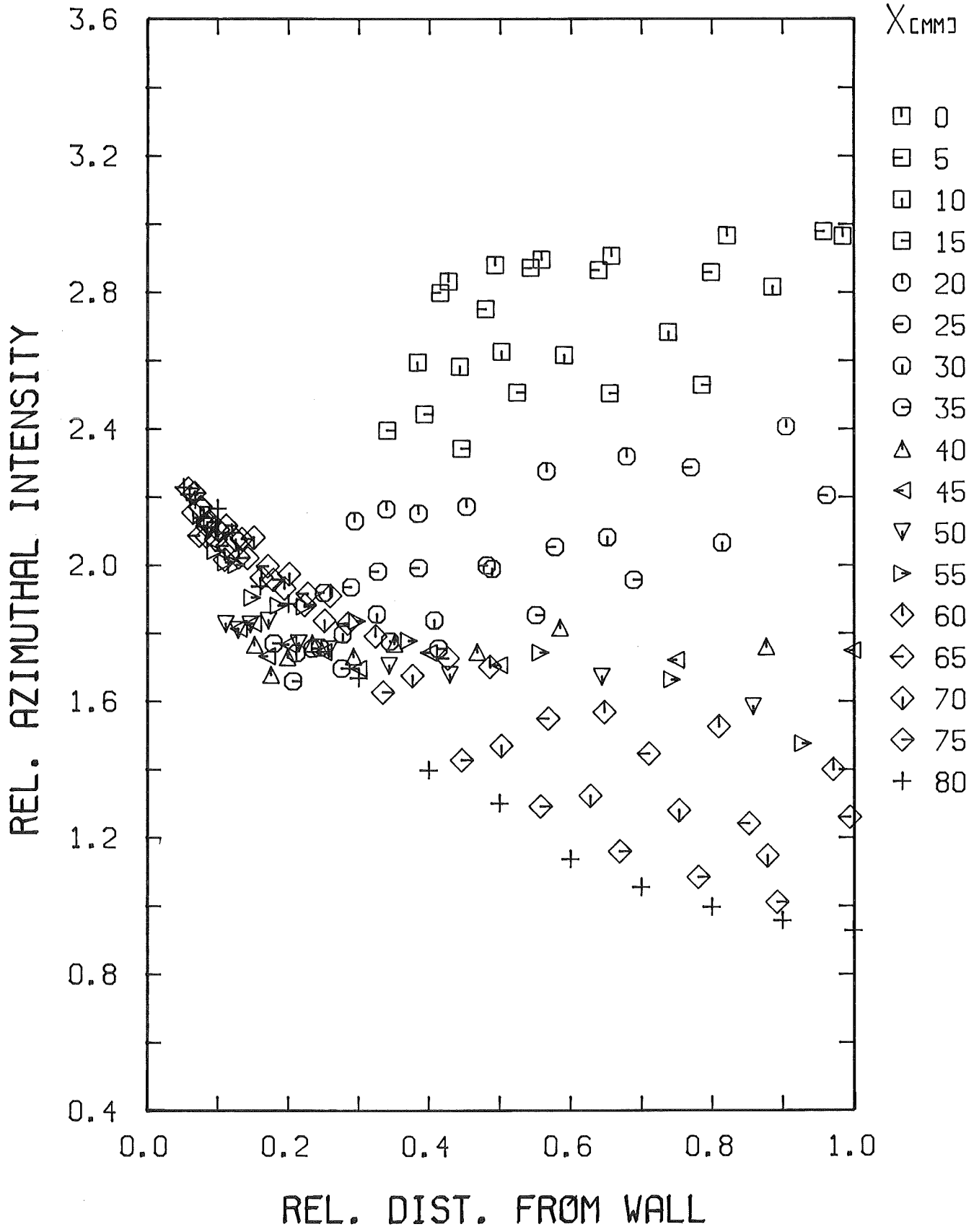

Fig. 14-2 Distribution of azimuthal intensity in the x/y-part of quadrant 2

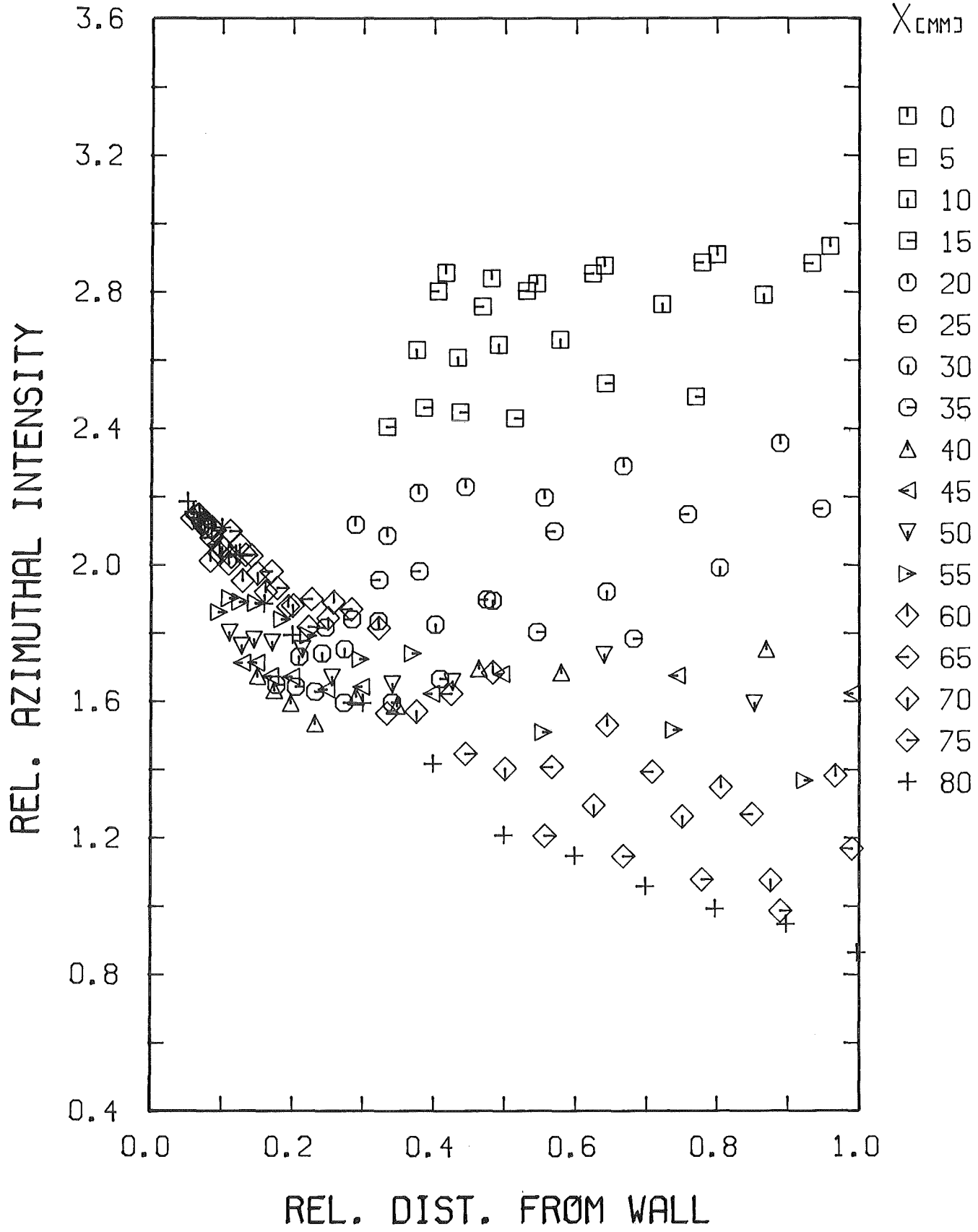

Fig. 14-3 Distribution of azimuthal intensity in the x/y-part of quadrant 3

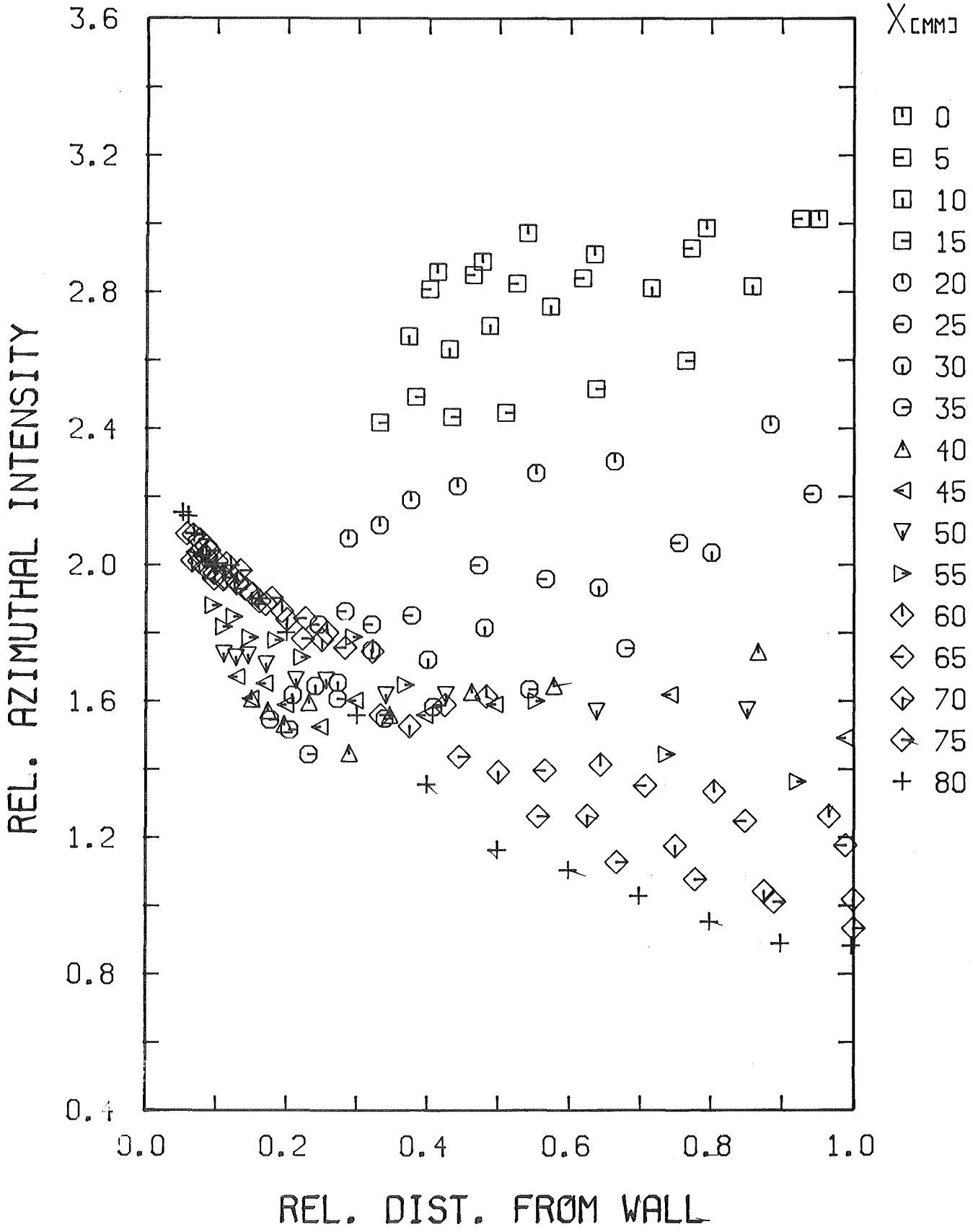

Fig. 14-4 Distribution of azimuthal intensity in the x/y-part of quadrant 4

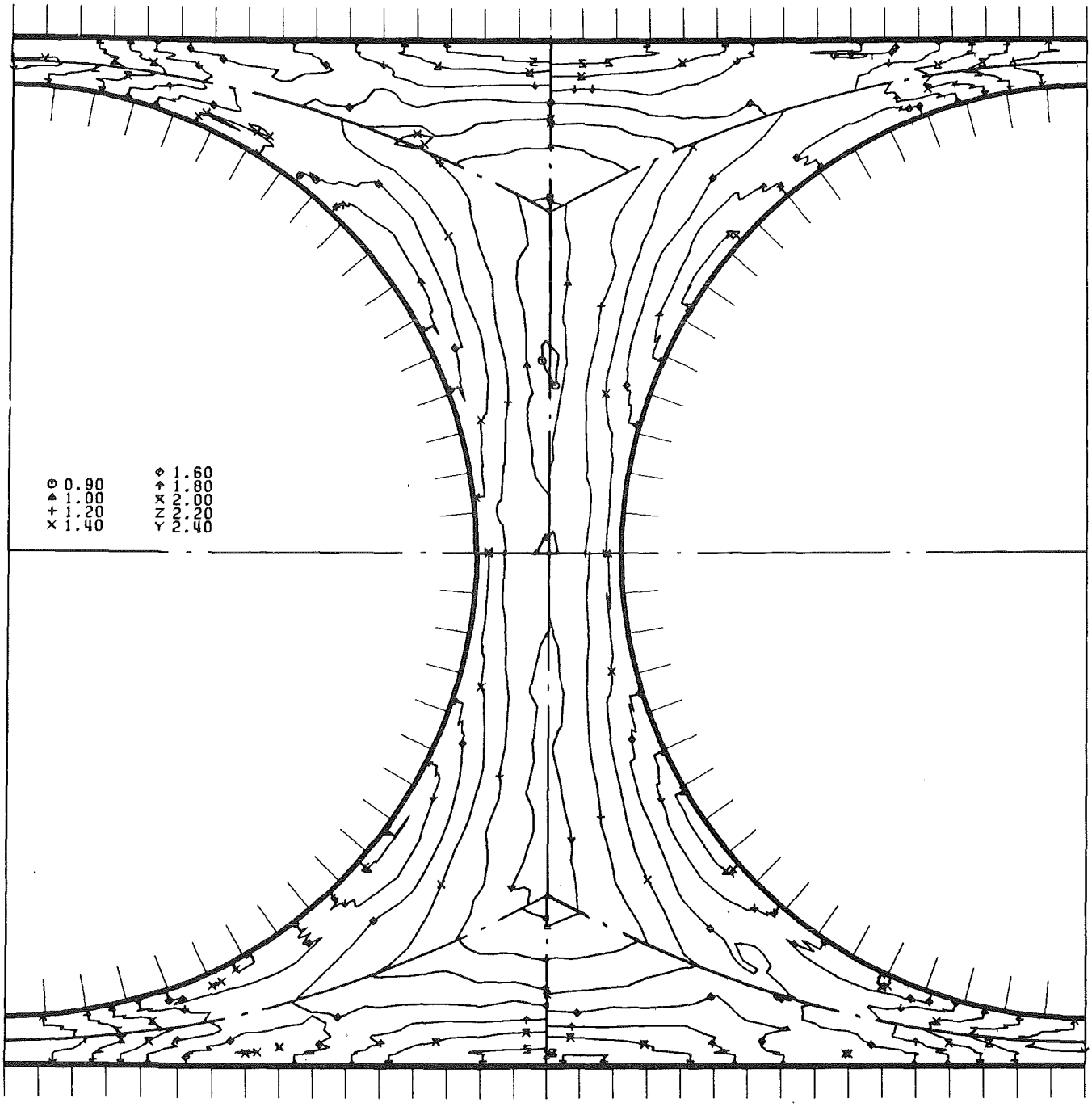

Fig. 15 Contorus of azimuthal intensity in the four quadrants

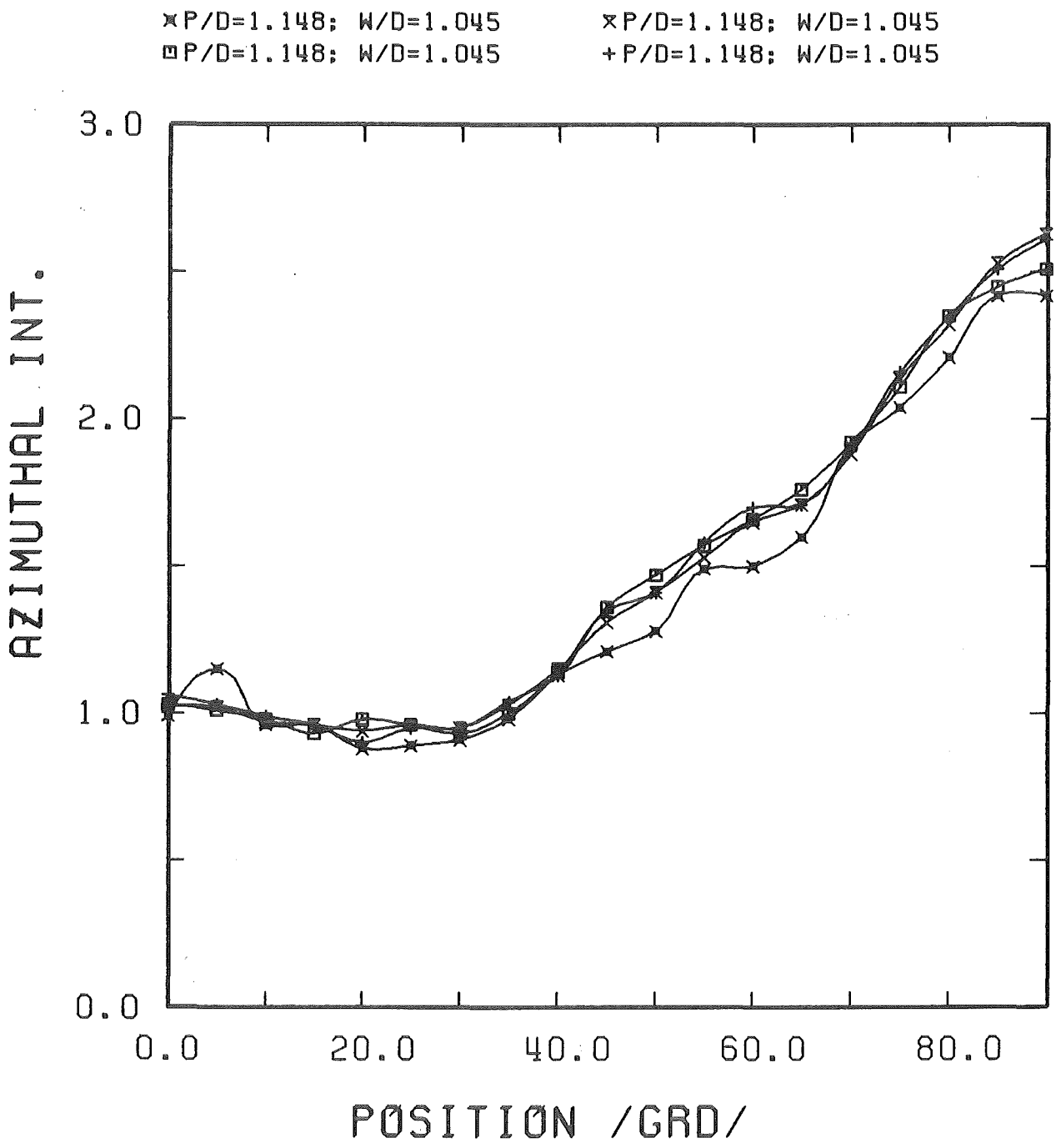

Fig. 15 a) Distribution of azimuthal intensity along the lines of maximum distance from the wall

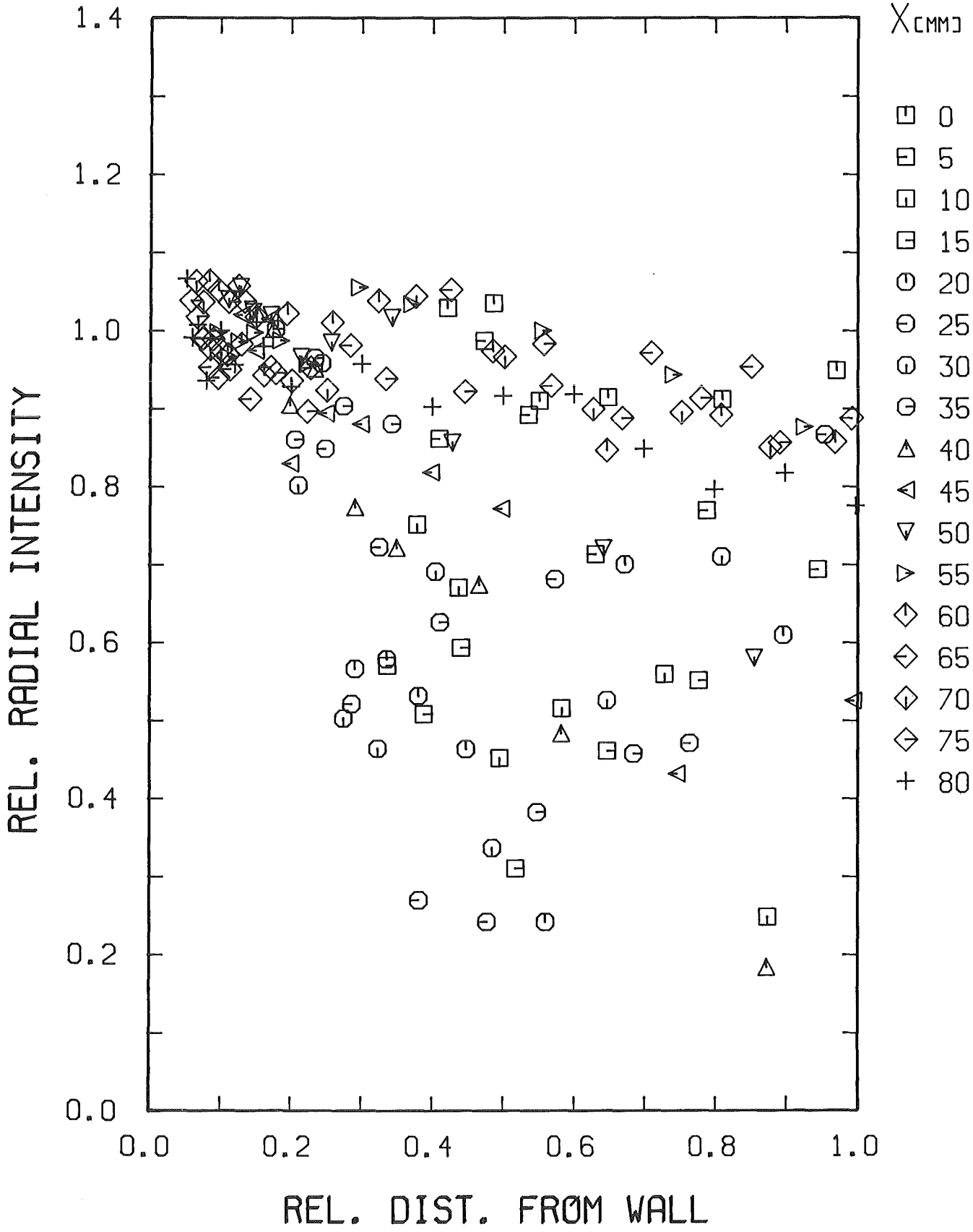

Fig. 16-1 Distribution of radial intensity in the x/y-part of quadrant 1

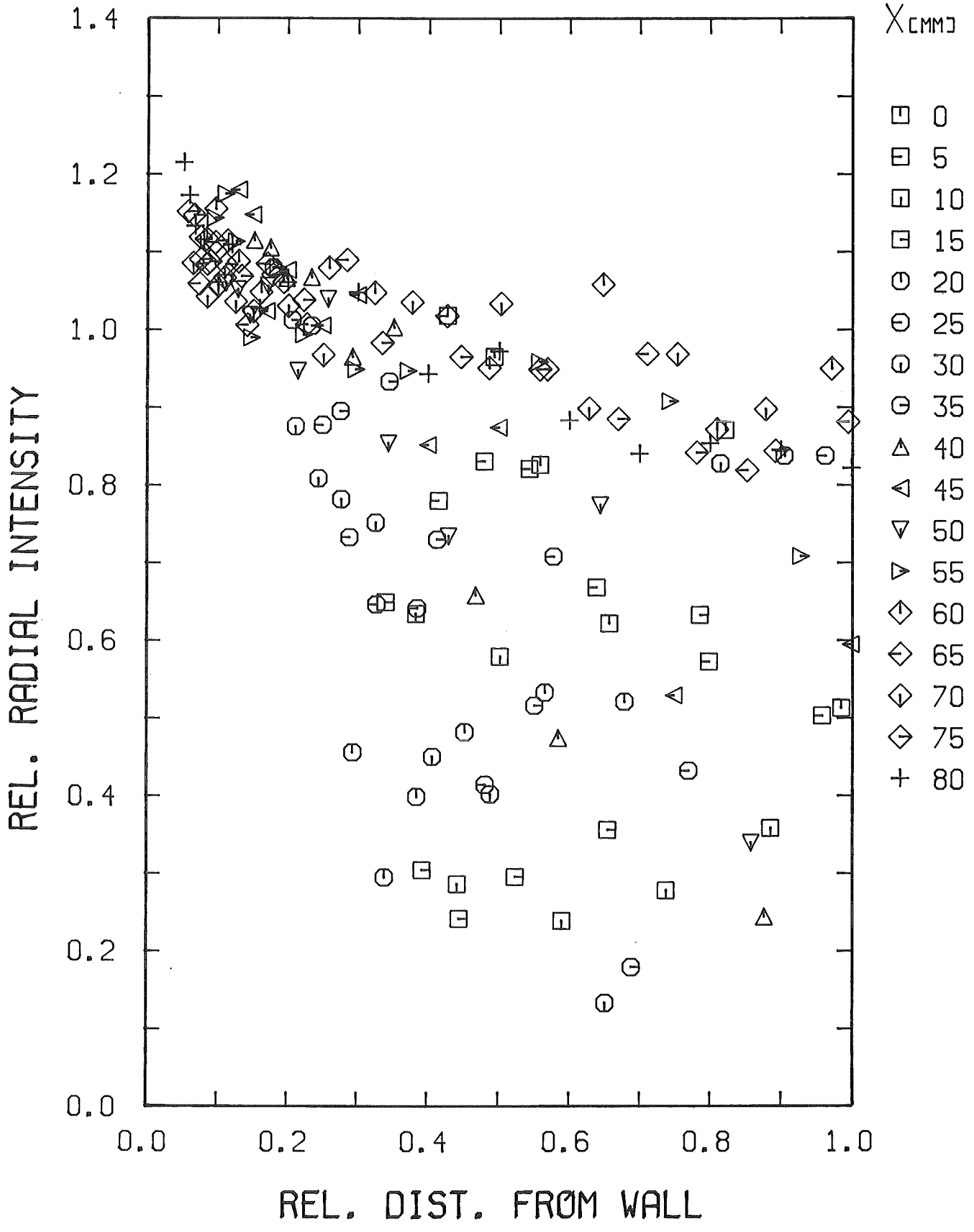

Fig. 16-2 Distribution of radial intensity in the x/y-part of quadrant 2

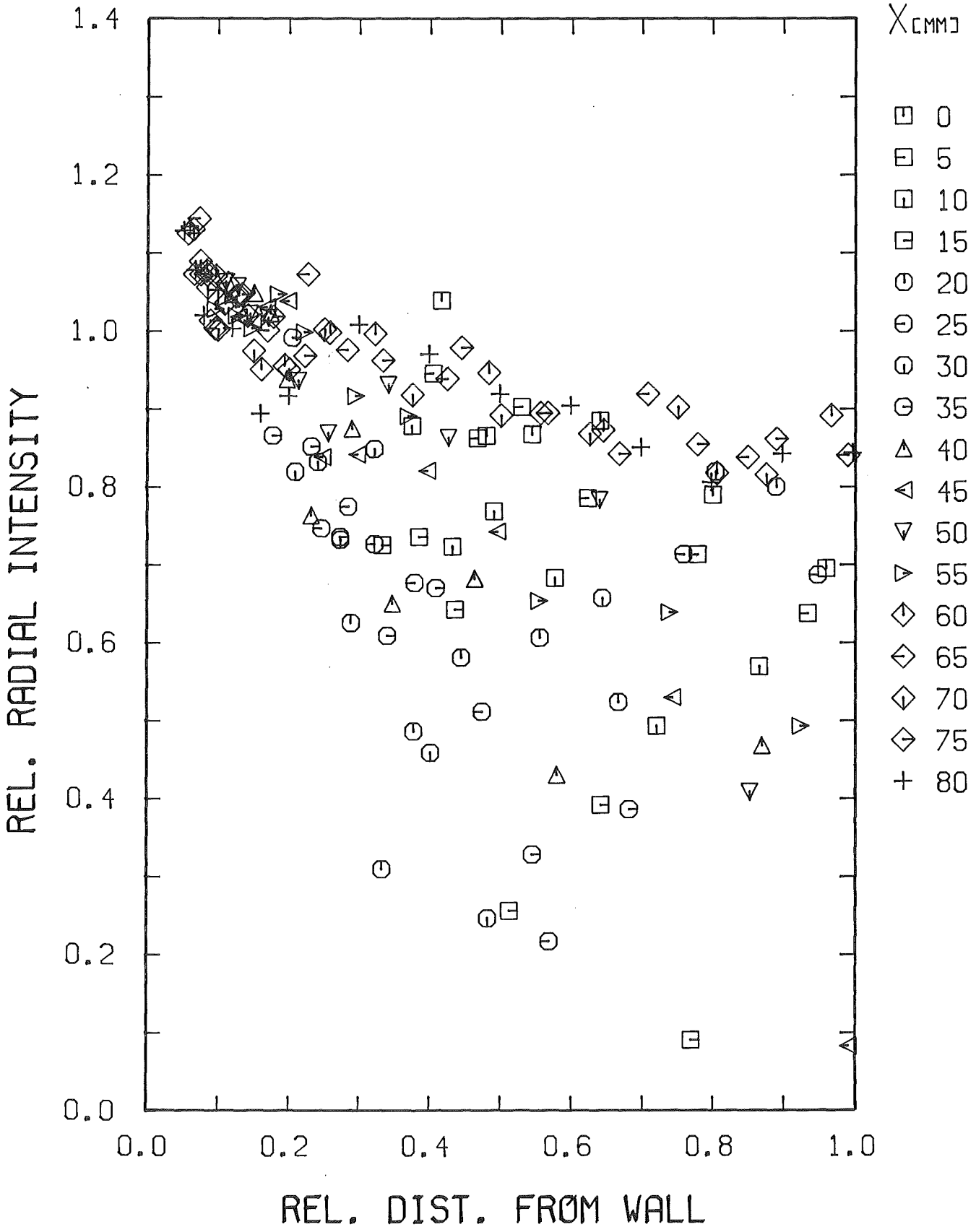

Fig. 16-3 Distribution of radial intensity in the x/y-part of quadrant 3

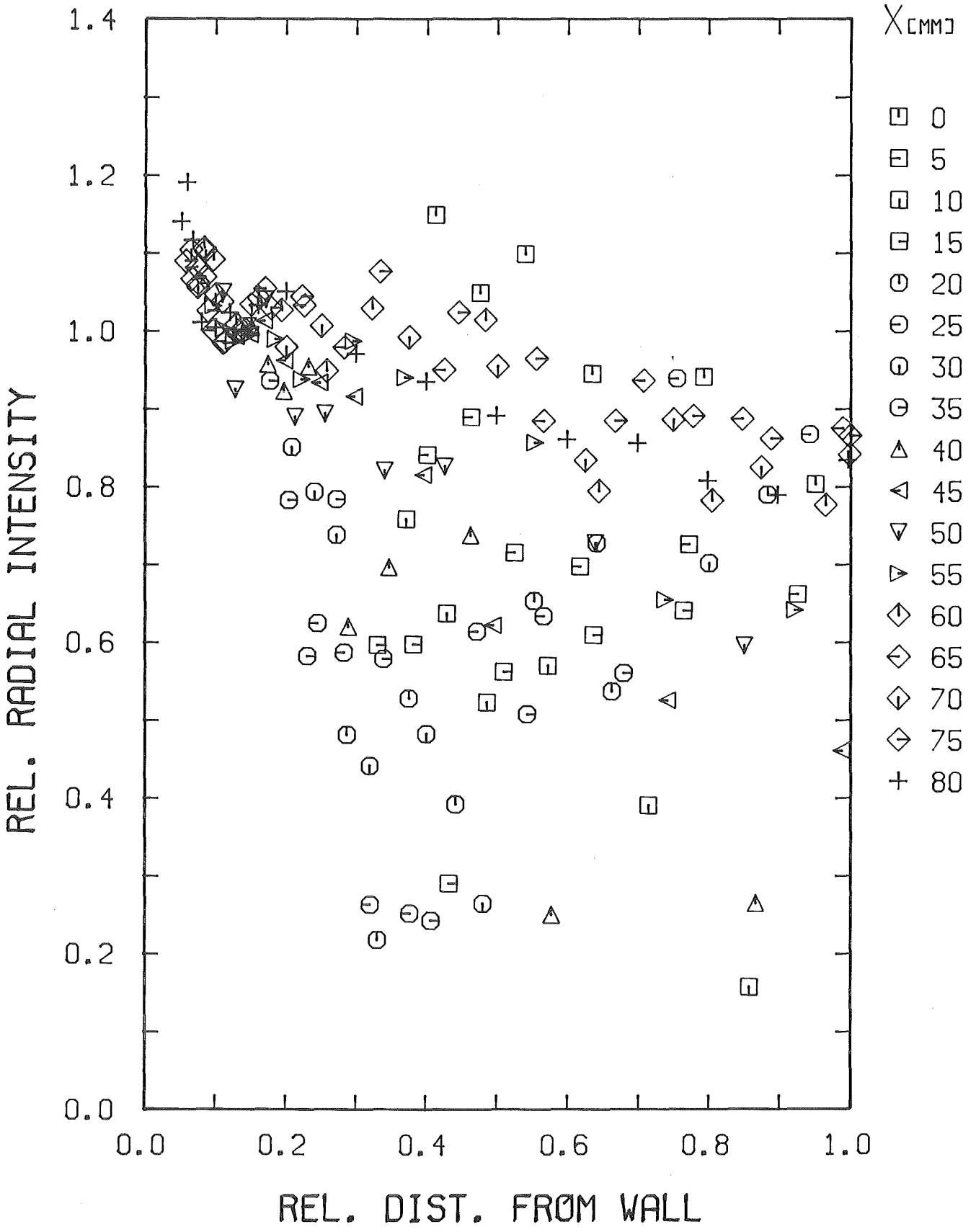

Fig. 16-4 Distribution of radial intensity in the x/y-part of quadrant 4

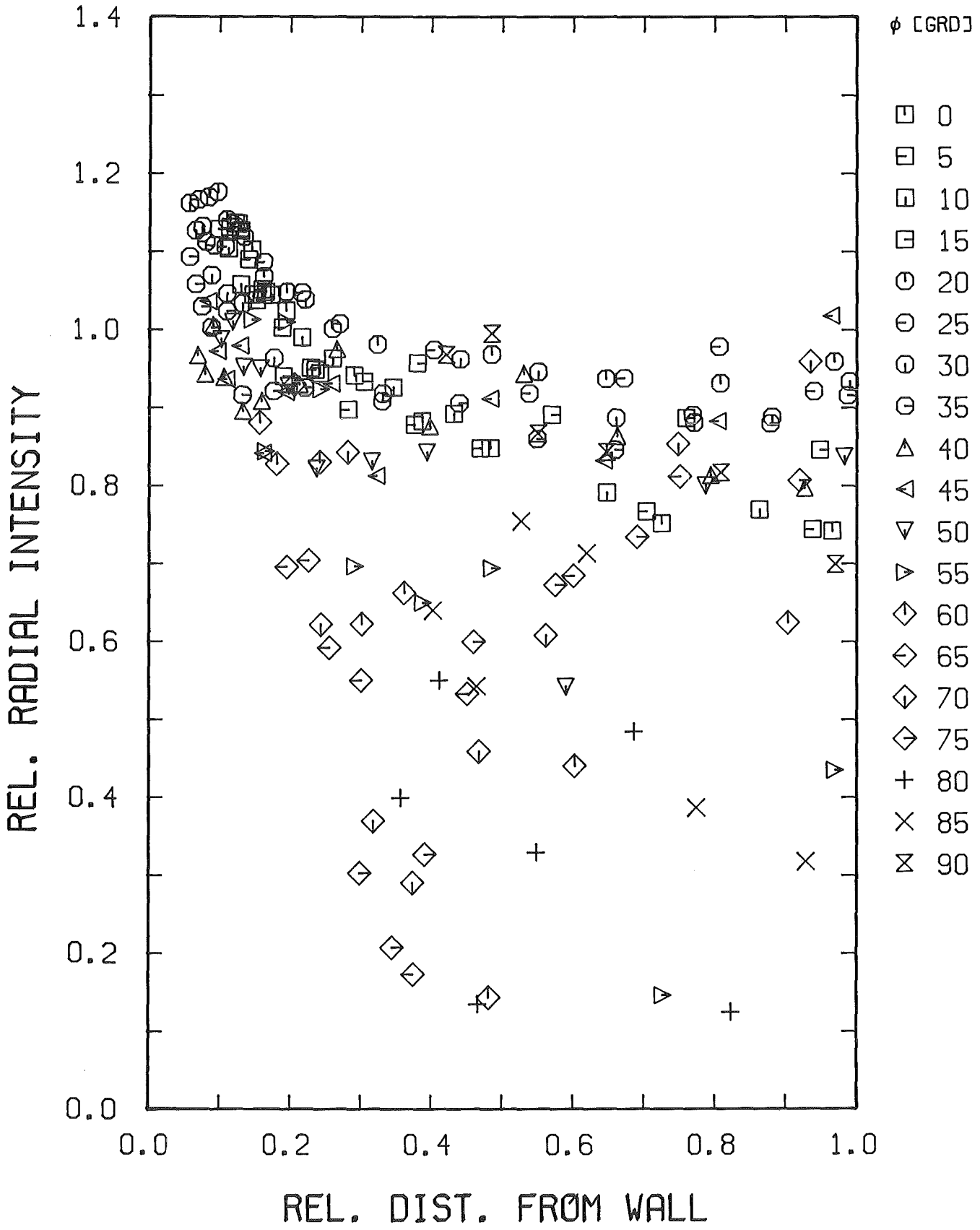

Fig. 17-1 Distribution of radial intensity in the r/ϕ-part of quadrant 1

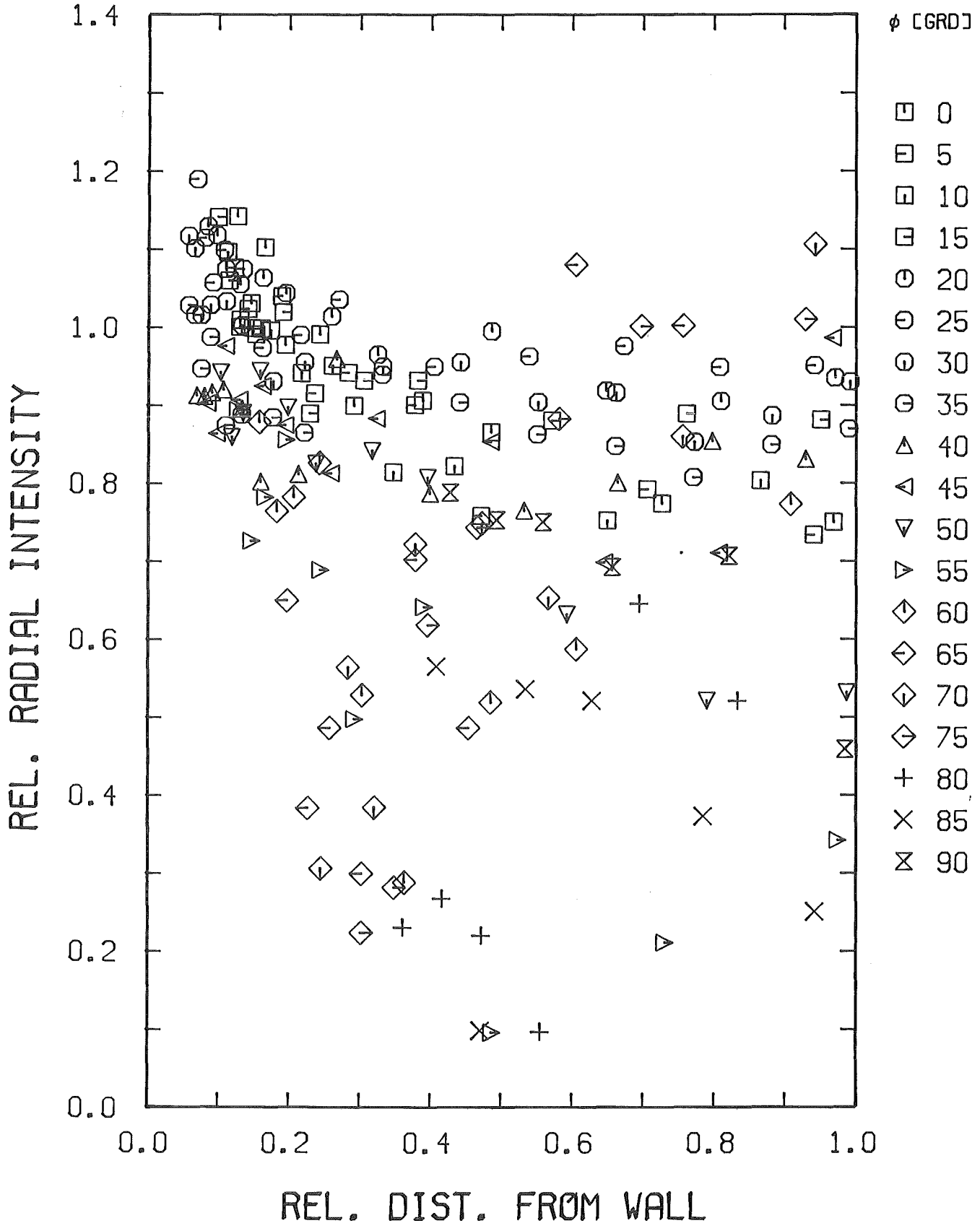

Fig. 17-2 Distribution of radial intensity in the r/ϕ-part of quadrant 2

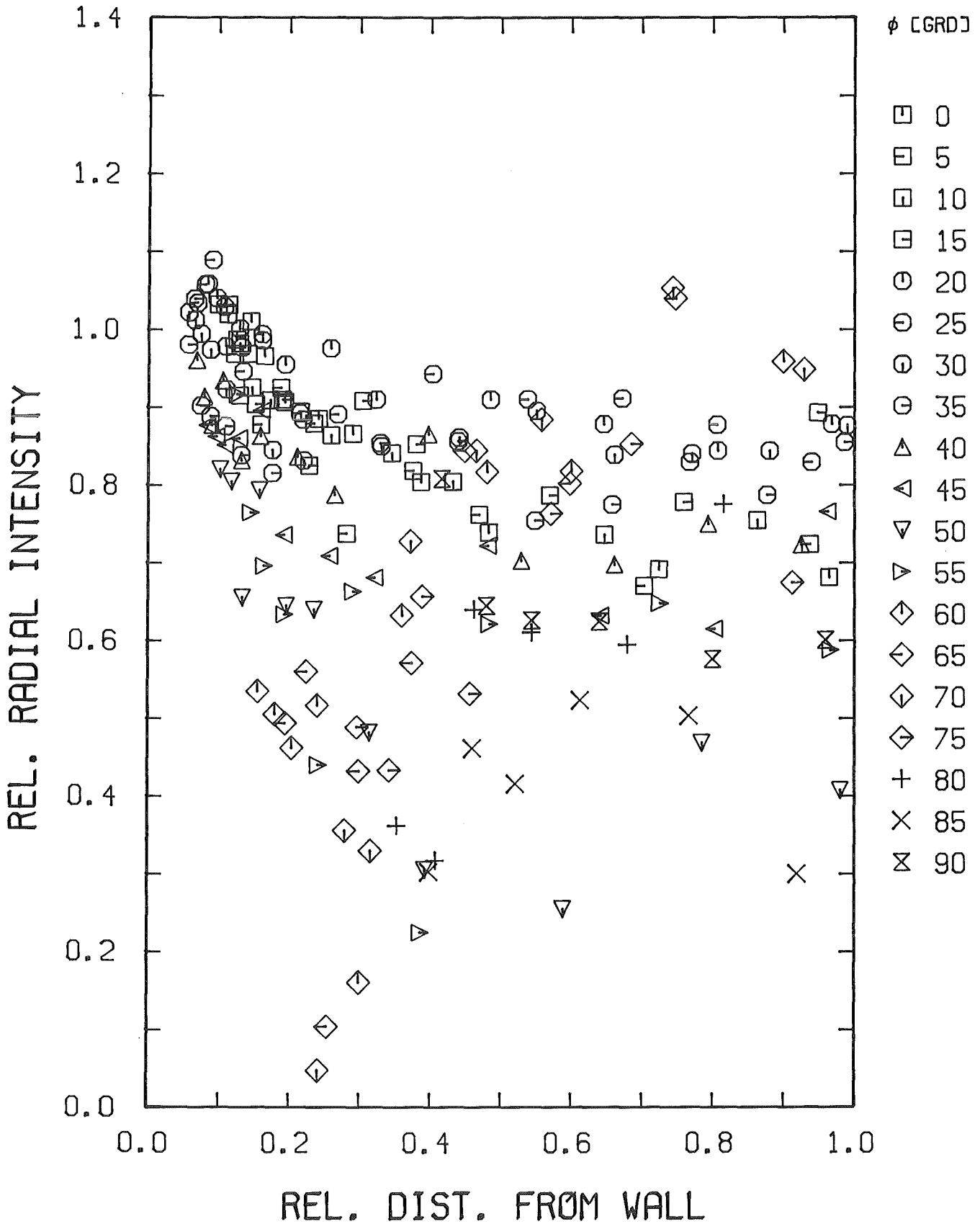

Fig. 17-3 Distribution of radial intensity in the r/ϕ-part of quadrant 3

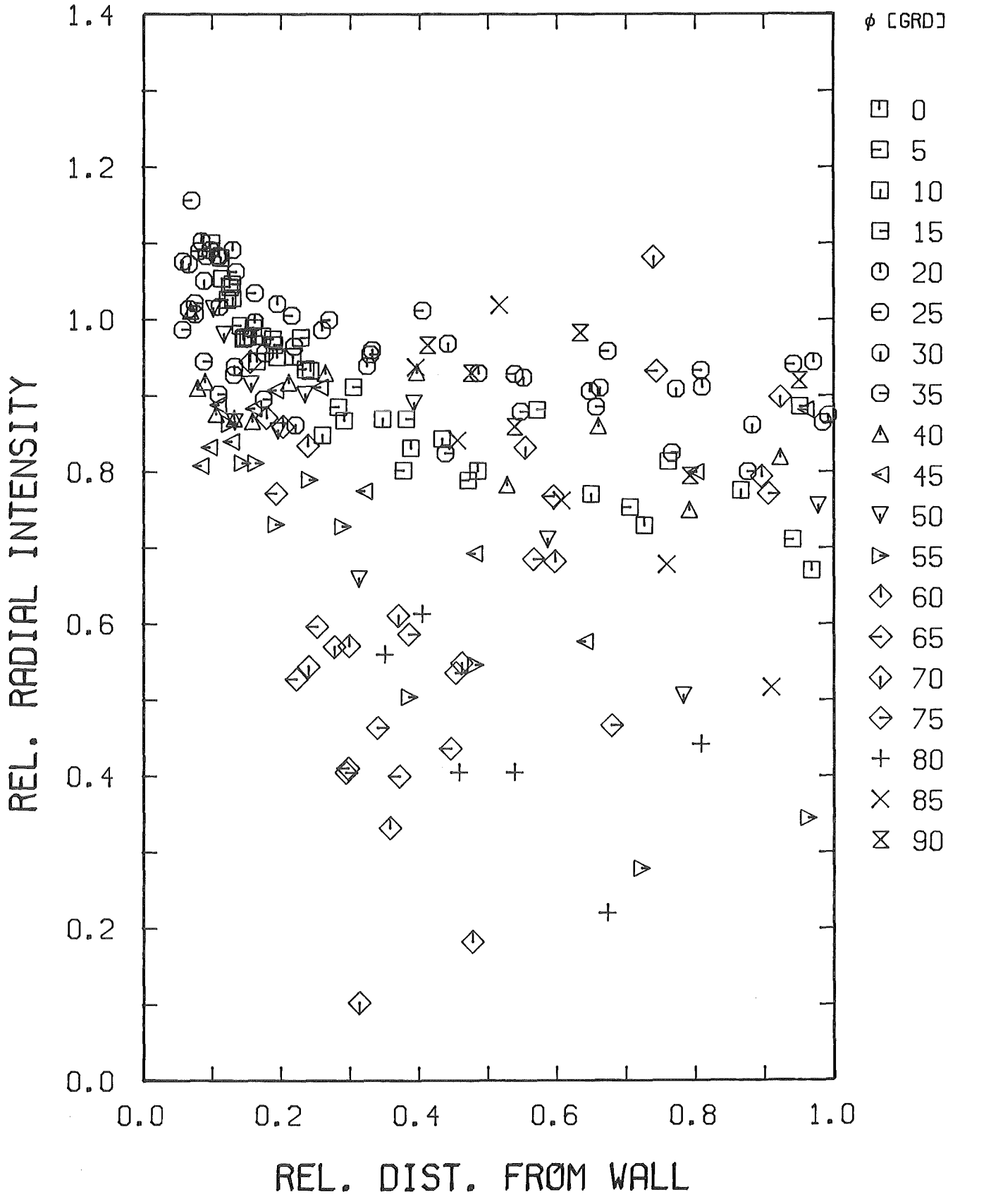

Fig. 17-4 Distribution of radial intensity in the r/ϕ-part of quadrant 4

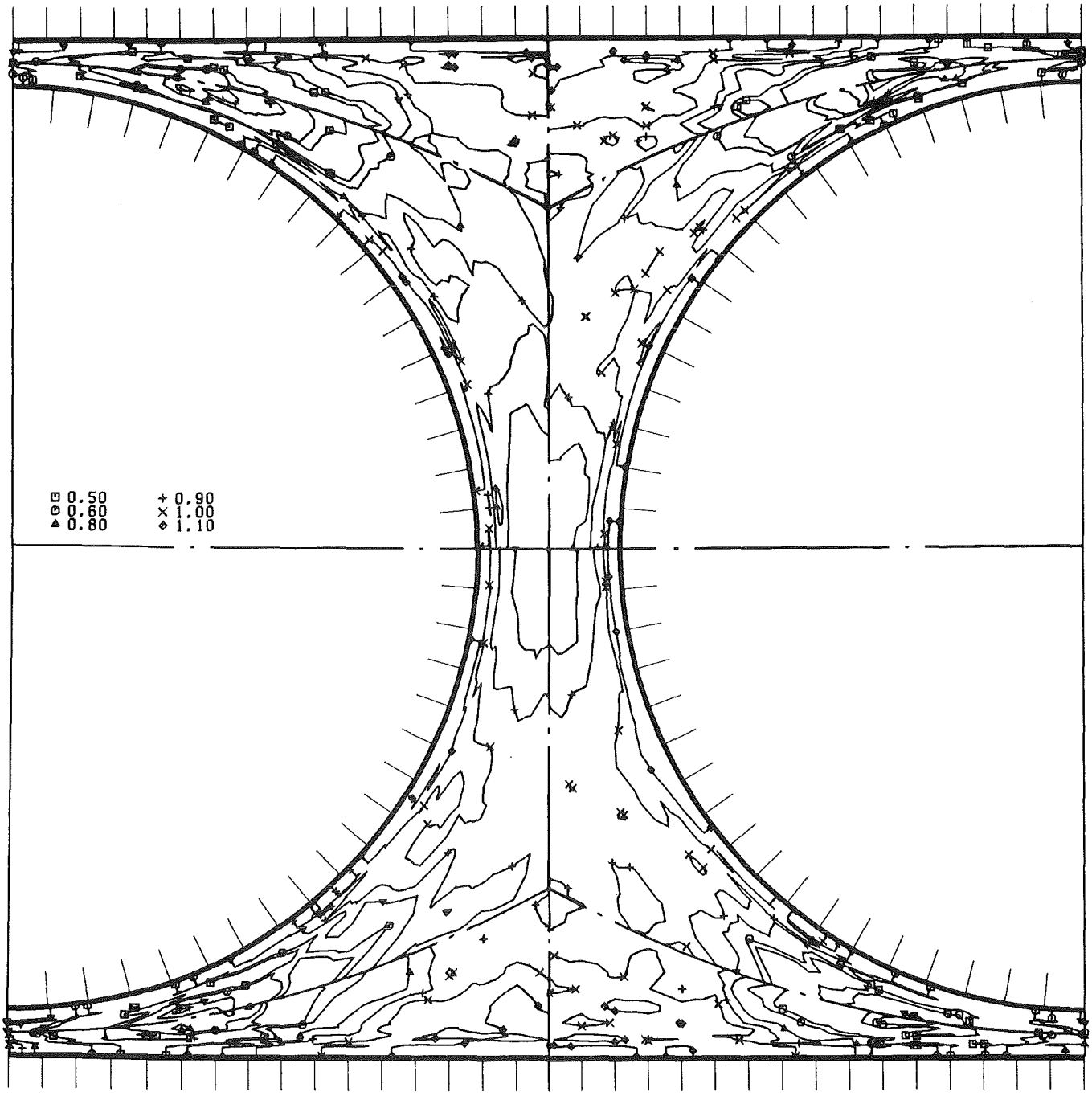

Fig. 18 Contours of radial intensity in the four quadrants

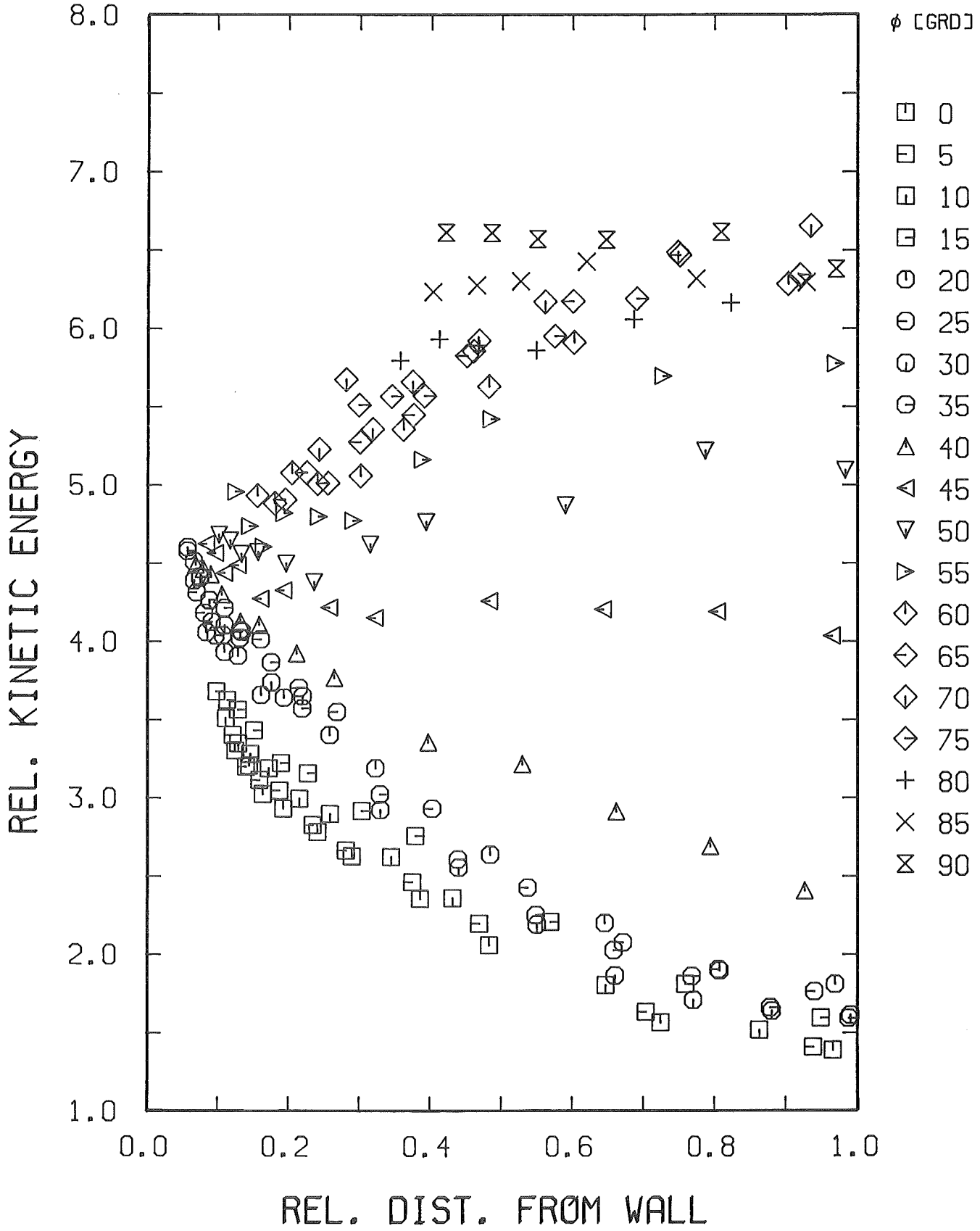

Fig. 19-1 Distribution of kinetic energy in the r/ϕ-part of quadrant 1

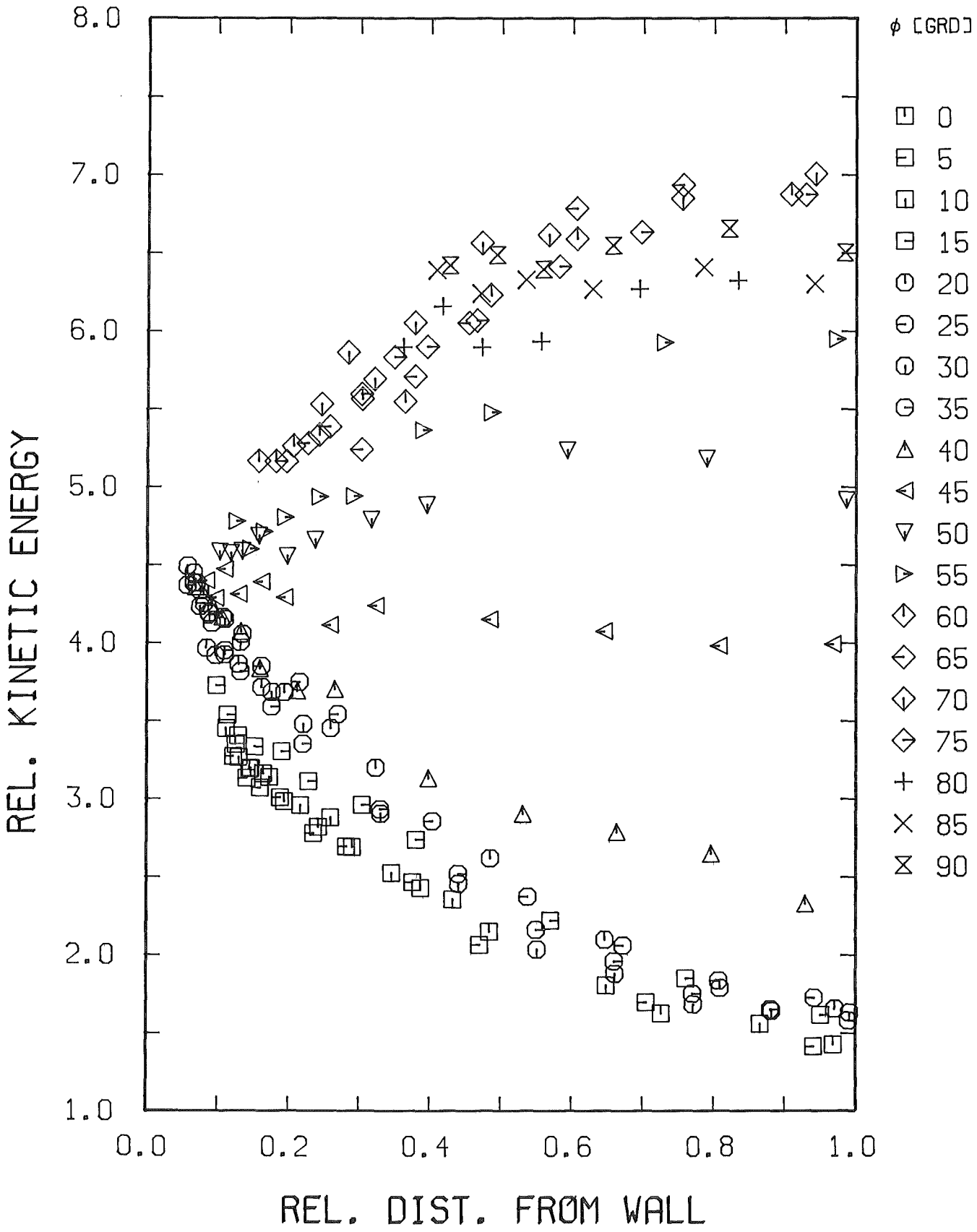

Fig. 19-2 Distribution of kinetic energy in the r/ϕ-part of quadrant 2

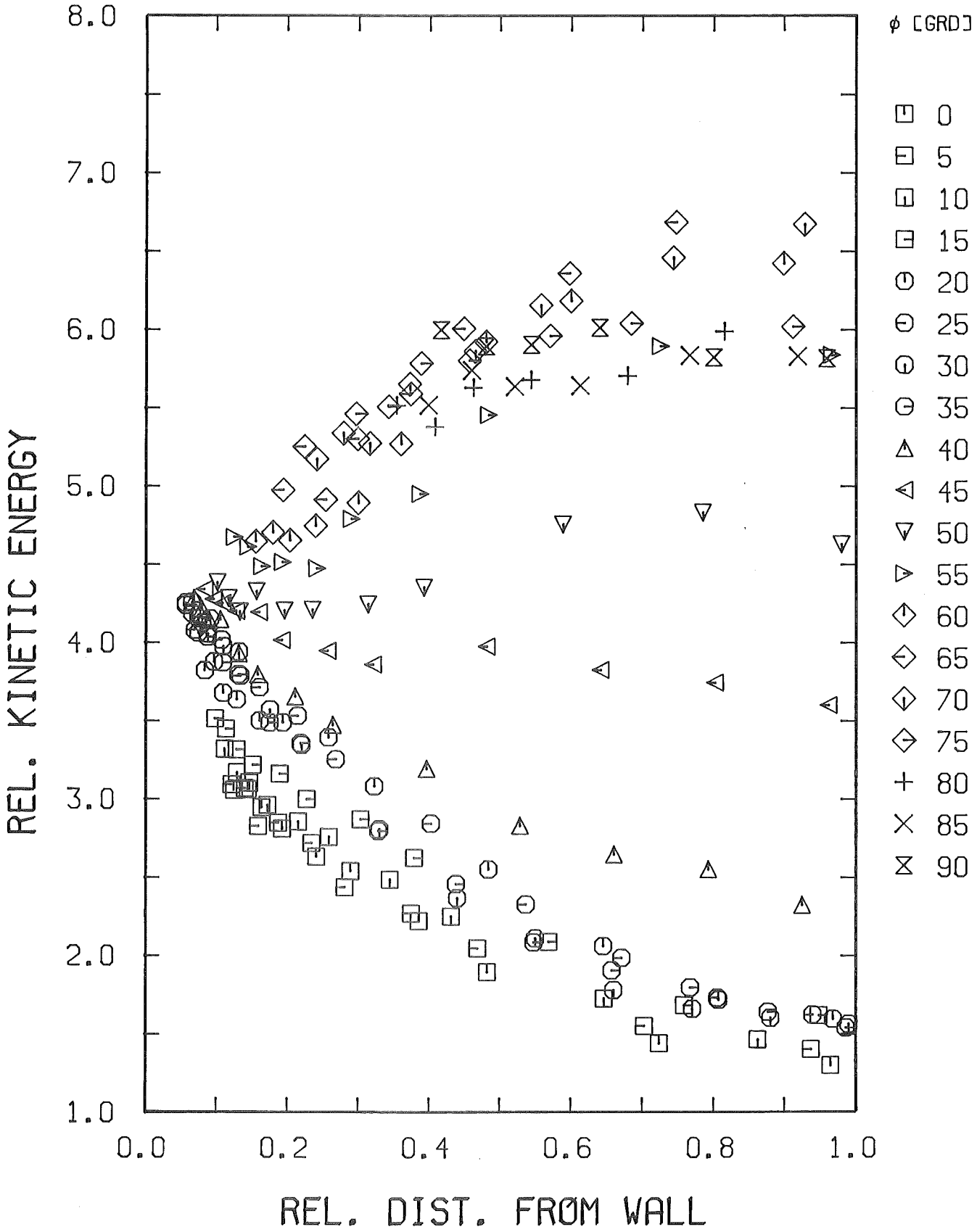

Fig. 19-3 Distribution of kinetic energy in the r/φ-part of quadrant 3

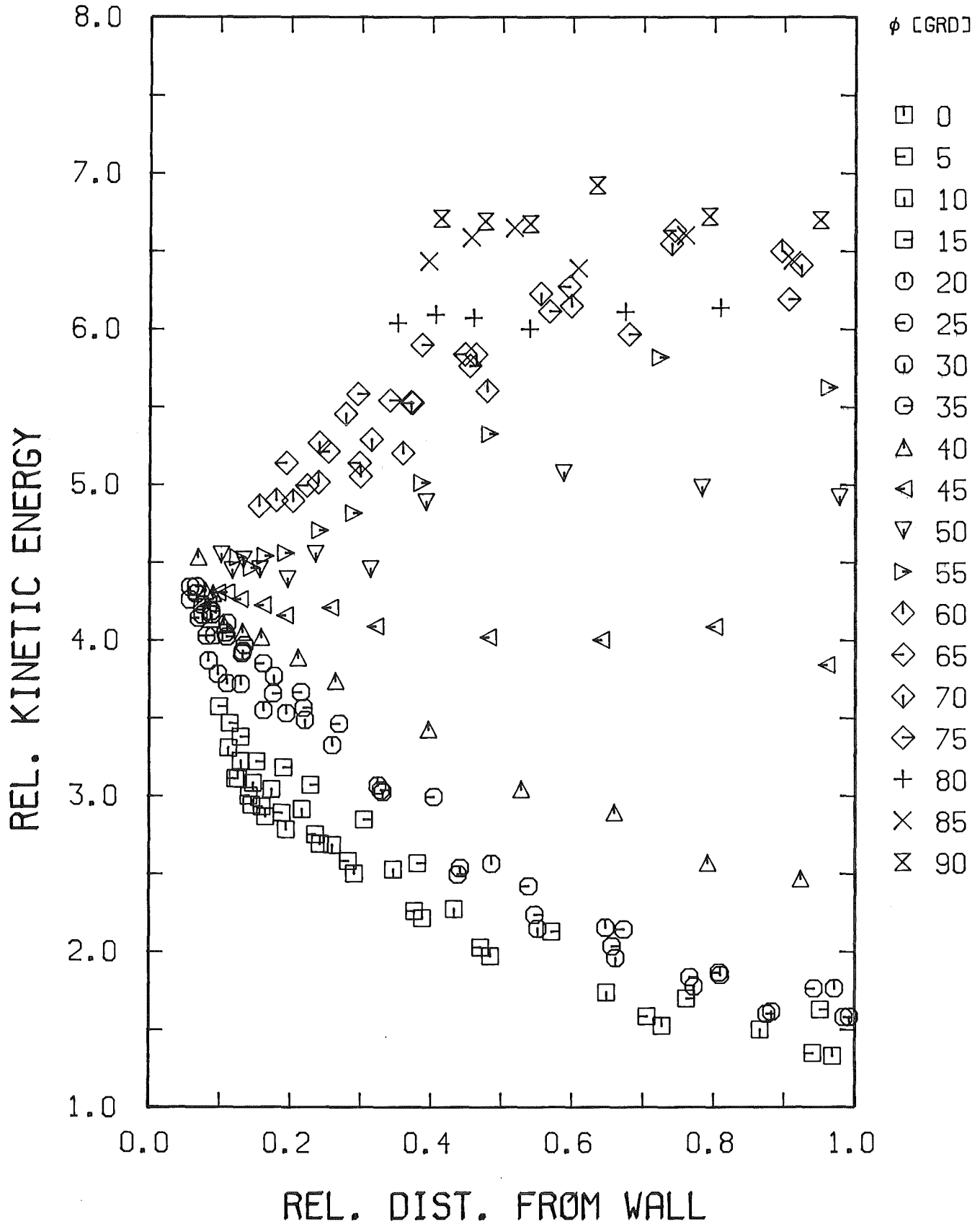

Fig. 19-4 Distribution of kinetic energy in the r/ϕ-part of quadrant 4

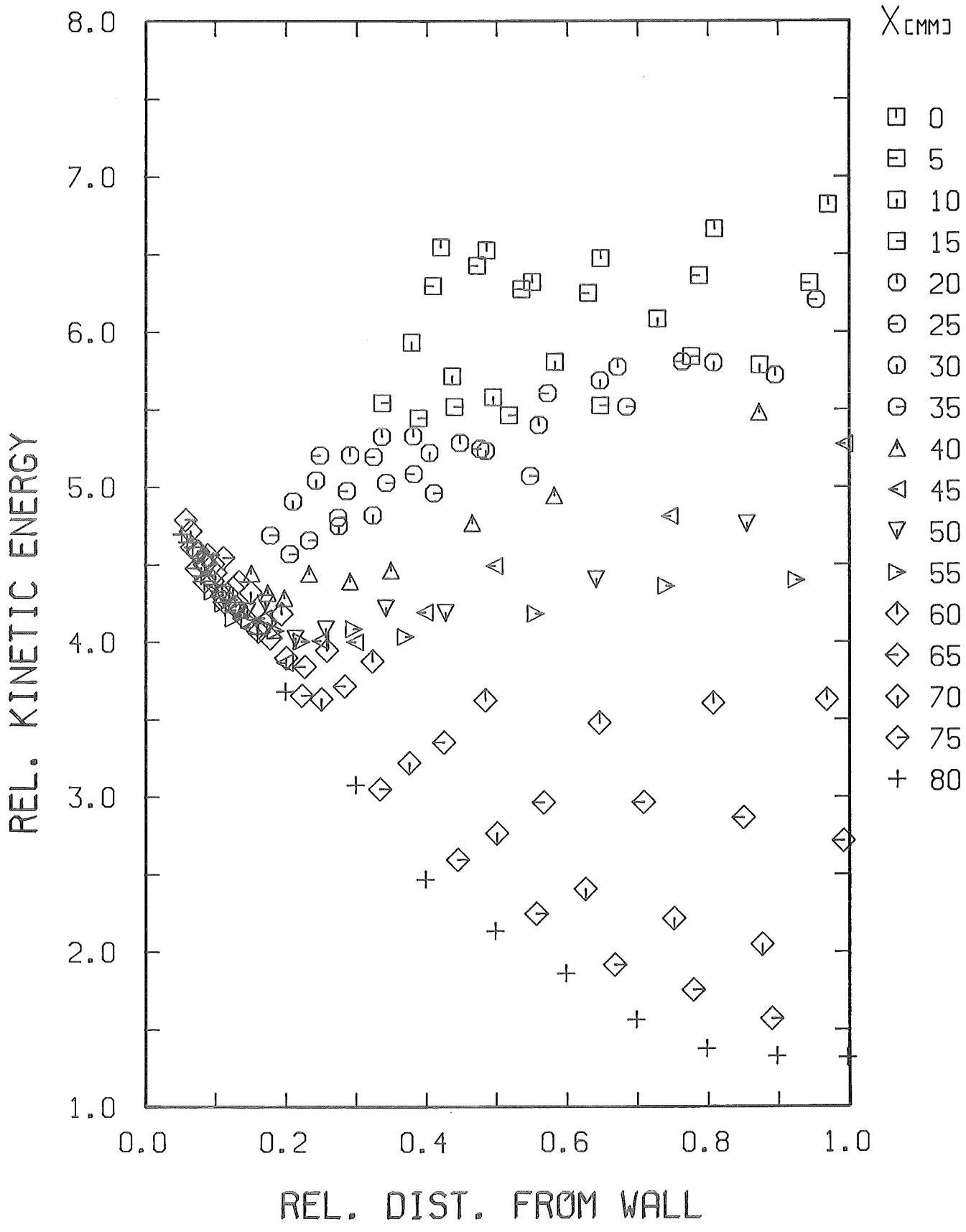

Fig. 20-1 Distribution of kinetic energy in the x/y-part of quadrant 1

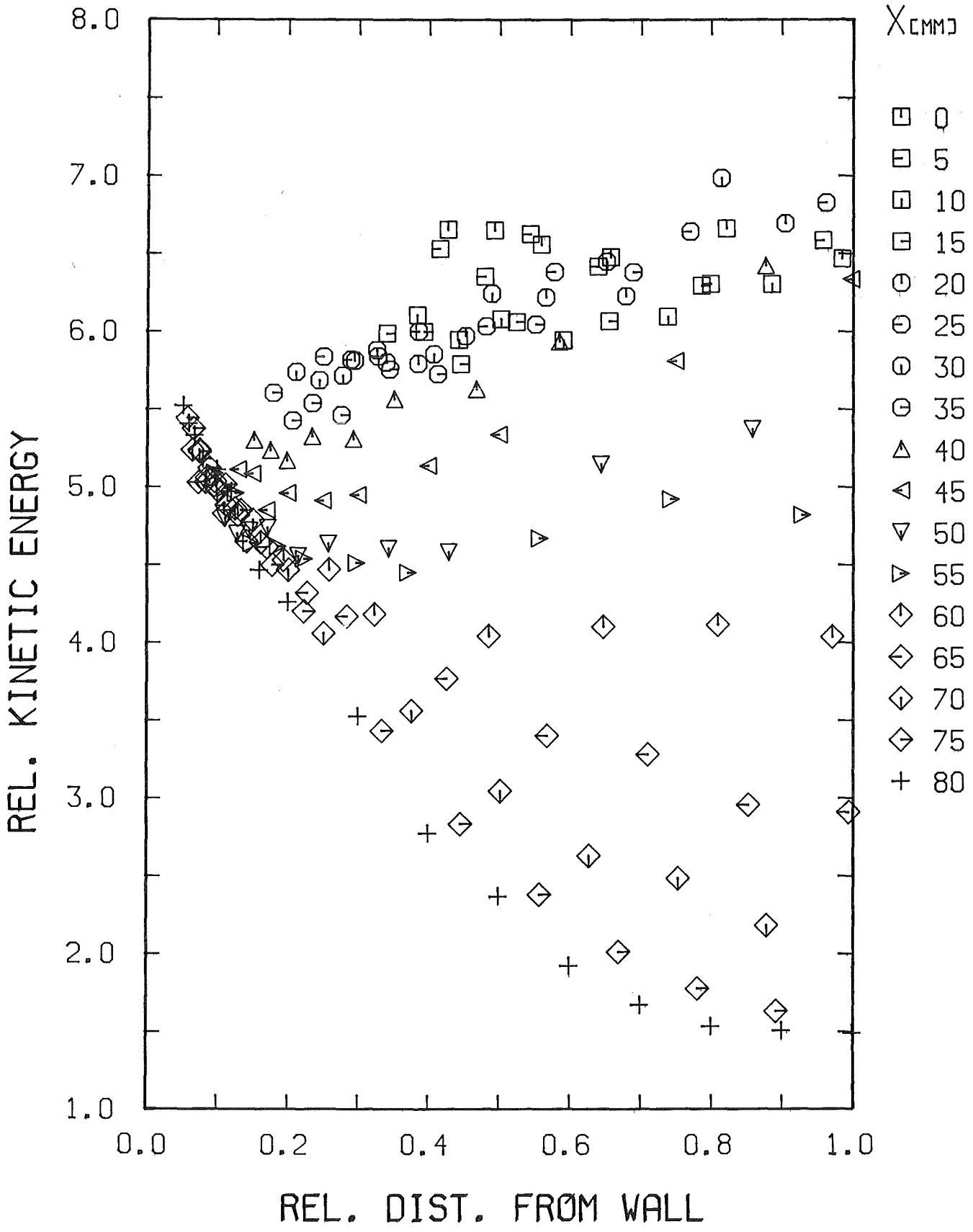

Fig. 20-2 Distribution of kinetic energy in the x/y-part of quadrant 2

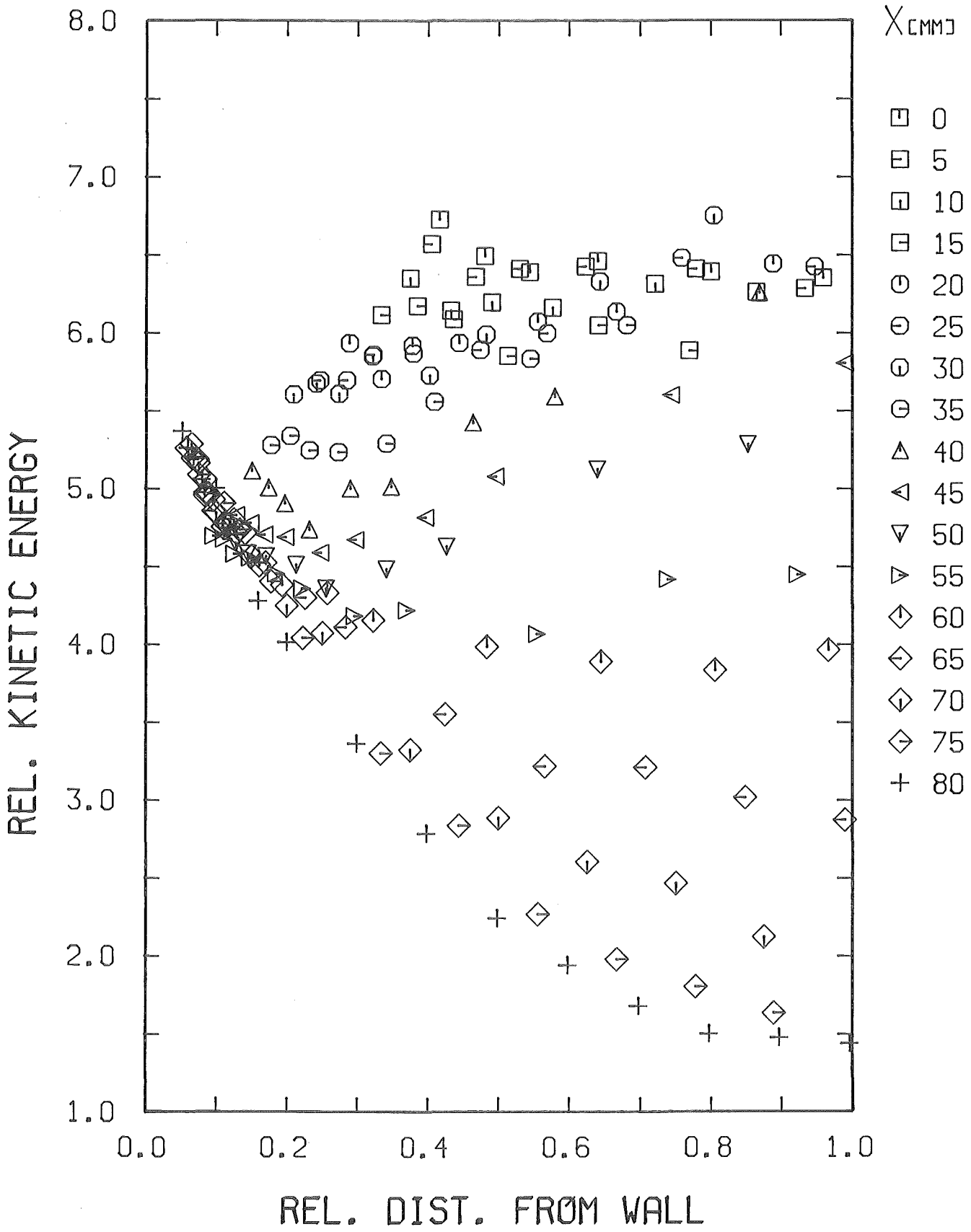

Fig. 20-3 Distribution of kinetic energy in the x/y-part of quadrant 3

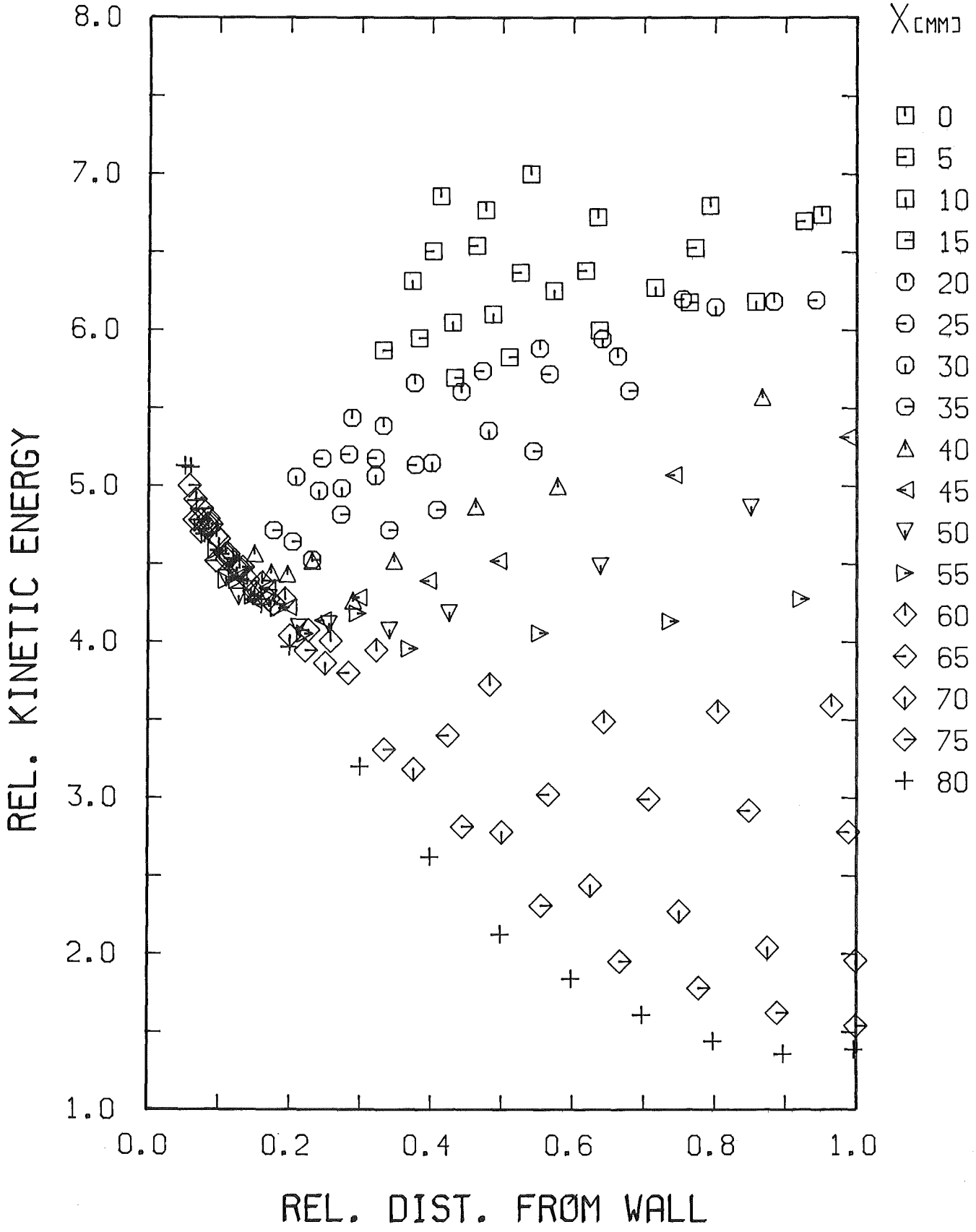

Fig. 20-4 Distribution of kinetic energy in the x/y-part of quadrant 4

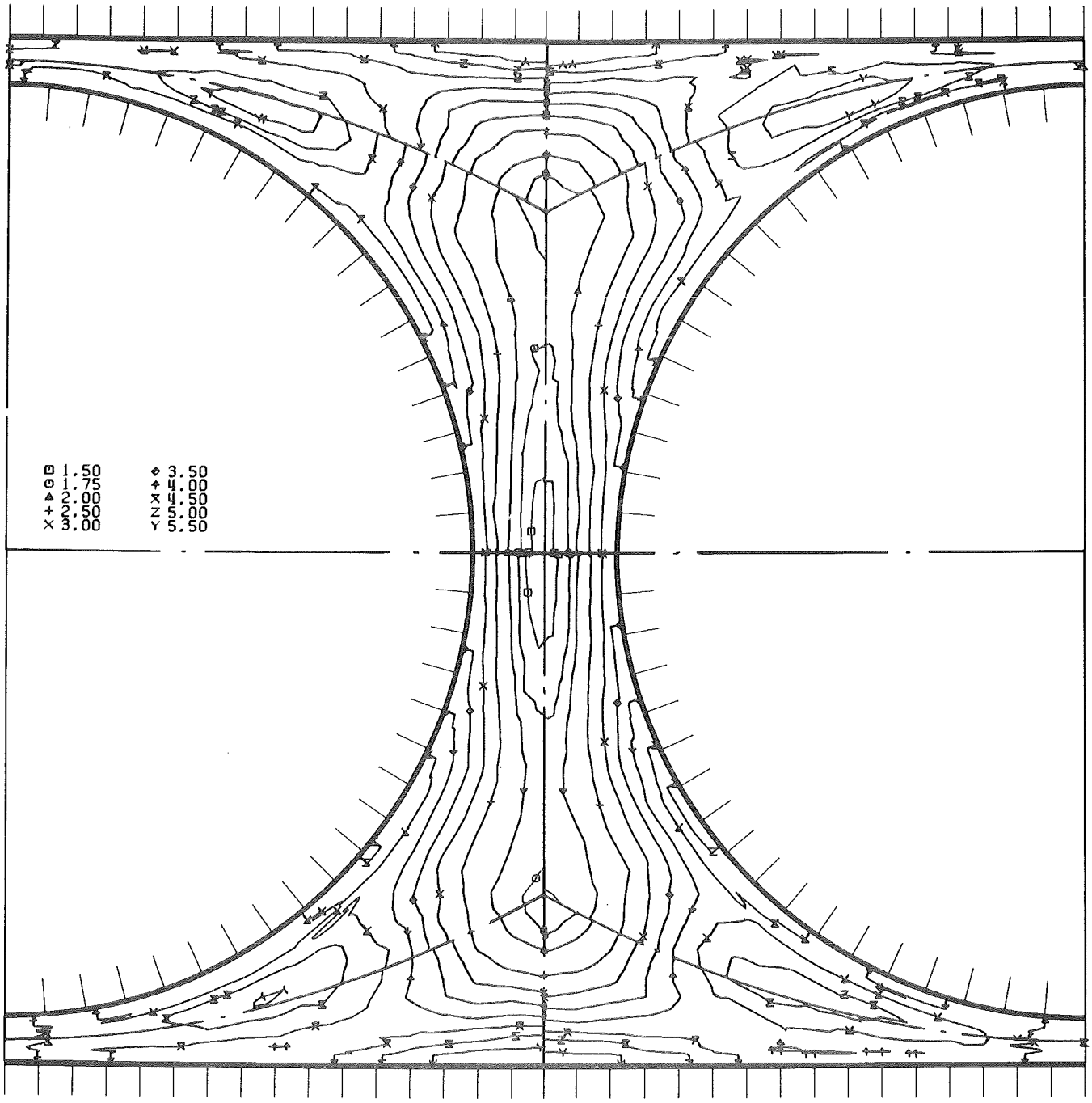

Fig. 21 Contours of kinetic energy in the four qudrants

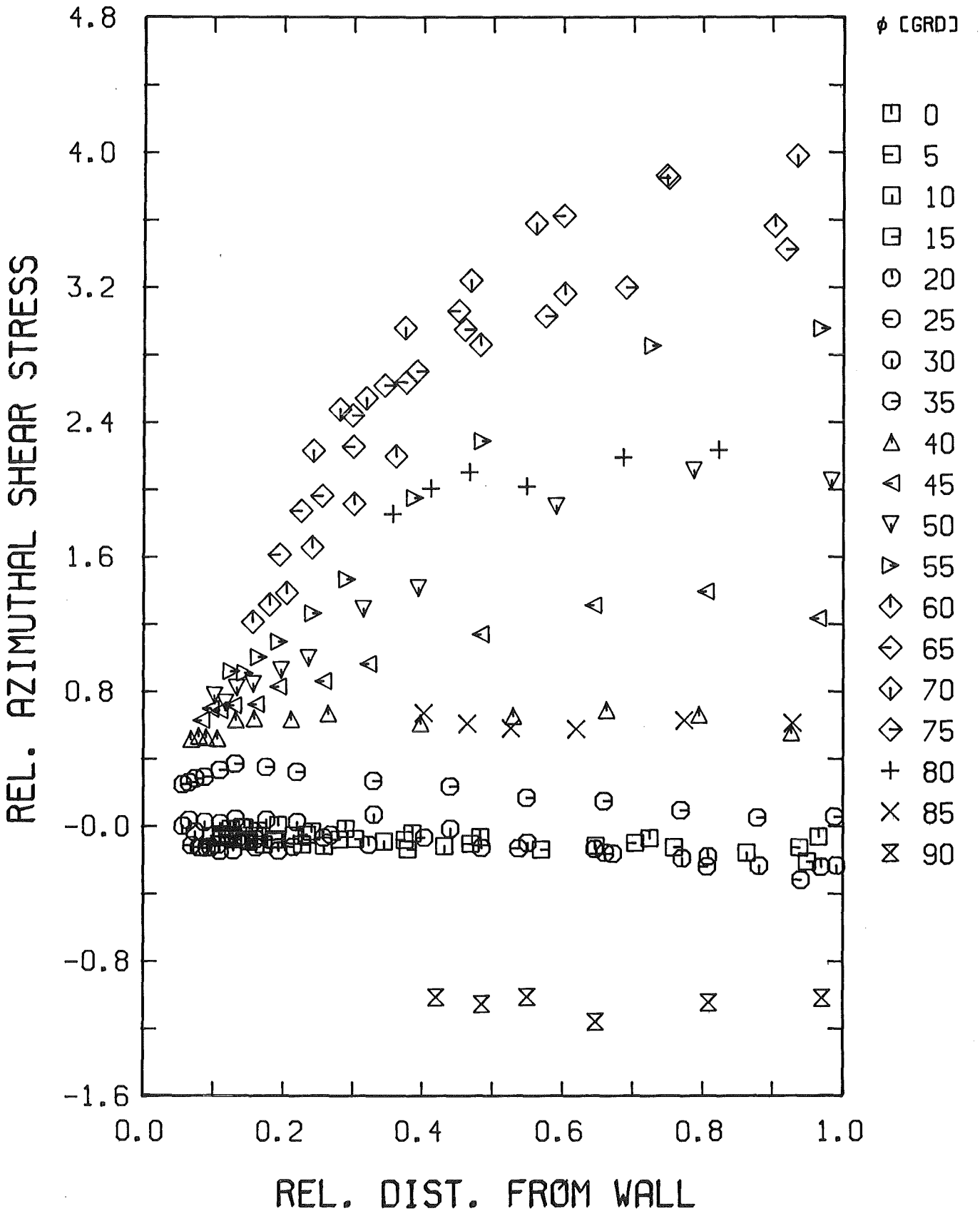

Fig. 22-1 Distribution of azimuthal shear stress in the r/φ-part of quadrant 1

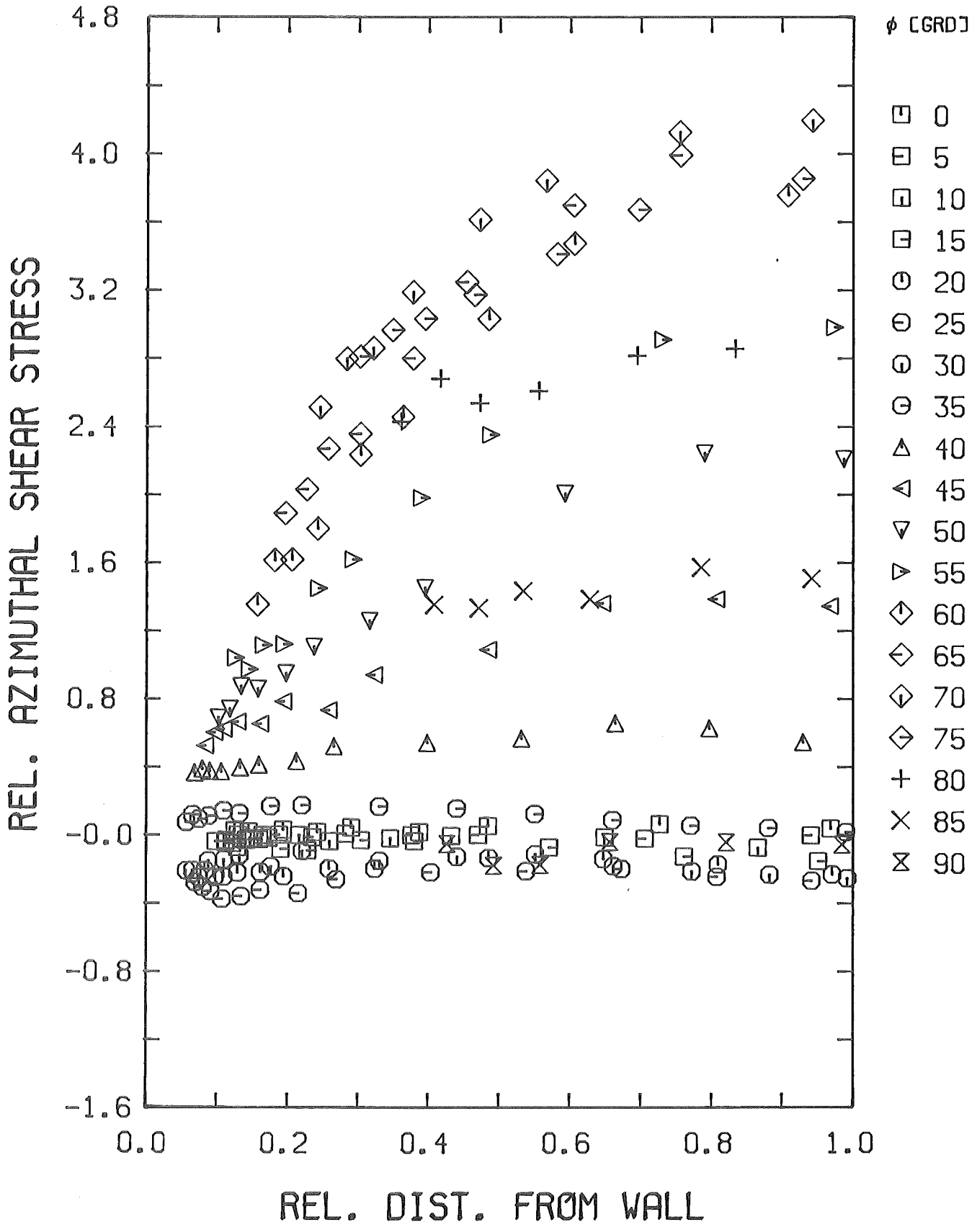

Fig. 22-2 Distribution of azimuthal shear stress in the r/ϕ-part of quadrant 2

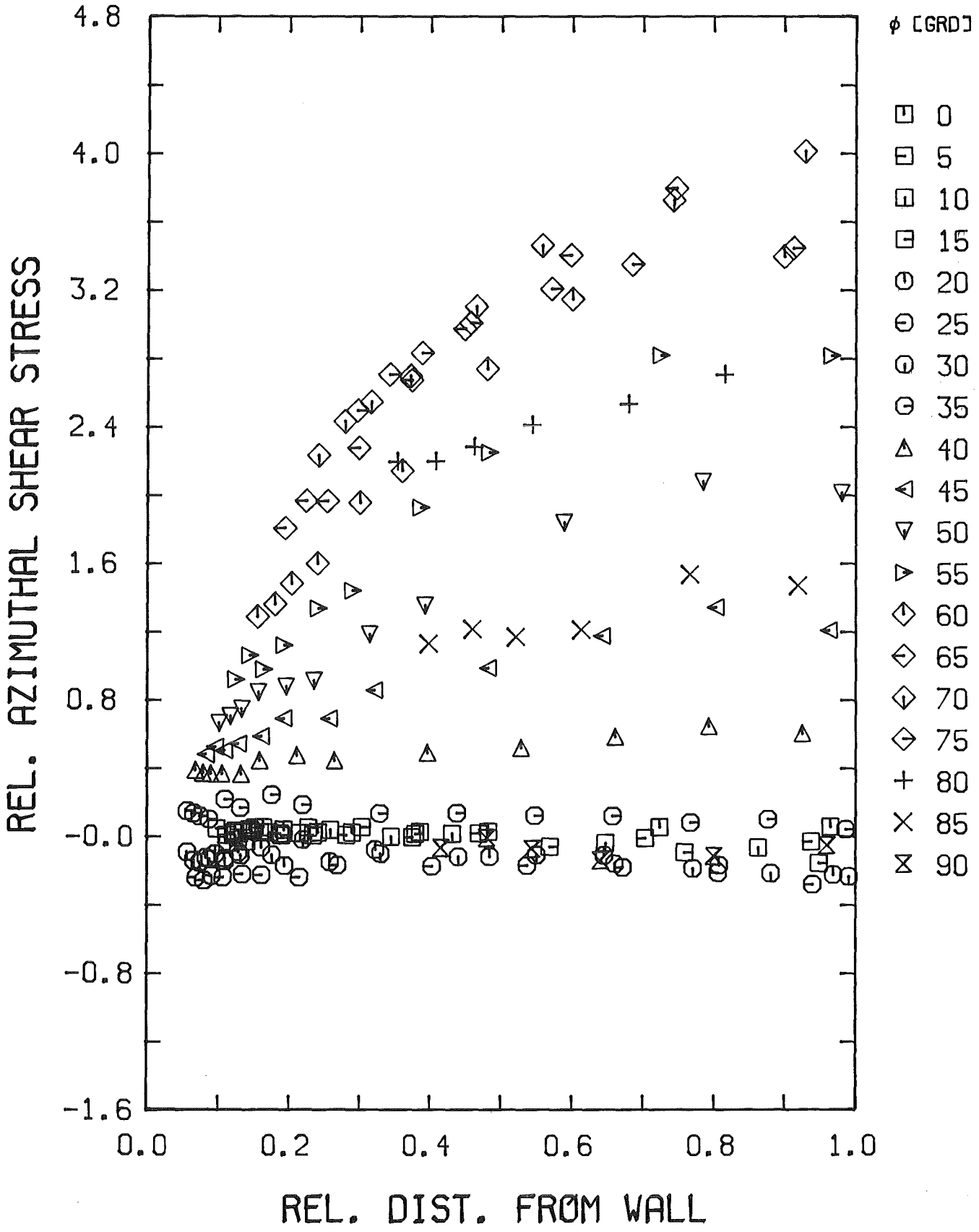

Fig. 22-3 Distribution of azimuthal shear stress in the r/ϕ-part of quadrant 3

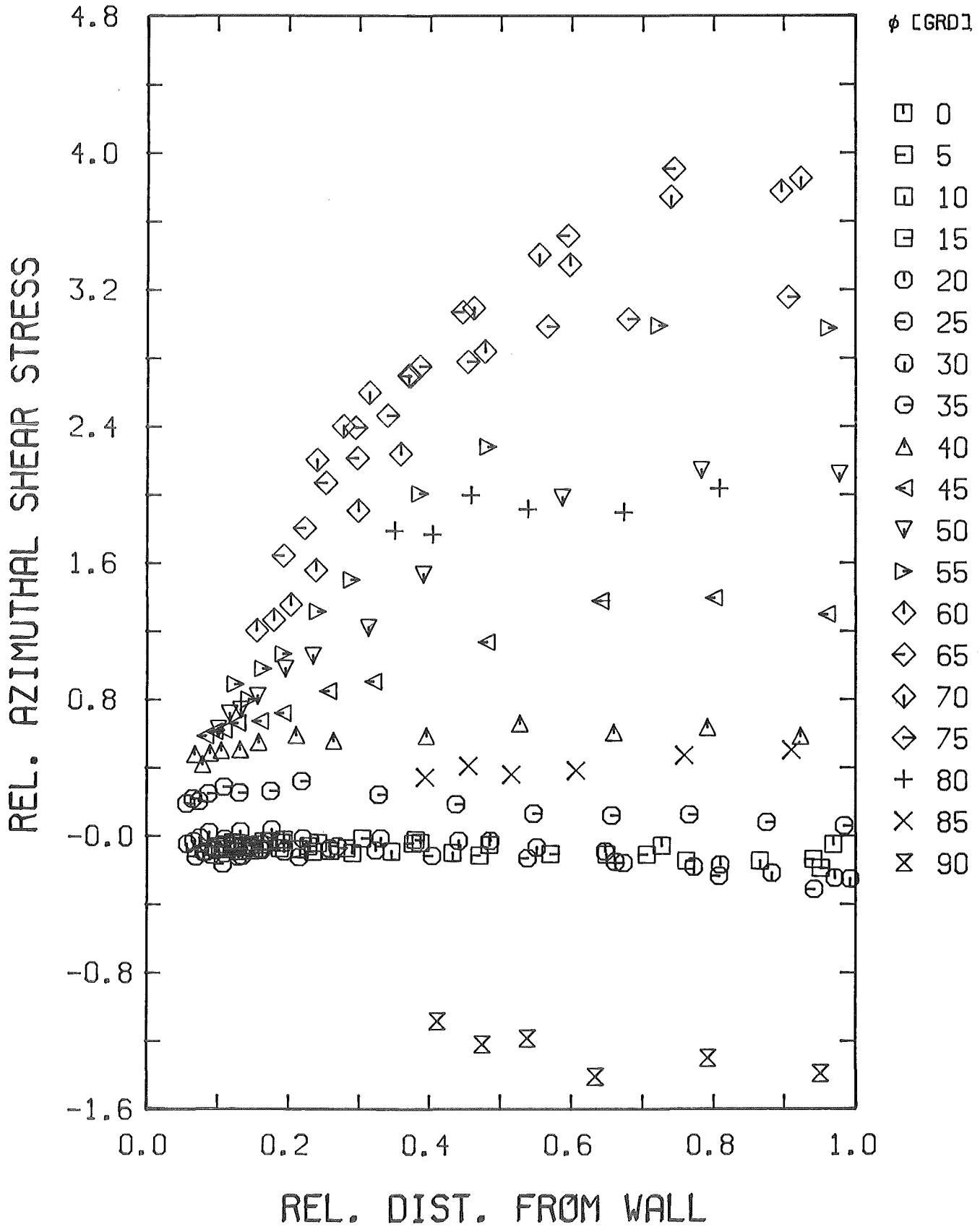

Fig. 22-4 Distribution of azimuthal shear stress in the r/φ-part of quadrant 4

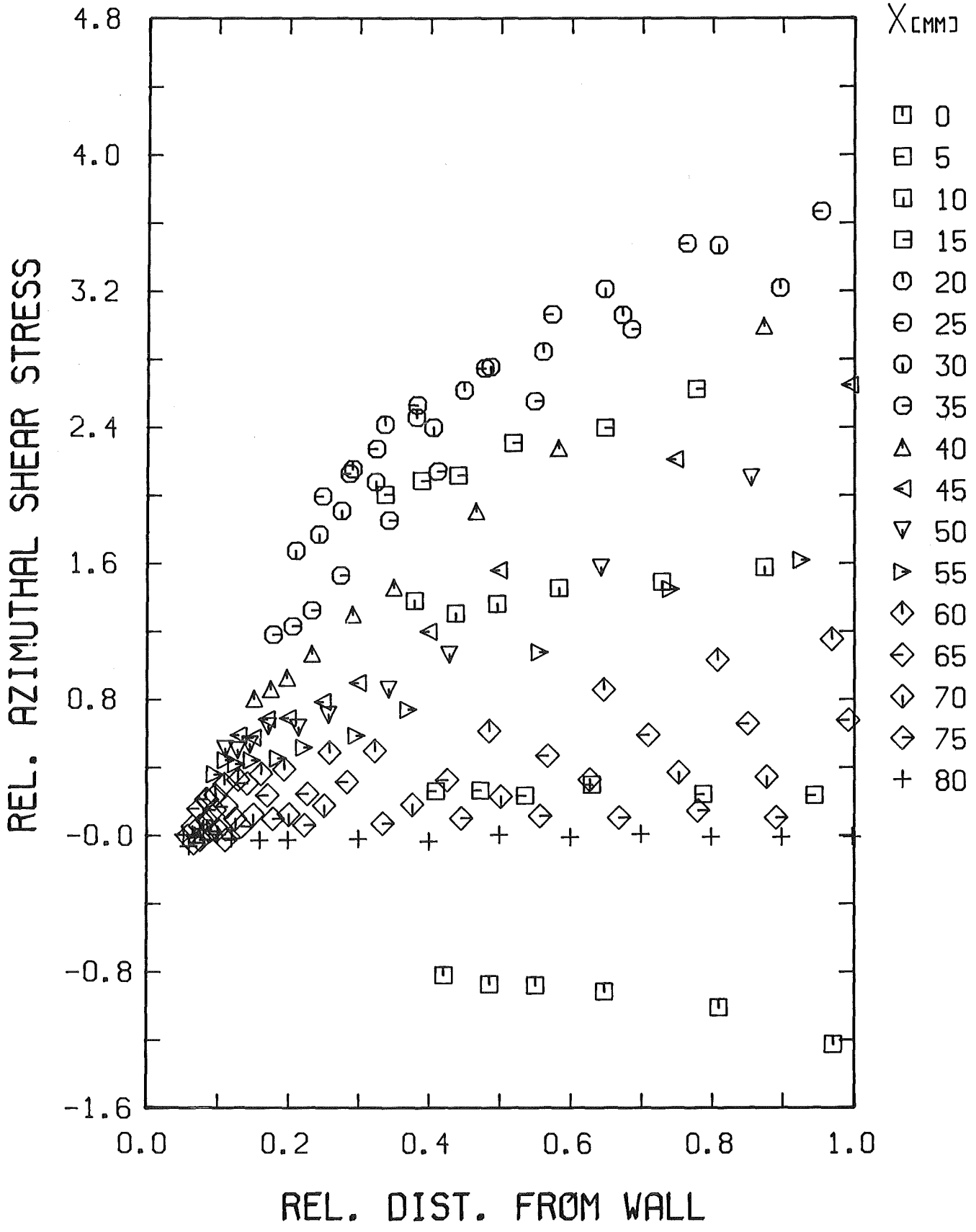

Fig. 23-1 Distribution of azimuthal shear stress in the x/y-part of quadrant 1

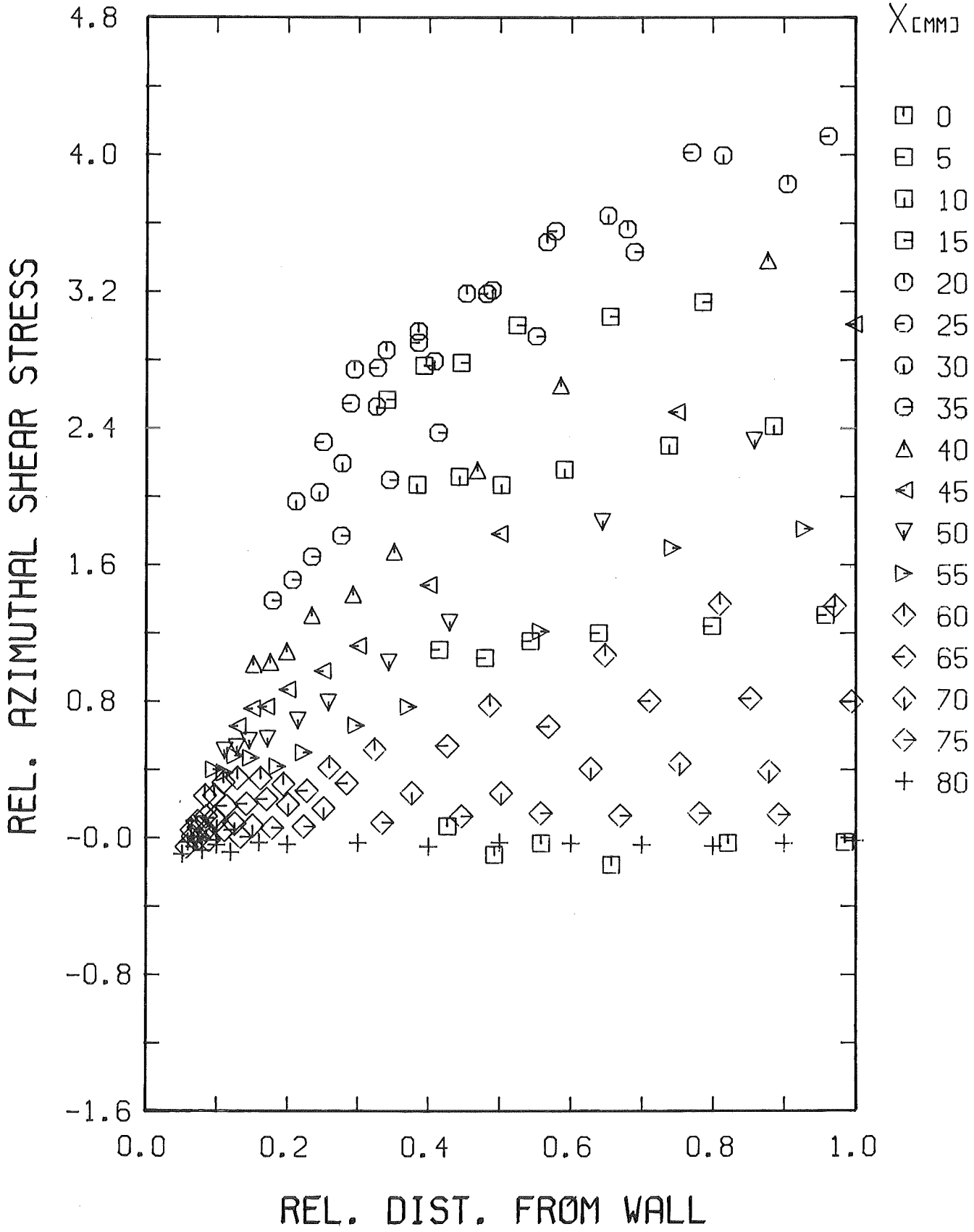

Fig. 23-2 Distribution of azimuthal shear stress
in the x/y-part of quadrant 2

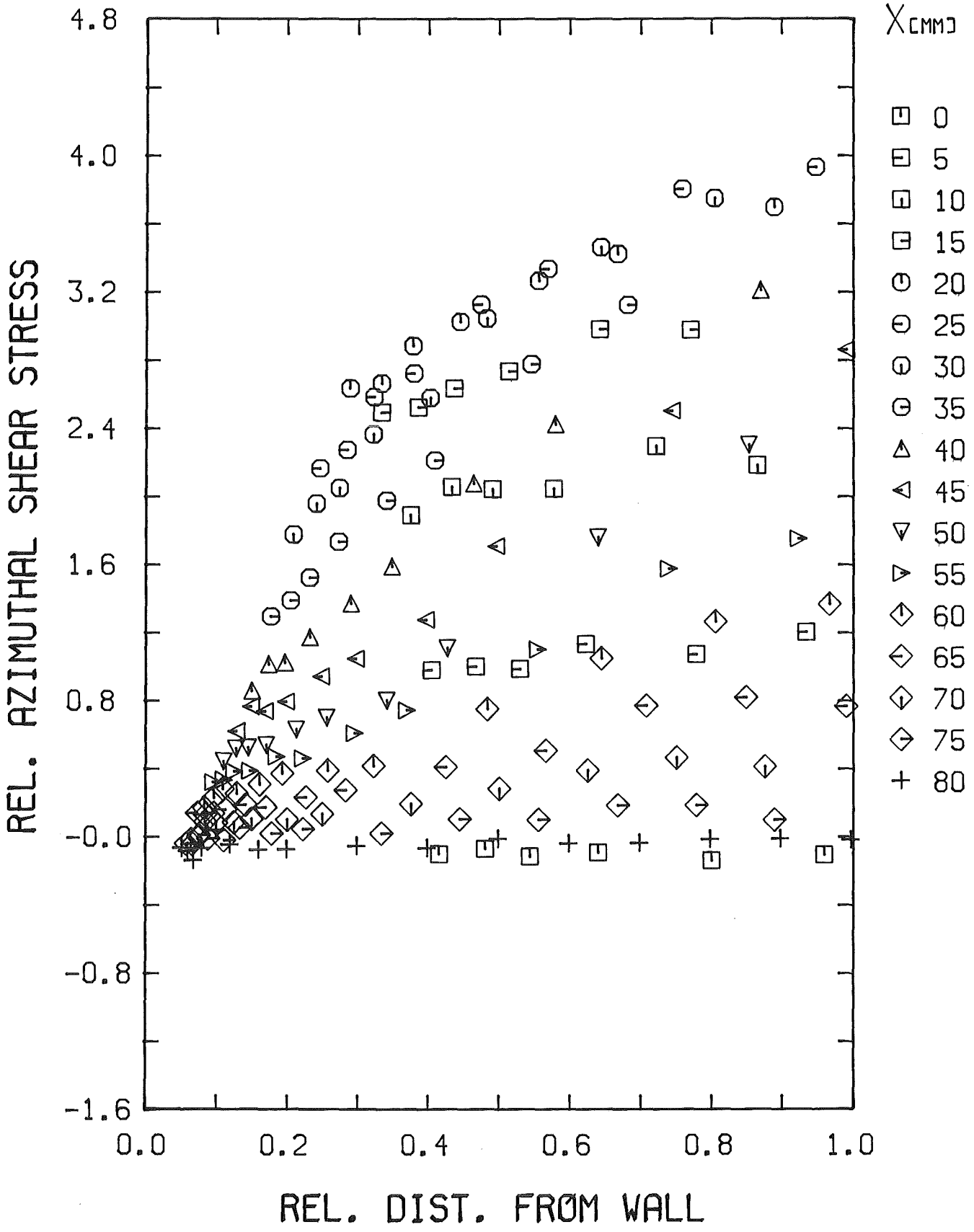

Fig. 23-3 Distribution of azimuthal shear stress in the x/y-part of quadrant 3

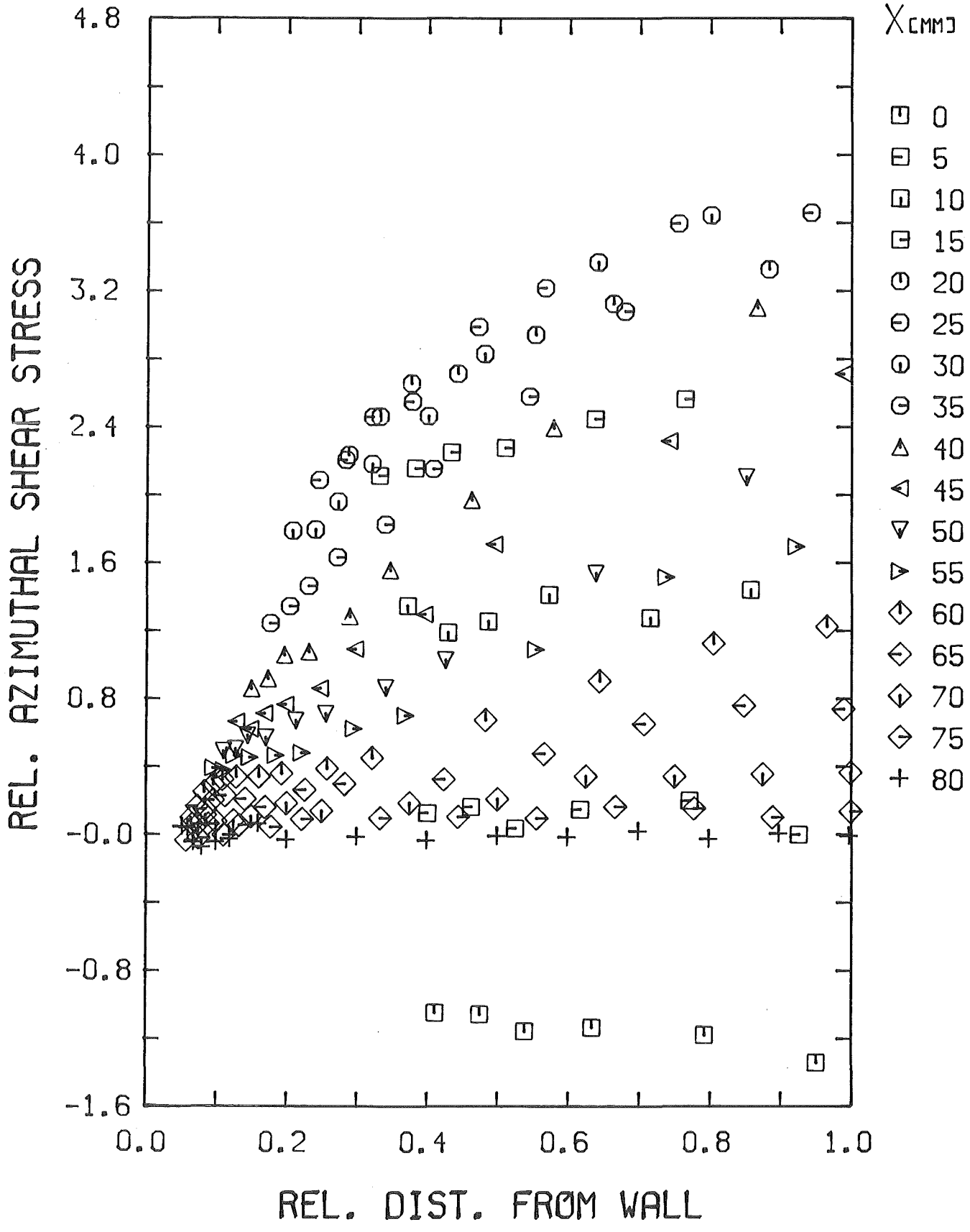

Fig. 23-4 Distribution of azimuthal shear stress
in the x/y-part of quadrant 4

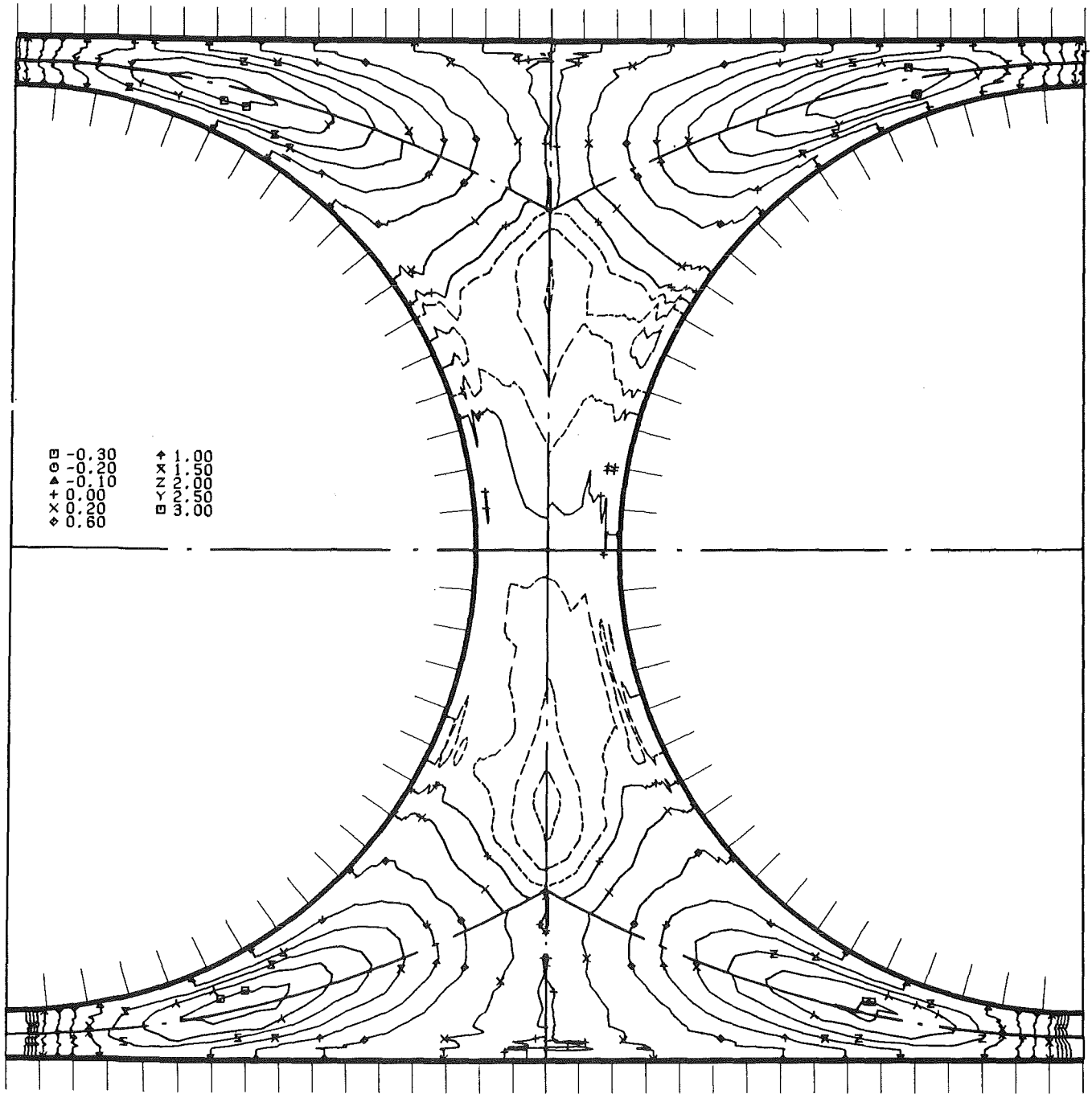

Fig. 24 Contours of azimuthal shear stress in the four qudrants

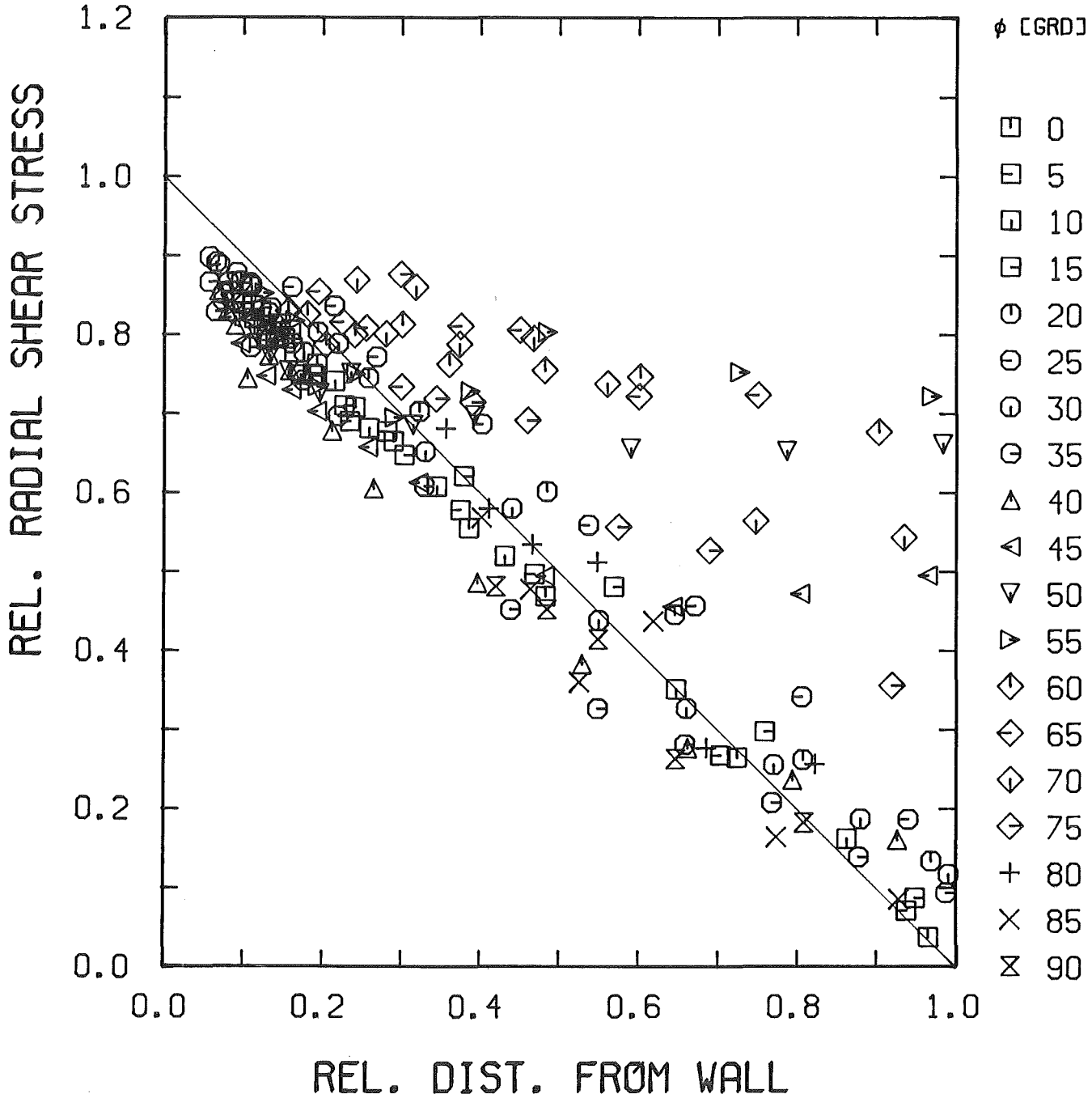

Fig. 25-1 Distribution of radial shear stress in the r/φ-part of quadrant 1

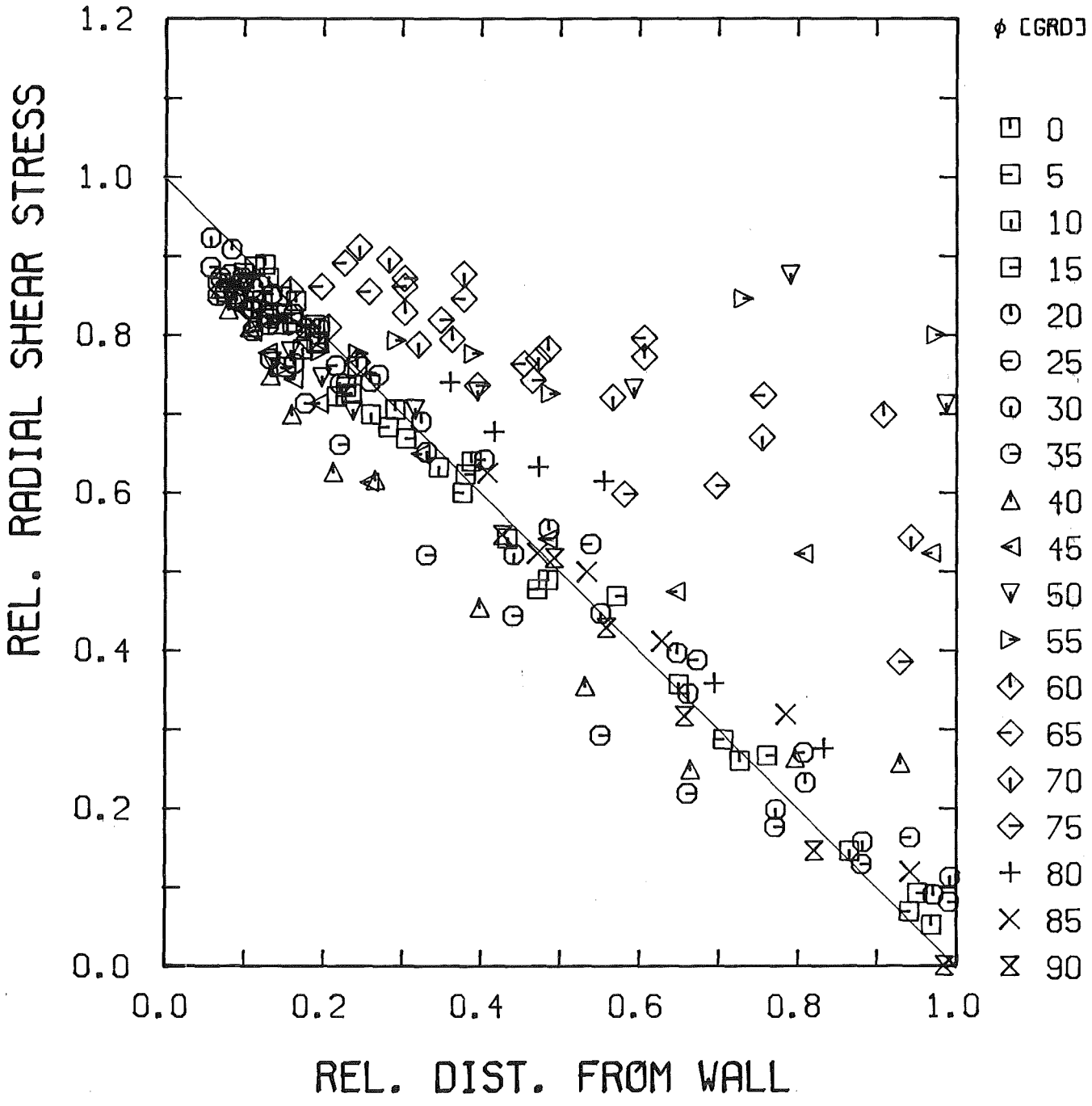

Fig. 25-2 Distribution of radial shear stress in the r/φ-part of quadrant 2

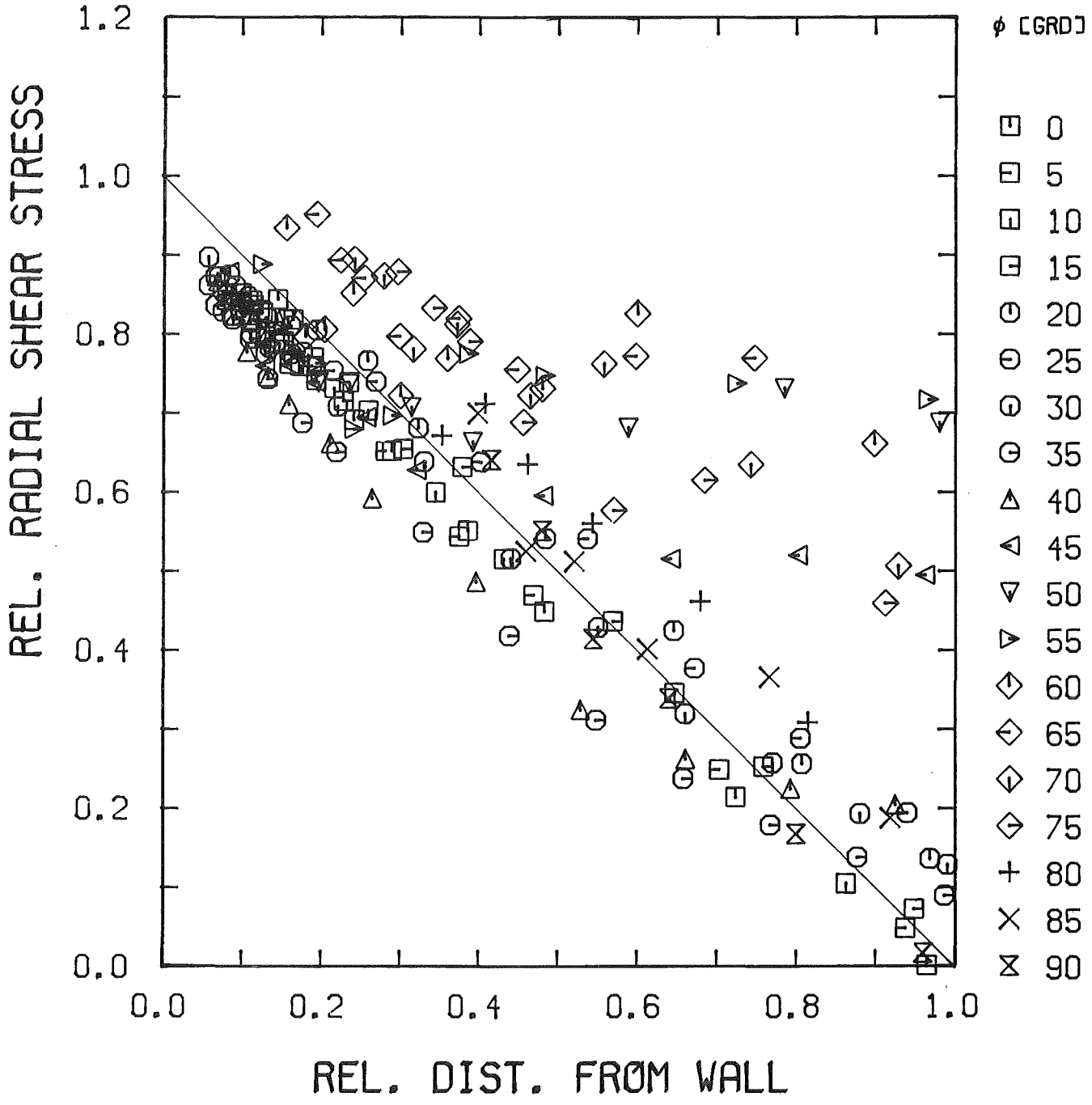

Fig. 25-3 Distribution of radial shear stress
in the r/ϕ-part of quadrant 3

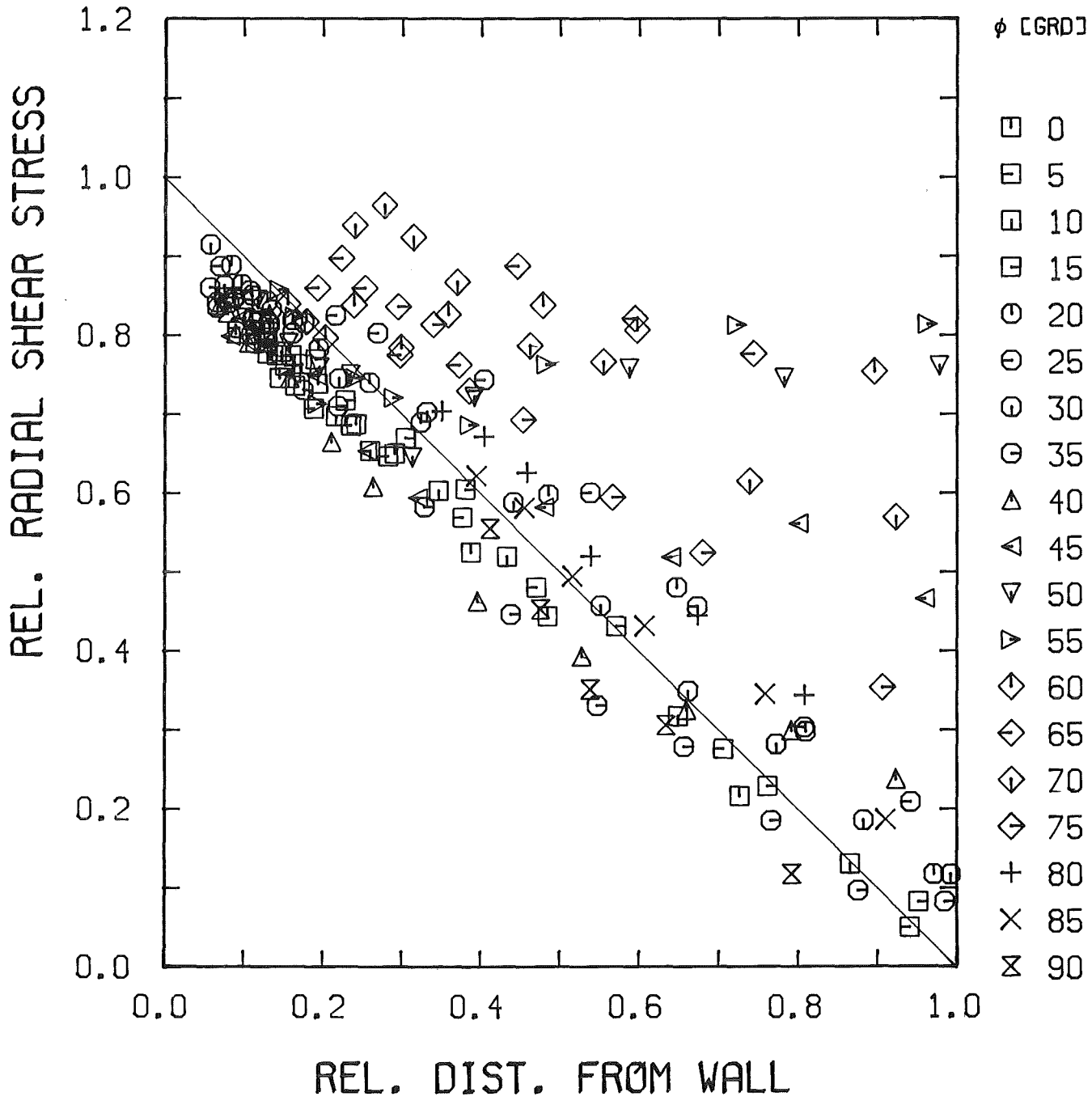

Fig. 25-4 Distribution of radial shear stress in the r/φ-part of quadrant 4

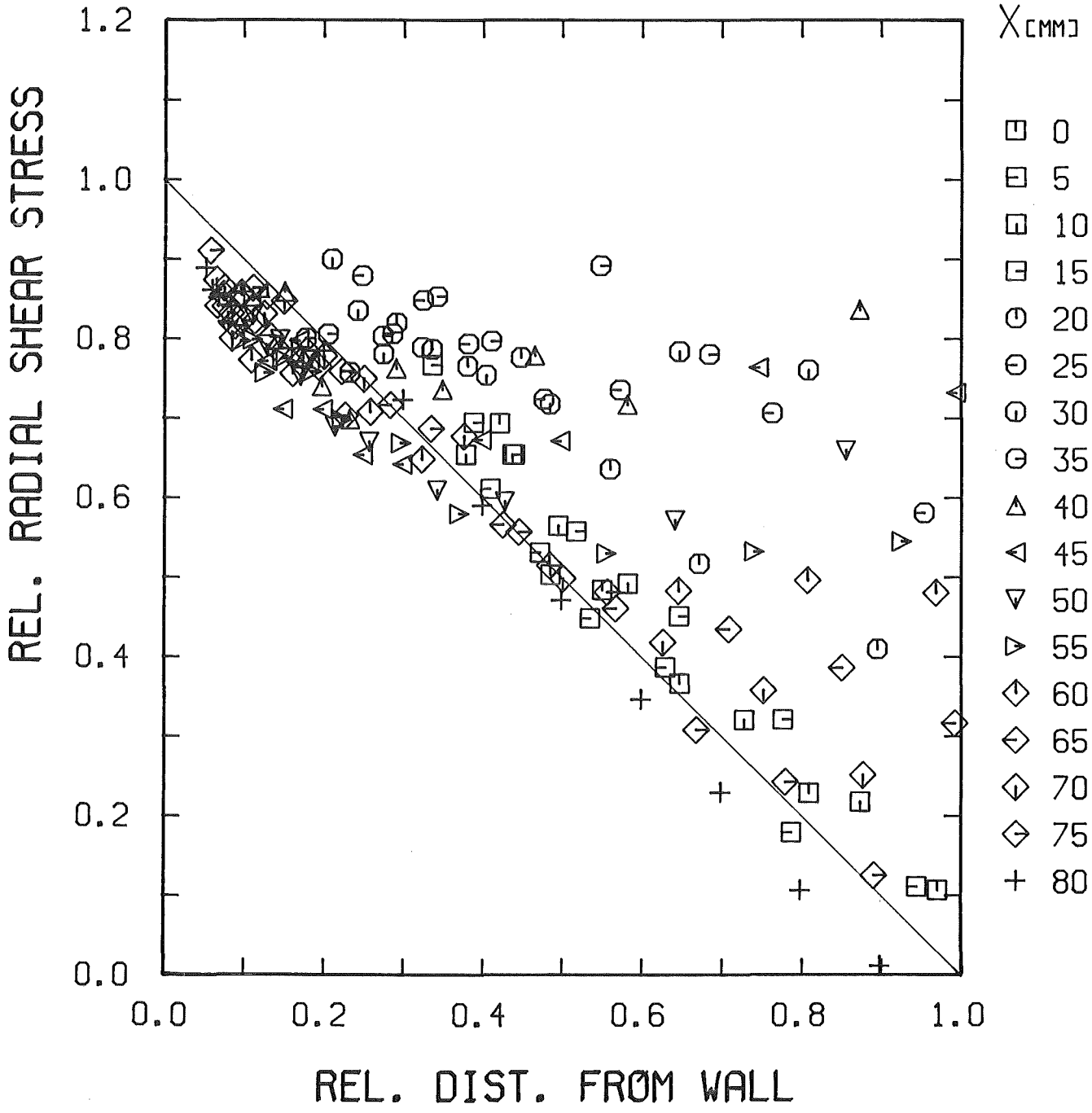

Fig. 26-1 Distribution of radial shear stress
in the x/y-part of quadrant 1

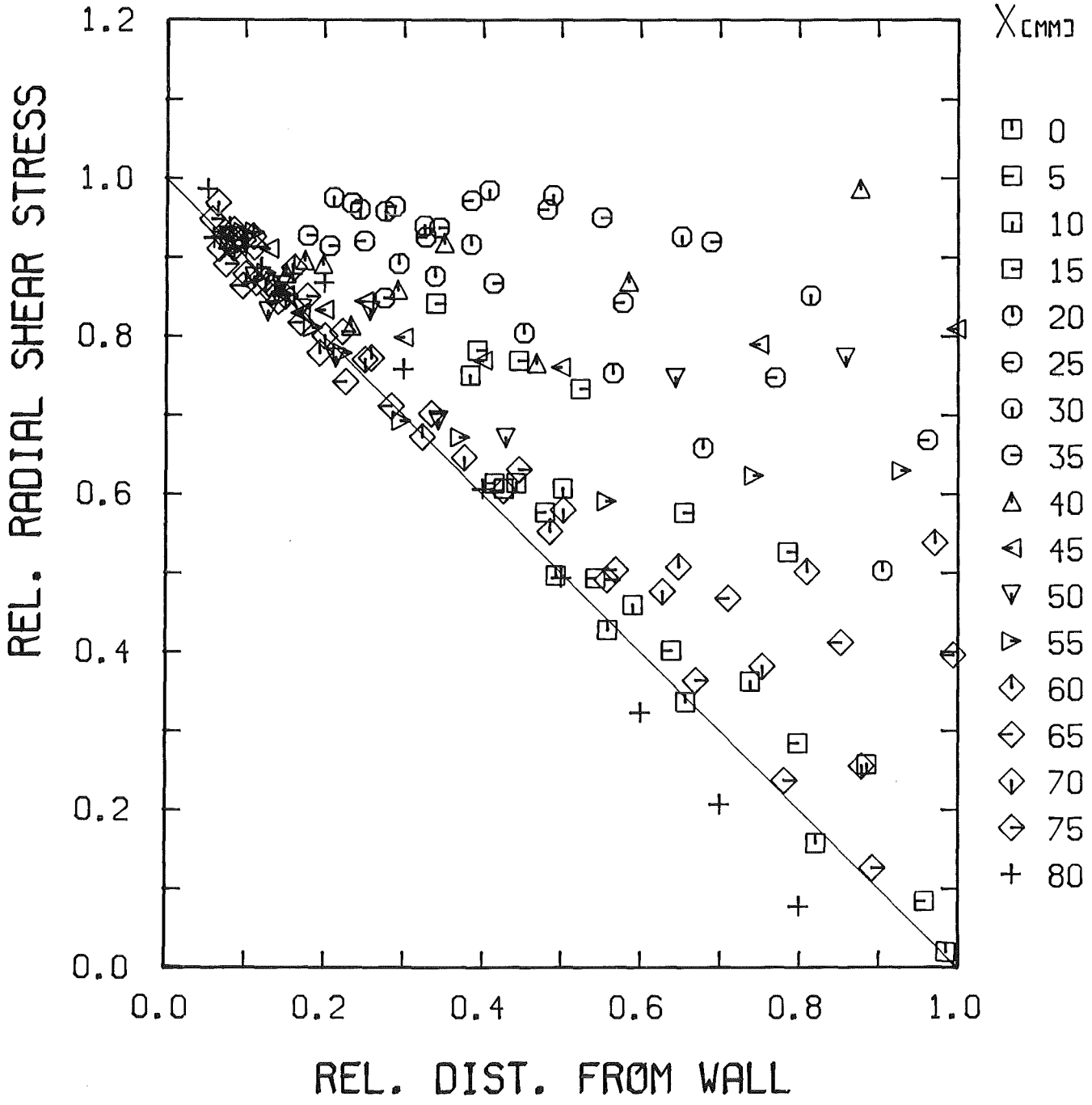

Fig. 26-2 Distribution of radial shear stress
in the x/y-part of quadrant 2

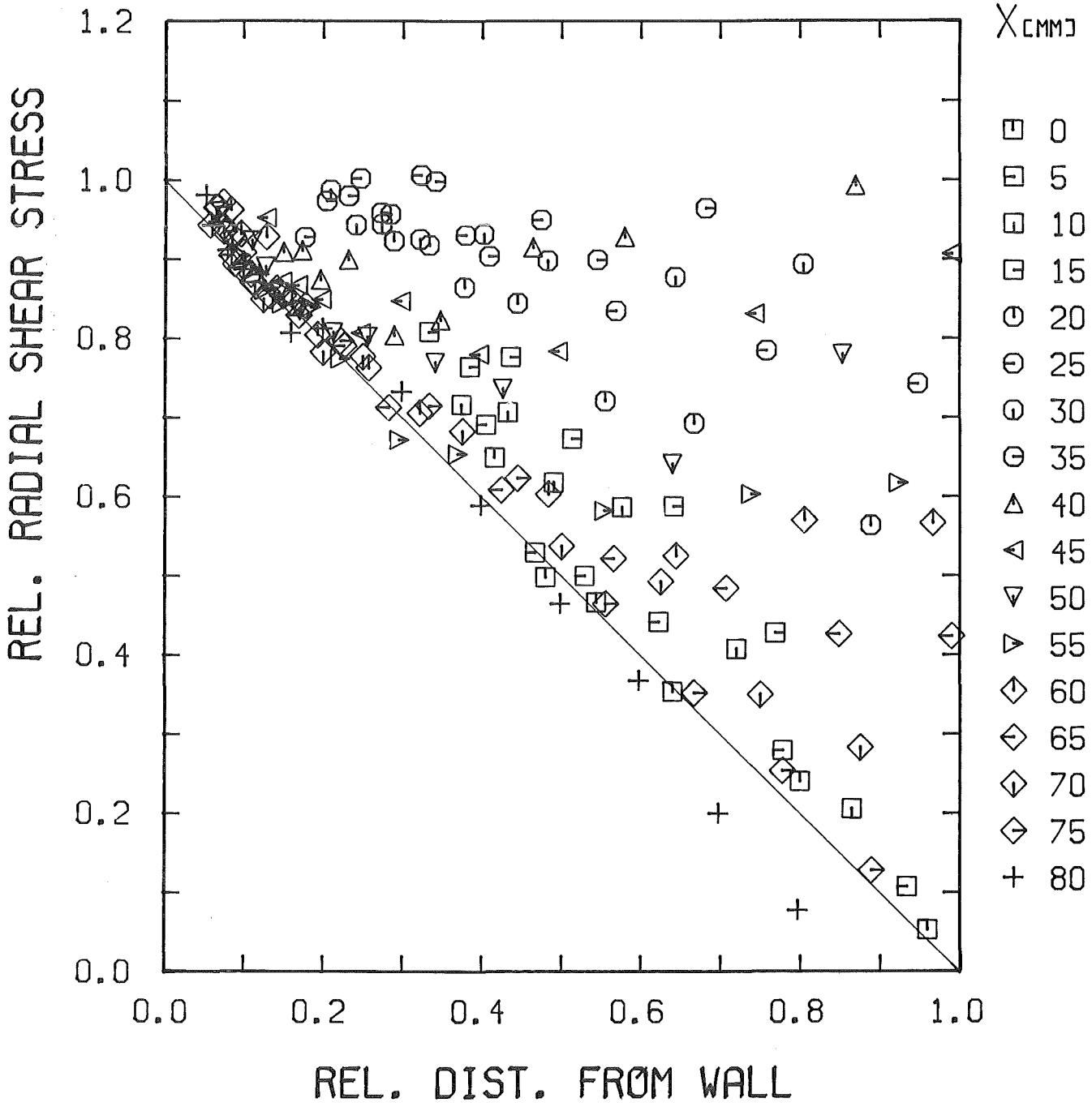

Fig. 26-3 Distribution of radial shear stress
in the x/y-part of quadrant 3

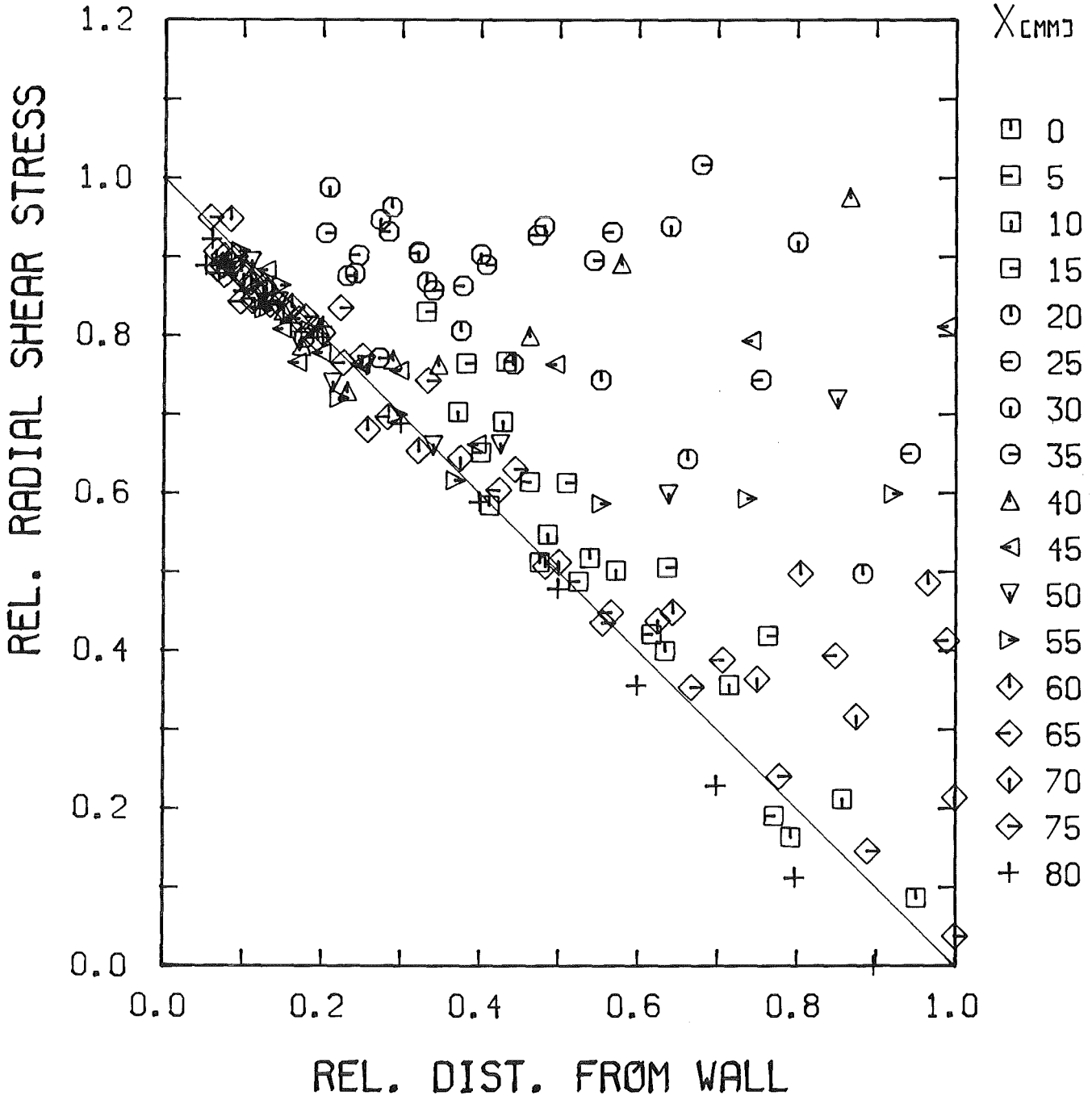

Fig. 26-4 Distribution of radial shear stress
in the x/y-part of quadrant 4

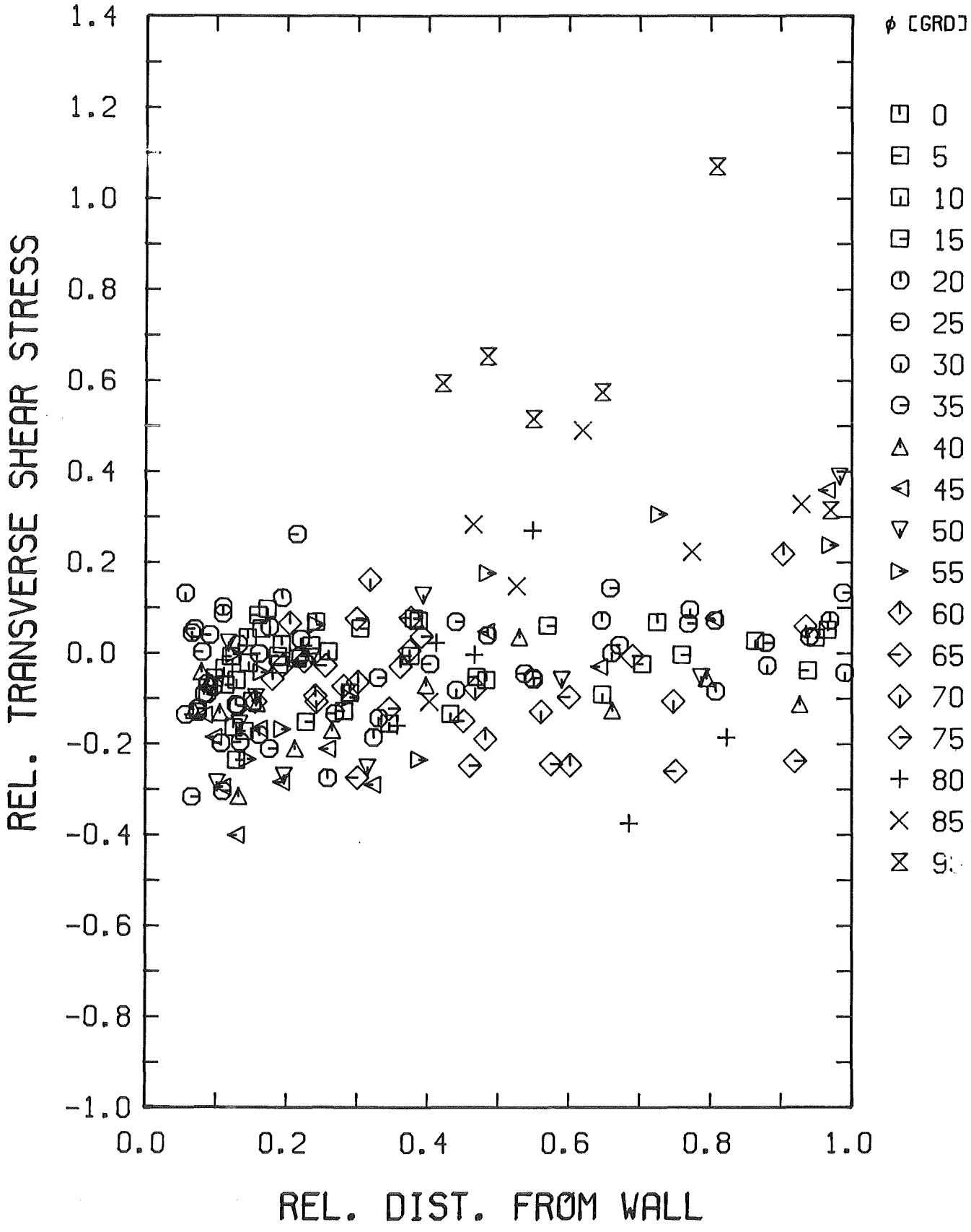

Fig. 27-1 Distribution of transverse shear stress in the r/φ-part of quadrant 1

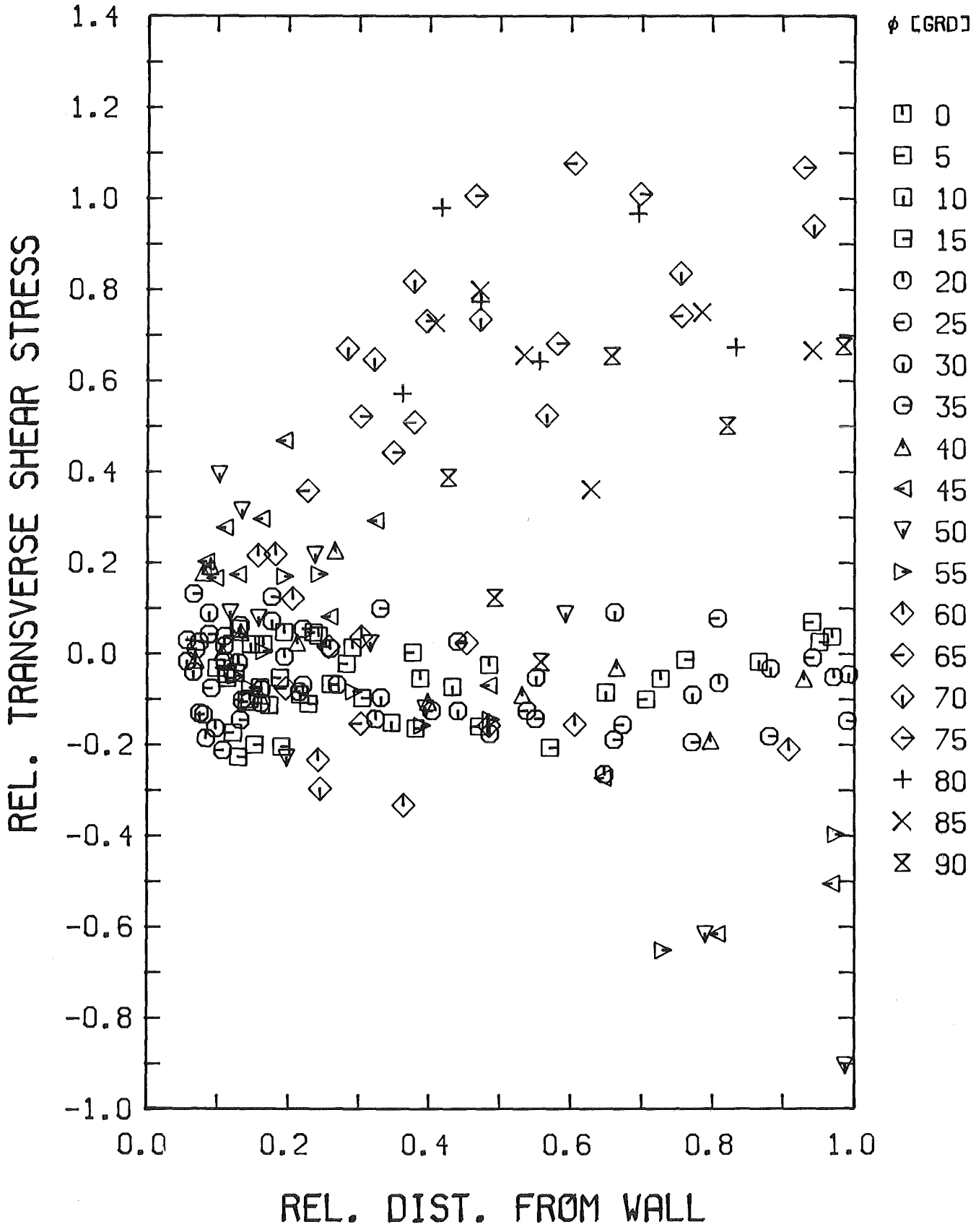

Fig. 27-2 Distribution of transverse shear stress in the r/φ-part of quadrant 2

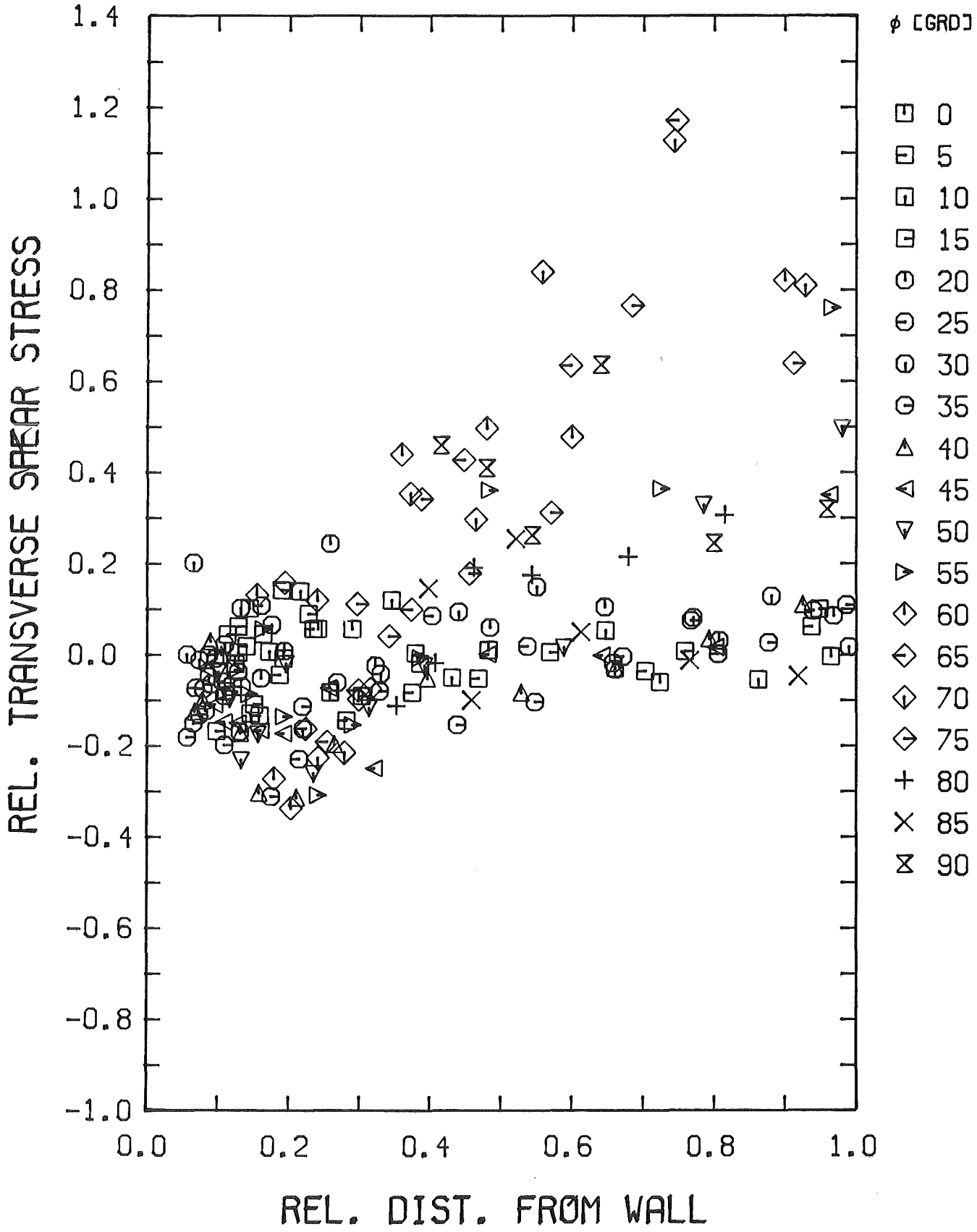

Fig. 27-3 Distribution of transverse shear stress in the r/φ-part of quadrant 3

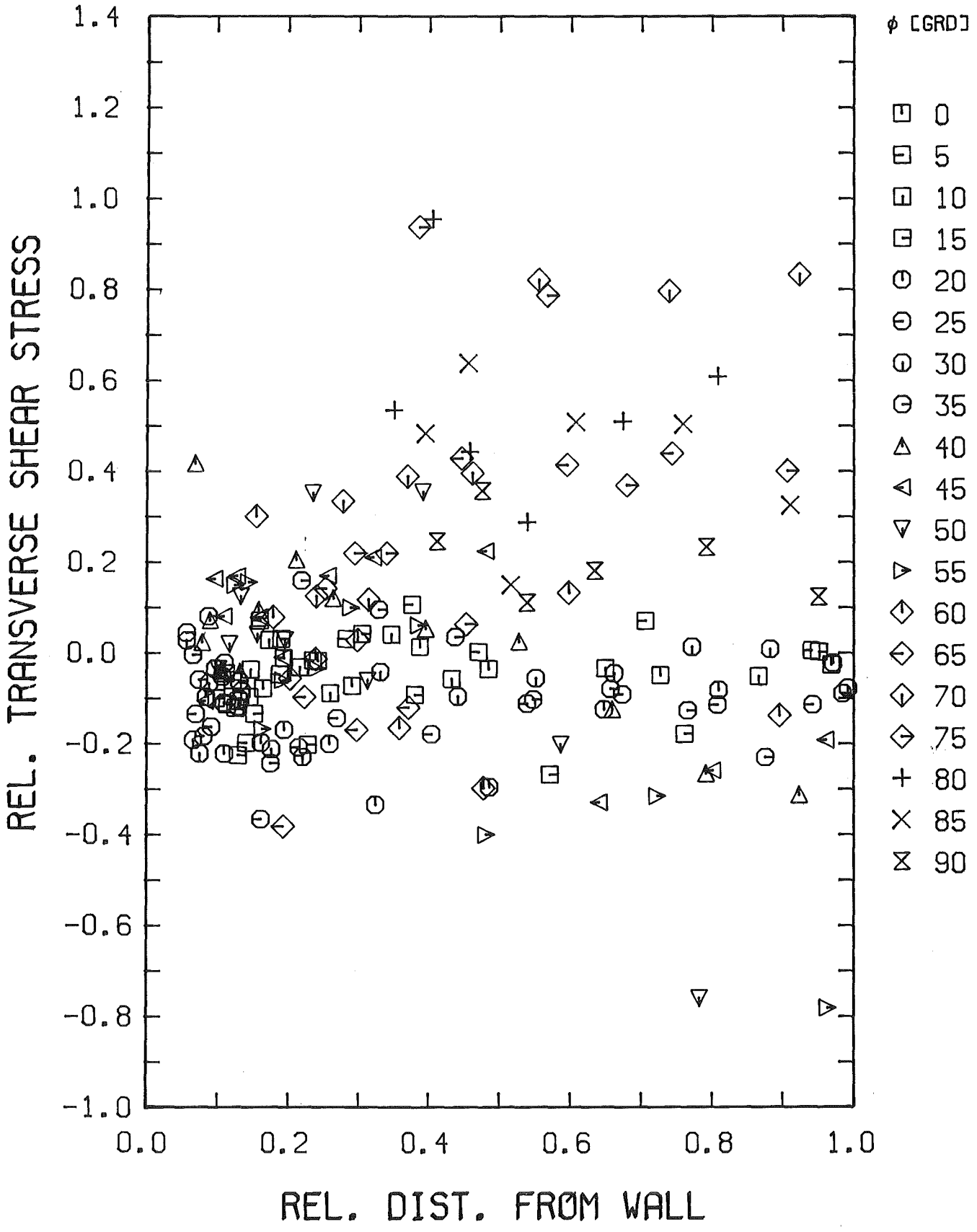

Fig. 27-4 Distribution of transverse shear stress in the r/ϕ-part of quadrant 4

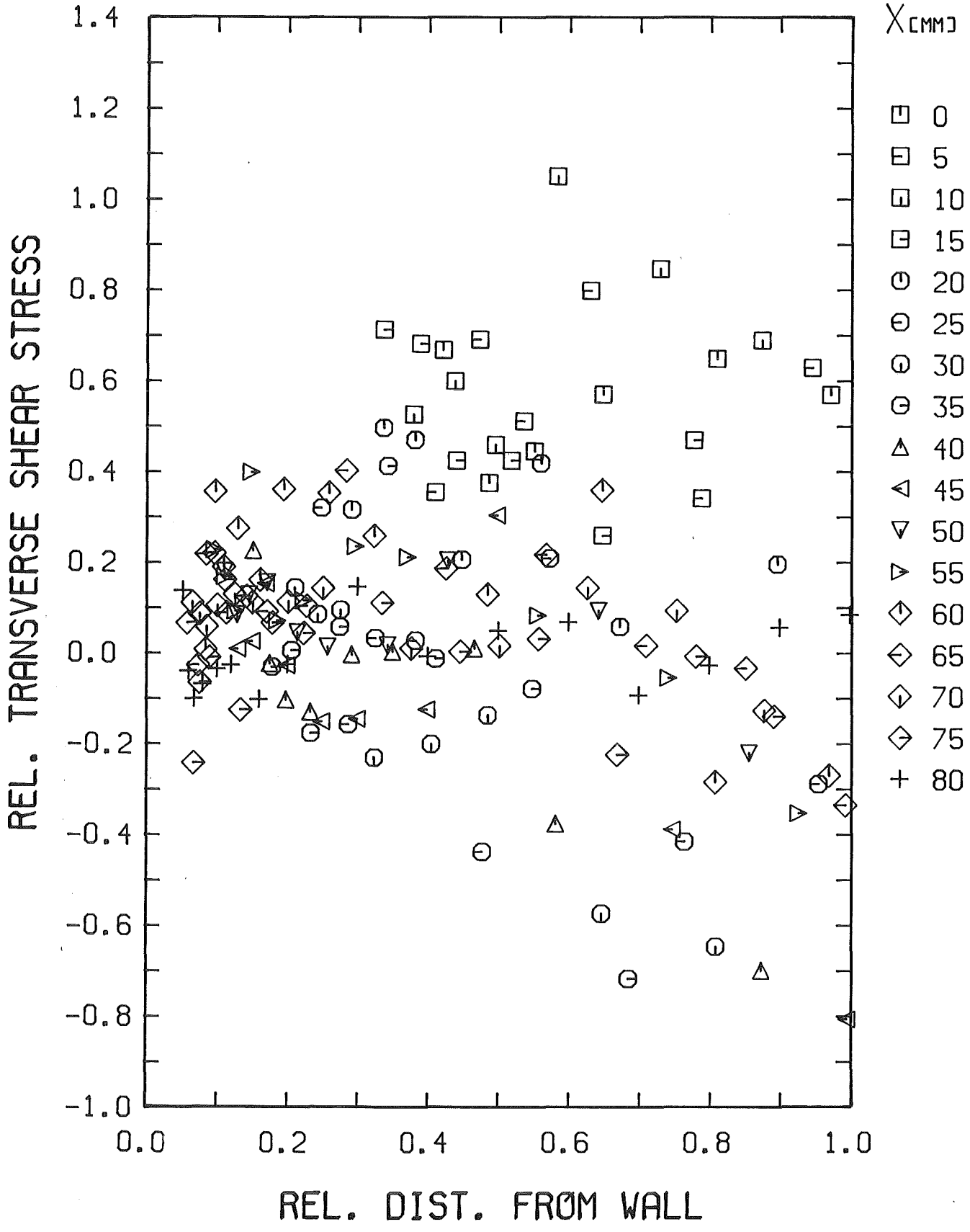

Fig. 28-1 Distribution of transverse shear stress in the x/y-part of quadrant 1

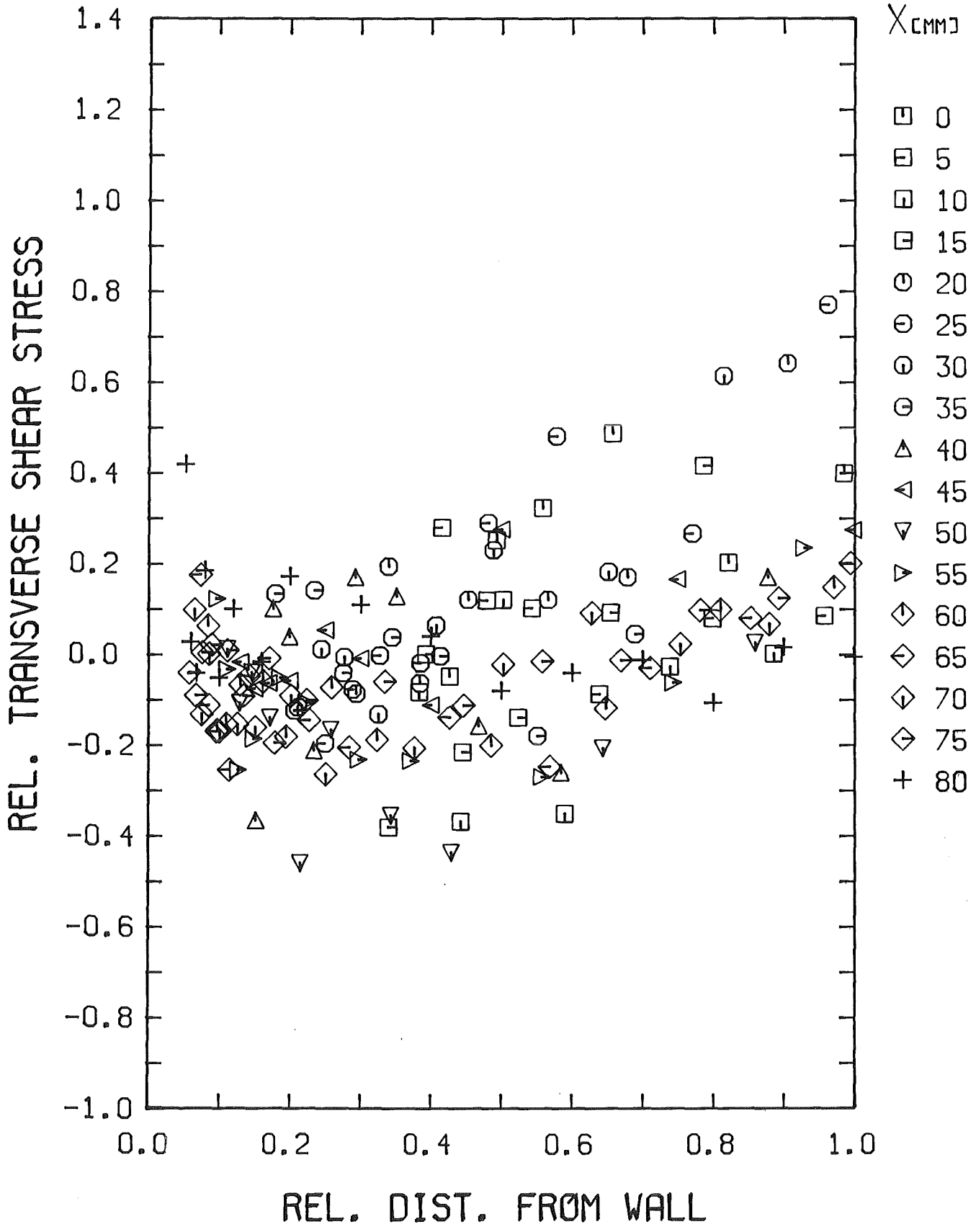

Fig. 28-2 Distribution of transverse shear stress in the x/y-part of quadrant 2

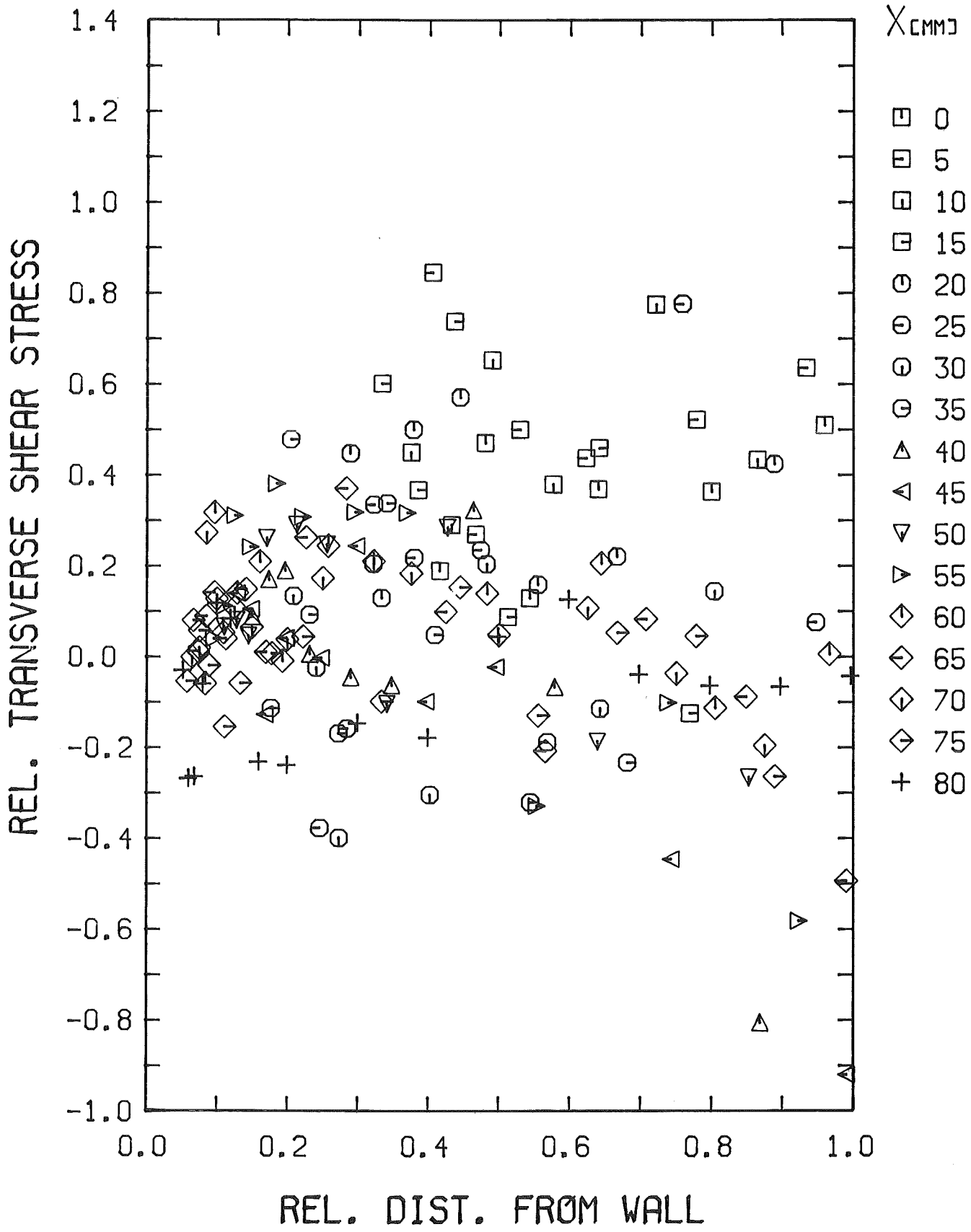

Fig. 28-3 Distribution of transverse shear stress in the x/y-part of quadrant 3

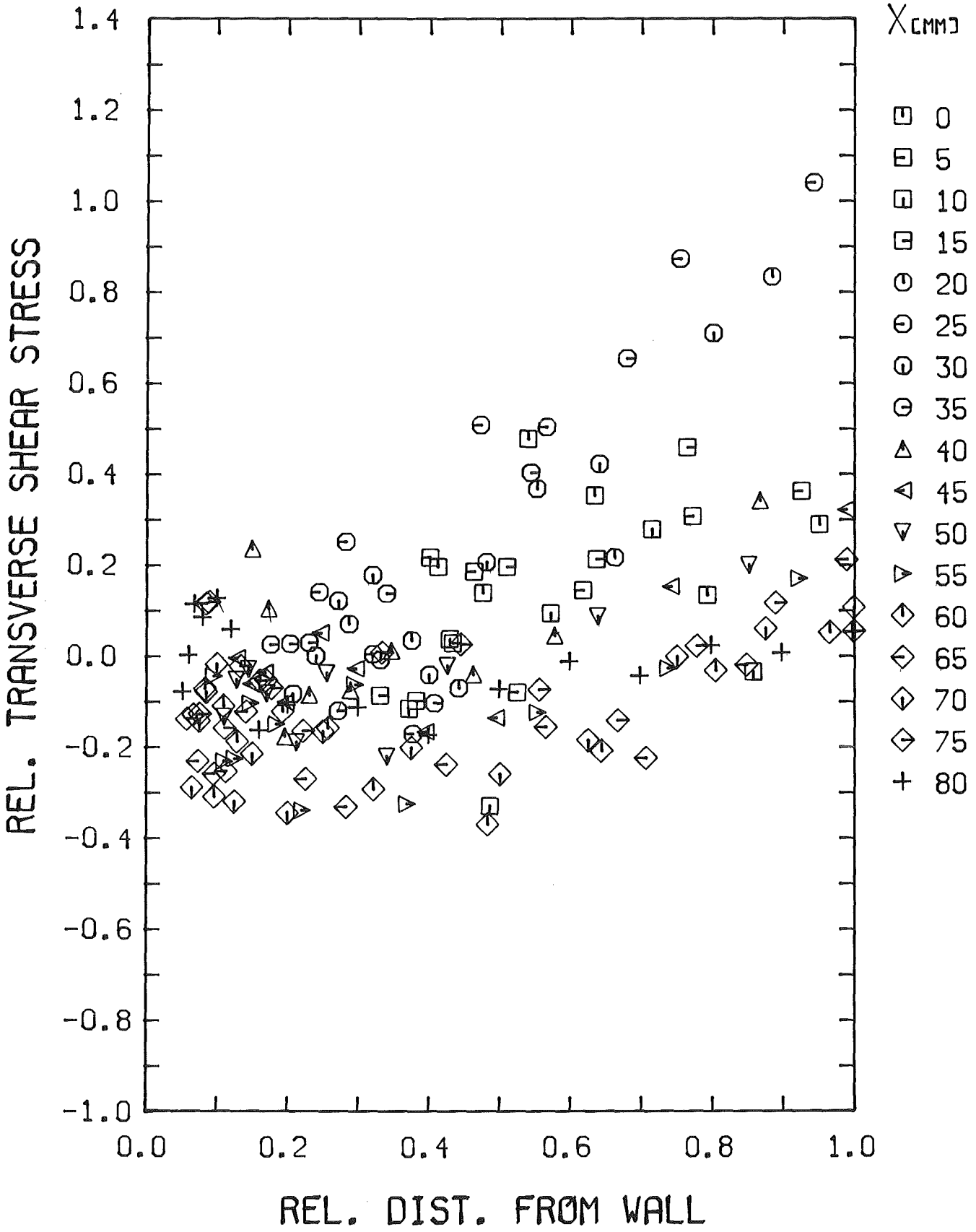

Fig. 28-4 Distribution of transverse shear stress in the x/y-part of quadrant 4

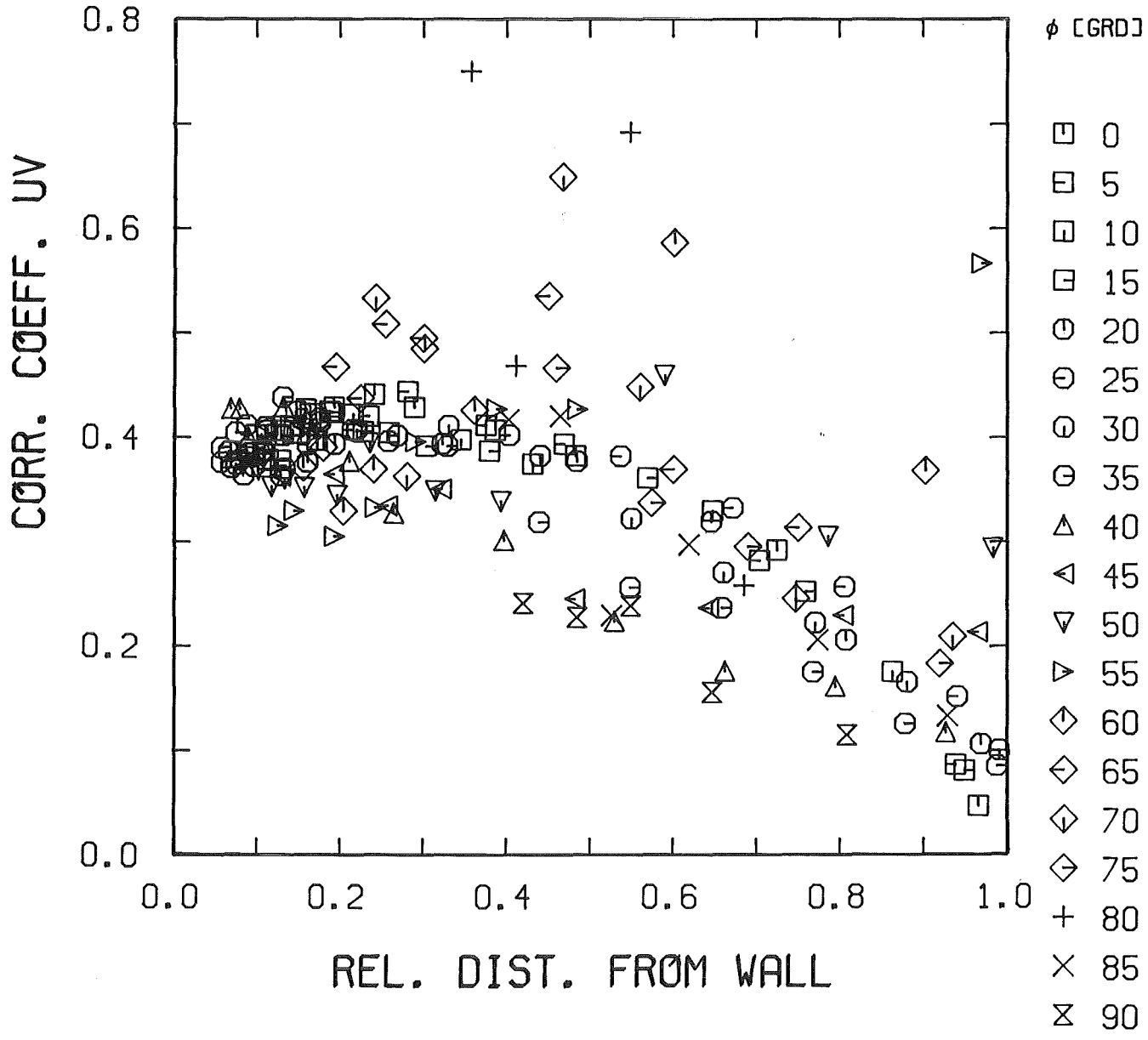

Fig. 29-1 Distribution of the correlation coefficient perpendicular to the wall in the r/ϕ-part of quadrant 1

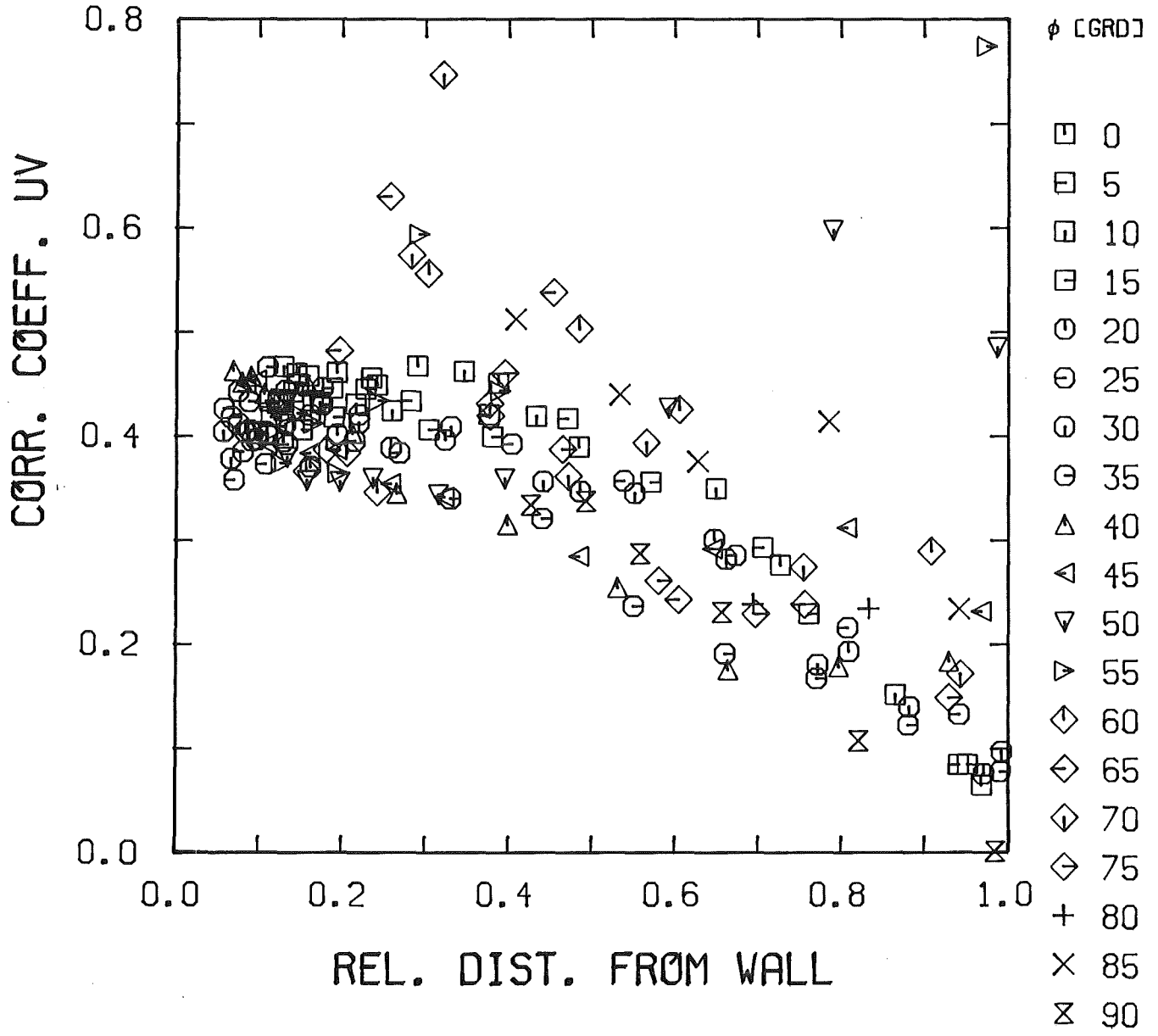

Fig. 29-2 Distribution of the correlation coefficient perpendicular to the wall in the r/ϕ-part of quadrant 2

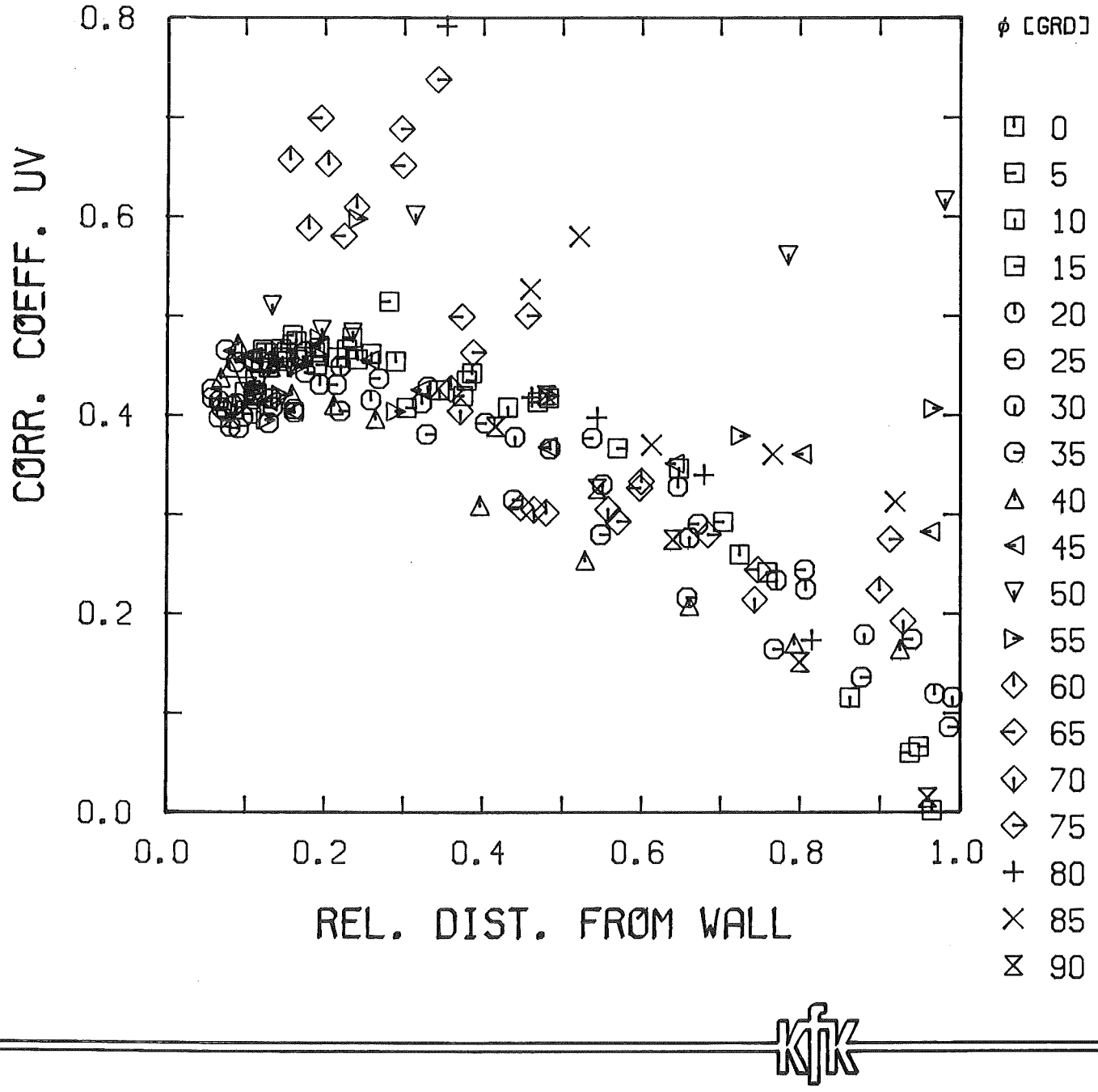

Fig. 29-3 Distribution of the correlation coefficient perpendicular to the wall in the r/ϕ-part of quadrant 3

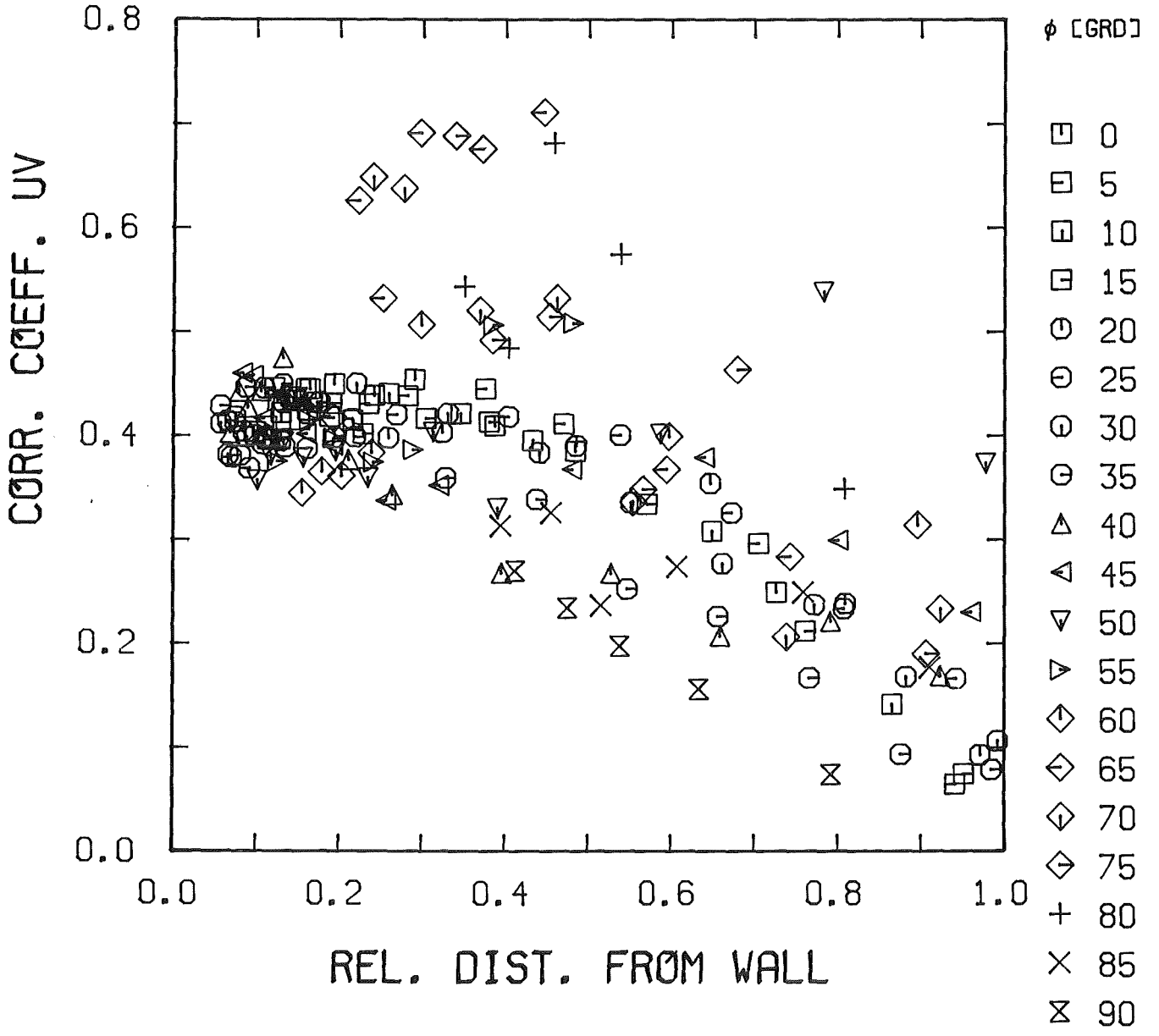

Fig. 29-4 Distribution of the correlation coefficient perpendicular to the wall in the r/ϕ-part of quadrant 4

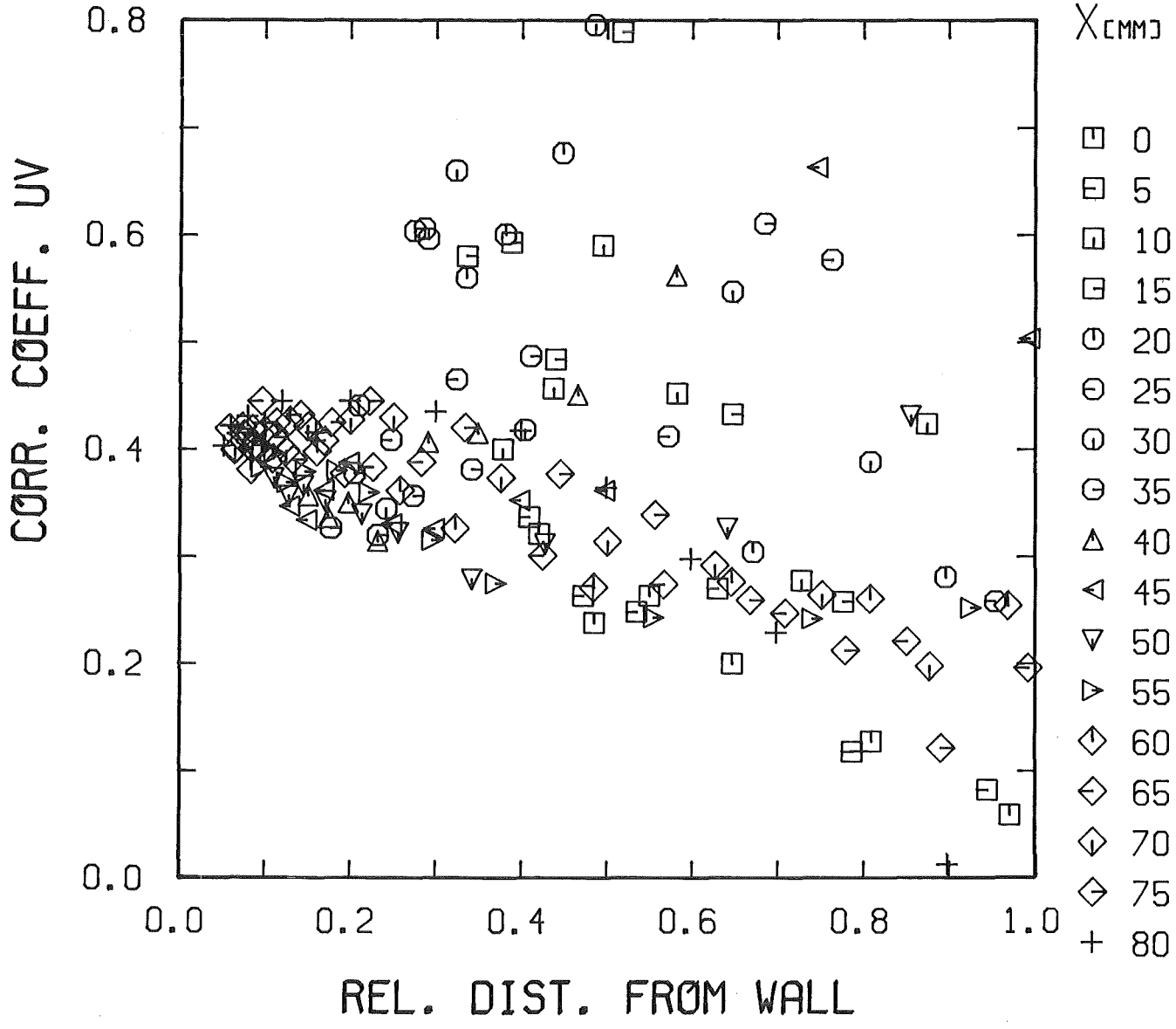

Fig. 30-1 Distribution of the correlation coefficient perpendicular to the wall in the x/y-part of quadrant 1

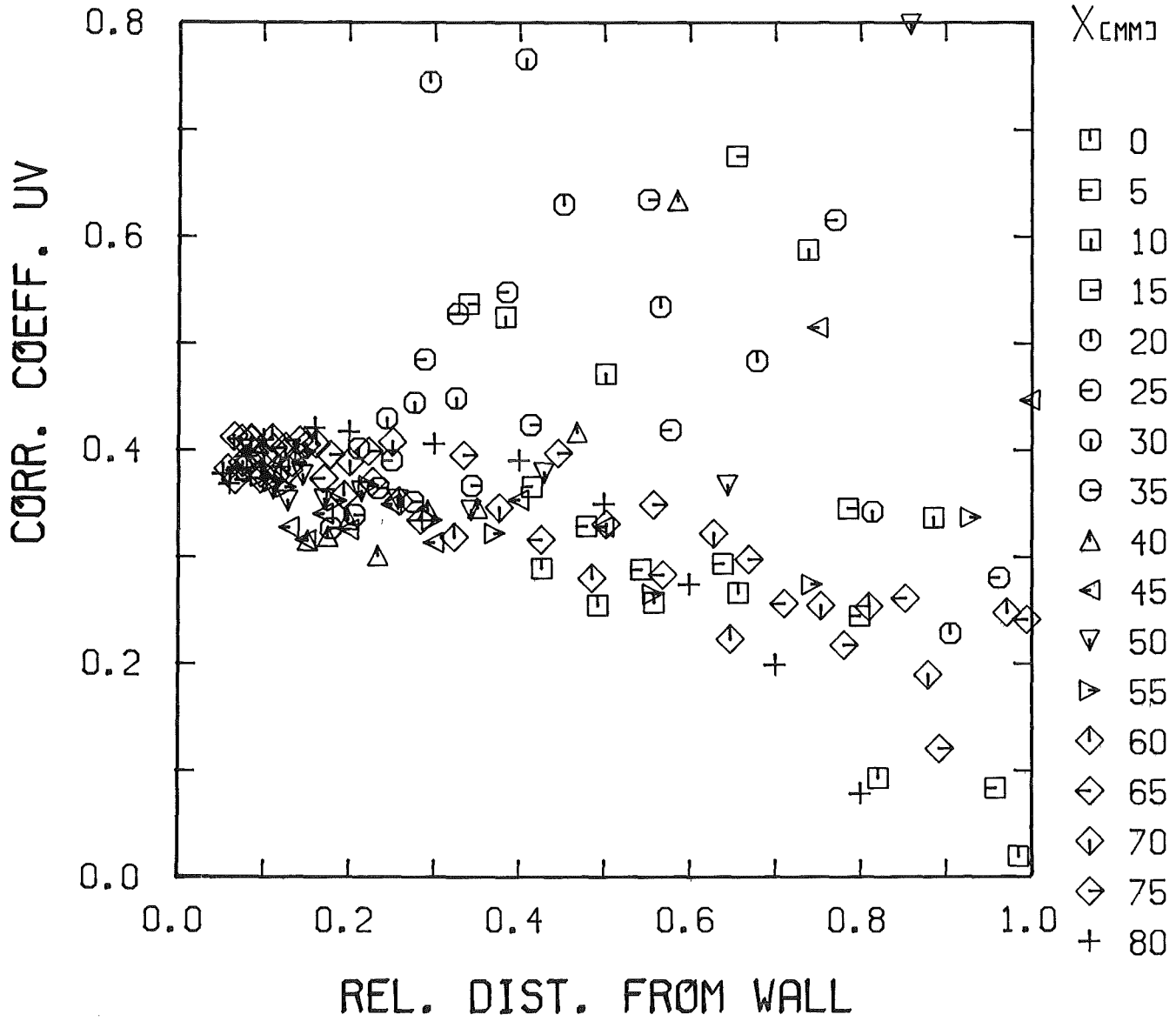

Fig. 30-2 Distribution of the correlation coefficient perpendicular to the wall in the x/y-part of quadrant 2

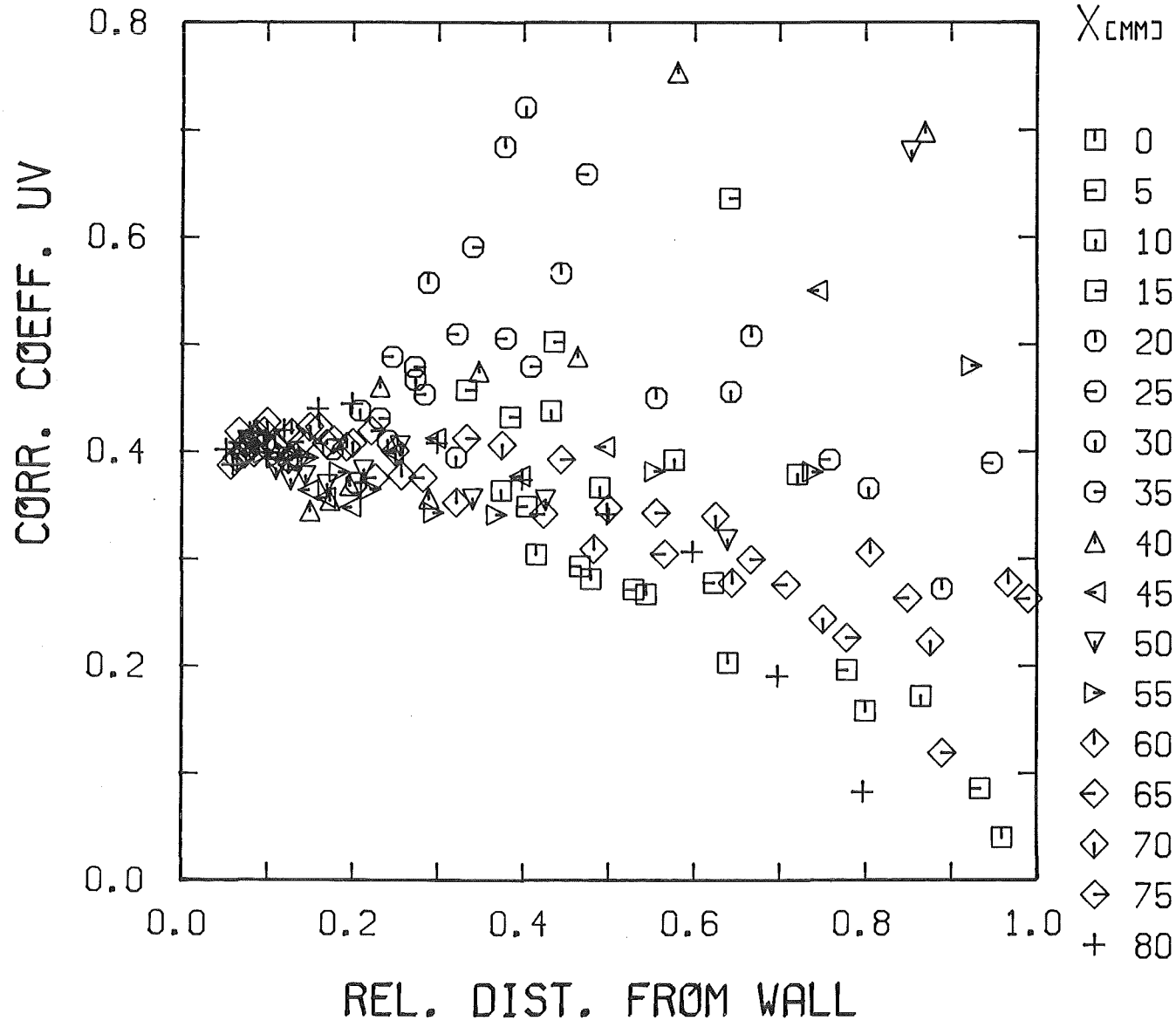

Fig. 30-3 Distribution of the correlation coefficient perpendicular to the wall in the x/y-part of quadrant 3

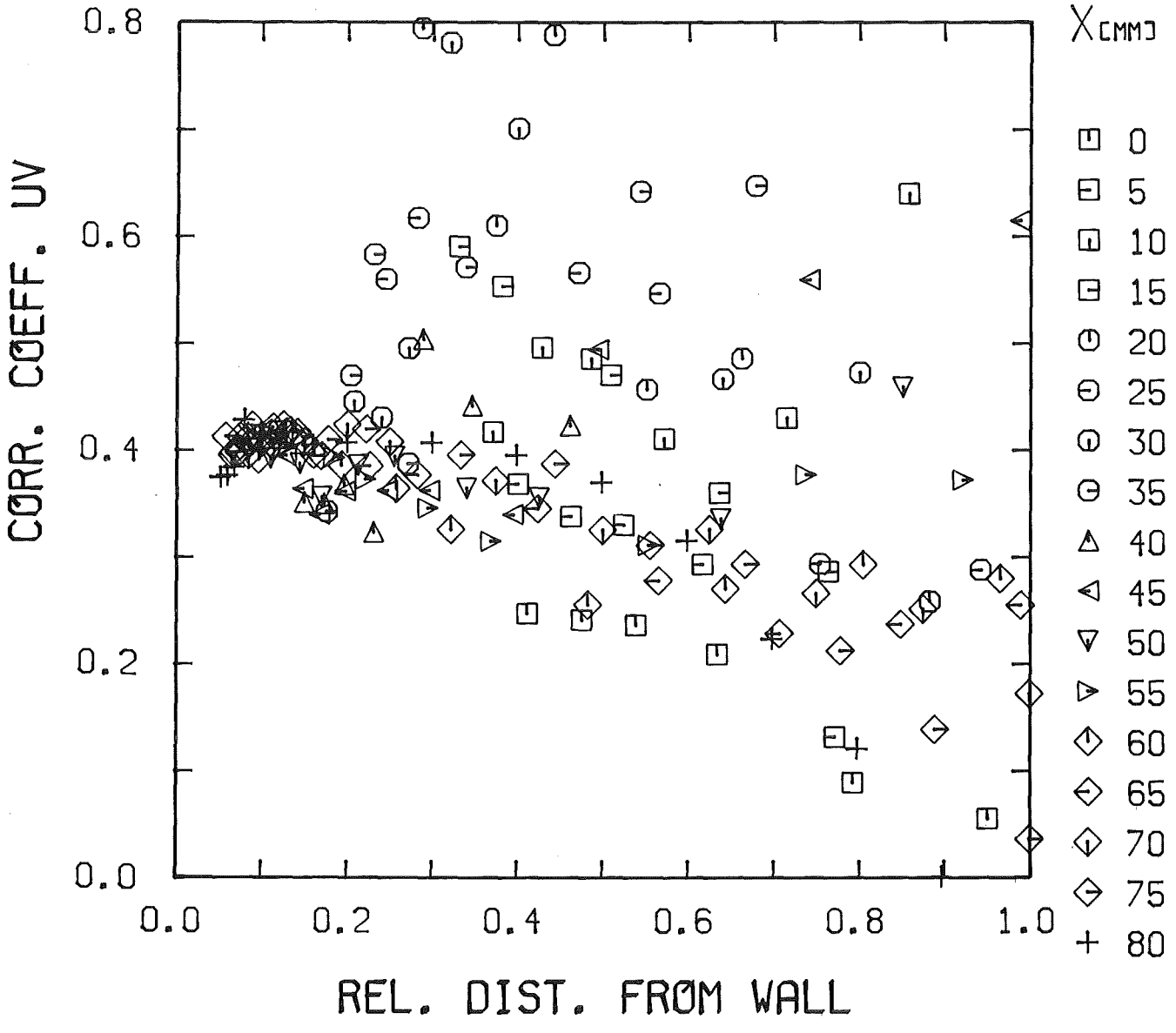

Fig. 30-4 Distribution of the correlation coefficient perpendicular to the wall in the x/y-part of quadrant 4

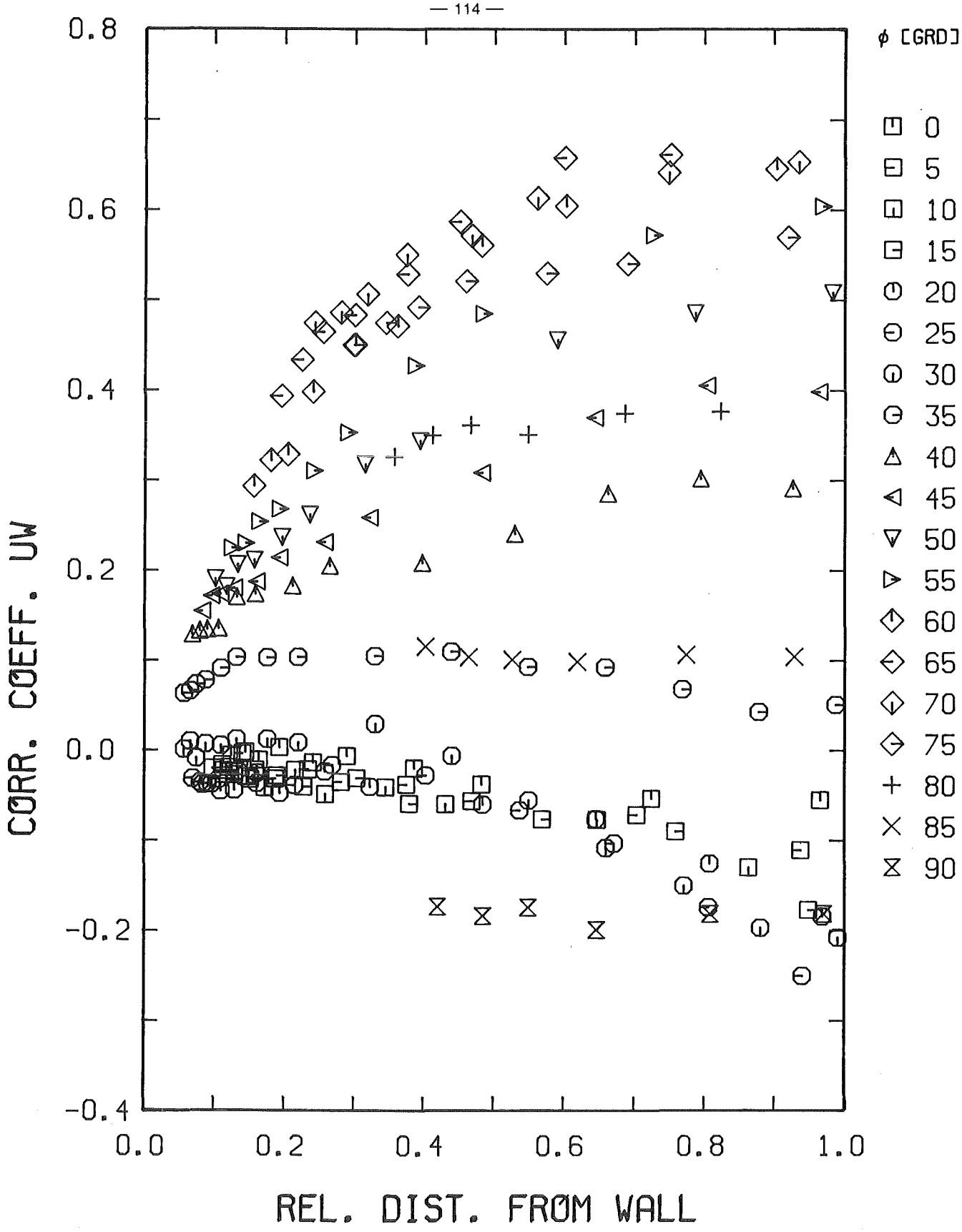

Fig. 31-1 Distribution of the correlation coefficient parallel to the wall in the r/ϕ-part of quadrant 1

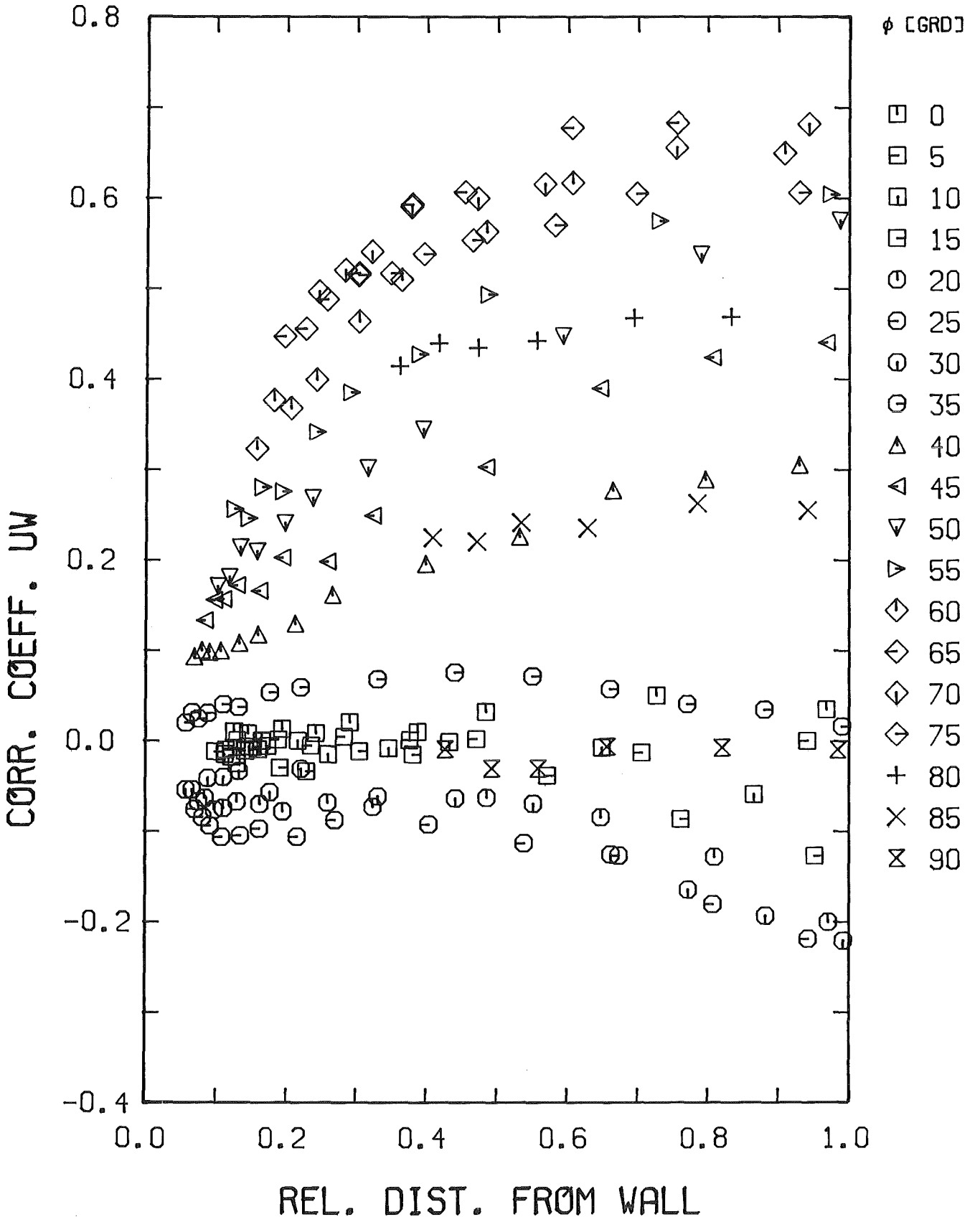

Fig. 31-2 Distribution of the correlation coefficient parallel to the wall in the r/ϕ-part of quadrant 2

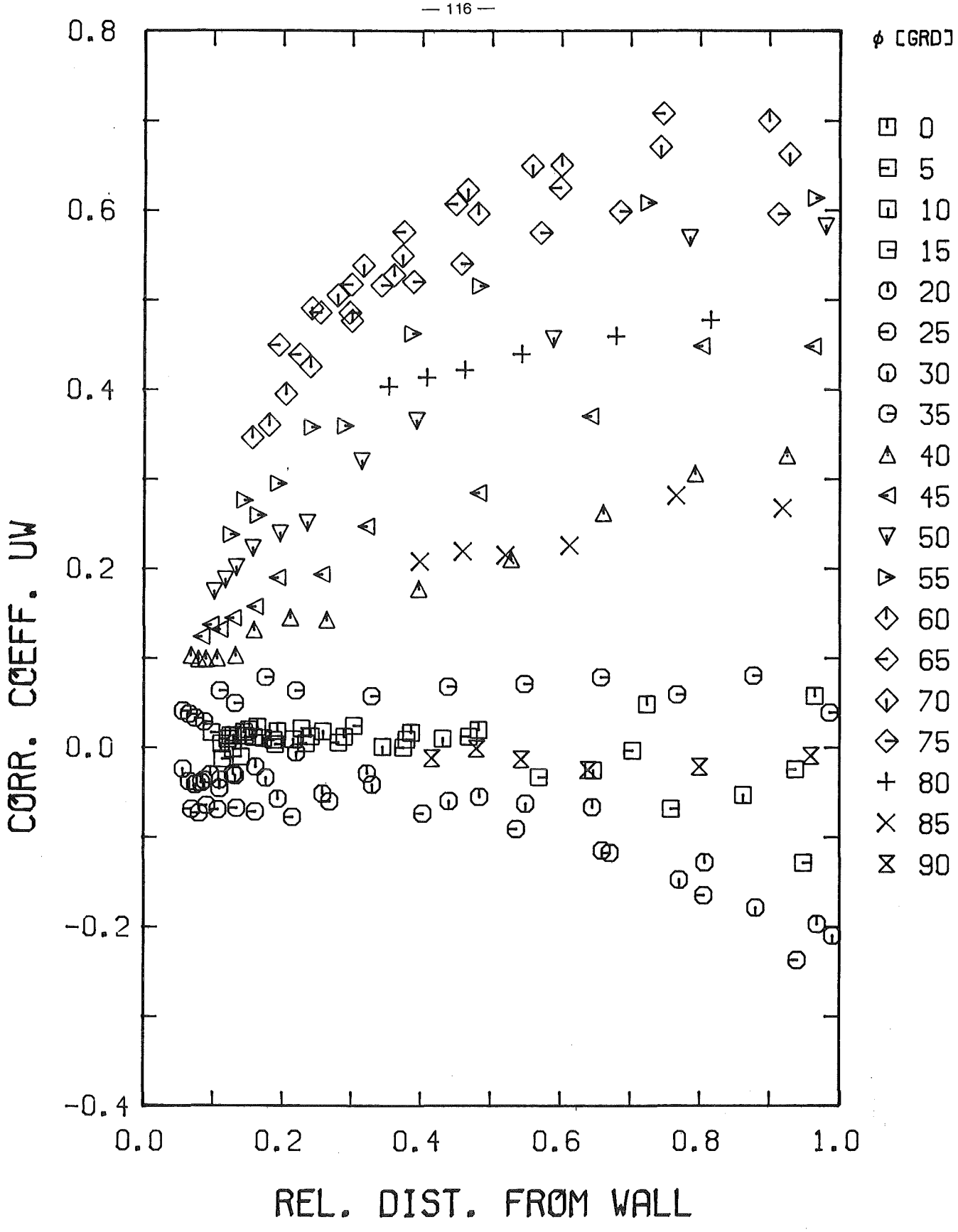

Fig. 31-3 Distribution of the correlation coefficient parallel to the wall in the r/ϕ-part of quadrant 3

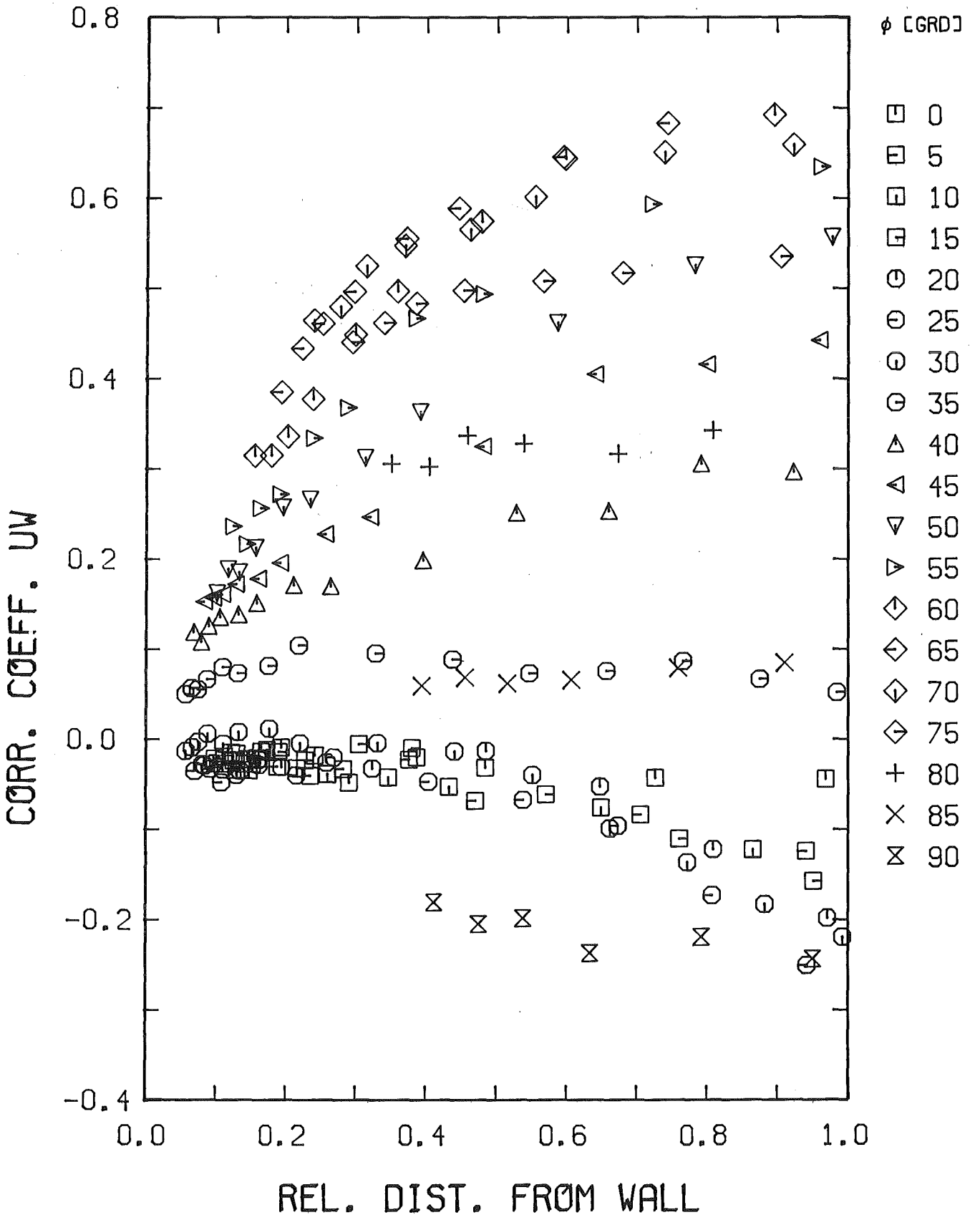

Fig. 31-4 Distribution of the correlation coefficient parallel to the wall in the r/ϕ-part of quadrant 4

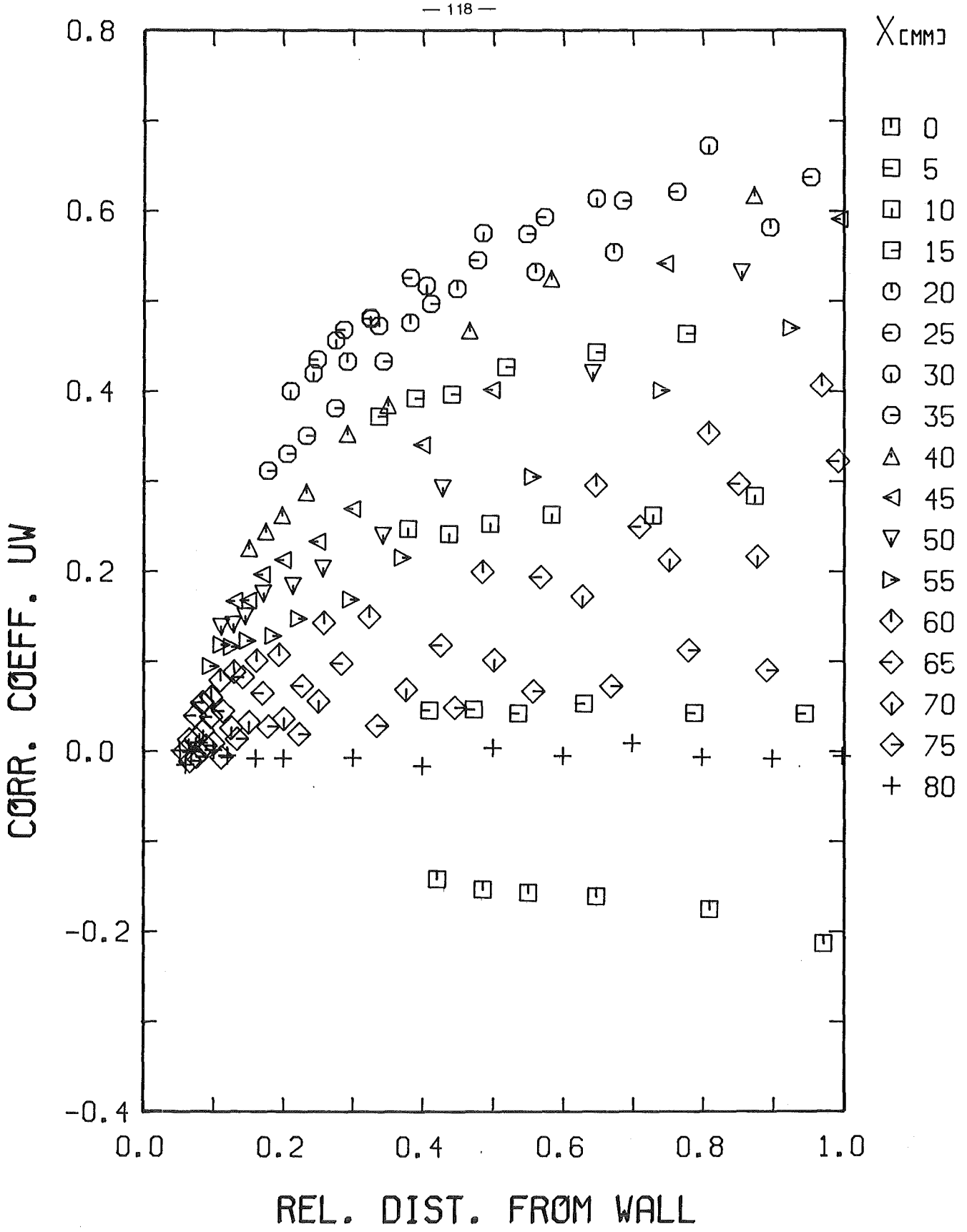

Fig. 32-1 Distribution of the correlation coefficient parallel to the wall in the x/y-part of quadrant 1

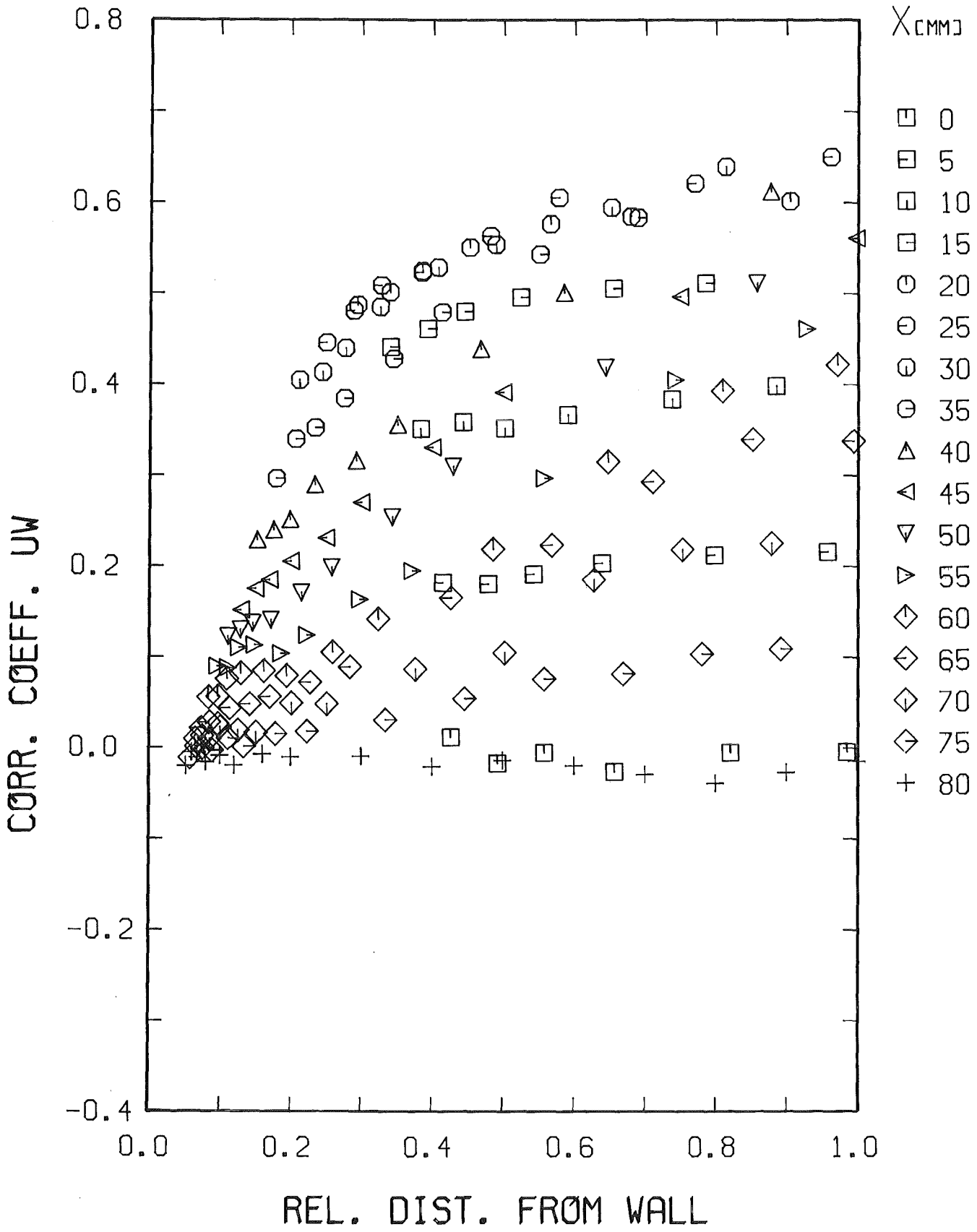

Fig. 32-2 Distribution of the correlation coefficient parallel to the wall in the x/y-part of quadrant 2

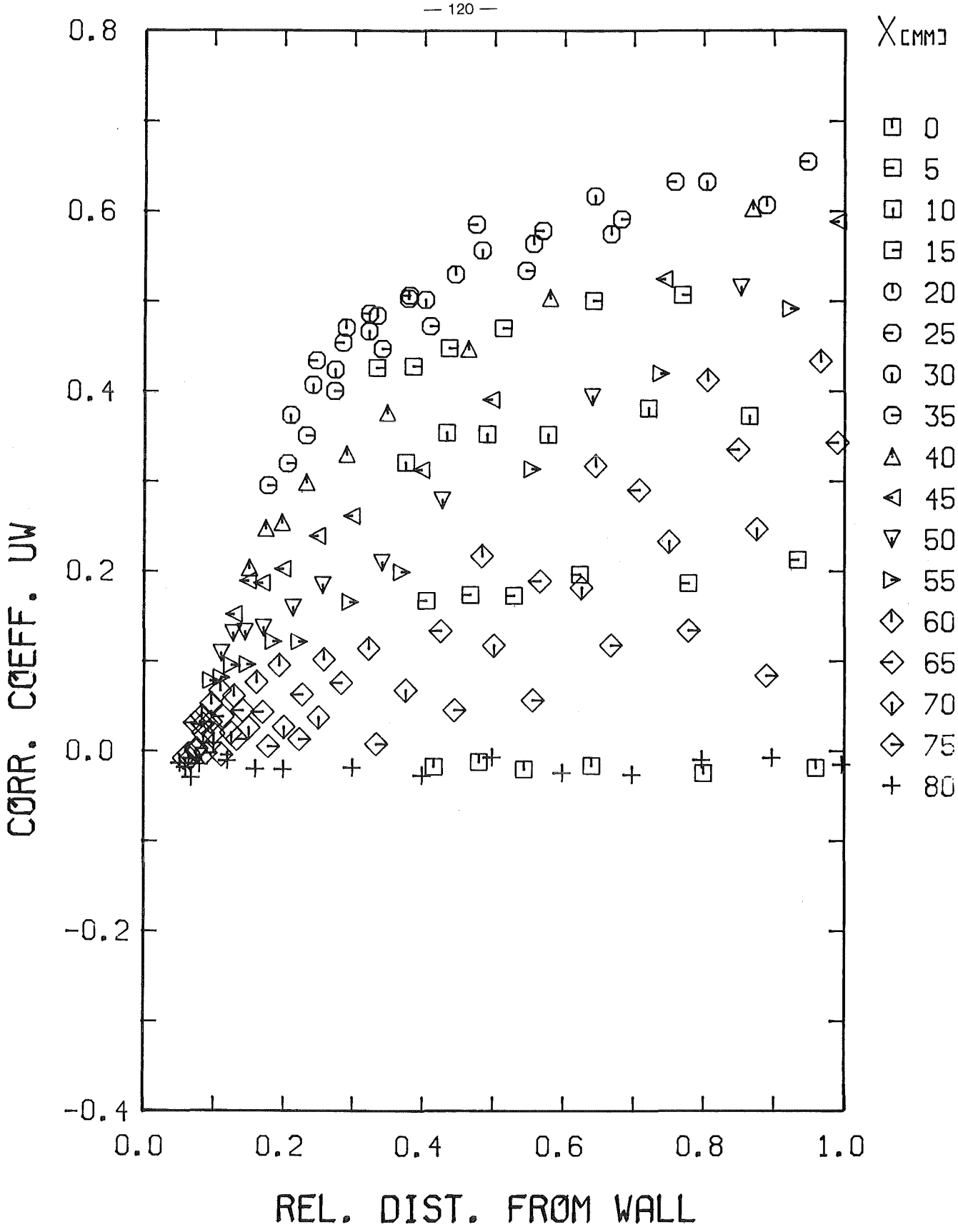

Fig. 32-3 Distribution of the correlation coefficient parallel to the wall in the x/y-part of quadrant 3

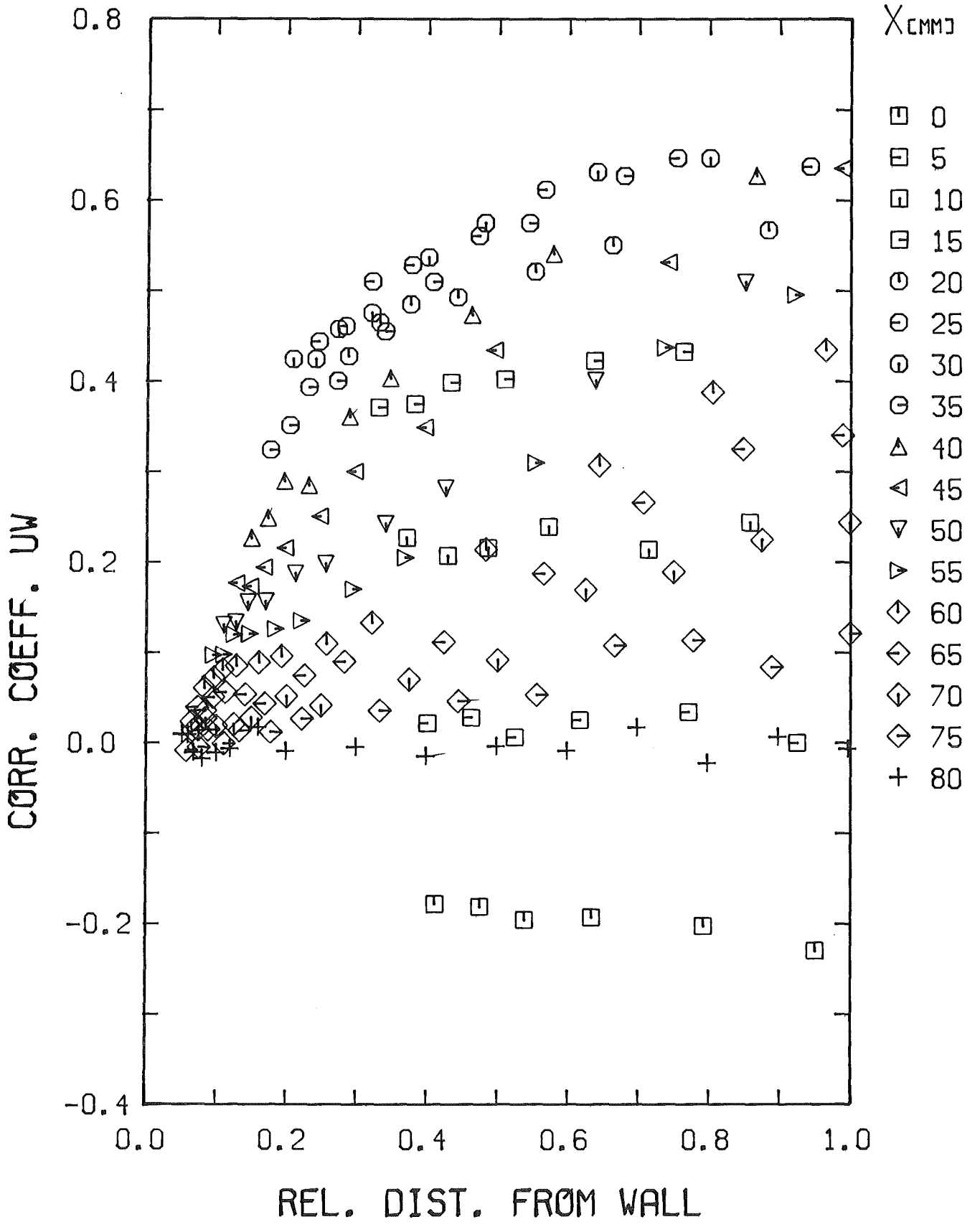

Fig. 32-4 Distribution of the correlation coefficient parallel to the wall in the x/y-part of quadrant 4

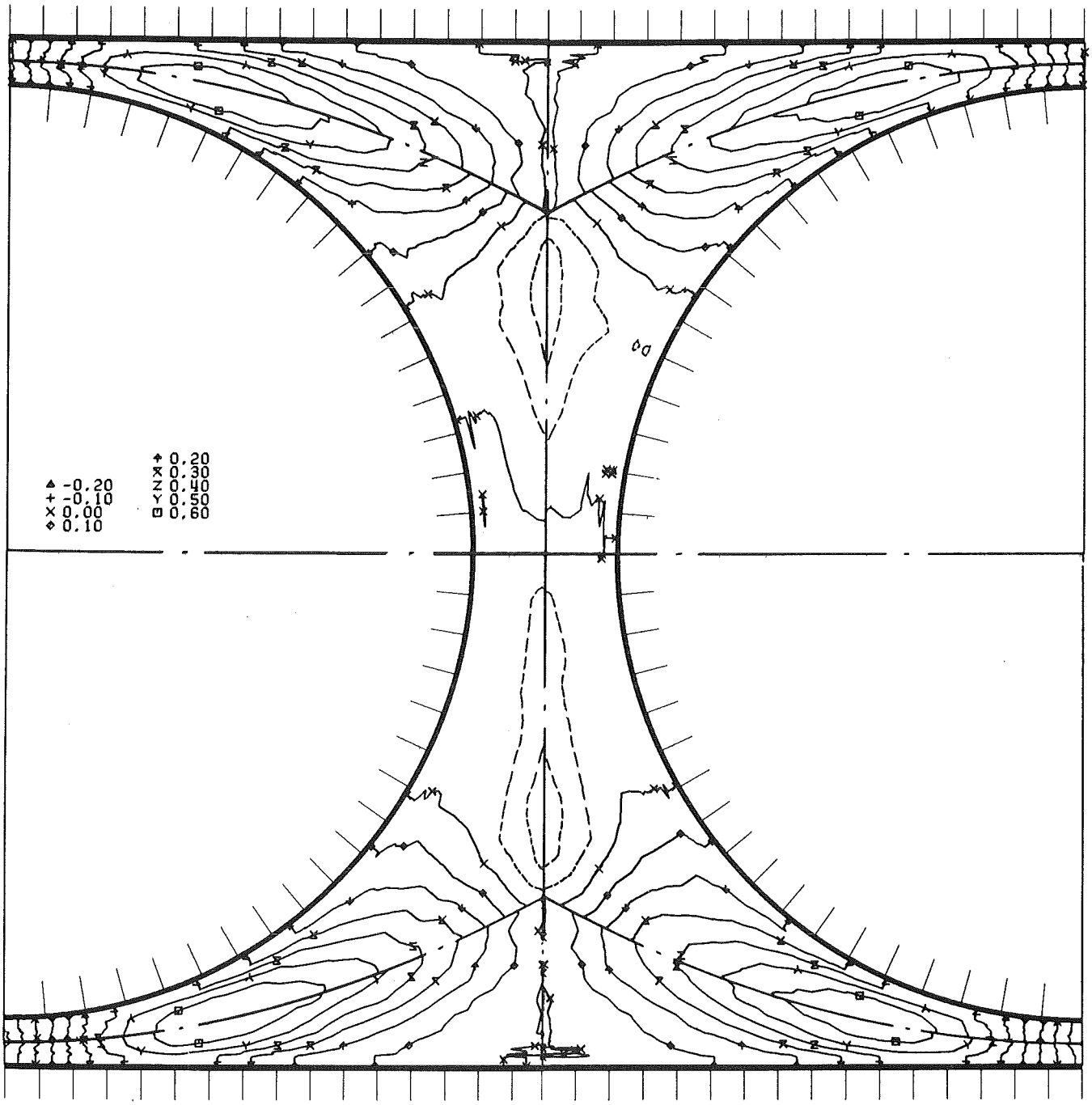

Fig. 33 Distribution of the correlation coefficient parallel to the wall in four quadrants

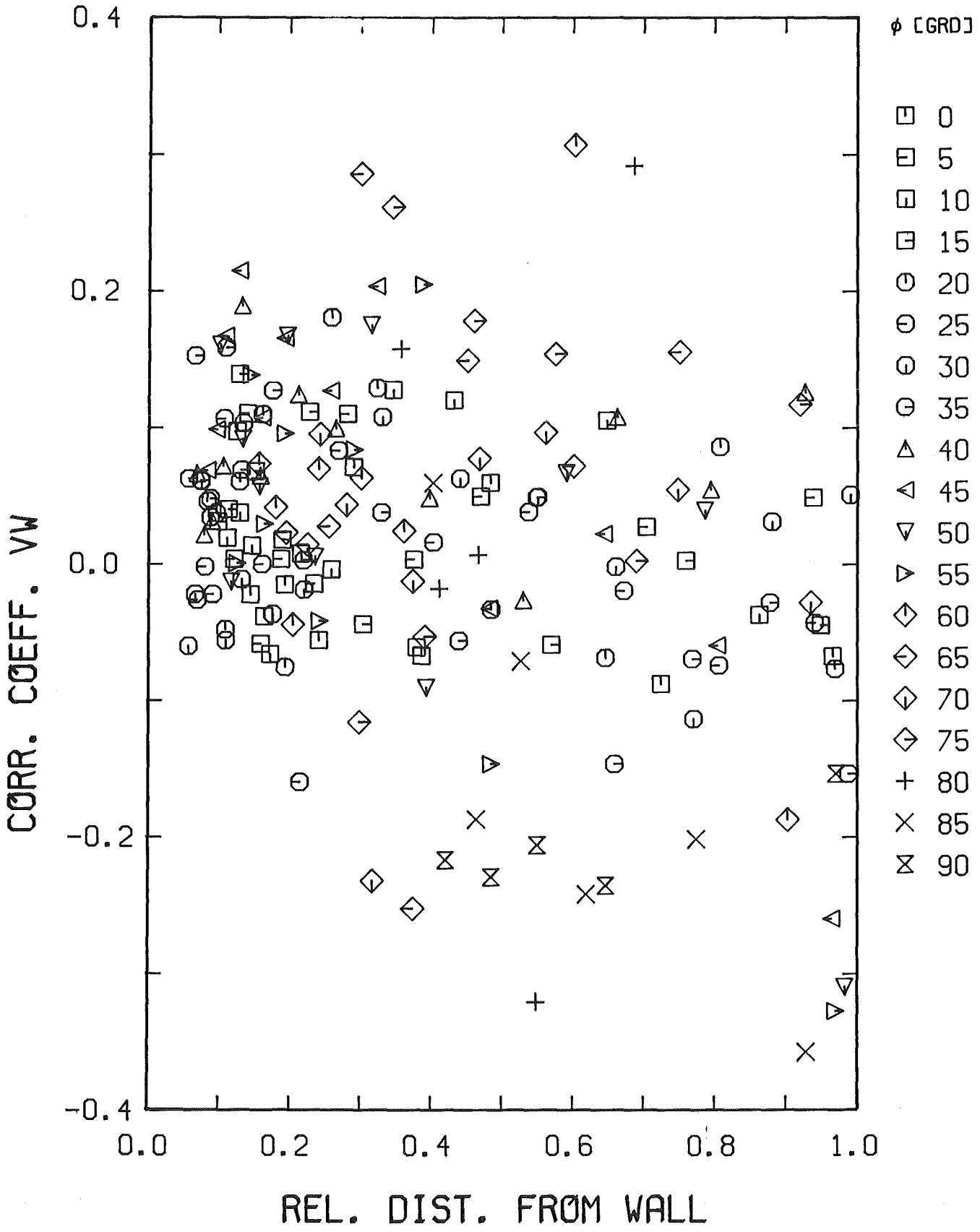

Fig. 34-1 Distribution of the correlation coefficient transverse to the wall in the r/ϕ-part of quadrant 1

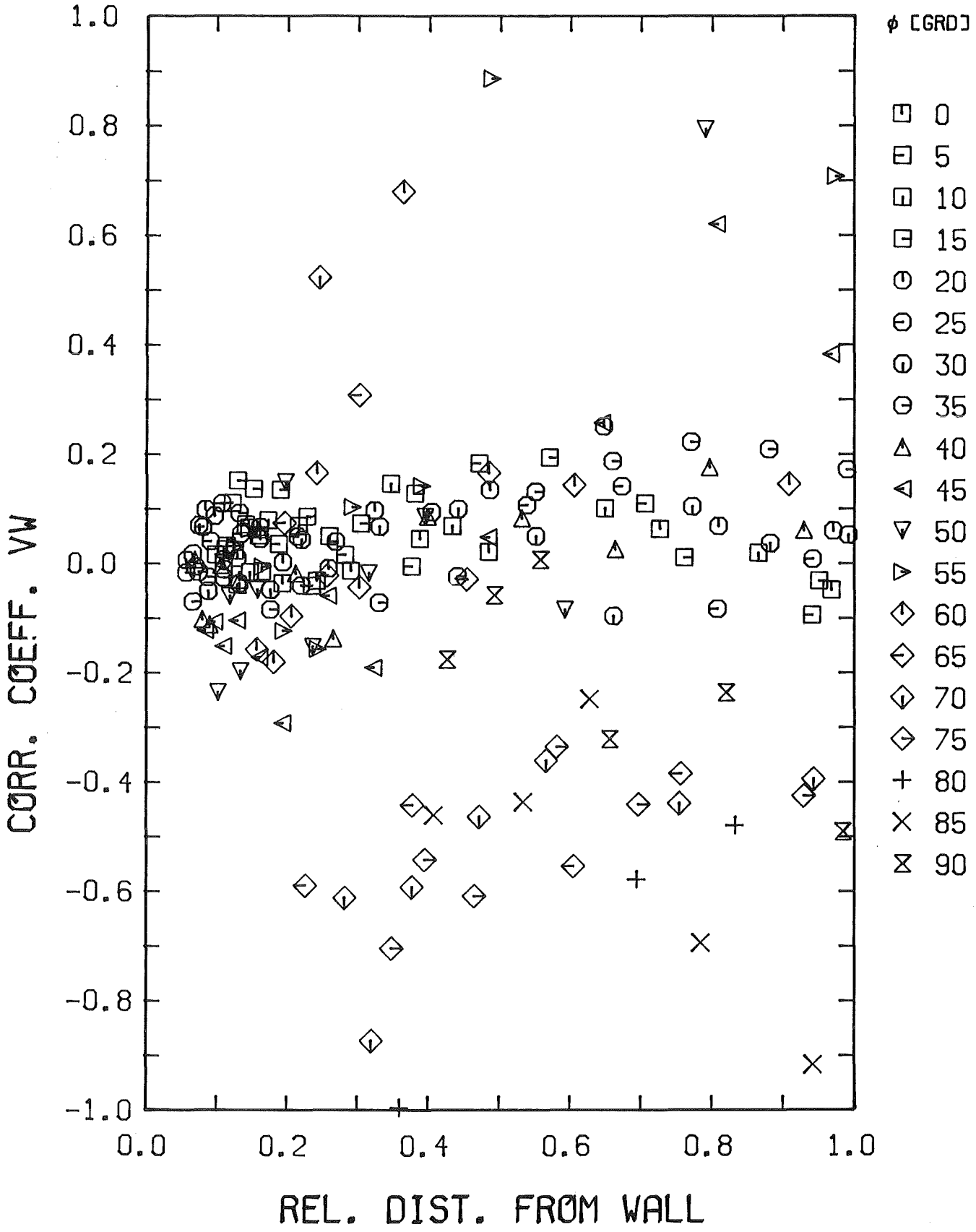

Fig. 34-2 Distribution of the correlation coefficient transverse to the wall in the r/ϕ-part of quadrant 2

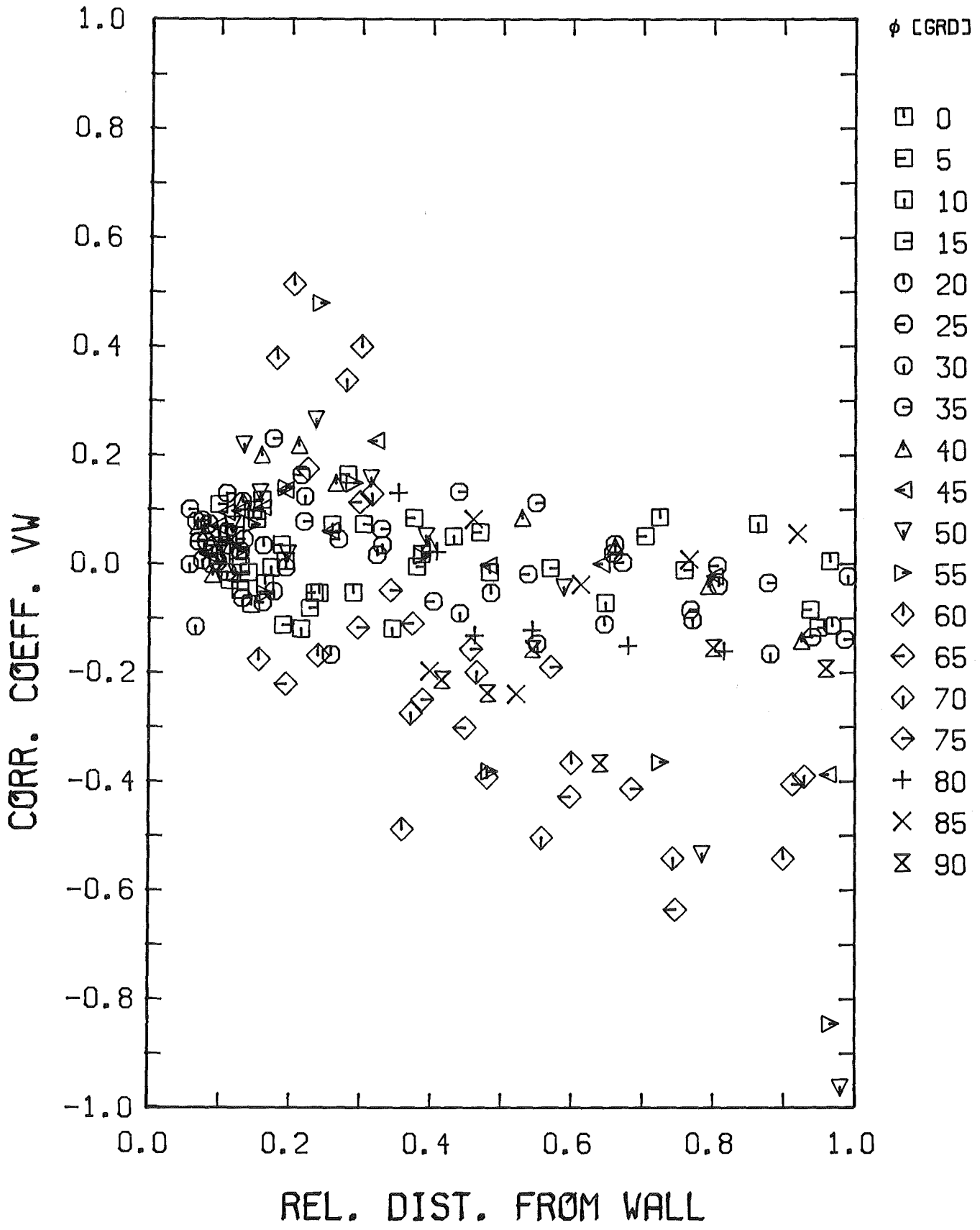

Fig. 34-3 Distribution of the correlation coefficient transverse to the wall in the r/ϕ-part of quadrant 3

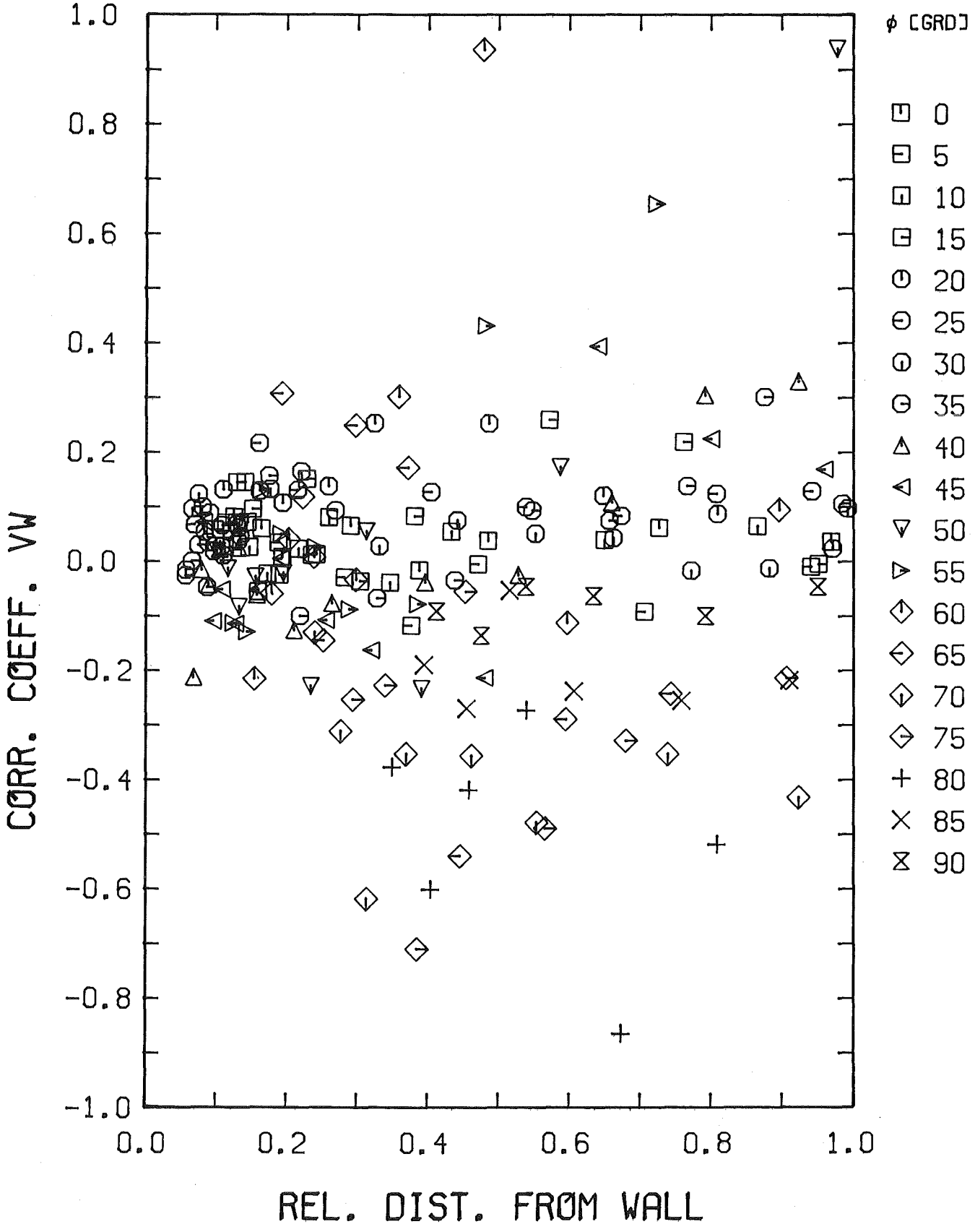

Fig. 34-4 Distribution of the correlation coefficient transverse to the wall in the r/ϕ-part of quadrant 4

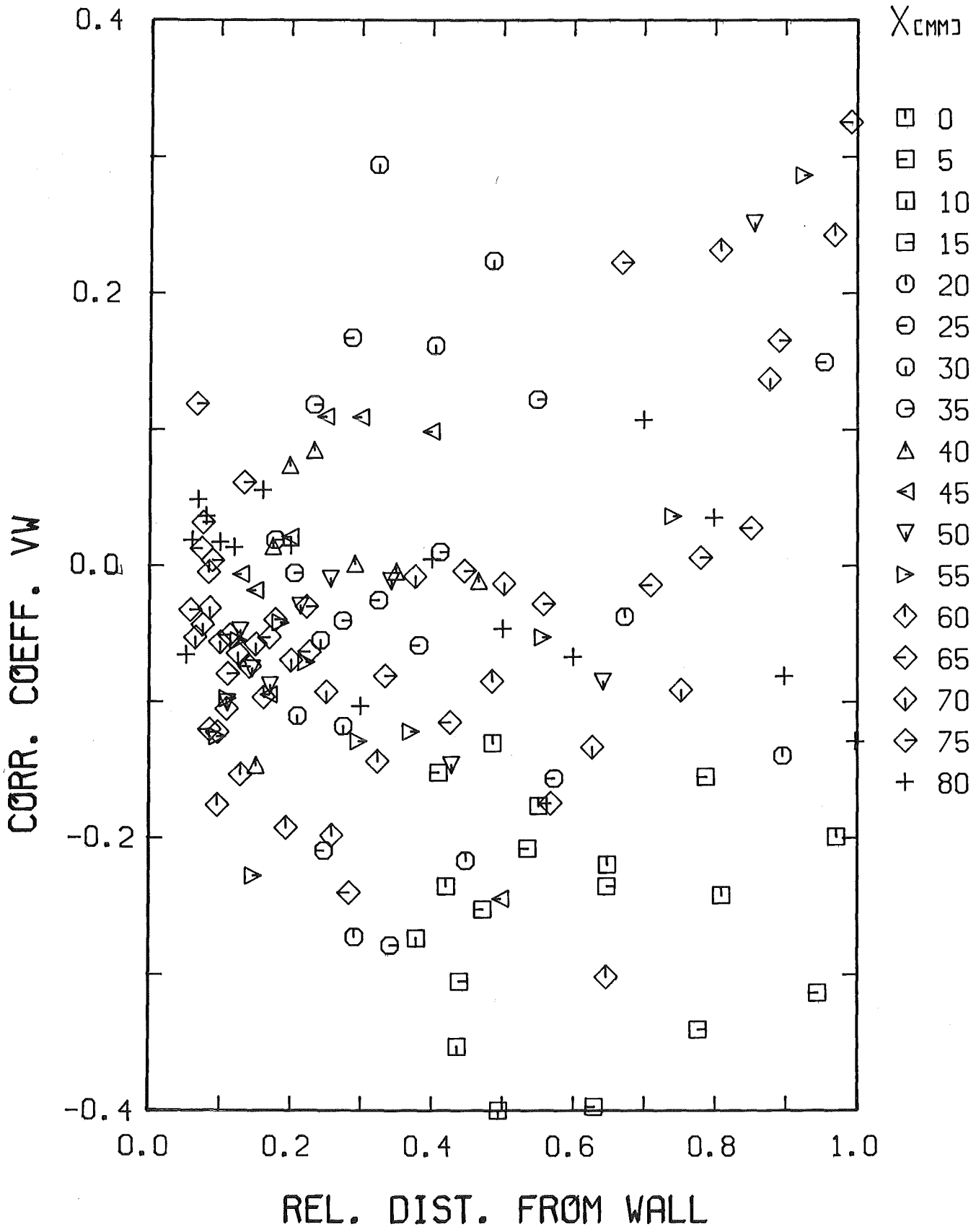

Fig. 35-1 Distribution of the correlation coefficient transverse to the wall in the r/ϕ-part of quadrant 1

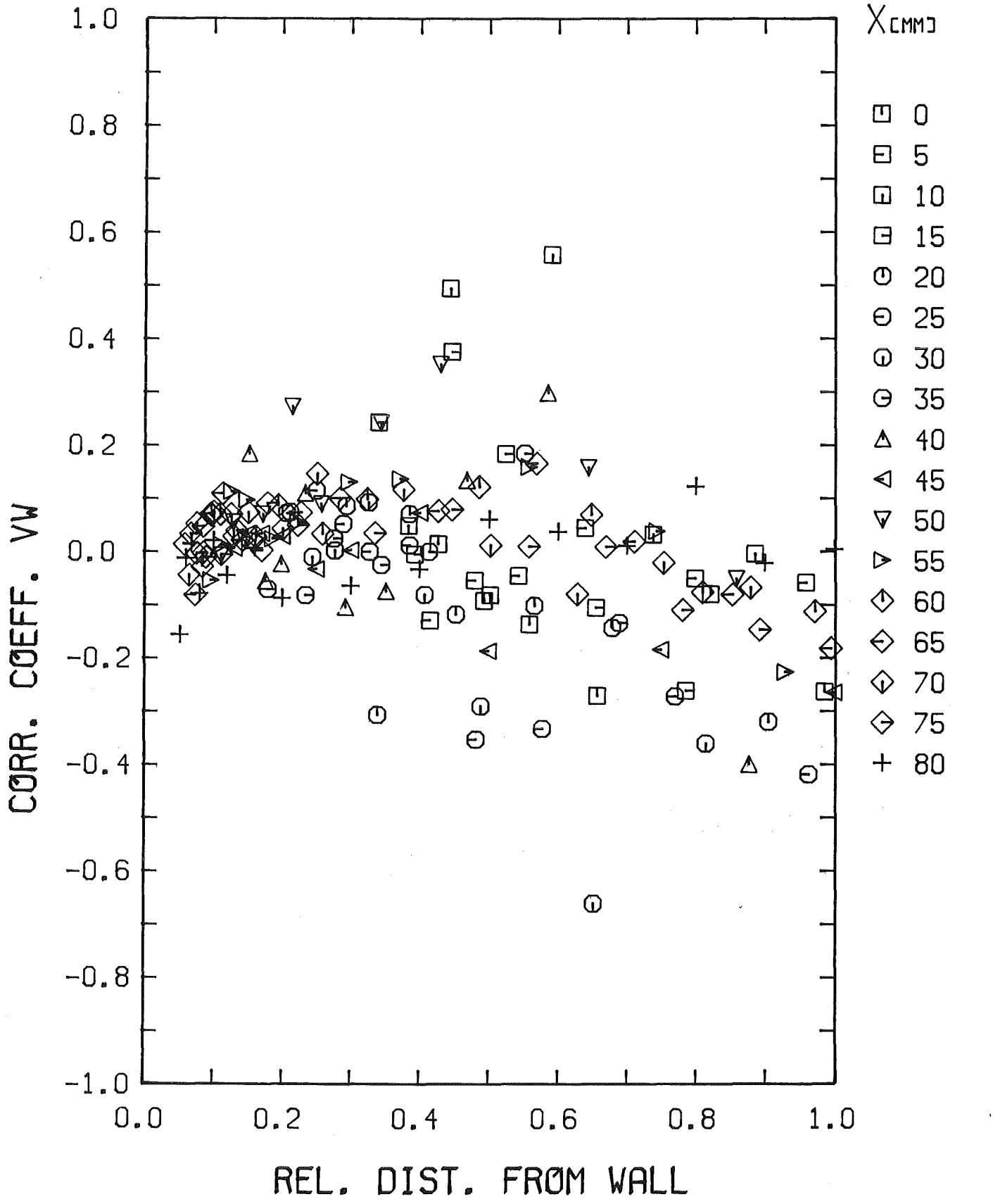

Fig. 35-2 Distribution of the correlation coefficient transverse to the wall in the r/ϕ-part of quadrant 2

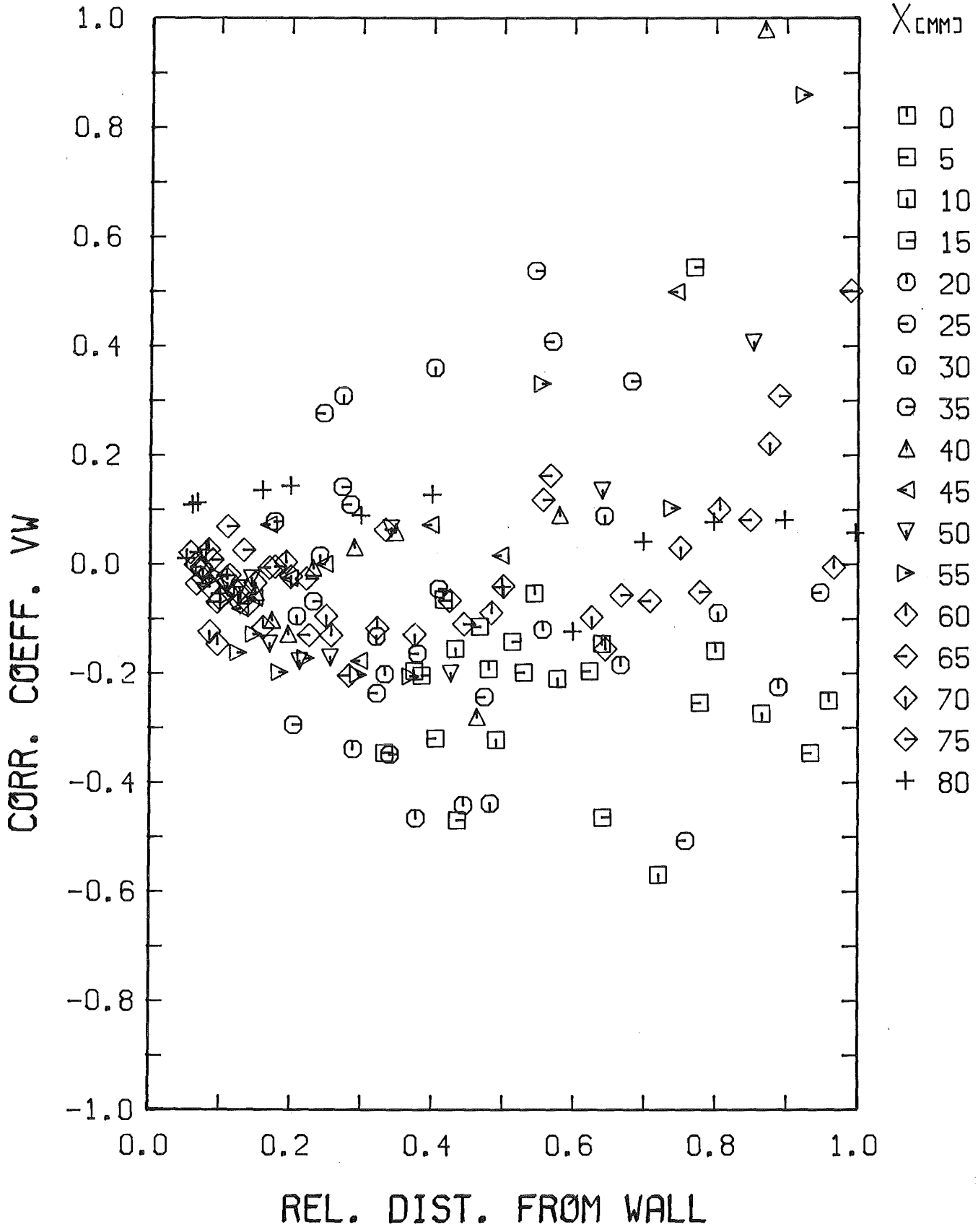

Fig. 35-3 Distribution of the correlation coefficient transverse to the wall in the r/ϕ-part of quadrant 3

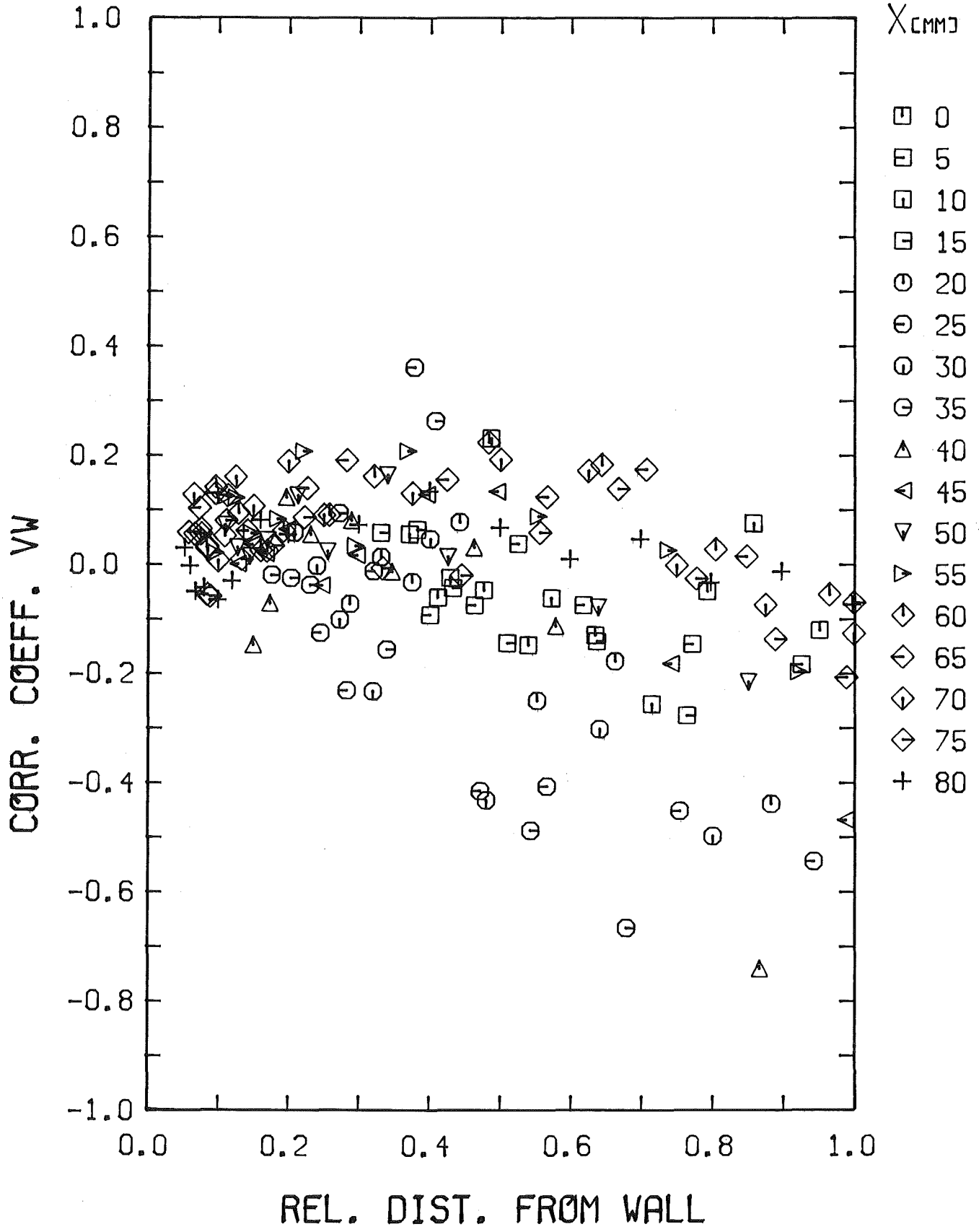

Fig. 35-4 Distribution of the correlation coefficient transverse to the wall in the r/ϕ-part of quadrant 4

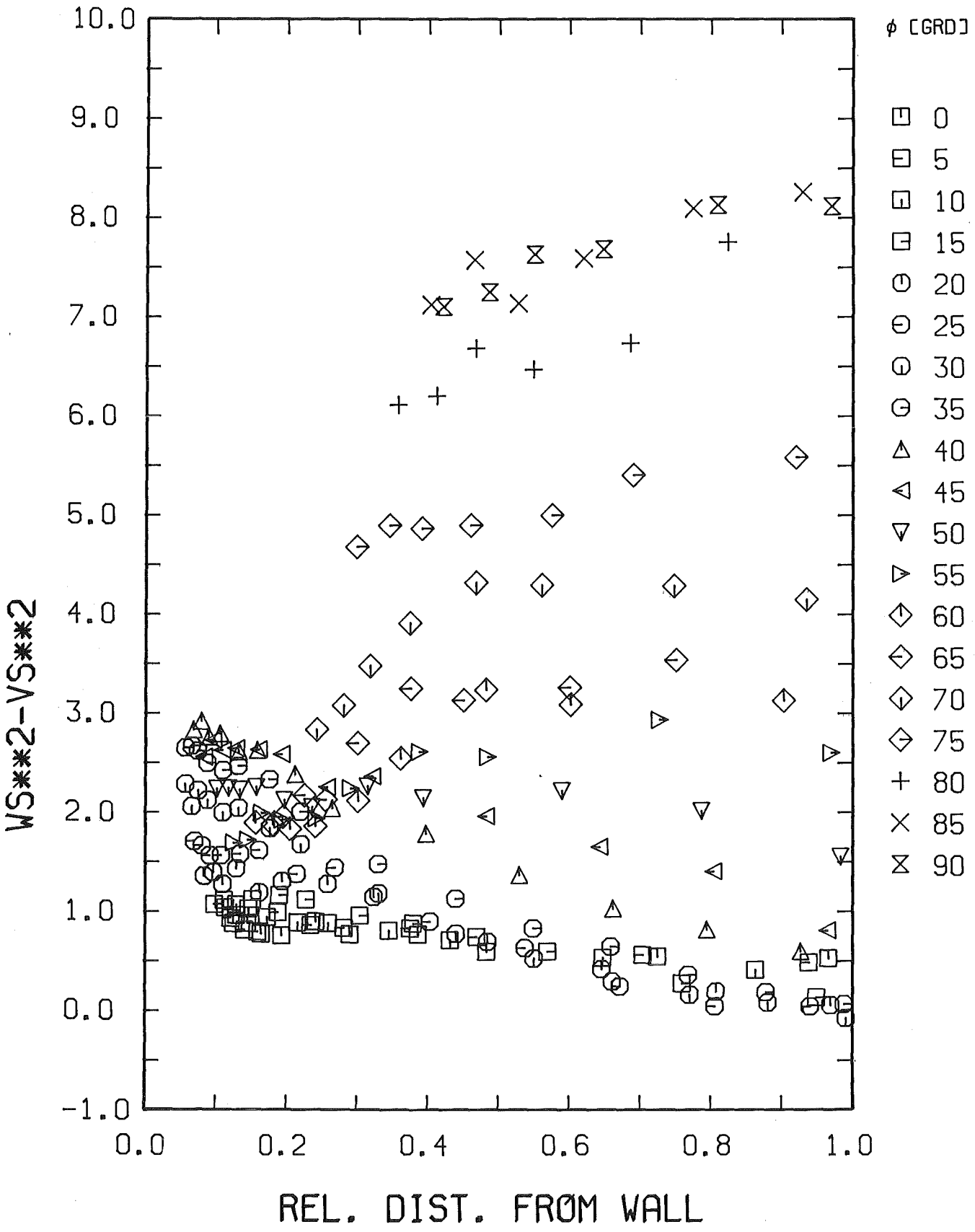

Fig.36-1 Distribution of the difference between the turbulence intensities parallel and perpendicular to the wall in the r/ϕ-part of quadrant 1

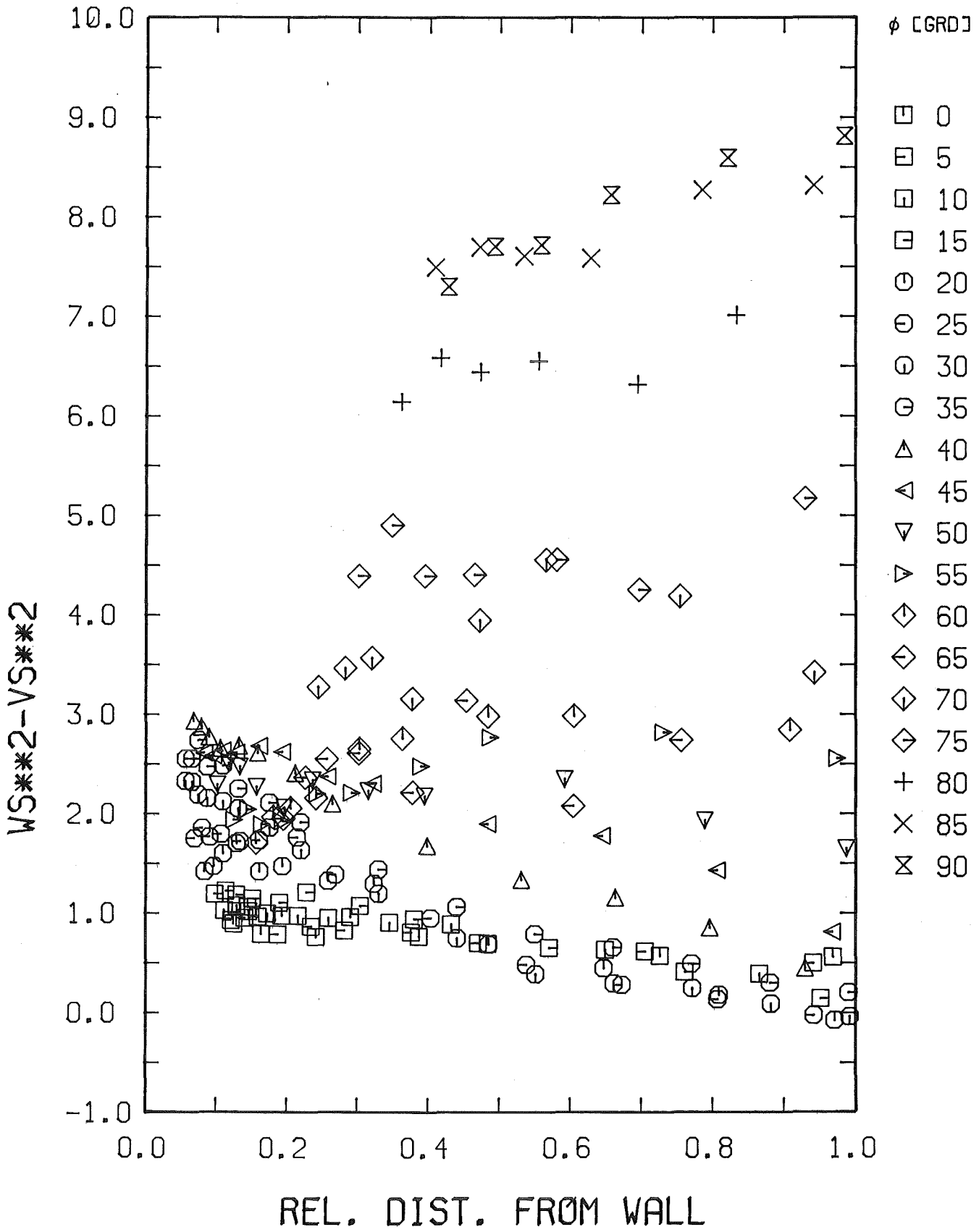

Fig.36-2 Distribution of the difference between the turbulence intensities parallel and perpendicular to the wall in the r/ϕ-part of quadrant 2

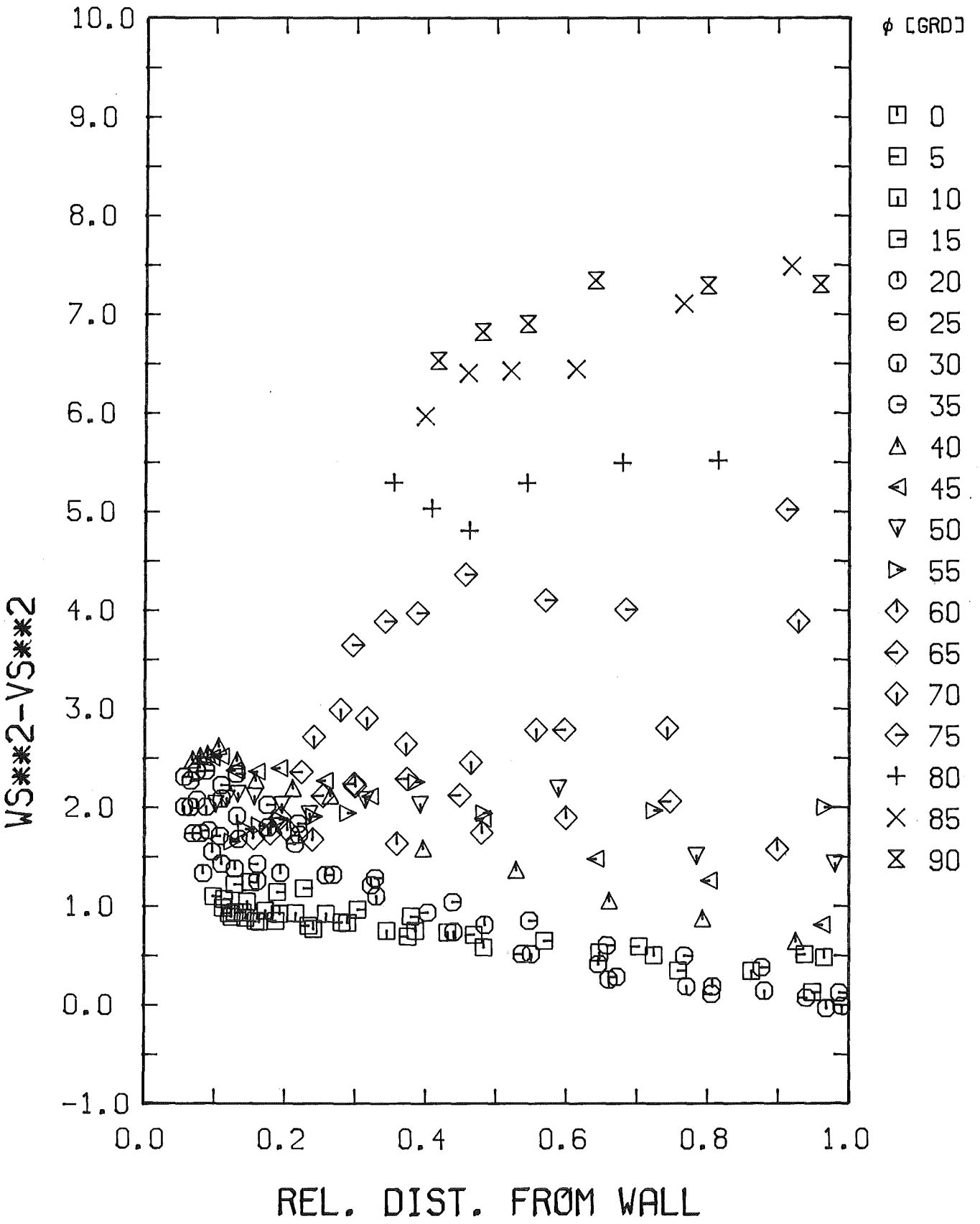

Fig.36-3 Distribution of the difference between the turbulence intensities parallel and perpendicular to the wall in the r/ϕ-part of quadrant 3

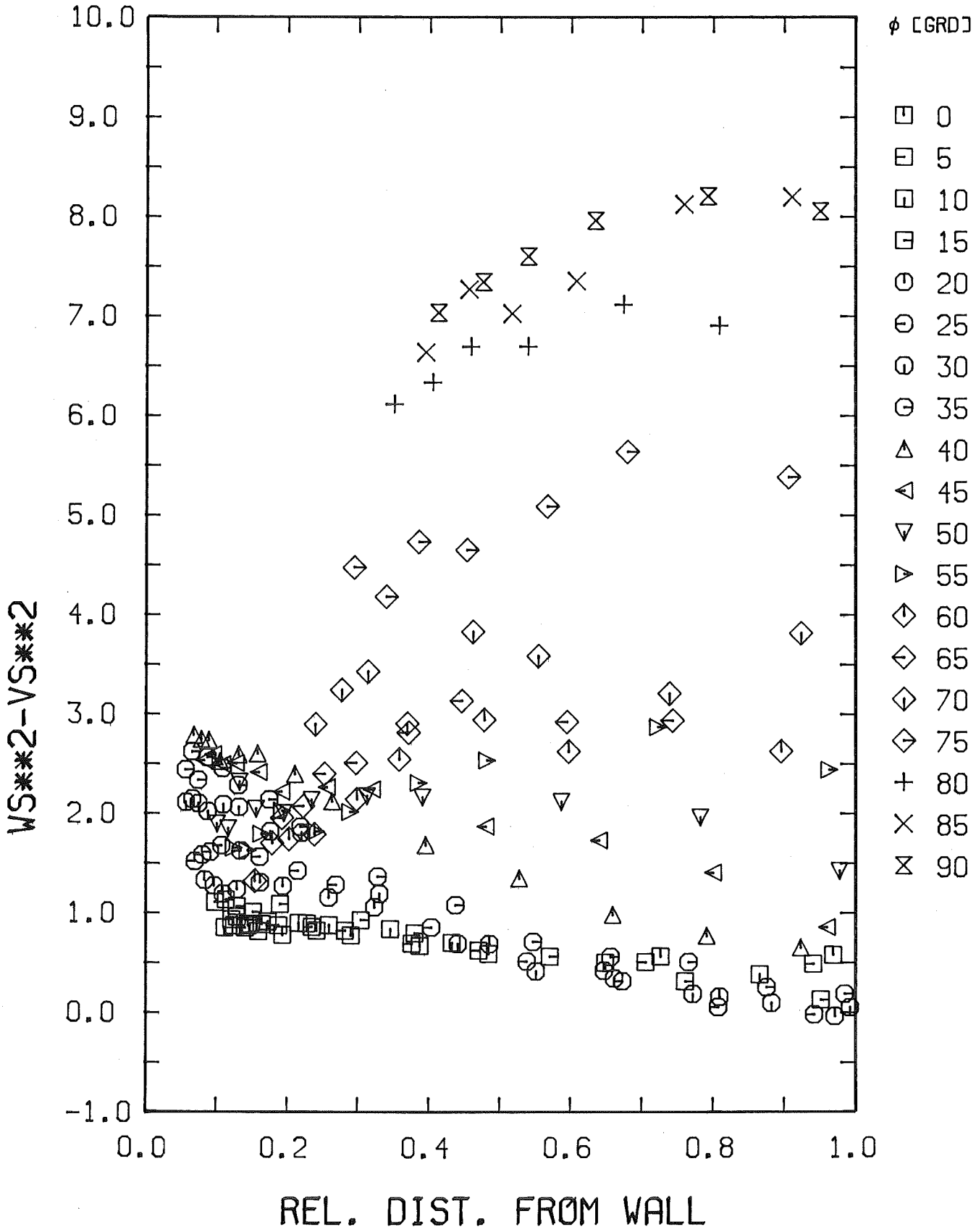

Fig.36-4 Distribution of the difference between the turbulence intensities parallel and perpendicular to the wall in the r/ϕ-part of quadrant 4

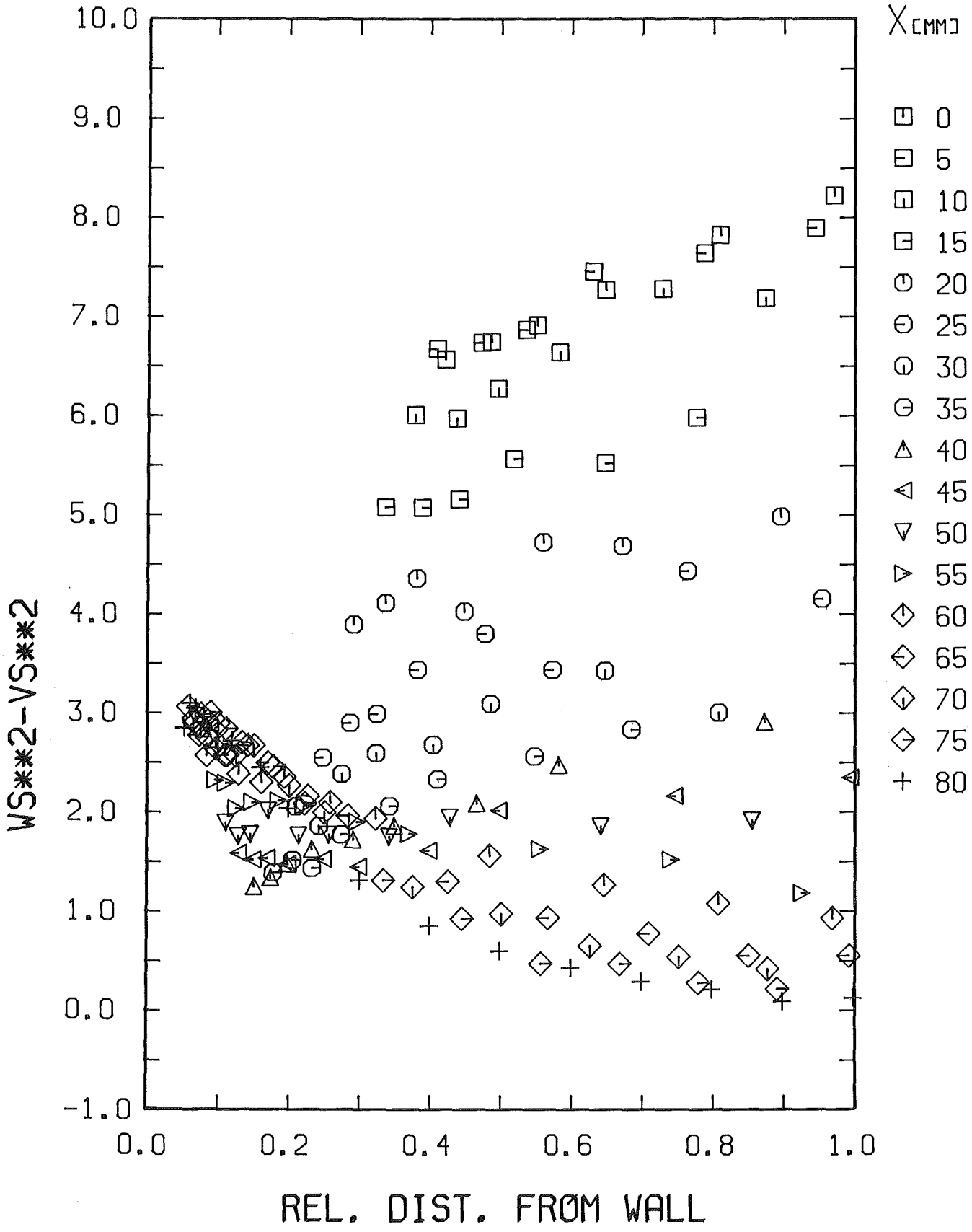

Fig.37-1 Distribution of the difference between the turbulence intensities parallel and perpendicular to the wall in the x/y-part of quadrant 1

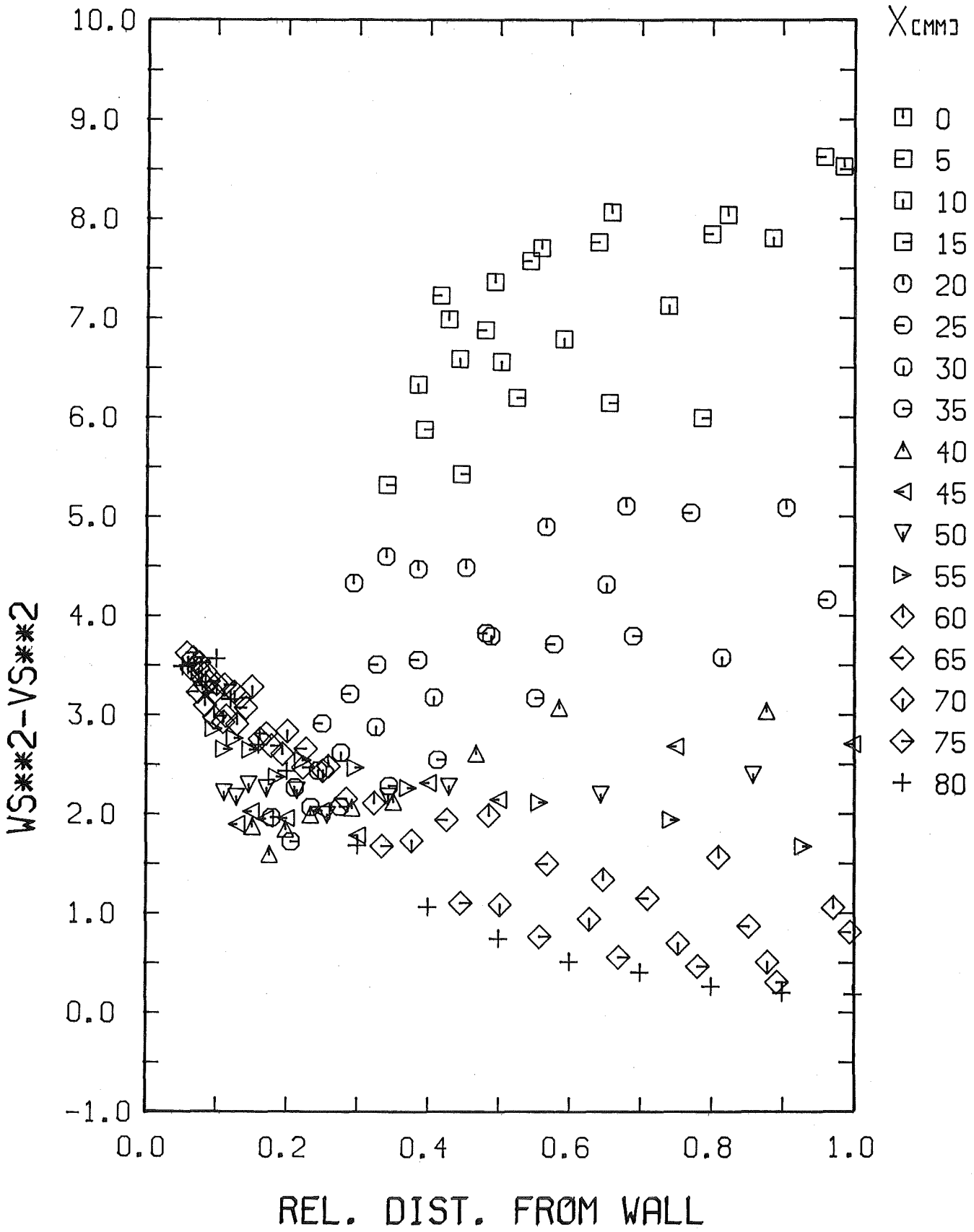

Fig.37-2 Distribution of the difference between the turbulence intensities parallel and perpendicular to the wall in the x/y-part of quadrant 2

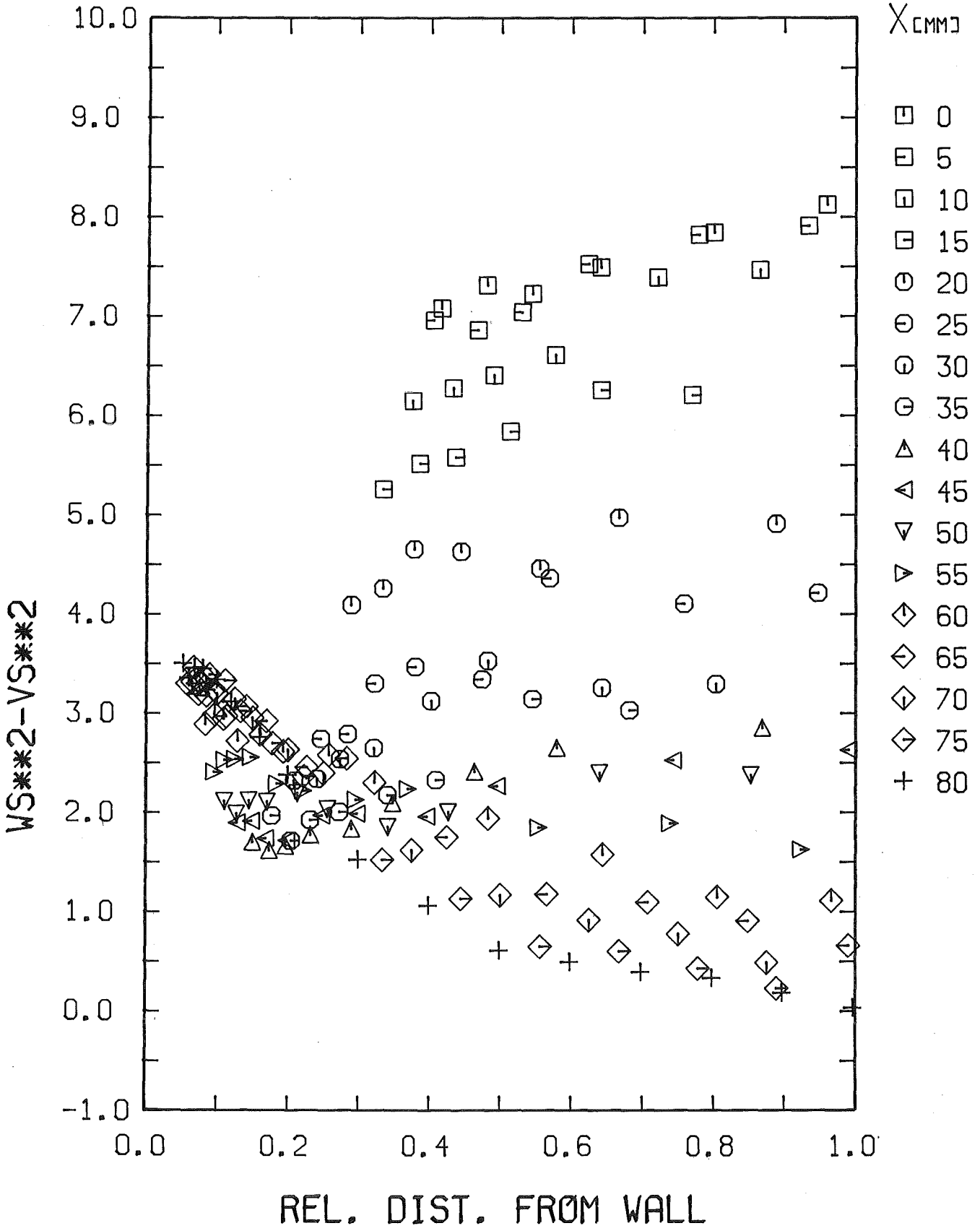

Fig.37-3 Distribution of the difference between the turbulence intensities parallel and perpendicular to the wall in the x/y-part of quadrant 3

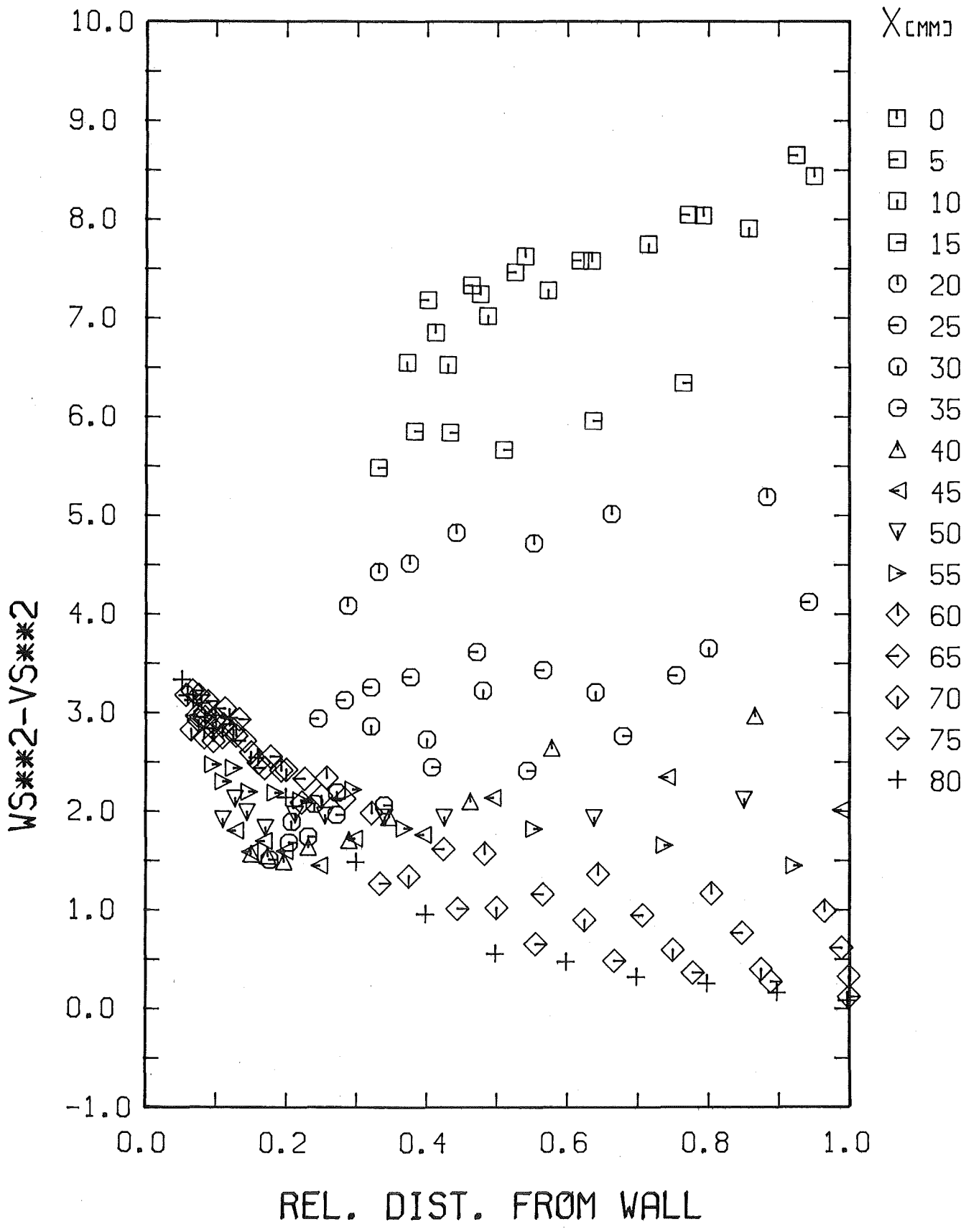

Fig.37-4 Distribution of the difference between the turbulence intensities parallel and perpendicular to the wall in the x/y-part of quadrant 4

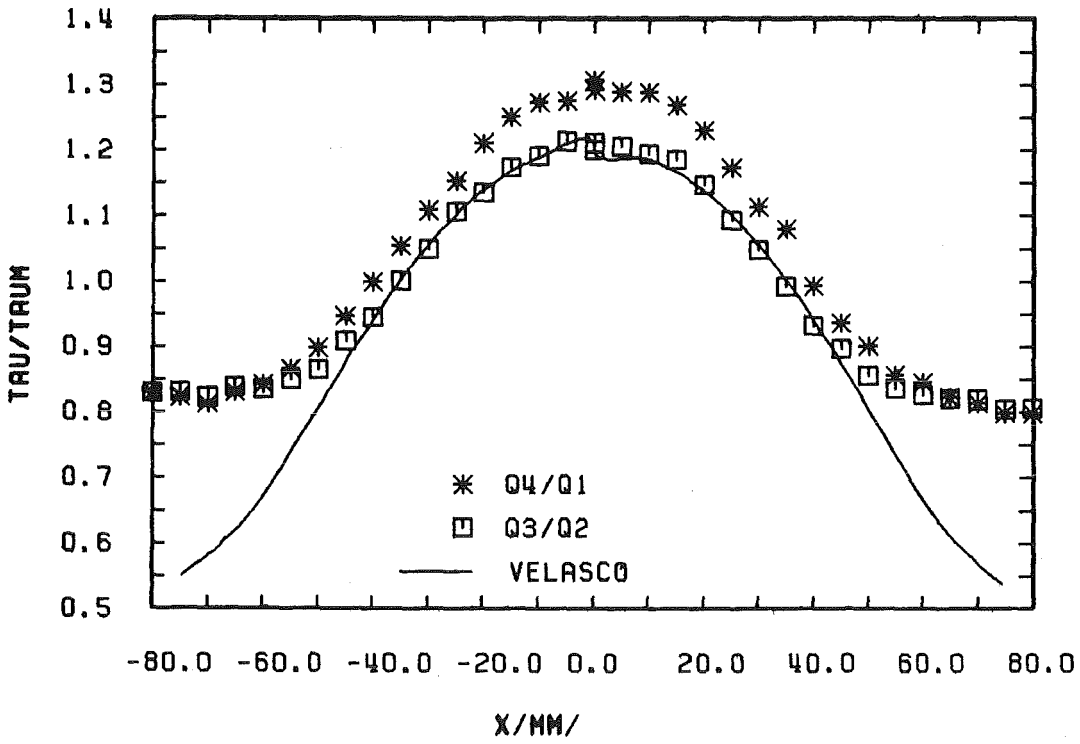

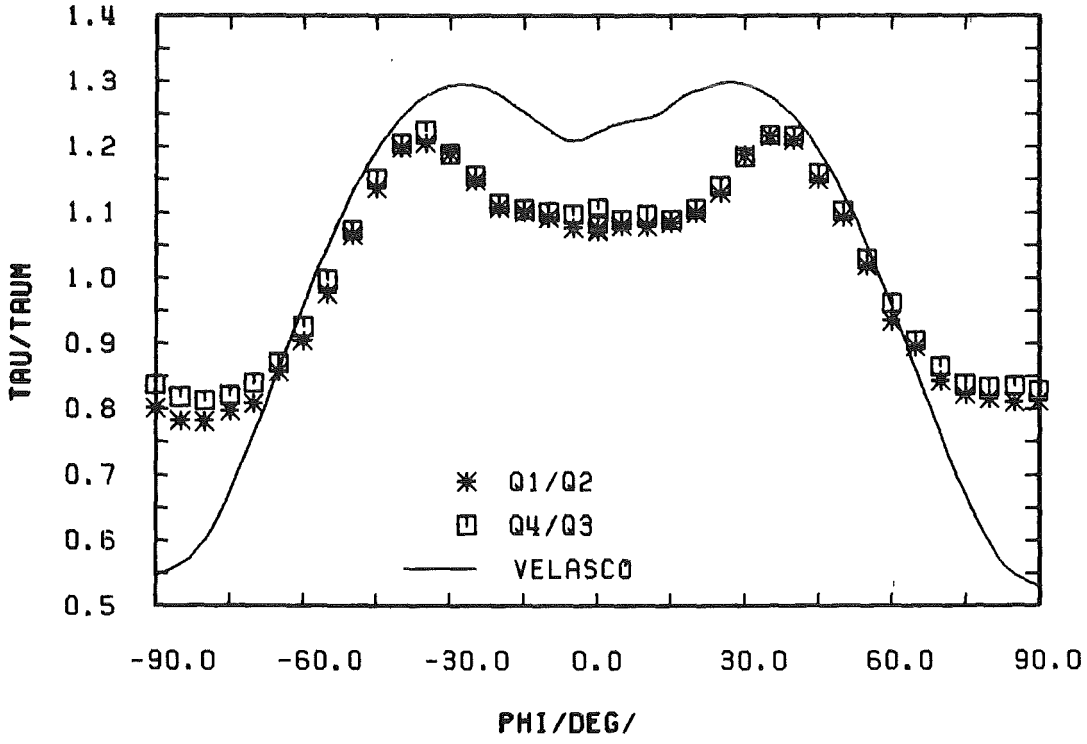

Fig. 38 Comparison between experimental wall shear stresses and prediction by VELASCO

Table 1: Geometry parameters of the four quadrants

	AH	AXS	ARW	F	P	D_h*10
	mm	mm	mm	mm^2	mm	mm
Q1	75.71	79.88	69.53	2250.77	189.10	4.76
Q2	75.62	79.85	69.53	2241.31	189.07	4.74
Q3	75.75	79.86	69.50	2255.73	189.03	4.77
Q4	75.81	79.82	69.50	2257.48	188.99	4.78

F:Flow area — $F=AH*AXS-0.25*3.1416*ARW^2$

P:Wetted perimeter — $P=AXS+0.5*3.1416*ARW$

D_h:Hydraulic diameter — $D_h=4*F/P$

Table 2 : Average velocity in the quadrants and in the parts of the quadrants

Channel		Relative velocity U_{mit}	Velocity ms^{-1}	Discrepance %
Q1	R/Φ	0.7362	20.431	0.12
	X/Y	0.7130	19.786	0.03
Q1		0.7276	20.192	0.02
Q2	R/Φ	0.7359	20.423	0.08
	X/Y	0.7177	19.917	0.42
Q2		0.7292	20.236	0.20
Q3	R/Φ	0.7326	20.331	0.47
	X/Y	0.7142	19.819	0.08
Q3		0.7258	20.141	0.27
Q4	R/Φ	0.7367	20.445	0.18
	X/Y	0.7140	19.815	0.09
Q4		0.7283	20.211	0.08
$U_{av,mit}$		0.7277	20.195	------

U_{ref}=27.752 ms^{-1}

$U = U_{mit} * U_{ref}$

Discrepance=X/X_{av}

D_{max}=Maximal Discrepance in Symmetrical Parts

$D_{max,R/\Phi}$=0.47% (in Q4)

$D_{max,X/Y}$=0.42% (in Q2)

$D_{max,Q}$ =0.27% (in Q2)

Table 3: Maximum difference between the local velocities in the parts of the quadrants

Channel		** Relative Velocity U_{mit}	Discrepance %
Q1	R/Φ	0.647	0.73
	X/Y	0.558	2.67
Q2	R/Φ	0.668	2.49
	X/Y	0.578	1.72
Q3	R/Φ	0.650	0.27
	X/Y	0.575	1.19
Q4	R/Φ	0.642	1.50
	X/Y	0.562	1.11

** the relative velocity at four symmetrical points with maximum difference of velocity

WANDSCHUBSPANNUNGS-MESSERGEBNISSE

MITTLERE WANDSCHUBSPANNUNG TAUAV = 1.1383 PA

POSITION GRAD/MM	R/PHI VERS.-NR. 3	X/Y VERS.-NR. 4
0.0	1.0736	0.7982
5.0	1.0755	0.7971
10.0	1.0905	0.8142
15.0	1.0992	0.8218
20.0	1.1066	0.8439
25.0	1.1473	0.8555
30.0	1.1903	0.8999
35.0	1.2044	0.9355
40.0	1.1975	0.9922
45.0	1.1355	1.0783
50.0	1.0644	1.1124
55.0	0.9756	1.1727
60.0	0.9027	1.2289
65.0	0.8560	1.2672
70.0	0.8081	1.2884
75.0	0.7962	1.2877
80.0	0.7810	1.3059
85.0	0.7815	
90.0	0.8006	

Table 4: Wall Shear Stress in Quadrant 1

WANDSCHUBSPANNUNGS-MESSERGEBNISSE

MITTLERE WANDSCHUBSPANNUNG TAUAV = 1.1247 PA

POSITION GRAD/MM	R/PHI VERS.-NR. 1	X/Y VERS.-NR. 2
0.0	1.0836	0.8142
5.0	1.0918	0.8133
10.0	1.0910	0.8287
15.0	1.0958	0.8291
20.0	1.1105	0.8359
25.0	1.1417	0.8453
30.0	1.2006	0.8653
35.0	1.2295	0.9060
40.0	1.2238	0.9423
45.0	1.1634	1.0030
50.0	1.1054	1.0587
55.0	1.0297	1.1051
60.0	0.9445	1.1600
65.0	0.9050	1.1986
70.0	0.8525	1.2073
75.0	0.8315	1.2195
80.0	0.8251	1.2132
85.0	0.8193	
90.0	0.8211	

Table 5: Wall Shear Stress in Quadrant 2

WANDSCHUBSPANNUNGS-MESSERGEBNISSE

MITTLERE WANDSCHUBSPANNUNG TAUAV = 1.1361 PA

POSITION GRAD/MM	R/PHI VERS.-NR. 7	X/Y VERS.-NR. 8
0.0	1.1076	0.8305
5.0	1.0901	0.8310
10.0	1.0964	0.8234
15.0	1.0901	0.8384
20.0	1.1061	0.8355
25.0	1.1412	0.8508
30.0	1.1845	0.8651
35.0	1.2191	0.9092
40.0	1.2168	0.9461
45.0	1.1599	1.0015
50.0	1.1030	1.0494
55.0	1.0288	1.1066
60.0	0.9618	1.1362
65.0	0.9054	1.1741
70.0	0.8650	1.1922
75.0	0.8386	1.2148
80.0	0.8342	1.2119
85.0	0.8361	
90.0	0.8286	

Table 6: Wall Shear Stress in Quadrant 3

WANDSCHUBSPANNUNGS-MESSERGEBNISSE

MITTLERE WANDSCHUBSPANNUNG TAUAV = 1.1476 PA

POSITION GRAD/MM	R/PHI VERS.-NR. 5	X/Y VERS.-NR. 6
0.0	1.0730	0.8222
5.0	1.0871	0.8165
10.0	1.0903	0.8056
15.0	1.0940	0.8229
20.0	1.1028	0.8342
25.0	1.1447	0.8584
30.0	1.1781	0.8895
35.0	1.2130	0.9377
40.0	1.1929	0.9905
45.0	1.1413	1.0438
50.0	1.0629	1.0982
55.0	0.9881	1.1421
60.0	0.9169	1.1985
65.0	0.8628	1.2396
70.0	0.8322	1.2617
75.0	0.8137	1.2638
80.0	0.8055	1.2801
85.0	0.8110	
90.0	0.8291	

Table 7: Wall Shear Stress in Quadrant 4

Table 8: Measured Friction Factors

	Q1	Q2	Q3	Q4	Av
τ_{av}, Pa	1.138	1.125	1.136	1.148	1.137
U_m, m/s	20.19	20.24	20.14	20.21	20.19
$Re*10^4$	6.102	6.091	6.103	6.132	6.106
λ_τ	0.0191	0.0188	0.0192	0.0193	0.0191
$\lambda_{\Delta p}$	0.0194	0.0193	0.0196	0.0195	0.0194

Table 9 : Comparison between average velocities and wall shear stresses in all quadrants and the parts of the quadrants

Channel		U_{rel} m/s	$U^{1.8}_{rel}$	τ_{rel} Pa	D %
Q1	R/Φ	1.117	1.021	1.010	1.13
	X/Y	0.980	0.964	0.990	2.65
Q1		1.000	1.000	1.001	0.18
Q2	R/Φ	1.011	1.020	1.023	0.27
	X/Y	0.986	0.975	0.943	3.40
Q2		1.002	1.004	0.989	1.44
Q3	R/Φ	1.007	1.012	1.035	1.37
	X/Y	0.981	0.967	0.951	1.71
Q3		0.997	0.995	1.000	0.40
Q4	R/Φ	1.012	1.022	1.026	0.34
	X/Y	0.981	0.966	0.987	2.13
Q4		1.000	1.001	1.010	0.80

$U_{tot,av}$=20.195 m/s

$\tau_{tot,av}$=1.137 Pa

U_{rel}:Average velocity related to overall average

τ_{rel}:Average wall shear stress related to overall average

$D=(U^{1.8}_{rel}-\tau_{rel})/\tau_{rel}*100$ / % /